

# Action Spectroscopy of Strongly Bound Clusters in the Gas Phase

vorgelegt von  
Diplom-Physiker  
Marko Härtelt  
aus Berlin

Von der Fakultät II - Mathematik und Naturwissenschaften  
der Technischen Universität Berlin  
zur Erlangung des akademischen Grades  
Doktor der Naturwissenschaften  
Dr. rer. nat.

genehmigte Dissertation

Promotionsausschuss:

Vorsitzende: Prof. Dr. rer. nat. Sabine Klapp

Berichter: Prof. Dr. rer. nat. Thomas Möller

Berichter: Prof. Dr. rer. nat. Gerard Meijer

Tag der wissenschaftlichen Aussprache: 16.08.2012

Berlin 2012

D 83



# Abstract

Marko Härtelt,

## **Action Spectroscopy of Strongly Bound Clusters in the Gas Phase**

The work presented in this thesis aims to provide experimental spectroscopic data to determine the geometric structures of strongly bound gas-phase clusters as function of their size and charge state. The development of spectroscopic methods which allow the study of the infrared spectra of clusters while using less common IR sources, infrared free electron lasers, was among the major objectives. Very generally applicable methods are presented, which allow previously inaccessible systems to be investigated. These new techniques are combined with more established methods to obtain a deeper insight into the properties of a single system, magnesium oxide clusters.

Tunable IR-UV two-color ionization allows the investigation of the IR spectra of neutral clusters. It is used to study semiconductor and metal oxide clusters in the mid and far-IR with the Free Electron Laser for Infrared eXperiments (FELIX) as the IR light source.

For anionic (transition metal) clusters IR spectra are obtained using IR resonance enhanced multiple photon electron detachment spectroscopy, a technique that recently became possible with the availability of a more intense IR light source, the Free Electron Laser for Intra-Cavity Experiments (FELICE). The experiments are among the first utilizing this new laser. Instrument development and proof-of-principle experiments are performed for metal carbide clusters, which are also studied by anion photoelectron spectroscopy to provide useful information about the energetics of the electron detachment process. The method is then applied for the IR spectroscopy of the transition metal cluster anions of niobium.

Magnesium oxide clusters of different size, charge state, and stoichiometry are studied by different IR spectroscopy methods. These cluster systems serve as models for a promising catalyst for the activation of methane. The structural differences between differently charged gas-phase clusters and the bulk structure are investigated, as well as the effects of the addition of oxygen and/or hydrogen to the clusters. Furthermore, reactions of the clusters with different ligands, such as water, methane, or carbon monoxide are examined.





# Zusammenfassung

Marko Härtelt,

## **Action Spectroscopy of Strongly Bound Clusters in the Gas Phase**

Ziel der Doktorarbeit ist es, spektroskopische Informationen über die Geometrie von stark gebundenen Clustern in der Gasphase als Funktion ihrer Größe und ihres Ladungszustandes experimentell zu ermitteln. Der Schwerpunkt liegt auf der Entwicklung von Methoden zur Infrarot-Spektroskopie von Clustern unter Verwendung von weniger üblichen Lichtquellen, Infrarot Freie-Elektronen-Lasern. Dabei werden Verfahren mit breiter Anwendbarkeit präsentiert, welche die Untersuchung bisher unzugänglicher Systeme erlauben. Diese neuen Techniken werden mit etablierteren Methoden kombiniert, um tiefere Einblicke in ein einzelnes System (Magnesiumoxid) zu erlangen.

Mittels abstimmbarer IR-UV-Zwei-Farben-Ionisation werden die IR-Spektren von neutralen Clustern bestimmt. Halbleiter und Metalloxid Cluster werden mit ihr im fernen und mittleren Infrarotbereich untersucht. Dabei kommt der Freie-Elektronen-Laser für Infrarot-Experimente (FELIX) zum Einsatz.

Für anionische (Übergangsmetall-) Cluster können IR-Spektren mittels IR-Resonanz-Verstärkter-Mehr-Photonen-Elektronenablösung aufgenommen werden. Diese Technik wurde erst kürzlich durch die Verfügbarkeit einer intensiveren Infrarot Strahlungsquelle, dem Freie-Elektronen-Laser für Intra-Cavity-Experimente (FELICE), ermöglicht. Die hier vorgestellten Experimente zählen zu den ersten, die diesen neuen Laser verwenden. Die Instrumentenentwicklung und der Nachweis des Funktionsprinzips der Messmethode erfolgen durch Messungen an Metallkarbiden. Diese wurden zusätzlich mit Anionen-Photoelektronen-Spektroskopie untersucht, welche nützliche Informationen über die Energetik des Elektronenauslöseprozesses liefert. Die Methode wird anschließend dazu genutzt, IR-Spektren von Übergangsmetall-Clustern aus Niob zu gewinnen.

Magnesiumoxid-Cluster mit unterschiedlicher Größe, Ladungszustand oder Stoichiometrie werden mittels verschiedenster IR Spektroskopiemethoden untersucht. Diese Cluster dienen als Modellsysteme für einen der vielversprechendsten Katalysatoren für die Aktivierung von Methan. Die strukturellen Unterschiede zwischen verschiedenen geladenen Gasphasen-Clustern und der Festkörperstruktur, sowie der Einfluss von zusätzlichem Sauerstoff und/oder Wasserstoff, werden er-

forscht. Zusätzlich wird die Reaktivität der Cluster mit verschiedenen Liganden, wie Wasser, Methan und Kohlenstoffmonoxid analysiert.

# Contents

<b>1. Introduction</b>	<b>1</b>
1.1. Outline of the thesis . . . . .	4
<b>2. Experimental methods</b>	<b>7</b>
2.1. Photoelectron spectroscopy . . . . .	7
2.2. IR spectroscopy . . . . .	10
2.2.1. IR spectroscopy methods for low-density gas-phase species .	12
2.2.2. Multiple photon absorption and internal vibrational redistri- bution . . . . .	16
2.3. IR free electron lasers - The FELIX facility . . . . .	18
2.4. The setups . . . . .	21
2.4.1. The molecular beam setup in Berlin . . . . .	21
2.4.1.1. Laser ablation cluster sources . . . . .	22
2.4.1.2. Time-of-flight mass spectrometer . . . . .	25
2.4.1.3. UV-VIS and photoionization efficiency measure- ments . . . . .	26
2.4.1.4. Photoelectron spectroscopy via velocity map imaging	27
2.4.2. The cluster setup at the FELIX facility . . . . .	31
2.4.2.1. IR-MPD spectroscopy - Experimental . . . . .	33
<b>3. Spectroscopy of neutral silicon clusters</b>	<b>35</b>
3.1. Introduction . . . . .	35
3.2. Experimental . . . . .	38
3.2.1. Dissociation – IR multiple photon dissociation spectroscopy .	38
3.2.2. Ionization – Tunable IR-UV two-color ionization spectroscopy	40
3.3. Theory . . . . .	42
3.4. Results and discussion . . . . .	43
3.5. Conclusions . . . . .	51

<b>4. Charged and neutral magnesium oxide clusters</b>	<b>53</b>
4.1. Stoichiometric $(\text{MgO})_n^{+,0}$ clusters	55
4.1.1. Cationic clusters	57
4.1.1.1. $(\text{MgO})_n^+$ clusters – IR-MPD spectroscopy of mes-senger complexes (Ar vs. $\text{O}_2$ )	57
4.1.1.2. Theoretical method	64
4.1.1.3. Results and discussion	64
4.1.2. Neutral clusters	68
4.1.2.1. $(\text{MgO})_n$ clusters – IR-UV2CI spectroscopy	68
4.1.2.2. Results and discussion	69
4.1.3. Comparison between neutral and cationic $(\text{MgO})_n$ clusters	79
4.1.4. Conclusions	79
4.2. Activation of molecular oxygen in MgO clusters	81
4.2.1. Experimental	82
4.2.2. Results and discussion	84
4.2.2.1. The observation of different oxygen species using the example of $\text{Mg}_6\text{O}_7$	85
4.2.2.2. (Di-)oxygen species in larger MgO clusters	89
4.2.2.3. Cationic and neutral cluster containing 4 and 5 Mg atoms	94
4.2.2.4. Comparison to surface studies	95
4.2.3. Conclusion	95
4.3. Ligand complexes of MgO	96
4.3.1. $\text{O}_2$ and $\text{H}_2\text{O}$ complexes of the magnesium superoxide cation $\text{MgO}_2^+$	97
4.3.2. Hydroxilation of $\text{Mg}_n\text{O}_m^+$	102
4.3.3. CO on cationic MgO clusters	106
4.3.4. Methane on MgO	109
4.4. Summary and outlook	111
<b>5. Metal and metal-carbon cluster anions</b>	<b>113</b>
5.1. FELICE and the molecular beam setup	115
5.2. IR-REMPED spectroscopy – Experimental	118
5.3. $\text{Ta}_n\text{C}_m^-$ cluster anions	123
5.3.1. IR-REMPED spectra	123
5.3.2. Photoelectron spectra	125
5.3.3. Theoretical method	127
5.3.4. Discussion	128
5.4. Metal cluster anions	135
5.4.1. IR-REMPED spectroscopy of $\text{Nb}_n\text{C}_{1,2}^-$	135

---

5.4.2. IR-REMPED spectroscopy of $\text{Nb}_n^-$ clusters . . . . .	146
5.5. Conclusions . . . . .	150
5.6. Outlook . . . . .	150
<b>6. Summary and concluding remarks</b>	<b>153</b>
6.1. Summary . . . . .	153
6.2. Perspectives for future research . . . . .	155
<b>Appendix A. Low energy isomers for <math>\text{Mg}_n\text{O}_{n+1}^{+,0,-}</math> clusters</b>	<b>157</b>
<b>Bibliography</b>	<b>165</b>
<b>List of Publications</b>	<b>195</b>
<b>Lebenslauf</b>	<b>197</b>
<b>Acknowledgements</b>	<b>199</b>



# 1. Introduction

Nano-sized particles, clusters, composed out of only a few atoms are a unique state of matter whose characteristics differ from those of the atoms or the bulk [1]. Their properties can vary dramatically with cluster size. Many catalysts make use of the special properties of these particles, although these are often not completely understood.

In heterogeneous catalysis often disperse metal particles are used that are distributed on an inert support material [2]. The activity (and selectivity) is governed by the metal particles and their interaction with the support. Due to the complexity of real catalysts, model systems are used in surface science [3], which capture only some of the complexity of the real catalyst. Different approaches can be followed, for instance, metal particle of controlled size can be deposited or grown on a (perfect) metal oxide support. The thickness of the support can then be varied to induce a charge transfer from the underlying metal support on which the metal oxide was grown, which thereby allows the electronic structure of the particle to be changed. A crucial step for understanding the catalytic activity is the determination of the (surface) structure, which is sometimes difficult to access via surface science approaches [3].

Here gas-phase studies can come into play. The geometric and electronic structure, as well as the reactivity of clusters of a given size and charge state are experimentally accessible and can be used to benchmark theoretical predictions. These results can then be correlated with more complex systems. Mass spectrometric detection schemes can be employed to selectively investigate clusters with a well-defined number of atoms.

The prototype system illustrating best the interaction between surface and gas-phase cluster science is the CO oxidation reaction observed for gold nano-particles deposited on a metal oxide support. Haruta *et al.* were the first who realized that compared to bulk gold, nano-particles are not noble [4, 5] and initiated many different studies [6–14]. Although deposited on a support, the nano-particles are not necessarily neutral, as charge transfer processes from the support or by co-deposition of other clusters can occur [15–18]. In the gas phase, the properties of neutral clusters and those of the (usually singly charged) cationic and anionic ones can be separately studied, and therefore be compared.

Structures of singly charged cationic and anionic gold clusters have been stud-

ied, for instance, by ion mobility [19, 20] and electron diffraction in an ion trap [21–23]. For neutral clusters, vibrational spectra have been measured via IR multiple photon dissociation spectroscopy [24]. All these methods are connected with quantum chemical calculations to assign cluster structures.

Other studies investigated the reactivity of free Au clusters with CO and O<sub>2</sub> and showed that anionic clusters are particularly reactive [25–28]. These studies even allow to access reactive intermediates [27, 28], which provides information to test the potential energy landscape of a reaction path obtained from theory. The results in the gas phase correlate well with the surface results, supporting the common assumption that the reactive gold particles are negatively charged [10, 29, 30].

Gas-phase studies do not necessarily only focus on the species directly responsible for the reactivity. The support material is also investigated. Depending on the stoichiometry (*i.e.* the oxygen to metal ratio for a metal oxide) and cluster size, it is possible to prepare clusters representing the pristine or defective surface. This is important as defect centers can interact with the nano-particles but can also be reactive on their own. The cluster sizes required to structurally model a perfect surface can be relatively small, as has been shown for vanadium oxide [31].

Often, gas-phase cluster and surface science approaches are combined to prepare nano-particles of a given size and deposit them later on the surface [10, 15, 17, 18, 32, 33]. This dramatically improves the knowledge on the model system. However, agglomeration of the clusters is a potential problem, when high densities are used. In the gas phase the clusters are isolated. By using clusters as models of the support and for the metal nano-particle, the surface cluster interaction could, in principle, be studied.

However, the exceptional degree of control of size and charge state achievable for gas-phase clusters comes at a cost, as many ‘standard’ spectroscopy methods cannot be applied. Most systems of interest can only be made in low quantities, and then not selectively. Instead, broad distributions in cluster size and charge states are produced. Only systems that can be *selectively* made in high quantities can be studied by direct absorption spectroscopy. Improvements in the sensitivity have been achieved, for instance, by increasing the interaction length, as done in cavity ring down spectroscopy [34], but most methods use mass spectrometry to size select a certain cluster ion.

Most spectroscopic experiments on clusters have to monitor the response of the system to pumping by light, an approach often referred to as ‘action spectroscopy’. This approach is applied in all wavelength regions from the infrared to the visible and ultraviolet to the x-ray regime, and allows spectroscopic information about the geometric and electronic structure of the cluster to be obtained. Optical spectroscopy, *i.e.* UV/VIS [35–37], (anion) photoelectron [38–41], or reso-



nance enhanced multiple photon ionization spectroscopy [42] probes the cluster molecular orbital structure. More recently, x-ray absorption spectroscopy has been developed, which can give selectively information on the electronic structure of certain elements in the cluster via inner-shell excitation [43–47]. Such experiments can also be used to measure the spin and orbital magnetic moments of a cluster via magnetic dichroism spectroscopy [48, 49]. Common to all these techniques is the detection of the absorption via monitoring fragmentation or ionization (using the formed ions or electrons) of the cluster. Such changes of the charge or mass state can be very sensitively detected using mass spectrometry.

IR spectroscopy is particularly well suited to reveal the geometric structure of clusters and their complexes. Different binding motifs lead to absorptions in different regions of the spectrum which can therefore be seen as a fingerprint of the cluster structure. However, in the IR spectral range the photon energy is small, and the absorption of a single photon is often not sufficient to drive a fragmentation or ionization of the cluster. A sufficiently intense light source capable to drive the absorption of multiple IR photons on a vibrational transition, which can cause dissociation (fragmentation) or thermionic electron emission (ionization) is the CO<sub>2</sub> laser, but it allows only spectroscopy in a narrow range around 10  $\mu$ m, which only allows certain cluster complexes to be studied [50]. Through the application of IR free electron lasers to spectroscopy an intense and widely tunable light source, covering also the far-IR, became available. A range of vibrational spectroscopy methods has been developed, including IR resonance enhanced multiple photon ionization, but in particular multiple photon dissociation spectroscopy [51–53], which is the most general of all methods. For the latter, dissociation of the bare cluster, or a more loosely bound messenger complex, is used [54].

Clusters made out of many different substances have been investigated by these methods, such as fullerenes [51], semiconductors [55], transition metals [56], and metal oxides and carbides [52]. These methods are also applicable to systems with an even further increased complexity, such as biomolecules and proteins.

Despite the success of vibrational spectroscopy using IR free electron lasers and multiple photon dissociation spectroscopy, in particular, there are limits. Strongly bound systems, with binding energies of a few eV per atom can often only be studied using messenger tagging. Complex formation, however, can be difficult, cause perturbations of the system, or change the isomer energetic ordering. Methods relying on a different principle to obtain the vibrational spectra are therefore highly desirable.

Two such methods will be presented in the following, both relying on a change of the charge state instead of fragmentation of the cluster. In the first method, a tunable infrared-ultraviolet two-color ionization method is applied to neutral

clusters. The second method is applicable to (transition metal) cluster anions, for which an IR spectroscopy method was missing. This method, IR resonance enhanced multiple photon electron detachment, requires particularly high IR fluence, which only recently became available with the development of the first intra cavity free electron laser.

Besides the development of new methods, the application of the different available methods to investigate various aspects of a single system forms a complementary scientific approach. Quantum chemistry is nowadays able to predict many cluster properties, however, there is often the lack of knowledge, which method is particularly suited for a certain system. The computational cost in treating many-electron systems, such as transition metal clusters, correctly, are still so high, that significant approximations have to be used. Standard density functional theory allows electronic ground state properties to be determined, which is the reason why its predictions are compared with measured vibrational spectra, and often decent agreement is found. Description of the electronic spectra and multiple excited states is much more demanding. Such calculations profit, however, from knowing the geometric structure as this allows one property to be constrained. The combination of two methods, such as anion photoelectron spectroscopy and IR resonance enhanced multiple photon electron detachment, that probe electronic and geometric structure separately, will be shown in the following.

The work presented in this thesis is part of the cluster of excellence ‘Unifying Concepts in Catalysis’ (UniCat) coordinated by the TU Berlin. Within this project a potentially industrially important catalyst for methane activation, (lithium doped) magnesium oxide, was chosen and was tackled by a variety of methods. These range from fundamental investigations on surface and gas-phase model systems trying to reveal an understanding for the reaction mechanism, which may allow the yield and selectivity to be improved, to methods investigating and improving the reaction process in the real (industrial) reactor. In the following work, a variety of different model systems for the active catalyst, and species (presumably) important in the catalytic cycle are studied by several vibrational spectroscopy methods.

## 1.1. Outline of the thesis

This work focusses on the vibrational spectroscopy of strongly bound clusters in the gas phase. A number of different systems has been investigated including bare metal clusters, carbides, and oxides. A key aspect of the investigations has been the development of unique experimental methods that allow to obtain mass-selective vibrational spectra of clusters in different charge states.

Chapter 2 gives a brief introduction into IR spectroscopy and methods avail-

able to obtain the vibrational fingerprints of gas-phase clusters. The basics of the excitation mechanism are described. All these experiments have been performed using an IR free electron laser. Its basic operation principle is explained. Several different experimental setups have been used throughout this work, and two of them are exemplified in more detail. For anionic metal clusters anion photoelectron spectroscopy has also been used, which is also outlined.

In chapter 3, tunable IR UV two-color ionization spectroscopy will be introduced and compared to IR multiple photon dissociation spectroscopy. Both methods are applied to neutral silicon clusters in order to obtain vibrational spectra of clusters in a broader size range. By comparison with theory the detailed cluster structures will be assigned that show the appearance of different structural motifs. A simple modeling of the absorption mechanism used in tunable IR-UV two-color ionization will be discussed.

The next chapter, chapter 4, deals with magnesium oxide. Clusters of different size, charge state, and stoichiometry are investigated, using a wide repertoire of IR spectroscopy methods. Large differences between the clusters and the bulk structure will be demonstrated. Fascinating structures, such as nanotubes for neutral  $(\text{MgO})_n$  clusters, are for the first time unambiguously confirmed experimentally. Species presumably important in the activation of methane using MgO are also studied. It will be shown that clusters of the stoichiometry  $\text{Mg}_n\text{O}_{n+1}$  contain activated dioxygen species, and the type of species can be easily tuned by the charge state of the cluster, which mimics a charge transfer from a metal substrate for thin surface layers of MgO. Complexes with different ligands, such as water, carbon monoxide, and methane are also investigated.

A new IR spectroscopy method for (transition metal) cluster anions is presented in chapter 5. These studies are among the first experiments using an intra cavity IR free electron laser. Only this unique light source provides a sufficient IR fluence in the far-IR to allow for IR resonance enhanced multiple photon electron detachment spectroscopy (IR-REMPED) on such weakly absorbing species as transition metal clusters. The integration of the experimental setup into the FEL cavity is discussed in this chapter and the realization of IR-REMPED is described. First of all, the feasibility of the method is proven using tantalum carbide clusters. Results obtained with this method are then used for comparison with photoelectron spectra measured for the same systems. These show the prospects achievable when combining both methods, but also provide further information about the system, helping to test the limits of IR-REMPED. In a second step, the sensitivity of the method is increased to allow for spectroscopy of bare metal clusters, which finally results in the first IR spectra for niobium cluster anions. From these results it can be concluded that IR resonance enhanced multiple photon electron detachment

has the potential of becoming a widely applicable method.

## 2. Experimental methods

The following chapter gives a general overview of the different experimental methods and setups used in this thesis to probe the electronic and geometric structures of clusters in their various charge states.

The electronic structure of a neutral cluster in the geometric structure of the anion can be studied by anion photoelectron spectroscopy (PES). This is a widely used spectroscopic technique as it relies on laser sources more readily available in the laboratory. We use it here for obtaining complementary information to the vibrational spectra that are discussed in the major part of this thesis. Section 2.1 describes the general principle, and velocity map imaging PES in particular.

Most of the experiments investigated the vibrational spectra and therefore the geometry of cationic, neutral, and anionic clusters. These vibrations are found in the infrared (IR) region. The theoretical background of IR spectroscopy is very briefly discussed in section 2.2. Several methods are available to study IR spectra of gas-phase clusters. The most established method, IR multiple photon dissociation spectroscopy, which will also be extensively used in this thesis, will be explained in more detail (section 2.2.1). Two further methods have been developed to investigate clusters, IR-UV two-color ionization and IR resonance enhanced multiple photon electron detachment. They are explained in detail in chapters 3 and 5, respectively. All these methods require the absorption of multiple IR photons. The current picture of the absorption mechanism is explained in section 2.3. These experiments require an especially intense and tunable IR light source, *e.g.*, a free electron laser (FEL). The basic principle of a FEL and the specifications of the (normal) IR-FELs used in the experiments will be explained in section 2.3.

The chapter closes with section 2.4, which gives a description of two of the experimental setups. A third setup, which has been used in the experiments on anionic metal clusters, will be described in connection with the intra-cavity FEL FELICE, in section 5.1.

### 2.1. Photoelectron spectroscopy

The electronic structure of neutral clusters and molecules can be studied by anion photoelectron spectroscopy (PES) [40, 41, 57]. This method, which is a variant

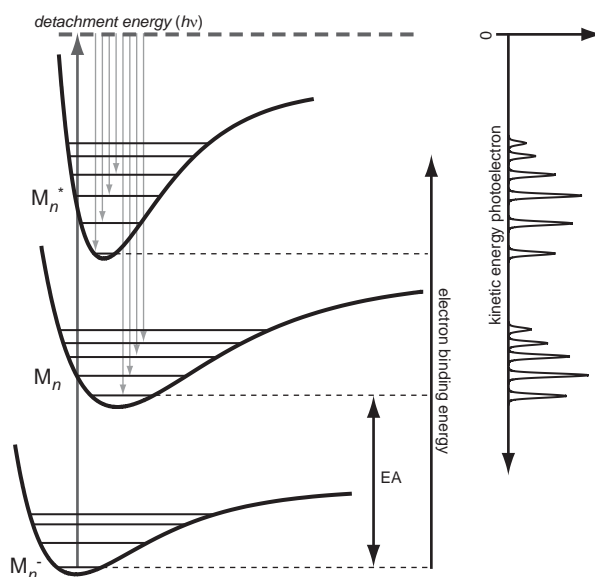


Figure 2.1.: Basic principle of anion photoelectron spectroscopy for a diatomic molecule. From the electronic ground state of the anion,  $M_n^-$ , the system is excited by one-photon absorption. When the photon energy is above the EA of the system the electron can be detached, leaving behind the neutral species. Depending on the final state, which can be the ground or an excited state,  $M_n$  and  $M_n^*$  respectively, the kinetic energy of the photoelectron is different. All excess energy is taken away by the electron, which is then being measured in photoelectron spectroscopy. Within a single electronic state the molecule can also be vibrationally excited, which can, in principle, also be resolved.

of photoelectron spectroscopy that is applied to neutral species, benefits from the possibility of mass selection provided by starting with ions.

By irradiating a mass selected negatively charged cluster or molecule with monochromatic light with a photon energy,  $h\nu$ , above the electron binding energy a photoelectron can be detached. In anions this energy corresponds to the electron affinity (EA). The kinetic energy and angular distribution of the photoelectrons can then be measured.



From the  $e^-$  kinetic energy spectrum the electronic energy level structure of the ground and excited states of the neutral can be derived. Figure 2.1 shows an example for a simple diatomic molecule with two accessible electronic states  $M_n$  and

$M_n^*$ . As the detachment process is fast compared to structural rearrangements it is often stated that PES probes the electronic structure of the neutral in the geometric structure of the anion. Because of the low EA of the anion it is usually assumed that only a single electronic state,  $M_n^-$ , is involved. The electron binding energy,  $E_{bind}$ , can be determined from the kinetic energy of the electron,  $E_{kin}$ , and the excitation or detachment energy, which is equivalent to  $h\nu$ , by

$$E_{kin} = h\nu - E_{bind}. \quad (2.2)$$

In molecules, in addition to different electronic states, different vibrational states may also be involved. In favorable cases, these can also be resolved with anion PES. Resolution of vibrational structure is highly dependent on the kinetic energy resolution of the detection method.

Several different methods have been developed, for instance, hemispherical energy [58], or field-free [59] and magnetic bottle time-of-flight analyzers [60, 61]. The energy resolution that can be obtained with such methods is typically limited to 5–10 meV [41].

A better resolution can be achieved by using narrow-band tunable lasers, and anion zero electron kinetic energy (ZEKE) spectroscopy [62]. Here, only electrons with nearly zero kinetic energy are detected, which means that only a single transition can be probed at a time.

A big impact on the field of anion PES (and also photoion imaging) has been caused by the development of velocity map imaging (VMI) [63]. The 3-D velocity distribution of the photoelectrons produced by photodetachment is projected onto a 2-D detector (usually) consisting of a multichannel plate, a phosphor screen and a camera. The detachment is made in the constant electric field of a velocity map imaging lens, which has the property of projecting all of the electrons or ions with the same velocity onto the same point on the detector regardless of their initial positions. With other detection methods the angular distribution of the photoelectrons can only be deduced by moving the detector with respect to the polarization direction of the detachment laser, in VMI the distribution is directly mapped onto the 2-D detector.

The energy resolution that can be achieved in VMI is typically 2–5 % of the electron kinetic energy [41], but can be significantly improved [64]. The absolute energy resolution is not limited in VMI, in contrast to other detection methods, and can be made very high by limiting the detection to slow electrons, which can be made by selecting a wavelength just above the detachment threshold. This is the basic principle of slow electron velocity-map imaging, in which many high resolution spectra, each for a restricted narrow energy range, are pieced together [41].

Because of the projection of the 3-D velocity distribution onto a 2-D detector

the original distributions need to be reconstructed from the images to obtain all of the information. Several reconstruction methods have been developed which either use an inversion, such as Abel, Hankel, Polar-Onion-Peeling, BASEX, etc., or a forward convolution method, which are more commonly used in photoion experiments [65]. All these methods yield the velocity and angular distributions. The observed velocities are proportional to the radius,  $r$ , of the rings observed in VMI, and can be related to the kinetic energy by

$$kr^2 = E_{kin} \quad (2.3)$$

in which  $k$  depends on the kinetic energy to which the electrons are accelerated by the VMI lens in the direction to the detector and the length of the field free drift zone.

The intensities observed in the kinetic energy spectra depend on the photodetachment cross section,  $\sigma$ , and the Frank-Condon overlap between the vibrational states of the anion and neutral. The angular distribution, on the other hand, reflects the symmetry of the initial and final state of the photodetachment. For single-photon absorption and a randomly oriented ensemble of anions the photoelectron angular distribution (given by the intensity  $I$  and the angle  $\theta$  between laser polarization axis and detection axis) is described by

$$I(\theta) = \frac{\sigma}{4\pi} (1 + \beta P_2(\cos \theta)) \quad (2.4)$$

with  $\beta$  being the anisotropy parameter and  $P_2$ , the Legendre polynomial of second order [41]. The  $\beta$  parameters can be obtained from the Cooper-Zare formula [66], but are difficult to predict from first principle calculations for more complex systems [41].

## 2.2. IR spectroscopy

In this section we aim to give a short description of the theory of molecular vibrations and vibrational spectroscopy. The energetic and dynamical properties of molecules are described by the solutions of the Schrödinger equation [67–69]. For polyatomic molecules containing more than two electrons an analytic solution of this equation is missing. Therefore, approximations have to be used. For most systems of interest the Hamilton operator,  $\hat{H}$ , describing the energy of the system, does not depend on time, which simplifies the problem to the time-independent Schrödinger equation.

$$\hat{H}(R, r)\psi(R, r) = E\psi(R, r) \quad (2.5)$$



The wave function,  $\psi$ , depends only on the nuclear,  $R$ , and electronic coordinates,  $r$ . A further simplification can be achieved with the Born-Oppenheimer approximation, which assumes that due to the large mass difference between electrons and nuclei the electrons instantaneously adjust to changes in the nuclear positions and therefore electrons and nuclei can be treated separately. The solutions of the electronic Schrödinger equation still depend parametrically on the nuclear coordinates and define the potential energy surface.

Molecular vibrations are described by the nuclear Schrödinger equation

$$\hat{H}_n(R)\psi_n(R) = E_n\psi_n(R). \quad (2.6)$$

For a diatomic molecule the Hamiltonian has the simplest form when the nuclei move in a parabolic potential around their equilibrium positions  $R_e$  (defined by the displacement from equilibrium  $q$ )

$$\hat{H}_n(R) = \hat{T}_n + \hat{V}_n = \frac{1}{2}\omega\dot{q}^2 + \frac{1}{2}kq^2. \quad (2.7)$$

The solution of the Schrödinger equation is then that of a harmonic oscillator with eigenenergies  $E_v = \hbar\omega(v + \frac{1}{2})$  and frequencies  $\omega = \sqrt{k/\mu}$  defined by the reduced mass  $\mu = m_1m_2/(m_1 + m_2)$  of the two nuclei (with masses  $m_1$  and  $m_2$ ) and the vibrational force constant,  $k$ . The harmonic approximation is only good at small displacements around the equilibrium, as anharmonicities and a dissociation are not included in this model. A often more suitable approximation is the Morse potential [70] which depends on the dissociation energy of the molecule,  $D_e$ , and is given by

$$\hat{V}_n(R) = D_e \left[ 1 - e^{-a(R-R_e)} \right]^2. \quad (2.8)$$

In contrast to the harmonic oscillator, a decrease of the level spacing with increasing quantum number,  $v$ , is observed, which better reproduces experimental results. The eigenvalues depend on the vibrational constants  $\omega_e$  and  $\omega_e\chi_e$  and can be written as

$$E_v = \omega_e \left( v + \frac{1}{2} \right) - \omega_e\chi_e \left( v + \frac{1}{2} \right)^2. \quad (2.9)$$

Molecules containing more than two atoms do not have only a single vibrational mode, but  $3N - 5$  for a linear and  $3N - 6$  for a general molecule (with  $N$  being the number of atoms). At the equilibrium position of the nuclei the potential of the vibrating molecule can be expanded in a Taylor series. For small displacements the series can be truncated after the quadratic term and the potential becomes again that of a harmonic oscillator. However, the vibrations of the nuclei couple, which results in a set of coupled differential equations. By an appropriate coor-

dinate transformation into normal coordinates,  $Q_k$ , it is possible to uncouple the equations again. The Hamilton operator becomes the sum of  $3N - 6$  independent harmonic oscillators. The wavefunction is the product of the harmonic oscillator wavefunctions. In the system of normal coordinates all nuclei vibrate with the same frequency and the same or opposite phase [67]. An arbitrary vibration can be composed as a linear combination of normal modes [69] with total energy

$$E = \sum \hbar \omega_i \left( v_i + \frac{1}{2} \right). \quad (2.10)$$

Transitions between two different vibrational levels  $|i\rangle$  and  $|j\rangle$  within the same electronic state for which the transition dipole matrix element is non-zero characterizes the IR spectrum of the molecule. For a vibrating molecule in addition to the permanent dipole moment,  $p_N$ , a correction for the change of the dipole moment induced by the displacements of the nuclear coordinates needs to be added.

$$p_N(Q) = p_N(0) + \sum_{n=1}^{3N-6} \left( \frac{\partial p_N}{\partial Q_n} \right)_0 Q_n \quad (2.11)$$

The dipole matrix element  $(M_{ik})_{vib}$  simplifies in that case to

$$(M_{ik})_{vib} = \sum_{n=1}^{3N-6} \left( \frac{\partial p_N}{\partial Q_n} \right)_0 \int \psi_i^{vib} Q_n \psi_k^{vib} d\tau_{vib}. \quad (2.12)$$

Only vibrational transitions for which the dipole moment changes with the vibrational displacements of the nuclei for a normal vibration are allowed, and called IR active. A permanent dipole moment is not required.

Transitions from the ground to the first excited state of the same normal mode ladder are called fundamental transitions, whereas transitions to higher levels are overtone transitions. Transitions that excite simultaneously several vibrational modes and therefore involve the vibrational ladders of more than a single normal mode are called combination modes [67].

### 2.2.1. IR spectroscopy methods for low-density gas-phase species

IR spectra are commonly measured directly via absorption spectroscopy. The intensity of incoming light of intensity  $I_0$  decreases due to absorptions when going through a sample of concentration  $c$ , sample path length  $l$ , and molecular absorption coefficient  $\epsilon$ . The Lambert-Beer law [69] describes the change in intensity,  $I$ , that is observed.

$$I = I_0 e^{-\epsilon c l} \quad (2.13)$$

The application of such a technique to molecular beams is usually not possible as the achievable densities are too low. The change in intensity is too small to be detectable, and only by a dramatically enhanced path length, *e.g.* in cavity ring-down spectroscopy [34], do direct absorption measurements become feasible. The cluster sources commonly used usually produce broad distributions rather than a single species. The measurement of cluster size specific spectra in a molecular beam is therefore not possible. In the gas phase, both problems can be overcome by employing mass spectrometric detection schemes. Instead of using the changes of the light by the sample, the problem is inverted, and the changes of the sample induced by the light are used for detection.

Mass spectrometric detection schemes are able to separate molecules and clusters by their mass to charge ratio. The absorption of light by a cluster can therefore be easily detected when it changes its mass or charge state.

The change of the charge state typically corresponds to the removal of a single electron. The electron binding energies of a neutral or anionic species are the ionization energy (IE) or electron affinity (EA), respectively. This is the minimum energy, to which the cluster needs to be excited for electron detachment. For a change of the mass, the bond dissociation energy (BDE) must be overcome.

Here, we focus on clusters which are strongly bound, and that have typically total binding energies of a few eV per atom. The EA and IE of the systems are also in the same range. The spectral range of the fundamental vibrations of these systems is usually in the far- and mid-IR ( $50\text{--}2000\text{ cm}^{-1}$ ) where the photon energy ( $6\text{--}250\text{ meV}$ ) is much lower than the BDEs, IEs, and EAs. A single photon is therefore not able to drive any dissociation or ionization reaction.

During the last decades, several vibrational spectroscopic methods have been developed which either lower the energy that is required to be contributed by the IR photons or use very intense light sources in order to allow for multiple photon absorption.

In Figure 2.2 an overview of the different available methods is shown, along with the new methods described later.

Depending on the charge state of the system different schemes are conceivable. For neutral clusters and molecules, in particular, several methods exist. Among the oldest is ion-dip spectroscopy [71]. Internally cold molecules are resonantly ionized from the ground state by (a) UV laser(s) tuned to an electronic transition frequency to produce a constant ion signal typically via two-photon ionization. An additional IR laser is used, which when it is in resonance with a vibrational mode of the molecule, leads to a depopulation of the ground state. For these excited states the UV laser is no longer in resonance and a drop in the ion intensity is observed. Most other methods do not rely on the knowledge of the electronic

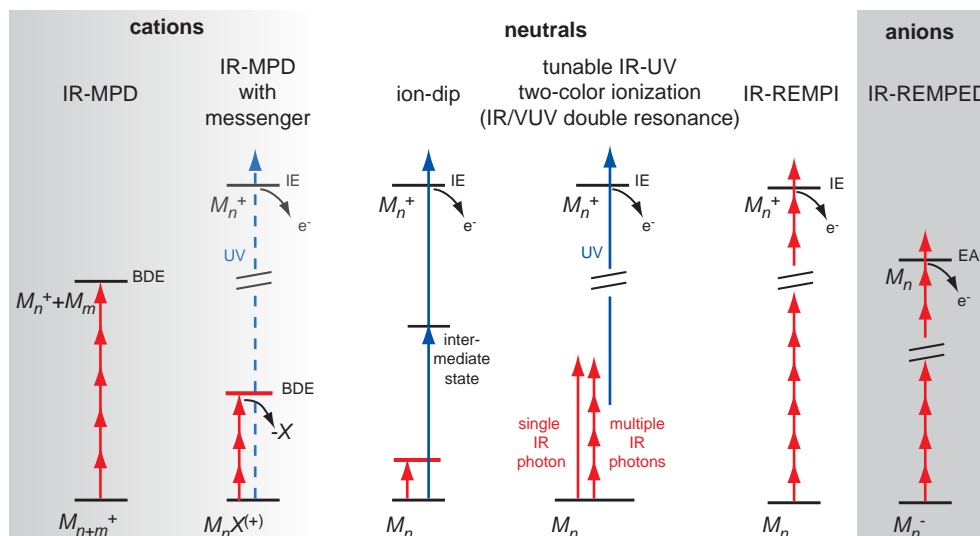


Figure 2.2.: IR action spectroscopy methods used to obtain vibrational spectra of cationic, neutral and anionic molecules and clusters.

structure of the system.

The first IR spectroscopic measurement of a neutral molecule using a free electron laser as the IR light source has been obtained for para amino benzoic acid (PABA) by IR/VUV double resonance spectroscopy [72]. The VUV photon energy was chosen to be  $1000\text{ cm}^{-1}$  below the IE of the system. The resonant absorption of a  $1000\text{ cm}^{-1}$  IR photon a few  $\mu\text{s}$  before the VUV laser pulse increases the internal energy of the system. The energy of the photon is randomized in this system by fast internal vibrational distribution and ionization from the vibrationally excited states becomes possible. This can be used to record an IR spectrum. In these experiments only low IR fluences were employed, however, indications for the absorption of more than a single IR photon were found. This is a major requirement if one wishes to use this method at lower IR photon energy. In chapter 3 it is shown that such an approach can be used to record vibrational spectra for clusters in a molecular beam in the far-IR region. As the amount of absorbed IR photons can strongly vary with IR photon energy we use a more general name for the method indicating only the properties of the employed lasers – tunable IR-UV two-color ionization.

The absorption of multiple IR photons is also characteristic for all other methods depicted in Fig. 2.2. Instead of using an additional (UV) laser for ionization it is, under certain circumstances, also possible that the system absorbs enough IR photons that it undergoes thermionic electron emission and ionization. This method, called IR resonance enhanced multiple photon ionization (IR-REMPI), has been

used to record spectra of fullerenes, metal carbides and oxides [51, 52, 73]. A similar approach would also work for anionic clusters, except that instead of the IE the EA, which is usually lower, needs to be overcome. Such an approach - IR resonance enhanced multiple photon electron detachment (IR-REMPED) - is presented for very weakly absorbing metal cluster anions in a molecular beam in chapter 5.

The most generally applicable method is IR multiple photon dissociation spectroscopy. It can be applied to cations, neutrals, and (with restrictions) to anions. Because of its general importance and as it is used for many of the current experiments it is explained in detail below.

**IR multiple photon dissociation spectroscopy.** Photodissociation studies in the visible and ultraviolet range [35–37, 74] have provided a wealth of information on the electronic structure of clusters. As long as only one-photon absorption processes are concerned, this method is limited by the height of the barrier for cluster dissociation (the BDE) with respect to the photon energy. By using several photons (eqn. 2.14) of the same (or different) color the accessible energy range can be significantly increased. For a few systems, such as for metal oxides clusters [31, 75], this allows spectra to be obtained even in the mid-IR, probing the geometric rather than the electronic structure.

For more strongly bound systems, such as transition metal and semiconductor clusters, which have lower IR absorption cross sections, and therefore do not readily absorb a sufficient number of photons, the amount of energy required can be significantly reduced by using weakly bound spectator ligands [54] which are vaporized from the cluster upon excitation (see eqn. 2.15).

The sensitivity of this method becomes particularly high when using physisorbed messengers, *e.g.* N<sub>2</sub> or rare gas atoms, that have low binding energies towards the cluster, which can lower the BDE below the photon energy. As the binding energies of such complexes are often very small, low temperatures are required for complex formation. UV, optical and near infrared absorption spectra of neutral and charged transition metal [74, 76–81] and silicon clusters [82] have been measured via the dissociation of such weakly bound complexes. More recently, far-IR spectra of such clusters have been measured, by using the intense radiation from a free electron laser [24, 56, 83]. Here, the photon energy becomes again smaller than the typical binding energies and multiple photon absorption is necessary.



The basic assumption behind the application of the messenger atom technique is that the cluster acts as chromophore while the weakly bound atomic or molecular ligand acts only as a messenger and does not perturb the structure and IR spectrum of the cluster. For highly polarizable messengers this assumption does not necessarily hold. The polarizability of the rare gas atoms as well as of molecular oxygen is given in Table 2.1. The messenger can dramatically influence the IR absorption cross section [24, 84], or can distort the structure compared to that of the bare cluster [74]. As the binding strength between the messenger and the cluster can vary significantly for different isomers the relative energy ordering of the isomers can also be altered [84].

The advantage of IR-MPD is its wide range of application. It is not limited to a specific charge state as ionization methods are, and spectra of cationic, anionic and neutral clusters can be measured, provided that a complex can be formed.

Table 2.1.: Static electric dipole polarizabilities for ground state rare-gas atoms and dioxygen derived from measured dielectric constants [85].

Atom	Polarizability $10^{-24}\text{cm}^3$
He	0.205
Ne	0.394
Ar	1.641
Kr	2.484
Xe	4.044
O <sub>2</sub>	1.581

### 2.2.2. Multiple photon absorption and internal vibrational redistribution

Many of the IR spectroscopic methods described rely on the absorption of a few up to several tens or even hundreds of IR photons. Because of the anharmonicity of the vibrational energy ladders, absorption of many monochromatic photons is not possible by a completely coherent process [52, 86, 90]. This effect, known as the anharmonicity bottleneck, is circumvented by a mechanism that assumes a stepwise process. It consists out of three different regimes, which depend on the internal energy of the species, and are illustrated for SF<sub>6</sub> in Fig. 2.3(a): (I) the resonant, (II) the quasi-continuum, and the (III) dissociation or ionization region.

In the resonant region the molecule climbs up the discrete states of a vibrational ladder via coherent multiphoton excitation. The increasing vibrational excitation leads to a dramatic rise in the density of states. The bright states used for the absorption of the IR light couple via anharmonic coupling to the bath of dark back-

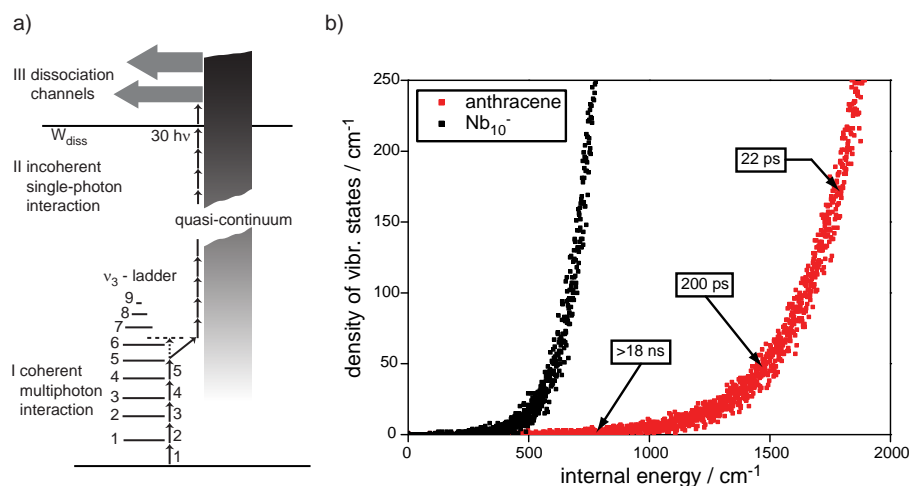


Figure 2.3.: (a) Schematic energy level-diagram for the multiphoton dissociation of  $\text{SF}_6$ . The figure is adapted from Ref. [86] b) Vibrational density of states for the neutral anthracene molecule and the  $\text{Nb}_{10}^-$  cluster. The density of states have been calculated using the Beyer-Swinehart algorithm [87] using the calculated harmonic frequencies of anthracene from Ref. [88] and our own calculations for  $\text{Nb}_{10}^-$  (see chapter 5). Characteristic times for IVR in anthracene are taken from Ref. [89].

ground states and the energy is distributed. This process is known as internal vibrational redistribution (IVR). For large molecules and higher internal energies the large density of states leads to very fast IVR which removes population from the excited states and allows the molecule to absorb the next photon. The short lifetime of the vibrational states results in a broadening of the absorption lines. The molecule goes over to the second region, the quasi-continuum. Here, IR photons in zones near the original fundamental transitions are absorbed semi-resonantly [91].

Only at very high internal energies the third region, the true continuum region, is reached. Photons of any wavelength can be absorbed. Strong (anharmonic) coupling between the many vibrational states results in very fast IVR, which becomes much faster than the absorption rate. The vibrational energy is at any time statistically distributed over the vibrational degrees of freedom and the excitation is described by statistical approaches. Rate equations can be used to describe the dissociation or ionization of the molecule.

In many IR spectroscopy experiments the absorption of a single photon is sufficient to bring the molecule into the quasi-continuum. There, the IVR rates are sufficiently fast to allow the multiple photon absorption process. When going to

the low frequency modes this becomes questionable, as the IVR rates can become very slow. These have been measured, for example for anthracene [89], and are shown in Fig. 2.3(b) along with the vibrational density of states as function of internal energy. For transition metal clusters, which have their vibrations at very low energies, the density of states usually rises already at lower energies. However, because of the low photon energy, several IR photons may be required to bring the molecule into the quasi-continuum. The IVR rates can be even slower than for anthracene as these depend not only on the vibrational density of states, but also on the cross anharmonicities [89]. Long interaction times with the IR radiation may therefore be required.

### 2.3. IR free electron lasers - The FELIX facility

Several different types of Free Electron Lasers (FELs) exist nowadays covering the microwave to X-ray range [93, 94]. The basic principle for all these FELs is the same, however, depending on the wavelength range certain differences exist. Numerous textbooks [95, 96] and reviews [97, 98] have been devoted to the physics of FELs. Here, only a very brief description of the IR-FELs, and their operation conditions, that are used for the experiments presented in this thesis, are given.

Common for all FELs is that its radiation results from the interaction of an optical wave with a relativistic electron beam passing through a periodic magnetic field. The relativistic electron beam serves as the gain medium and is injected into an assembly of alternating permanent magnets with period length  $\lambda_u$ , the undulator (see Fig. 2.4(a)). There they are transversely accelerated and emit synchrotron radiation given by the FEL resonance-condition shown in Fig. 2.4(a) at the resonant wavelength,  $\lambda_R$  (and its harmonics) [96].

The wavelength of the radiation emitted by the electrons corresponds to the period of the magnetic field experienced by the electrons in their rest frame. This period is shortened by the Lorentz factor,  $\gamma$ , and usually falls into the mm to cm range. Relativistic Doppler shift leads to a strong shortening of the wavelength (and emission into forward direction), which shifts the radiation into the IR range [95]. The wiggling motion due to the magnetic field lowers the velocity along the undulator axis. This reduces the Lorentz factor by a factor of  $(1 + K^2)$ , with  $K$  being the undulator parameter, which is directly proportional to the magnetic field strength on the electron beam axis.

The spontaneous emission is usually very weak and incoherent. Therefore, for IR-FELs, the undulator is installed in an optical resonator consisting of two highly reflective (gold) mirrors. The length of the resonator is adapted to the recurrences of the electron bunches. This allows the interaction between optical wave and



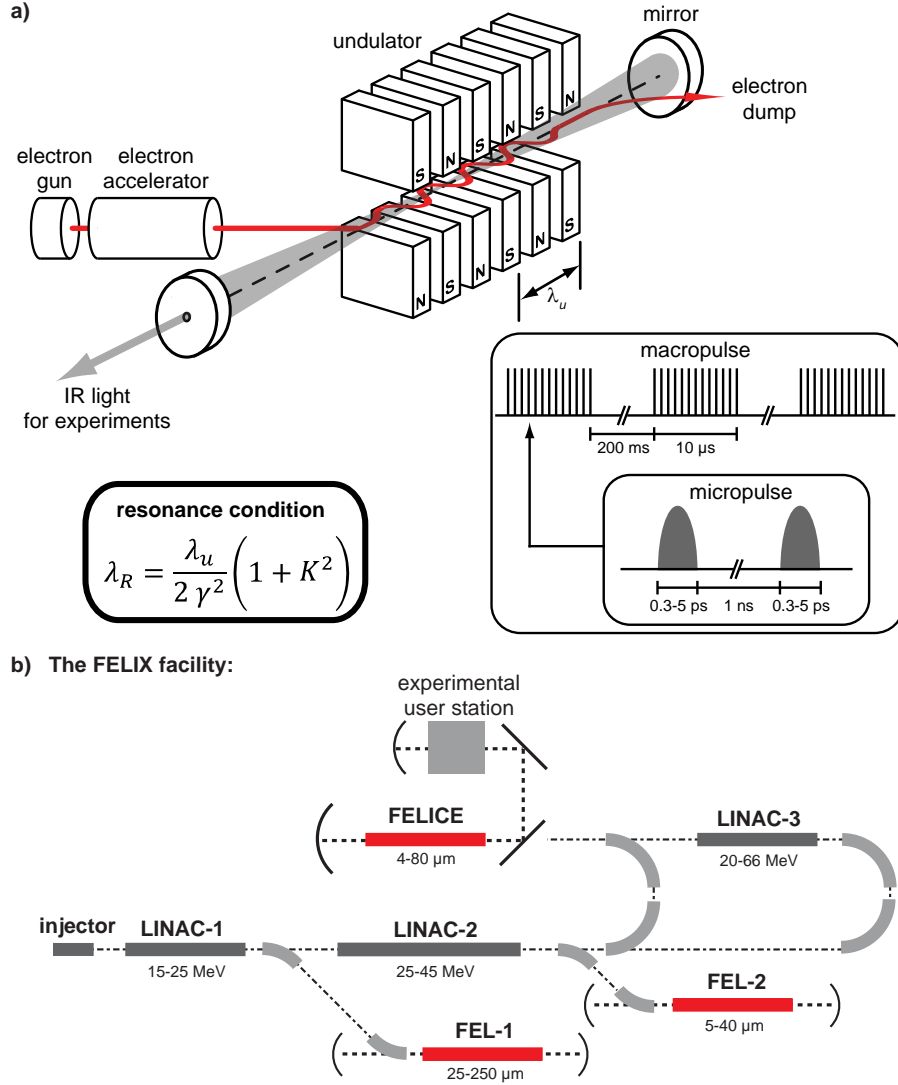


Figure 2.4.: (a) Schematic layout of an IR Free Electron Laser. A relativistic electron beam is injected into a magnetic undulator structure. The wiggling motion caused by the alternating magnetic field forces the electrons to radiate light at the wavelength,  $\lambda_R$ , given by the resonance condition. A two-mirror cavity around the undulator stores the light and induces a coherent amplification. The inset shows the pulse structure from a normal conducting accelerator and thus from the light. The figures have been adapted from Ref. [92]. b) Schematic diagram of the vault of the FELIX facility.

electron bunch to take place on every passage. Both can interchange energy, which can lead to a modulation of the electron density at the wavelength of the light (microbunching), which phases the emission and restores coherence. The intensity of the optical wave stored inside the resonator increases non-linearly until saturation sets in. This coherent emission is usually  $10^6$ – $10^8$  times higher than the spontaneous emission.

The experiments described in this thesis have been performed at the FELIX facility at the FOM Institute for Plasma Physics Rijnhuizen, Nieuwegein, The Netherlands. This facility houses three different IR-FELs (or beamlines). All three FELs share major parts of their electron beamline (see Figure 2.4(b)). An injector, composed out of a thermionic triode gun, a prebuncher and a buncher, produce a  $<10$   $\mu\text{s}$  long electron macropulse with a beam energy of 3.8 MeV at a maximum repetition rate of 20 Hz.

Two normal conducting (room-temperature) radio frequency accelerators (LINAC-1 and LINAC-2) can be used to reach electron beam energies up to 25 or 45 MeV, for LINAC-1 and LINAC-2, respectively. Behind each accelerator the electron beam can be deflected into one of the undulators, each surrounded by an optical resonator, forming FEL-1 and FEL-2. From the FEL resonance-condition it becomes apparent that the emitted wavelength depends on the electron beam energy (included in  $\gamma$ ), the undulator period, and the undulator parameter. The undulators of both FELs have the same  $\lambda_u$  and  $K$  parameter, only the available beam energy is different, which allows to reach different wavelengths.

Table 2.2.: Characteristics of the FELIX beamlines FEL-1 and FEL-2.

Wavenumber range	40-2500 $\text{cm}^{-1}$
Energy per macropulse	$<150$ mJ
Macropulse length	4-6 $\mu\text{s}$
Macropulse repetition rate	5, 10, or 20 Hz
Energy per micropulse	1-50 $\mu\text{J}$
Relative spectral bandwidth	0.2-1 % FWHM

The electron macropulse consists out of a pulse-train of 0.3 to several picosecond long micropulses with a spacing of 1 ns (compare inset in Fig. 2.4(a)). The optical pulse mimics the structure of the electron pulse, but its duration is shorter. The bandwidth is Fourier transform limited and is for the experiments usually 0.2–1 % FWHM. To drive a multiple photon excitation process this temporal structure is perfectly suited, as it allows for vibrational redistribution between consecutive micropulses. The wavelength is tuned, which is the key requirement for spectroscopy, by changing the electron beam energy or the gap size of the undulator, which changes the magnetic field strength. The latter allows to vary the

wavelength continuously by approximately a factor of 3 within several minutes. Changing the electron beam energy usually requires longer for optimization of the electron beam optics.

The light is coupled out of the resonator by a hole in one of the end-mirrors and is transported in an evacuated beam transport system to the experiments. In Table 2.2 the most important specifications of FEL-1 and FEL-2 for the following experiments are given. More information for these two FELs, which are usually not treated separately and are jointly named FELIX, can be found in Refs. [52, 92, 99].

The third beamline, the Free Electron Laser for Intra-Cavity Experiments (FELICE) will be discussed separately in chapter 5.

## 2.4. The setups

In the course of this work several different setups have been used. One is located at the Fritz-Haber-Institut, and was originally equipped with a single-target cluster source and a velocity map imaging spectrometer for anion photoelectron spectroscopy. During the project this setup has been improved and expanded by a dual-target cluster source and a reflectron time-of-flight mass spectrometer. Besides photoelectron spectroscopy it now allows for optical spectroscopy, UV/VIS dissociation and photoionization efficiency spectroscopy. In the current work, only the VMI spectrometer will be used, but the extensions to the setup will be discussed in section 2.4.1 to illustrate future possibilities.

A second setup, used for all IR spectroscopy experiments with FELIX, is permanently installed at the FELIX facility. This setup is described in section 2.4.2.

### 2.4.1. The molecular beam setup in Berlin

The setup consists out of three different vacuum chambers - the source chamber, the mass spectrometer chamber and the VMI chamber. All can be separated from each other by gate valves. Details of the vacuum system can be found in Ref. [100] and are for brevity not given here. In the original design, the setup consisted out of a single-target laser ablation cluster source, a linear time-of-flight (ToF) mass spectrometer, and a velocity map imaging setup. During the project, the complete mass spectrometer and beam shaping part was replaced, and a new source has been designed. A schematic overview of the complete setup is shown in Figure 2.5. All modifications are explained individually below.

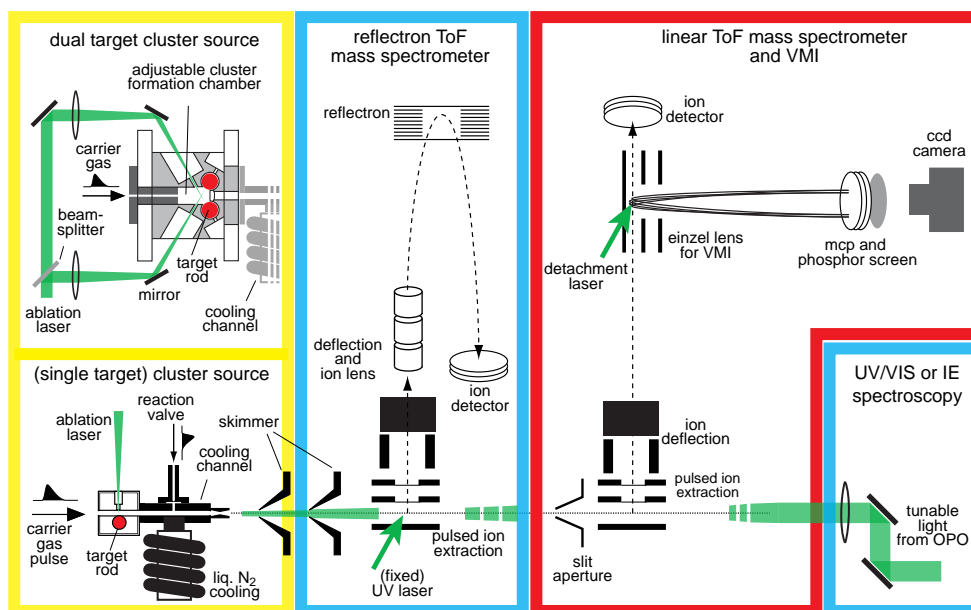


Figure 2.5.: Schematic layout of the Berlin molecular beam machine. Two different laser ablation cluster sources can be installed in the setup, a single target and a (single-laser) dual-target cluster source. Two different mass spectrometers are permanently installed, which can even be used interleaved. The first is a reflectron ToF-MS, with a mass resolution,  $m/\Delta m$ , of roughly 2000. It can be used, for instance, for UV/VIS and photoionization spectroscopy, using the tunable OPO laser coupled in at the far end of the setup. The linear MS is used for mass separation to perform velocity map imaging on mass separated cluster anions. A VMI lens is installed after  $\sim 80\%$  of the field free drift zone of the ToF-MS. A tunable laser can detach electrons, which are projected on an imaging detector, which is composed out of a MCP and phosphor screen. The image is recorded with a CCD camera.

#### 2.4.1.1. Laser ablation cluster sources

Several different types of cluster sources exist such as heated oven, discharge sputtering, or electrospray ionization sources [1, 101–103]. In the following only laser ablation cluster sources will be used. These allow clusters to be formed in different charge states (neutrals, and singly charged anions and cations) from a very wide variety of materials (semiconductors, metals, non-metals, metal-oxides, etc.) and consume very little target material. Furthermore, it is a pulsed source that produces relatively high densities within a short time period, and is therefore perfect for combination with pulsed detection lasers. Laser ablation cluster sources have

been invented by the Smalley group in 1981 (therefore they are often called ‘Smalley source’) [104, 105], and at about the same time by Bondybey [106]. Several different designs exist nowadays, which have been reviewed very recently [107].

The single-target cluster source installed in our setup and described in detail in Ref. [100] was inspired by the original Smalley design. Common to all ablation sources is that a laser is focussed onto a target. This vaporizes material and a plasma forms above the target. A gas flow, typically from a pulsed valve, is guided over the surface of the sample. The ions in the plasma undergo collisions with the carrier gas, which cools them, and causes cluster formation. In our source the target is a (metal) rod of 6 mm or 1/4 inch diameter, that is constantly translated and rotated to always provide a new spot on the surface. A General Valve (series 9) solenoid valve (produced by Parker Hannifin Corp.) is used to produce a short (helium) gas pulse. Cluster formation depends on several factors. The amount of ablated material, for instance, depends on the wavelength, pulse energy per  $\text{cm}^2$  and pulse length of the ablation laser, and the rate at which a new spot on the target is provided. These strongly effect the efficiency of the plasma formation, but also the plasma heating. The ablation laser can cause significant structural changes of the surface, which strongly changes the surface properties [108]. Cluster formation is influenced by the pressure in the cluster formation chamber, which controls the collision rates, and heat transfer [107].

The single-laser dual-target cluster source designed for the current project is based on a similar design to the single target source, but exhibits differences to other dual-target cluster sources. These are discussed bellow.

Both sources are extended with a thermally insulated cooling/reaction channel. This copper channel can be cooled with liquid nitrogen or heated by a heating cartridge, which allows the temperature of the channel to be controlled between 80 and 400 K. At the exit, a small conical nozzle is installed with an opening of 1 mm. For the reaction valve installed on top of the cooling channel a General Series 9 Valve is used, which is thermally insulated from the cooling channel and allows reaction gases to be added after the cluster formation process.

**The single-laser dual-target cluster source.** The single-laser dual-target cluster source has been designed to fit both machines in Berlin and at the FELIX facility described below. Its basic design follows that of the single target source, and both sources can be interchanged (see Fig. 2.5). Previous dual-target cluster sources used two ablation lasers and the two targets have either been installed along the gas-channel [109, 110], or side-by-side and additionally require two valves [111–113]. In the new source the two targets (both 6 mm to 1/4 inch rods) are installed side-by-side on the left and right side of the central gas channel, and the axes of the

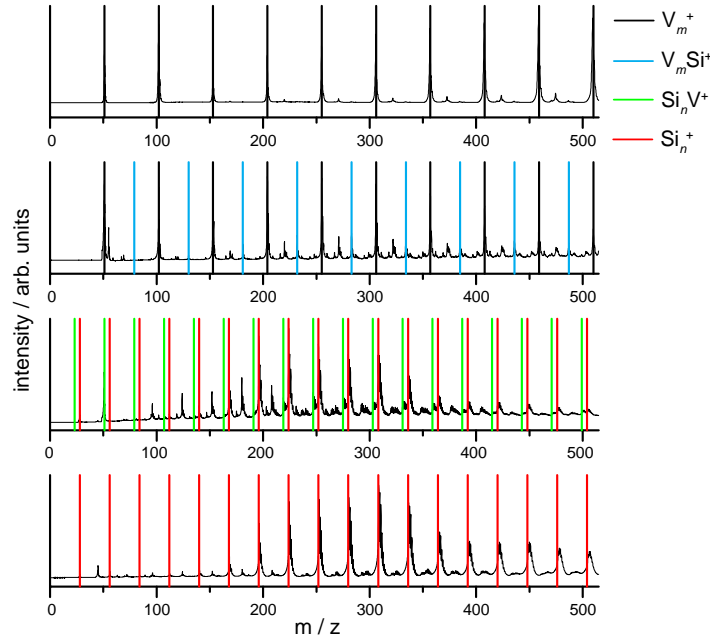


Figure 2.6.: Mass spectra of  $V_m Si_n^+$  clusters with different compositions produced with the single-laser dual-target cluster source.

rods are only 10 mm apart. The cluster formation channel is only slightly larger than in the single target source and its volume can be adjusted with a teflon insert. Both targets are translated and rotated by a mechanism that is installed for both targets on the same side of the source. The targets are attached to an outer thread, which rotates in a fixed inner thread. The outer thread has a rectangular cut-out in the center, in which a shaft slides that is constantly rotated by a vacuum compatible stepper motor and a worm gear. The transmission ratio between motor and rod is 34/1, which means that although a stepper motor is used, a very smooth (and very slow) movement of the target can be achieved.

The beam of the ablation laser is split by a beam splitter into two beams, whose pulse energies can be separately controlled and are focussed by two lenses onto the targets. The two laser beams enter the source chamber parallel from the backside of the source. Two mirrors installed in vacuum reflect the focussed beams onto the two targets. The beams hit the rods at an angle of  $120^\circ$  with respect to the gas flow direction. The plasma plumes go perpendicular to the surface, which means the material is ejected towards the gas flow. Both plumes can effectively mix, which has been shown to be crucial for making mixed clusters. Because of the symmetric configuration it is possible to make clusters under identical conditions for both target positions. This is quite different to the other dual-target cluster sources using

a single valve, where the targets are installed along the gas channel (compare to dual-target source shown in Figure 2.10(b)). The clusters have to undergo more collisions compared to a configuration where the plasma plume is ejected perpendicular or along the gas flow direction. This should aid in a more efficient cluster formation and cooling. The same should follow from the narrowing of the cluster formation chamber at the level of the two targets. By adjusting the pulse energies of the two laser beams it is possible to produce the two respective bare cluster distributions and mixed cluster distributions with arbitrary mixing ratios (see example for  $V_mSi_n^+$  clusters in Fig. 2.6). A similar source design has been used before for making diatomic species [114], cluster formation was not the aim for this source. The major difference to our source is that the material is vaporized along the gas flow direction.

#### 2.4.1.2. Time-of-flight mass spectrometer

Mass spectrometry allows ions to be separated by their mass-to-charge ratio. In our setups we use mass spectrometers which separate ions by their different time-of-flight. The basic principle of them is that ions with different masses,  $m$ , or charges,  $z$ , are accelerated in a homogeneous electric field,  $E$  to different velocities,  $v$ .

$$E_{kin} = z \cdot E = \frac{1}{2}mv^2 \Leftrightarrow v = \sqrt{2E\frac{m}{z}} \quad (2.16)$$

In a field free drift region the ions will spread out in time. A time resolved ion signal can be obtained by ion impact on a multichannel plate (MCP) detector which liberates electrons and amplifies the original signal. A simple anode can be used to measure the signal with a fast oscilloscope.

The mass resolution, defined by  $m/\Delta m$ , which can be achieved by such a device strongly depends on the ion's initial positions and velocities. To increase the mass resolution several different types of ToF mass spectrometer have been developed, which usually combine several acceleration and drift regions.

The setup contains two different types of mass spectrometer (MS), a linear and a reflectron ToF-MS. The (orthogonal) linear ToF-MS has a Wiley-McLaren design [115]. This means that the ion extraction region is made out of 3 electrodes to make two acceleration regions, which allow corrections to be made for differences in the initial ion positions within the first acceleration region. By adjusting the ratio of the potentials applied to the plates, ions originating from different positions are made to arrive at the detector at the same time (space-focus).

The resolution can be further improved by adding a reflectron [116], an ion mirror, to the linear ToF design. This also corrects for differences in the initial kinetic energy. The design that is used in our case employs also two acceleration regions

in the reflectron.

For the experiments the mass resolution that can be obtained with the different ToF-MSs is important. The linear ToF mass spectrometer has a resolution of 800 and the reflectron ToF-MS has a resolution of 2000. Both are permanently installed and can even be used interleaved.

#### 2.4.1.3. UV-VIS and photoionization efficiency measurements

Laser pulses in the visible and ultraviolet range that can be used for optical spectroscopy are produced by a Panther EX optical parametric oscillator pumped by a Surelite II Nd:Yag, both manufactured by Continuum. This system delivers tunable light from 205–2500 nm. For this kind of spectroscopy the reflectron ToF-MS is used, as it provides the higher mass resolution, and a more sensitive ion detector. This MCP detector allows a post acceleration of cations, which compensates, in parts, for the decrease in sensitivity observed for heavier ions. Furthermore, the molecular beam is better collimated for this mass spectrometer, which allows a better spatial overlap between molecular and laser beam.

Ionization efficiency measurements can be performed by making the desired clusters in the source and removing all ionic clusters by either applying a potential to the two skimmers or by leaving the extraction plates constantly on high voltage. The cluster beam is then either collinearly overlapped with the light from the OPO as shown in Figure 2.5, or it is fired in from the side. The photon fluence normalized ion count rate as function of wavelength gives the photoionization efficiency curve. As the cluster intensities show large shot-to-shot fluctuations several spectra are averaged per frequency interval. To correct for drifts on longer timescales a reference mass spectrum is measured on alternating shots by using a fixed frequency UV laser.

UV/VIS spectroscopy on (cationic and neutral) bare clusters and complexes with messengers can be measured in a very similar way. UV/VIS spectra are measured via depletion spectroscopy, similar to the IR-MPD spectra described below. Complexes are made in the source, *e.g.* by cooling the channel to attach rare gas atoms. In depletion spectroscopy it is essential that the majority of species detected by the MS has been irradiated. A second skimmer was installed to define the overlap between laser and molecular beam. A first skimmer is mainly used for differential pumping and produces an ion beam that is almost 10 mm in diameter at the center of the extraction region of the reflectron ToF-MS. This is too large to be covered by the OPO laser beam. The second skimmer that has been installed reduces the size sufficiently (down to <4 mm), such that all ions passing it are irradiated. The setup has been tested for cationic gold clusters, and an example spectrum is shown in Fig. 2.7.



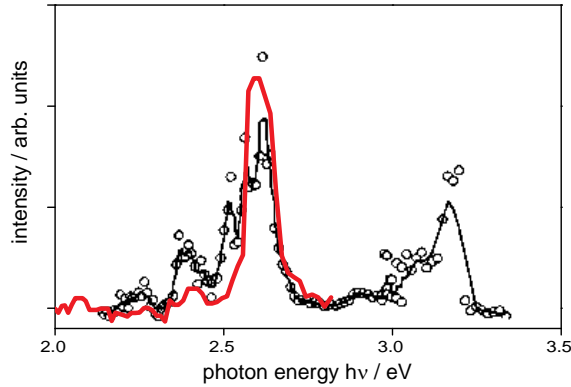


Figure 2.7.: Demonstration of UV/VIS spectroscopy with the Berlin setup for  $\text{Au}_4^+$  (red line). The data plotted in black is taken from Ref. [117].

#### 2.4.1.4. Photoelectron spectroscopy via velocity map imaging

Photoelectron spectra are measured via velocity map imaging. In order to obtain the spectrum of a single species, mass selection or separation is required. We use mass separation by using ToF mass spectrometry. The linear ToF mass spectrometer is used to separate ions of different masses. The lens of the VMI spectrometer is installed at approximately 80 % of the distance along the field free drift region of the linear ToF mass spectrometer. A detachment laser beam, which can either be one of the harmonics of a Nd:YAG or the Panther Ex OPO laser can be fired through the center of the lens. The laser beam axis crosses the ion beam at  $90^\circ$  and is defined by a set of light baffles, which also reduce scattered light. The potentials on the lens are applied  $\sim 200$  ns before the detachment laser is fired. The detached photoelectrons are accelerated onto an MCP (Chevron assembly, imaging quality) and phosphor screen (which is also pulsed to reduce dark counts). A CCD camera (Basler A102f,  $1392 \times 1040$  pixel, 15 frames/s) takes images of the phosphor screen, which are added together by a computer program. Typically a few hundred thousand laser shots are added for a single image. The repetition rate of the experiment is limited by the repetition rates of the lasers, which are usually 10 or 15 Hz. For some systems  $\approx 500,000$  laser shots (12 h acquisition time) were necessary. This sets high requirements for the stability of the experiment, as reference spectra also have to be measured for energy calibration of the imaging detector.

In total 4 cards of our homebuilt 4-channel delay generators (BU3008 delay generators made by the ELAB of the FHI Berlin) are used to trigger all devices used for the VMI experiment. These are combined such that jitters are minimized. The most sensitive parts, where the most accurate timing is required, *i.e.* the extraction of the

ToF-MS, the potential on the VMI lens and the phosphor screen, and the firing of the detachment laser, are all triggered by the same delay card. This minimizes the jitter to less than 10 ns. When different cards are used and interconnected in series, the jitters can add up to more than 100 ns.

All voltages of the setup are computer controlled. Except for the VMI lens, this is done by 16 bit digital-analog converters (16+8 channel Acromac IP231). The voltage is fed into the analogue set-voltage input of the 2 and 5 kV power supplies, NHQ212M and NHQ215M, respectively (made by ISEG Spezialelektronik GmbH). This allows the potentials to be set with a day-to-day reproducibility better than 1 V. For the two VMI lens potentials, a SHQ 222M 2 kV 2-channel power supply is used, which is controlled via a Labview program and its digital RS232 interface. This power supply can be set with a resolution of 30 mV and its stability is on the same order. The voltage ratio for the VMI lens needs to be set to an accuracy better than  $10^{-3}$ . After a warm-up of  $\sim 2$  h all voltages are sufficiently stable for operation. No influence of temperature fluctuations in the lab have been observed for the current experiments. The switched voltages for the extraction plates of the linear ToF-MS, and the VMI lens are stabilized by 0.5  $\mu$ F capacitors.

As the detachment laser is not fired at the position of the space-focus of the MS, the ion packets of two different species, such as  $\text{Ta}_4^-$  and  $\text{Ta}_4\text{H}^-$  may partly overlap. In particular, because of the limited mass resolution of the linear MS (compare the mass of the cluster 724 u vs. the mass resolution of  $\sim 800$ ). It is possible to move the space focus to the photodetachment region, but this means that an identification of the species investigated becomes more difficult. Usually this is done by blocking all ions with a field applied to an entrance grid in front of the MCP detector. Only the neutrals produced by photodetachment can pass it and, due to their high velocity, they are able to liberate electrons from the MCP.

To obtain the best mass resolution for the VMI experiments, the width of the extracted ion packet is reduced by a slit aperture installed in front of the extraction region, reducing the spread in the initial positions and velocities. Furthermore, the extraction voltages are reduced, which increases the ToF (the resolution will depend on the initial energy spread, and could become worse). The MCP is operated such that the entrance is (almost) at ground and the exit and the anode is on a high positive voltage. This allows slow anionic clusters to be detected, which can usually not enter the MCP, when the entrance is at high negative potential and the anode is kept on ground. The signal is coupled out via a capacitor. The ion packets spread sufficiently in time ( $\gtrsim 15$  ns) that it becomes possible to detach electrons with our ns lasers from the late and early part of a single ion packet. A mass resolution similar to the one of the linear ToF can be reached for the photodetachment.

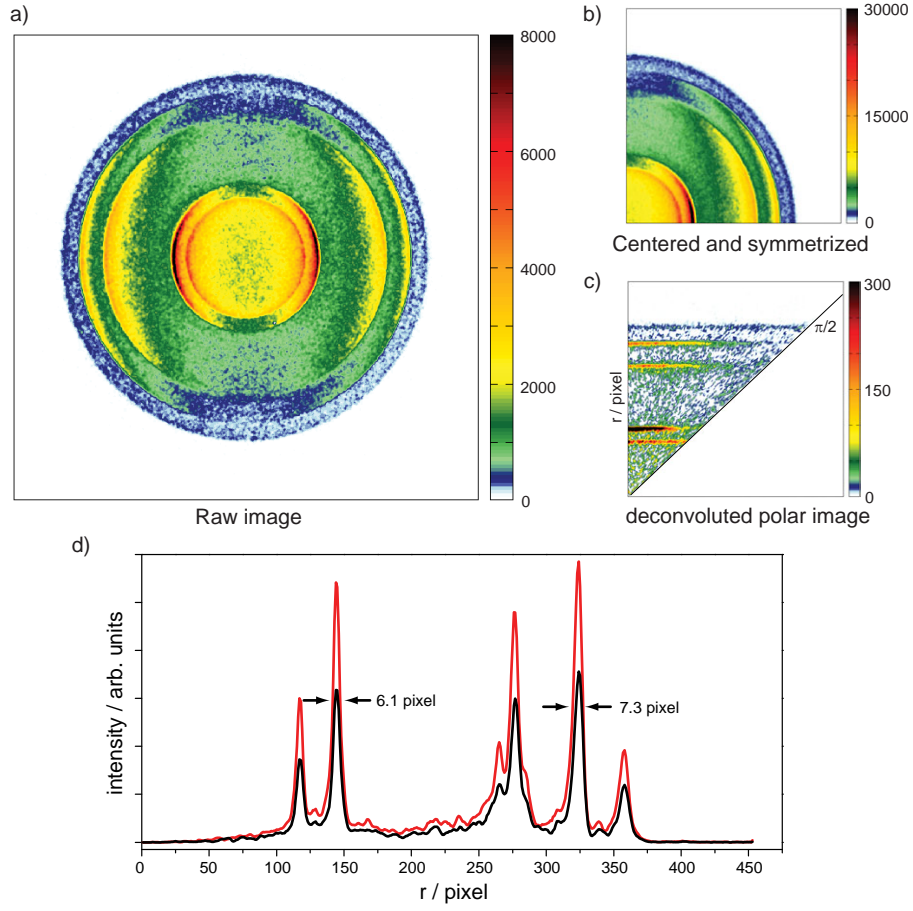


Figure 2.8.: Illustration of the different steps used to analyze the VMI images. A raw image (a), here for  $\text{Ir}^-$  at 355 nm, is centered and symmetrized (b). A coordinate transformation to polar coordinates is performed and the polar onion peeling algorithm [118] is employed. This creates a deconvoluted image (c). Integration over all angles produces the photoelectron spectrum (d). Red and black traces correspond to images taken 5 days apart.

**Analysis of the images.** The recorded images are 2D projections of the 3D velocity distributions of the photoelectrons. For a reconstruction of the original distributions the images first need to be centered. We apply our own algorithm that finds the center by using the cross correlation function along a line of the image in vertical and horizontal direction. For very asymmetric photoelectron distributions this can be done outside the center of the image.

The reconstruction is performed using the polar onion peeling algorithm described in Ref. [118] and available from [119] (we use version 1.1 of the program).

This reconstruction method performs the deconvolution in polar coordinates and confines the noise to the center of the image. Basis functions are used to speed up the deconvolution. The integration over all angles gives the radial photoelectron spectrum, and this is also calculated by the program. The whole analysis procedure is shown for images taken for  $\text{Ir}^-$  in Fig. 2.8(a)-(d).

In Figure 2.8(d) two photoelectron kinetic energy spectra taken with an interval of 5 days are compared; no differences are observed, which demonstrates the stability of the setup. The energy resolution, given by

$$\frac{\Delta E_{kin}}{E_{kin}} = 2 \frac{\Delta r}{r}, \quad (2.17)$$

which can be achieved depends on the velocity and therefore on the radius (or kinetic energy,  $E_{kin}$ ). For the two features shown in the figure it is 4.5 and 8 %. In principle a better resolution has already been achieved for this setup, but this was not the limiting factor for the current experiments.

Conversion to electron binding energies is done using the relation

$$E_{bind} = h\nu - kr^2. \quad (2.18)$$

For atomic anions the EA and the electronic structure of the neutral is often very precisely known. This allows the value of  $k$  to be determined, which can then be used for energy calibration of PES spectra for other, more complex, systems, as for instance the  $\text{Ta}_n\text{C}_m^-$  cluster studied in chapter 5.

For calibration of the PES spectrum of iridium the EA of 1.56436 eV from Ref. [123] can be used. The EA corresponds to a transition from the  $(5d^8 6s^2)^3F_4$  state of  $\text{Ir}^-$  to the  $(5d^7 6s^2)^4F_{9/2}$  ground state of Ir [121]. The calibrated PES spectra using 355 nm (3.49 eV) and 532 nm (2.33 eV) light are shown in Fig. 2.9 along with the energy level diagram of Ir. This allows the observed features in the PES spectrum to be assigned to specific transitions.

A few of the features observed in the PES spectrum cannot be explained by transitions from the ground state of the anion. Instead these illustrate a potentially major problem of this spectroscopy method. For  $\text{Ir}^-$ , besides the ground state, two more electronic states are predicted to be stable [121, 122]. One, the  $(5d^8 6s^2)^3F_3$  state, has already been observed experimentally by two-photon detachment [122] and is found  $7087 \text{ cm}^{-1}$  (0.88 eV) above the ground state, whereas the second one,  $(5d^8 6s^2)^3P_2$ , has not yet been seen experimentally. Transitions from such excited states can make the interpretation of experimental PES spectra considerably more demanding.

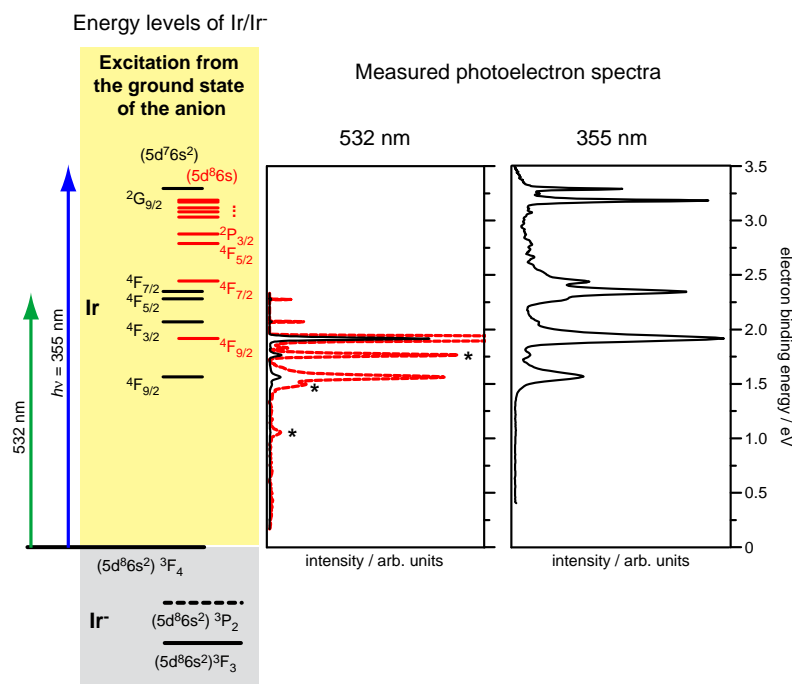


Figure 2.9.: Illustration of the energy levels of Ir [120] that are accessible from the  $(5d^8 6s^2)^3F_4$  ground state of  $\text{Ir}^-$  via photoelectron spectroscopy using 532 nm and 355 nm light. The two graphs on the right show the measured PES spectra. Transitions marked with an asterisk presumably originate from an excited state in the anion. Two have been predicted to be stable for  $\text{Ir}^-$  [121, 122]. Only the  $(5d^8 6s^2)^3F_3$  state has been observed experimentally [122]. However, transitions from this state would not explain the observed additional features. Another state,  $(5d^8 6s^2)^3P_2$ , was also predicted, but its position is not accurately known yet.

#### 2.4.2. The cluster setup at the FELIX facility

The pulsed molecular beam setup at the FELIX facility has been used before for many spectroscopy experiments using IR multiple photon dissociation and has been described for instance in Refs. [83, 100]. Its basic components are similar to the Berlin setup (see Figure 2.10(a)), which was based on this older setup. The setup has been equipped with two different laser ablation cluster sources, both using a pulsed valve manufactured by Jordan TOF Products Inc. [124] which employs a spring-steel current-loop design [125]. This valve makes shorter gas pulses (20–60  $\mu\text{s}$ ) compared to the solenoid valve used in the other setup (200–300  $\mu\text{s}$ ).

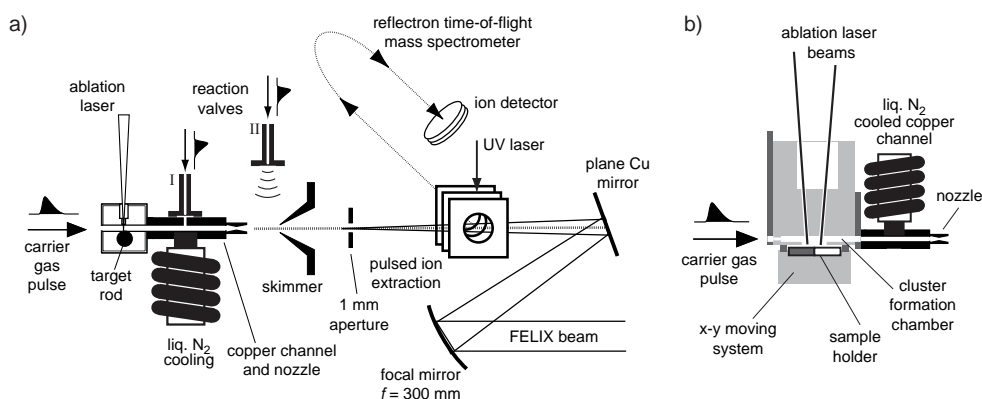


Figure 2.10.: a) FELIX setup with single target cluster source. b) Dual-target dual-laser cluster source.

The first source accepts 6 mm to 1/4 inch rods as targets. Clusters are formed in a source block and cooled in a copper extension channel, which can be temperature controlled by a flow of liquid nitrogen and a heating cartridge between 80–400 K. Two reaction valves allow the formation of different ligand complexes of the produced clusters. One is installed on top of the cooling channel (position I), whereas the second (position II) produces a second molecular beam, which crosses the cluster beam, and reactions can occur under single collision conditions [126].

For the second cluster source, the source block is exchanged with the one depicted in Figure 2.10(b). This dual-laser dual-target cluster source, developed by the Lievens group [110], uses flat rectangular targets ( $7 \times 25$  mm<sup>2</sup>) instead of rods. These are mounted side by side in a sample holder. This holder is pressed against the source block and continuously moved via two vacuum motors along the x-y directions to provide the lasers with new spots on the targets. On the opposite side are two laser entrance channels at an angle of 5° for two independent ablation lasers. Cluster composition is adjusted by the pulse energies of the lasers and their relative delay. In contrast to the single-laser dual-target cluster source described before, the plasma plumes cannot cross and cluster formation conditions strongly vary with respect to the up- and downstream target position.

For both cluster sources the molecular beam expands into vacuum and passes through a skimmer. The charged (cationic and anionic) cluster distribution can be directly analyzed with a pulsed reflectron ToF mass spectrometer with a mass resolution of approximately 2000. Post ionization of a neutral cluster distribution can be performed with different UV excimer lasers, which can be fired between the extraction plates.

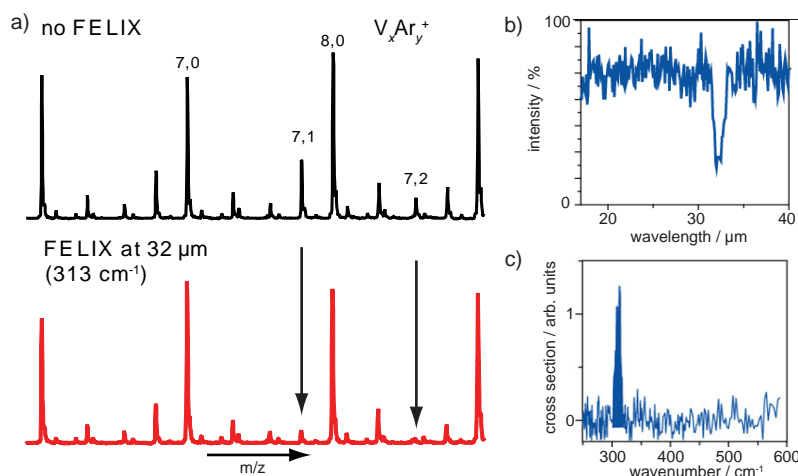


Figure 2.11.: a) Mass spectra of cationic vanadium cluster argon complexes without (upper) and with (lower panel) FELIX radiation at 313  $cm^{-1}$ . For  $V_7Ar_{1,2}^+$  a decrease in ion intensity is observed in the spectrum with IR light. b) Plot of the relative intensity of the two mass spectra for  $V_7Ar^+$  as function of IR wavelength. c) IR absorption spectrum of  $V_7Ar^+$  corrected for the changes in the FELIX pulse energies.

#### 2.4.2.1. IR-MPD spectroscopy - Experimental

IR-MPD spectroscopy of neutral or charged clusters can only be performed via depletion spectroscopy with our setup. Therefore, clusters are made with twice the repetition rate of FELIX (which was 5 Hz for all experiments later described). Mass spectra with and without IR radiation are measured on alternating shots.

The IR light from FELIX is coupled into the setup with two mirrors as shown in Fig. 2.10(a). The IR light is weakly focussed to a position approximately 3 cm upstream of a 1 mm wide aperture installed in front of the extraction region of the reflectron ToF mass spectrometer. At the aperture position the IR beam is larger than the orifice. Depending on the wavelength used, only 60–90 % of the IR light is transmitted. The IR light is sent into the setup approximately 30  $\mu s$  before the ions are extracted, to obtain temporal overlap between the IR beam and the part of the molecular beam which is in front of the aperture. This allows the detection of only those clusters which have interacted with the IR light.

An IR absorption spectrum can be constructed from the integrated mass spectrometric signals observed for a certain mass to charge ratio (see Fig. 2.11(a)). The relative intensity of the complex in the spectrum without IR radiation,  $I_0$ , to the intensity with IR light,  $I(\nu)$ , gives a depletion spectrum (Fig. 2.11(b)). Assuming single photon absorption, this can be converted to IR absorption cross sections,  $\sigma$ ,

normalized by variations in the FELIX laser intensity,  $P$ , by

$$\sigma(\nu) \simeq \frac{1}{P(\nu)} \ln \frac{I_0}{I(\nu)}. \quad (2.19)$$

For several systems it has been shown that this normalization approach yields spectra very similar to one photon absorption spectra [90] and often agrees well with calculated linear absorption spectra. For this PhD thesis, spectra over very wide wavelength ranges have been measured. For these, some larger deviations between experimental and calculated spectra have been observed. In particular the modes in the far-IR are usually overestimated. Therefore, the spectra have been corrected by the IR photon fluence instead of the pulse energy only. For more details please check Refs. [83, 100].



## 3. Ionization vs. dissociation – Neutral silicon clusters\*

### 3.1. Introduction

Silicon based semiconductor technology is the framework of our technological evolution. Further and further miniaturization allowed for development of faster and faster processors and Moore's famous prediction [127] remained valid for several decades. But the increasing costs in producing processors already foreshadow its limit [128]. Today's transistors have sizes not far from that of molecules and clusters and size-dependent effects will start to play a role for future nano-electronic devices. The top-down approach used to assemble current electronics will, in part, be replaced by the bottom-up approach, as can already be seen in molecular nano-electronic devices currently being developed [129]. At this transition region between the bulk and the molecular level fundamental understanding and, more importantly, predictability are required to achieve sufficient reliability and reproducibility for large scale-production of nano-electronic devices [128, 130].

Quantum chemistry aims for this, and can describe the physical and chemical properties from the bulk to the molecular level. Despite its enormous progress, which runs in parallel with increasing demands on computational power, sometimes 'simple' properties such as structure cannot be easily obtained. The potential energy surface can be accurately mapped nowadays by various methods, *e.g.*, simulated annealing, global optimization or basin-hopping. The major limitation, however, is the missing knowledge about the required level of theory to properly describe the system. Experiments can provide essential insights and work as a reference for the calculations.

Because of the technological relevance of silicon, many experimental studies have focused on nano-scale Si particles and clusters. In the gas phase, where iso-

---

\* This chapter is based on the following publications: *Vibrational spectroscopy of neutral silicon clusters via far-IR-VUV two color ionization*, A. Fielicke, J. T. Lyon, M. Haertelt, G. Meijer, P. Claes, J. de Haeck, and P. Lievens, *J. Chem. Phys.* **2009**, 131, 171105.  
*Gas-Phase Structures of Neutral Silicon Clusters*, M. Haertelt, J. T. Lyon, P. Claes, J. de Haeck, P. Lievens, and A. Fielicke, *J. Chem. Phys.* **2012**, 136, 064301.  
*Structure determination of neutral MgO clusters – hexagonal nanotubes and cages*, M. Haertelt, A. Fielicke, G. Meijer, K. Kwapien, M. Sierka, and J. Sauer, *Phys. Chem. Chem. Phys.* **2012**, 14, 2849-2856.

lated bare (and also doped) silicon clusters can be studied and therefore act as an ideal model system, the electronic as well as geometric properties of silicon clusters have been investigated. Charged silicon clusters have been thoroughly investigated, using the combination of ion mobility measurements [19] with high level theory, which made it possible to suggest a change in the structural motif for medium sized clusters, and even a structural assignment for smaller anionic and cationic clusters [131–133]. Other experiments on charged silicon clusters have focused on resonance enhanced multiphoton electron detachment [134] or anion photoelectron spectroscopy [135–139]

Most theoretical investigations, however, focused on neutral structures [140–146], in particular to test the performance of search algorithms in locating the global minima [147–150], despite the lack of experimental information about the neutral structures. For neutral systems the experimental information has been limited, up to now, to optical absorption spectroscopy [151], or Knudsen cell mass spectrometry [152–154] to determine bond energies. Measurements of the ionization energies (IEs) have been used to rule out some isomers predicted by theory, but it is often not sufficient to decide for a single isomer [132]. Because of the very high IEs of silicon clusters precise measurements are difficult, and have been limited to bracketing measurements [155] using fixed frequency excimer lasers. Only recently, synchrotron radiation has been used to measure photoionization efficiency curves for clusters up to  $\text{Si}_7$  [156]. Structural information from vibrational spectra has been obtained for neutral clusters up to  $\text{Si}_7$  only after their deposition and accumulation in cryogenic matrices and subsequent measurement of IR or Raman spectra [157–159].

Recently the measurements of vibrational spectra for  $\text{Si}_{6-21}^+$  by IR multiple photon dissociation using the evaporation of weakly bound Xe atoms as a messenger for the absorption have been reported [55]. As the vibrational fingerprint is particularly sensitive to the geometric structure, this led to the assignment of  $\text{Si}_8^+$  as an edge-capped pentagonal bipyramid structure, which had not been previously considered. For larger clusters the change in the structural motifs from pentagonal bipyramid-based to tricapped trigonal prism-based has been confirmed. In a similar way, structural information on cationic transition metal doped silicon clusters has been obtained using Ar atoms as a messenger [160].

The messenger technique has been applied very successfully for obtaining infrared spectra of strongly bound gas-phase clusters [53] in general, and, unlike many other methods, it is not only limited to charged species. Forming a complex with a weakly bound messenger, however, often becomes difficult for neutral species. In addition, it has the inherent disadvantage that it may induce perturbations of the cluster [74, 161]. Interaction with the messenger may even alter the

relative energetic order of cluster isomers [84]. These problems are exemplified for gold clusters, where complexes with Kr atoms have been observed only at 100 K, whereas atoms of lighter rare gases do not bind. However, the attachment of the highly polarizable Kr atoms has been found to affect the vibrational spectra of the parent Au clusters [24]. A method that reveals the absorption of IR photons by clusters without the need to form a messenger complex is therefore highly desirable. IR resonance enhanced multiple photon ionization IR-REMPI [51] is such a technique. IR-REMPI relies on the sequential absorption of a large number of IR photons by a single cluster followed by delayed thermionic ionization. This process only dominates if the IE is lower than the dissociation energy of the cluster, which is fulfilled only for a few types of clusters, mainly of refractory materials such as some transition metals, *e.g.*, Nb or W, several metal oxides and carbides, as well as fullerenes [52].

A more generally applicable method is the combination of IR excitation with near threshold photoionization. This tunable IR-UV two color ionization (IR-UV2CI) scheme relies on the absorption of a single or few IR photons prior to interaction with a UV photon to lift the total internal energy of the species above the ionization threshold. The direct photoionization generally prevails over the slower statistical fragmentation processes. The ions formed can be sensitively detected by means of mass spectrometry. By scanning the energy of the IR photons the ionization efficiency changes and the recorded ion intensity reflects the IR absorption spectrum of the corresponding neutral species. The high sensitivity of such an approach has been demonstrated for para-amino benzoic acid using a free electron laser as a tunable radiation source in the mid-infrared range, where other intense lasers are lacking [72]. Recently, such an approach has also been used in the mid-IR, using table-top IR-OPOs, to study the vibrational spectra of molecules [162, 163].

In the following, IR multiple photon absorption spectroscopy and near threshold photoionization spectroscopy are applied to a broader range of neutral Si clusters to obtain far-IR spectra between 225 and 550  $\text{cm}^{-1}$ . These results constitute the first vibrational spectra of isolated neutral silicon clusters in the gas phase, and in addition, demonstrate the application of the IR-UV2CI method in the far-IR. Whereas the earlier experiments on para-amino benzoic acid (presumably) required the absorption of only a single IR photon, in the far-IR the absorption of multiple photons is required. For clusters containing 6, 7, 9, and 10 silicon atoms this approach has been pursued. For  $\text{Si}_8$ ,  $\text{Si}_9$ , and  $\text{Si}_{15}$  IR multiple photon dissociation spectroscopy of a xenon messenger complex has been applied. For a single cluster size,  $\text{Si}_9$ , both approaches have been realized, allowing for a direct comparison of the two methods. Insight into the underlying mechanism of the near threshold photoionization

spectroscopy is obtained by modelling the absorption mechanism. For all investigated cluster sizes structural assignments are made by comparison with results from density functional theory calculations.

## 3.2. Experimental

A general description of the setup, the cluster sources and the messenger tagging method are given in the previous chapter. Here, the important aspects for IR-MPD of neutral silicon clusters will be discussed (see chapter 2.2.1 for a general description of IR-MPD) and a detailed explanation of the applied IR-UV two-color ionization method will be given.

For both methods Si clusters are produced via laser ablation in the dual-laser dual-target source described in chapter 2.4, which is also capable of producing binary clusters by coablation from two different targets in a helium atmosphere. The clusters are thermalized to 100 K in a liquid nitrogen cooled extension channel of the source. The cluster distribution is frozen out by expansion into vacuum and the formed molecular beam is shaped by a skimmer and an aperture with 1 mm opening. Ions are removed from the beam by a voltage applied to the aperture. The remaining neutral clusters are ionized within the extraction region of the mass spectrometer by a weakly focused beam from an F<sub>2</sub> laser emitting vacuum-ultraviolet (VUV) photons at 157.63 nm (7.87 eV) for the main laser line[164]. The resulting cationic distribution is analyzed in a reflectron time-of-flight mass spectrometer. Care has been taken to reduce the photon fluence to an extent that the cluster distribution (Fig. 3.1(a)) resembles the single photon ionization mass spectrum [165]. Under these conditions intense signals for Si<sub>8,9,n≥11</sub> are obtained. Si<sub>6,7,10</sub> show rather low intensity, while smaller clusters  $n \leq 5$  are essentially not observed. This corresponds to the known cluster size specific ionization energies shown in Figure 3.2, which are clearly below 7.87 eV for Si<sub>8,9,n≥11</sub>, distinctly higher than 7.97 eV for Si<sub>1–5</sub>, but within 7.87–7.97 eV for Si<sub>6,7,10</sub> [155].

Clusters with an IE below  $\sim 7.9$  eV can be studied with the messenger tagging technique, provided that a messenger complex can be formed, whereas clusters with an IE just above the photon energy of the VUV laser are studied with tunable IR-UV two-color ionization.

### 3.2.1. Dissociation – IR multiple photon dissociation spectroscopy

Direct dissociation of neutral silicon clusters to detect the absorption of IR light is not possible due to their large dissociation energies. For neutral silicon clusters these have been measured by Knudsen cell mass spectrometry. For Si<sub>6</sub> to Si<sub>8</sub> the fragmentation energies are 4.372, 4.18, and 3.68 eV, respectively [152–154]. For the

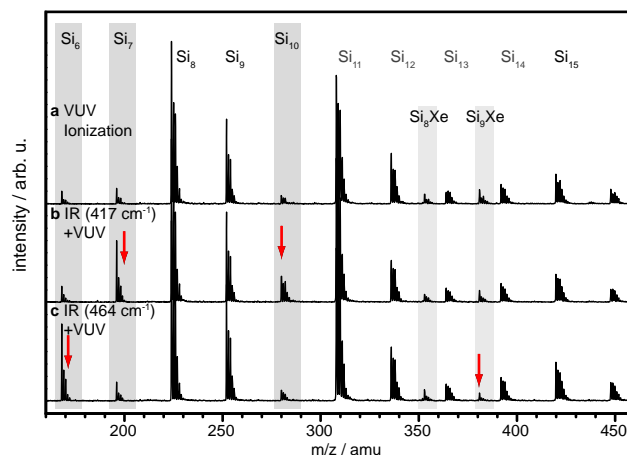


Figure 3.1.: Mass spectra of neutral Si clusters obtained under different ionization conditions. The upper panel shows a spectrum measured with the  $F_2$  ionization laser only, while the lower panels show spectra for a distribution irradiated with different frequencies of FELIX.

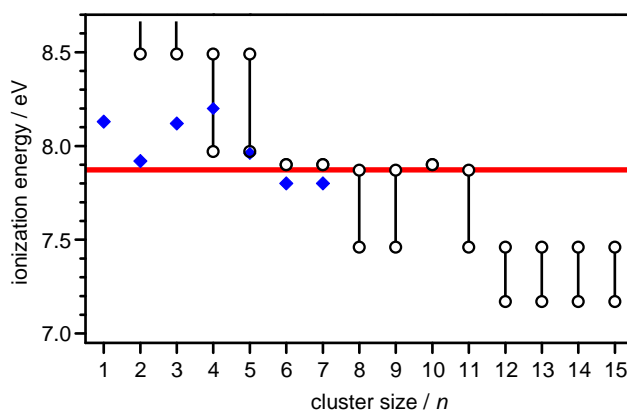


Figure 3.2.: Ionization energies of  $Si_n$  clusters. Bracketing measurements of reference [155] are shown as black open circles, adiabatic ionization energies from photoionization efficiency measurements of reference [156] are shown as blue diamonds. All values are in eV. The red line shows the photon energy of the  $F_2$  laser used for ionization.

other sizes similar values can be expected. Therefore, direct dissociation by IR light is very unlikely, and a messenger complex needs to be formed.

The formation of a messenger complex for silicon clusters is, however, difficult. Even at 80 K, the lowest temperature achievable with our setup, it is not possible to form a complex with either argon or krypton. Instead, an even more polarizable rare-gas has to be taken, xenon. Even then complex formation with Xe is possible for only a few cluster sizes. Xenon also has seven stable isotopes, which further smears out the mass peaks for the silicon clusters. Therefore isotopically enriched  $^{129}\text{Xe}$  is used, and 2 % of it is added to the carrier gas for complex formation. These complexes can be seen for  $\text{Si}_8$  and  $\text{Si}_9$  in Figure 3.1(a). Although it is expected that the IE shifts to slightly lower values upon the attachment of the Xe atom, see *e.g.* Ref. [166], the complexes for silicon clusters with an IE just above the photon energy of the photoionization laser are not observed.

It is assumed that the xenon is only physisorbed to the silicon clusters. For cationic clusters the binding energy between the xenon and the  $\text{Si}_9^+$  cluster was calculated to be only 0.04–0.06 eV [55]. For a neutral species an even weaker interaction is expected, due to the missing charge (induced) dipole interaction. Such a bond can be easily broken by the resonant absorption of a single or a few IR photons. The resulting evaporation of Xe can be seen for instance for  $\text{Si}_9\text{Xe}$  in Fig. 3.1(c) at  $464\text{ cm}^{-1}$ . The relative change of the mass spectrometric signal is recorded as a function of IR wavelength and an IR absorption spectrum is derived (see section 2.4.2.1).

### 3.2.2. Ionization – Tunable IR-UV two-color ionization spectroscopy

For silicon clusters with an ionization energy above the photon energy of the  $\text{F}_2$  laser, *e.g.*,  $\text{Si}_{6,7,9,10}$ , weak signals are observed. The fluence of the UV laser was reduced to avoid multiple photon ionization, however, the source conditions in general, and in particular at 100 K are not sufficient for a complete quenching of electronically and vibrationally excited states. Therefore, the residual signal can be assigned to the hot fraction of the thermal cluster distribution. The internal energy distribution for  $\text{Si}_7$  is shown in Fig. 3.3, and was derived with the help of the Beyer-Swinehart algorithm [87] by assuming a Boltzmann distribution close to the source temperature of 100 K. The majority ( $\sim 68\%$ ) of the clusters are in the vibrational ground state, but a small fraction of  $\ll 0.1\%$  has an internal energy larger than 0.1 eV ( $806\text{ cm}^{-1}$ ).

The ionization efficiency usually follows a S-curve behavior as a function of excitation energy, with a slope depending on the Franck-Condon overlap between neutral and cationic structure. For  $\text{Si}_7$  this curve has been measured by Kostko *et al.* [156] and is shown in Figure 3.4(a). A small rise of the internal energy of the

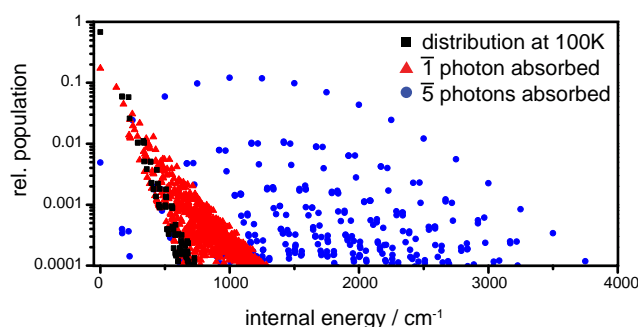


Figure 3.3.: Distribution of the internal energy for  $\text{Si}_7$  at 100 K (black squares) and after an average absorption of 1 and 5 photons at  $250\text{ cm}^{-1}$  shown as red triangles and blue dots, respectively.

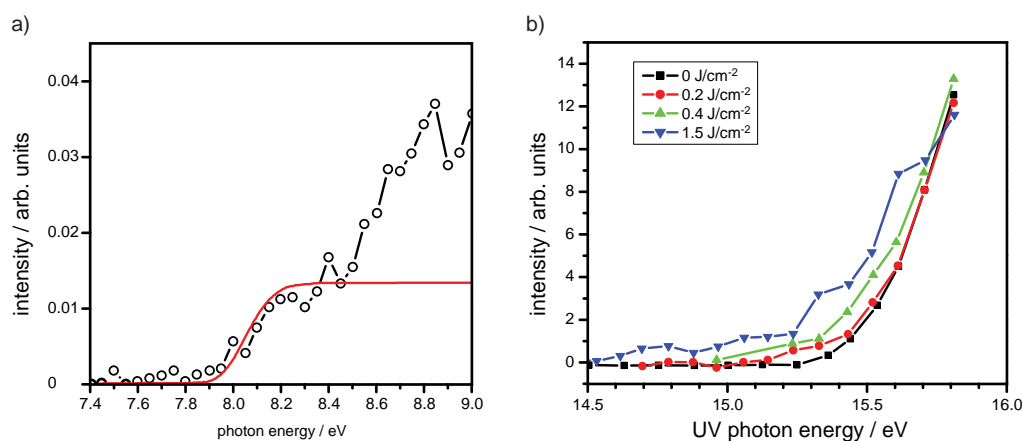


Figure 3.4.: a) Photoionization efficiency curve of  $\text{Si}_7$  as function of UV photon energy, taken from Ref. [156]. b) Photoionization efficiency curves of IR laser excited  $\text{SF}_6$  as function of the excitation power ( $\text{CO}_2$  laser at  $942.4\text{ cm}^{-1}$ ).

clusters dramatically increases the proportion of ionizable clusters[167]. This has been shown for the  $\text{SF}_6$  molecule, which was resonantly excited with a  $\text{CO}_2$  laser at  $942.4\text{ cm}^{-1}$ , and later ionized with a pulsed UV lamp. Depending on the IR laser intensity the photoionization efficiency curve shifts to lower UV photon energies [168], see Figure 3.4(b). This can be used to obtain cluster size specific IR spectra by resonant excitation with IR light.

A change in the photoionization efficiency expresses itself as a change in the relative mass spectrometric intensities, if the cluster beam is irradiated with resonant IR light before interaction with the VUV radiation [b) and c) in Fig. 3.1]. In these experiments, a beam of intense pulsed IR radiation emitted from the Free Elec-

tron Laser for Infrared eXperiments FELIX counterpropagates along the molecular beam and is focused onto the aperture shaping the cluster beam. This ensures that all clusters detected afterwards passed the focal range and interacted with the IR light. The IR pulse energies were about 20–40 mJ at a pulse length of 5  $\mu$ s. If the frequency of the IR light is in resonance with an IR active mode of the cluster it can absorb one or more IR photons. Subsequent internal vibrational energy redistribution leads to a thermal heating of the cluster. The enhancement is a purely thermal effect as the clusters are irradiated with IR light 30  $\mu$ s before interaction with the VUV photons. The traces b) and c) in Fig. 3.1 demonstrate the change in the ionization efficiencies upon pumping the neutral cluster distribution with 464 and 417  $\text{cm}^{-1}$  photons respectively, leading to strong signal enhancements for  $\text{Si}_6^+$  in the first case, and for  $\text{Si}_7^+$  as well as  $\text{Si}_{10}^+$  in the second (highlighted with red arrows in Fig. 3.1).

The increase of the relative proportion of ‘hot’ clusters can be modeled by a simple Monte-Carlo simulation with a fixed absorption probability. For  $\text{C}_{60}$  it has been found before that such an approach can give quantitatively similar results to a numerical modeling of the vibrational ladder climbing considering explicitly the effects of (cross-) anharmonicities [52]. The internal energy distribution of  $\text{Si}_7$  following the absorption of, on average, a single or five photons is shown in Fig. 3.3 with an assumed absorption probability of  $p=0.01$  and a photon energy of 250  $\text{cm}^{-1}$  for  $\text{Si}_7$ . The proportion of clusters with an internal energy above 0.1 eV rises dramatically, to 6 % for 1 photon absorption and to 78 % for 5 photon absorption.

The cluster-size specific IR spectra using this tunable IR-UV two-color ionization scheme are obtained by recording on alternating shots mass spectra with ( $I$ ) and without FELIX irradiation ( $I_0$ ) and by scanning the IR wavelength. Relative absorption spectra are derived from the relative enhancements of the ion signal by  $(I - I_0)/I_0$  and normalized by the photon fluence. The experimental spectra have been smoothed with a 5-point running average.

### 3.3. Theory\*

To assign the experimentally observed spectra to specific cluster structures, comparison with calculated IR spectra is required. A fairly large set of local minimum structures for (neutral) silicon clusters is available as such systems have been studied by many groups [140–150]. Furthermore, for cationic clusters of the sizes considered here an assignment for the structures observed in experiment has been

\* The calculations have been performed by Dr. J.T. Lyon from the Department of Natural Sciences of the Clayton State University, Morrow, GA, USA.



possible by combining IR-MPD spectroscopy with quantum chemical calculations [55]. These structures, and other theoretically predicted low energy structures have been considered in the calculations employing the Gaussian 03 program suite [169]. Density functional theory as well as MP2 calculations have been performed. Lyon *et al.* showed that for most cationic silicon clusters DFT with the BP-86 functional [170, 171] and the SVP basis set [172] using the resolution of identity (RI) approximation gave sufficient agreement between the measured IR-MPD spectra and theory. More involved methods, such as second-order Møller-Plesset perturbation theory (MP2), do not necessarily give better agreement. For the  $\text{Si}_{11}^+$  cluster it was shown that with the same relaxed cluster structure different calculated IR spectra are obtained [55]. Therefore, for all sizes DFT calculations on the same level as for the cations have been performed. The, in general, good agreement between the measured spectra and the DFT results justifies this approach. For a few selected sizes,  $\text{Si}_6$ ,  $\text{Si}_7$  and  $\text{Si}_{10}$ , calculations for the predicted global minimum have also been performed at the MP2 level using the def2-TZVP basis set [173]. Calculations were performed without symmetry constraints, except for the cluster sizes treated by both DFT and MP2. For these sizes subsequently the maximum symmetry has been imposed.

Relative energies of different isomers determined by DFT are given in kJ/mol and include zero point vibrational energy corrections. The messenger atom has not been explicitly considered, as the interaction between the neutral Si clusters and the Xe atoms is expected to be significantly weaker than for the cationic Si clusters that have calculated Xe binding energies lower than 0.1 eV [55]. The electronic state of all clusters corresponds to the lowest possible spin multiplicity (singlet). The analytically calculated IR frequencies are all real for the structures reported here and have been rescaled with multiplication factors of 1.03 (DFT) and 0.96 (MP2) as before [55], and have been convoluted with a Gaussian function with a full width at half maximum of  $8\text{ cm}^{-1}$ .

### 3.4. Results and discussion

The absorption spectra of  $\text{Si}_6$ ,  $\text{Si}_7$  and  $\text{Si}_{10}$  measured by IR-UV2CI spectroscopy in the  $225\text{--}550\text{ cm}^{-1}$  range are shown in Fig. 3.5. The spectra of  $\text{Si}_6$  and  $\text{Si}_7$  are dominated by a single peak at  $464 \pm 1$  and  $417 \pm 1\text{ cm}^{-1}$ , respectively, while the spectrum of  $\text{Si}_{10}$  is clearly more complex.

For  $\text{Si}_6$  and  $\text{Si}_7$  these findings can be compared with previous experimental results. In matrix isolation experiments using different rare gas hosts, a single IR absorption band found at  $462.9\text{ cm}^{-1}$  in Ne,  $460.9\text{ cm}^{-1}$  in Ar, and  $458.5\text{ cm}^{-1}$  in Kr has been assigned to the  $e_u$  modes of  $\text{Si}_6$  in the  $D_{4h}$  structure (see Fig. 3.5 and

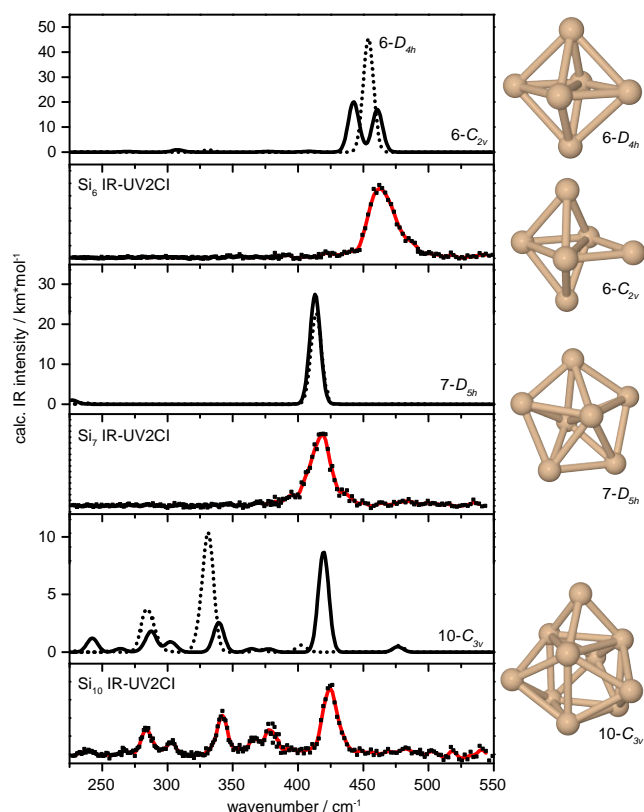


Figure 3.5.: IR-UV2CI spectra of  $\text{Si}_6$ ,  $\text{Si}_7$ , and  $\text{Si}_{10}$  clusters compared to infrared spectra of the lowest energy structures from DFT (solid lines) and MP2 calculation (dotted lines). In the experimental spectra reported here, the dots correspond to the original data points, the red line is a 5-point binomial weighted average. The y-axis for the experimental spectrum has arbitrary units.

Table 3.1), while a band at  $422.4 \text{ cm}^{-1}$  (Ar) and  $420.4 \text{ cm}^{-1}$  (Kr) was assigned to the  $e'_1$  modes of  $D_{5h}$   $\text{Si}_7$  [158]. Analysis of the vibrational progressions in the photoelectron spectrum of  $\text{Si}_7^-$  revealed a frequency of  $385 \pm 20 \text{ cm}^{-1}$  for neutral  $\text{Si}_7$  [135, 174]. This has been compared with the data from Raman spectroscopy measured in an  $\text{N}_2$  matrix. In that range  $\text{Si}_7$  has a Raman active mode at  $435 \text{ cm}^{-1}$  ( $a'_1$ ) [157, 159]. The differences between the frequencies obtained from the photoelectron spectrum and in the matrix isolation experiment has been suggested to be due to matrix effects. A comparison of the frequencies of the IR active modes of the gas-phase clusters reported here with those from the matrix experiments suggests, however, that there are only very minor shifts.

The experimental spectra in Fig. 3.5 are compared with the results of DFT and

Table 3.1.: Assignments of experimentally observed IR bands and comparison with values calculated by DFT (frequencies scaled by a factor of 1.03). The experimental frequencies have an estimated uncertainty of  $\pm 1 \text{ cm}^{-1}$ .

Cluster	Symmetry	$\nu_{\text{expt}}$ ( $\text{cm}^{-1}$ )	$\nu_{\text{calc}}$ ( $\text{cm}^{-1}$ )	Mode
Si <sub>6</sub> <sup>a</sup>	$D_{4h}$	464	453.9	$e_u$
Si <sub>7</sub>	$D_{5h}$	417	413.9	$e'_1$
Si <sub>10</sub>	$C_{3v}$	425	418.6	$e$
		380	376.0	$e$
		366	364.3	$a_1$
		342	341.0	$a_1$
		303	301.0, 303.8	$e, a_1$
		284	287.0	$e$
		267	262.5	$a_1$
		239	241.0	$e$

<sup>a</sup>Theoretical data from MP2 calculations scaled by 0.96.

MP2 calculations. A good agreement between the experimental and the DFT results is obtained, which indicates identification of the correct structures. For Si<sub>6</sub> MP2 calculations give a better representation of the spectrum, while for Si<sub>7</sub> the performance is nearly identical to the DFT approach. For Si<sub>10</sub> the calculated IR spectrum from the DFT calculations provides a good match to the experiment. The spectrum from MP2 is a less good match, mainly because the intensities are very different, although the structure is nearly unchanged with respect to the DFT predictions.

The reason for the differences between the spectra of Si<sub>6</sub> predicted by either DFT or MP2 is that depending on the method, different lowest energy structures are favored for Si<sub>6</sub> [157, 175–177]. DFT usually favors an edge-capped trigonal prism of  $C_{2v}$  symmetry, while with MP2 the distorted octahedron  $D_{4h}$  is found as the minimum energy structure. Higher level methods taking multiple electronic configurations into account reveal that the potential surface around the ground state is very flat and the structure fluctuates between the distorted octahedron, the edge-capped trigonal prism, and the face-capped trigonal prism[176]. Lately, this has been explained by Si<sub>6</sub> undergoing a pseudo Jahn-Teller distortion and it has been shown that the predictive capabilities of the theoretical methods depend on their treatment of the pseudo Jahn-Teller effect [177]. Within our DFT calculations Si<sub>6</sub> is found in a  $^1A_1$  state with  $C_{2v}$  symmetry and MP2 predicts the distorted octahedron  $D_{4h}$  in the  $^1A_{1g}$  state. The experimental finding is consistent with either of them, as the band splitting predicted for the  $C_{2v}$  structure might not be resolved in the

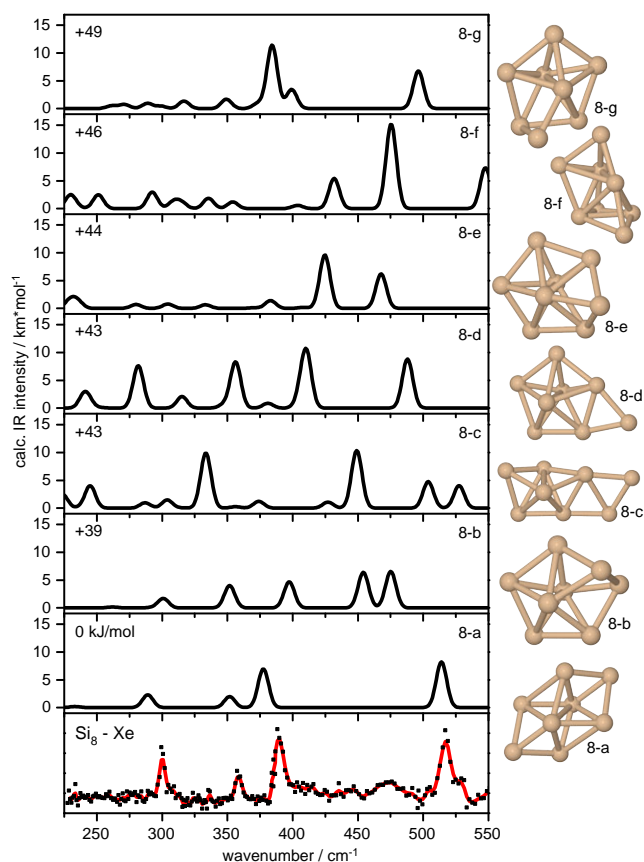


Figure 3.6.: IR-MPD spectrum of xenon-tagged  $\text{Si}_8$  cluster compared to infrared spectra of low lying isomers predicted by DFT. Relative energies are given in kJ/mol.

experiment. Regardless, the band observed for  $\text{Si}_6$  is noticeably broader in comparison with those observed for the other sizes.  $\text{Si}_7$  is a pentagonal bipyramid with  $^1A_1$  electronic configuration. The cluster structures for both  $\text{Si}_6$  and  $\text{Si}_7$  resemble the structure of their cationic counterparts. The discussion for  $\text{Si}_{10}$  is presented in detail later.

For  $\text{Si}_8$  Fig. 3.6 shows the measured IR-MPD spectrum of its Xe complex and calculated linear absorption spectra for several low lying isomers. The putative global minimum structure, 8-a, is a bicapped octahedron structure, 39 kJ/mol below the next isomer. All four experimentally observed bands at 300, 359, 390, and 517  $\text{cm}^{-1}$  are reproduced by the calculated spectrum, which predicts stronger absorption at 289, 352, 378, and 514  $\text{cm}^{-1}$ . Most of the other predicted isomers emerge from differently capping a pentagonal bipyramid, and none explains the observed experimental IR spectrum. For the cationic structure, an edge-capped pentagonal

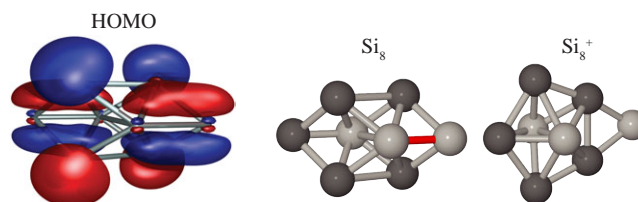


Figure 3.7.: HOMO of the neutral  $\text{Si}_8$  and a detailed comparison of the structures of cationic and neutral  $\text{Si}_8$ . In the neutral cluster the HOMO has bonding character along the bond marked in red. Upon ionization, this level gets partially depopulated and the structure becomes unstable. The atoms forming the pentagonal ring are colored in dark grey.

bipyramid structure was identified, and this structure was also considered for the neutral system, but this isomer (8-d) is much higher in energy (+43 kJ/mol).  $\text{Si}_8$  is a unique cluster size where a major difference between the cationic and neutral cluster structure is observed. Such a behavior was previously predicted, *e.g.*, by Liu *et al.* [132], although a slightly different cationic structure was suggested as the putative minimum. A comparison of the cationic and neutral structures reveals that both can interconvert with only a little atomic rearrangement, see Figure 3.7. This structural change may be rationalized by the character of the highest occupied molecular orbital (HOMO) of  $\text{Si}_8$  which has bonding character along the Si-Si bond that needs to break to form the cationic structure; ionization facilitates the destabilization of this Si-Si bond in the neutral (marked in red in Fig. 3.7).

The  $\text{Si}_9$  cluster is a system for which IR spectra could be obtained by both methods, IR-MPD and IR-UV2CI. The IR induced enhancement of the ionization efficiency is, however, less pronounced than for the clusters discussed before, which can be related to its lower IE. This is estimated to be in the range of 7.46–7.87 eV (for  $\text{Si}_8$  as well as for  $\text{Si}_9$ ) while for  $\text{Si}_{6,7,10}$  a value of about 7.9 eV has been reported [155]. These values are in accord with the mass spectra taken with the  $\text{F}_2$  laser ionization, see Figure 3.1, which shows that for the latter sizes a lower intensity is observed. However, the intensity of  $\text{Si}_8$  is almost a factor of two larger than for  $\text{Si}_9$ , which is an indication for significant differences in the IEs of these two systems. Most probably, the IE of  $\text{Si}_9$  is closer to the upper limit of the range given by Fuke *et al.* More recent measurements of the ionization efficiency curves using synchrotron radiation have shown some differences to the earlier experiments, in most cases the determined IEs are lower [156], see Figure 3.2. In particular for  $\text{Si}_{2,3}$  quite large deviations, of up to 0.5 eV, have been observed. However, these experiments strongly rely on the preparation of cold clusters and there seem to be differences in the thermalization of the clusters in these two experiments. Unfortunately these

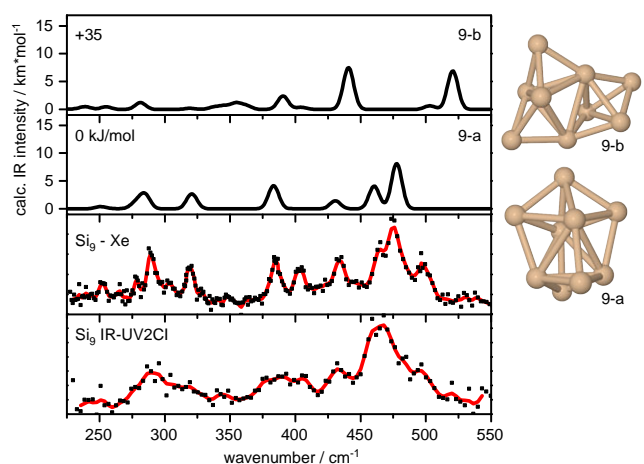


Figure 3.8.: IR-MPD and IR-UV2CI spectrum of  $\text{Si}_9$ . Two low lying isomers and their predicted IR spectra are shown for comparison.

results are limited to  $n < 7$ . Because of the lack of sufficiently precise measurements of the IEs for the larger systems, we have to rely on calculated vertical ionization energies (VIEs) to obtain information on the trend of the IE. The VIEs for  $\text{Si}_6$  ( $D_{4h}$  structure) and  $\text{Si}_7$  are 8.20 and 8.21 eV respectively. They compare reasonably well with the experimentally determined adiabatic values of  $7.8 \pm 0.1$  eV, taken from Ref. [156]. The calculated VIEs for  $\text{Si}_9$  and  $\text{Si}_{10}$  are 8.14 eV and 8.11 eV respectively, though our experiment suggests a slightly lower value for  $\text{Si}_9$  compared to  $\text{Si}_{10}$ , while the IE for  $\text{Si}_8$  is significantly lower (7.50 eV). Overall, this agrees well with the intensity pattern in the experimental mass spectrum obtained using an  $\text{F}_2$  laser for ionization.

For the  $\text{Si}_9$  cluster the IE seems to be just low enough compared to the photon energy for efficient ionization of the xenon complex, albeit still in the leading edge of the photoionization efficiency curve, below saturation. This allows the application of IR-MPD spectroscopy on the rare gas complex while an IR-UV2CI spectrum can also be recorded. The latter spectrum is measured without any Xe gas added, therefore excluding the possibility of enhancements stemming from the fragmentation of the Xe-complex. The spectra measured by the two different methods are shown in Figure 3.8. Both spectra look quite similar, however, the IR-MPD spectrum is better resolved and more features are observed. This is probably due to the lower internal energy required to dissociate the xenon complex vs. photoionization of the bare cluster.

The calculated isomer showing the best agreement with the experiment, a bi-capped pentagonal bipyramid (9-a), has the same structure as in the case of the

cation. Most features are explained by this structure, except for bands at 403 and 497  $\text{cm}^{-1}$ . These features can be found in both experimental spectra, and therefore cannot be attributed to a messenger effect. The feature at 403  $\text{cm}^{-1}$  may come from a calculated mode at 403  $\text{cm}^{-1}$ , which has only a very weak predicted IR intensity of 0.03  $\text{km/mol}$ , but may be enhanced in the experiment. Around 500  $\text{cm}^{-1}$  no vibrational fundamental is predicted and the isomers higher in energy also do not show an intense feature at this frequency (see Fig. 3.8). It may well be that another isomer is additionally present that has not been identified in the calculations. Nevertheless, it is noted that the depletion observed at 497  $\text{cm}^{-1}$  amounts to 50 % and for the most intense peak at 475  $\text{cm}^{-1}$  to 80 % of the total intensity of  $\text{Si}_9\text{Xe}$ . This may suggest that an additional isomer contributes significantly to the band at 475  $\text{cm}^{-1}$ .

For  $\text{Si}_{10}$  the trigonal prism, an important structural motif for larger Si clusters, becomes the structural base. Comparison between the IR-UV2CI spectrum and the DFT calculations for the fourfold capped trigonal prism structure of  $C_{3v}$  symmetry in a  $^1A_1$  state shows good agreement (see Figure 3.5). This is in agreement with previous predictions [131, 178, 179]. Other isomers of  $\text{Si}_{10}$  are at least 54  $\text{kJ/mol}$  higher in energy and exhibit rather different vibrational spectra. This structure was also observed for the cationic silicon clusters with 10 atoms. First indications for a new structural motif emerging at  $\text{Si}_{10}$  were already reported in ion mobility experiments, where a sudden jump in the mobilities was observed [132]. Later, IR-MPD experiments [55] confirmed these findings and proved the trigonal prism as structural subunit for  $\text{Si}_{11,13,15}$ , and  $\text{Si}_{18}$ .

Unfortunately, even though  $\text{Si}_{11}$  to  $\text{Si}_{14}$  were observed in the mass spectra and their IEs are well below the photon energy of the  $\text{F}_2$  laser, the intensities for the xenon complexes were too low to obtain IR spectra for these clusters. Only for the  $\text{Si}_{15}$  cluster was the complex intensity sufficient and the experimental IR-MPD spectrum can be seen in Figure 3.9. The lowest energy isomer found in the calculations is the same as for the cationic system, see Fig. 3.10. In both cases a tricapped trigonal prism with a six-atom triangle attached, isomer 15-a, is predicted as the global minimum structure. All of the major features of the IR-MPD spectrum are reproduced by the calculated spectrum of this isomer.

The broader band in the 425–450  $\text{cm}^{-1}$  range, which seems to contain several features, may also be explained by this isomer. Although the calculated spectrum appears as a single band, it is composed of three close-lying modes at 425.9, 426.2, and 432.6  $\text{cm}^{-1}$ , which may be split further by the presence of the messenger atom. Another explanation for this broad band might be the additional presence of the second lowest energy structure 15-b, which is 5  $\text{kJ/mol}$  above the putative global minimum. For this structure, the calculation predicts an intense absorp-

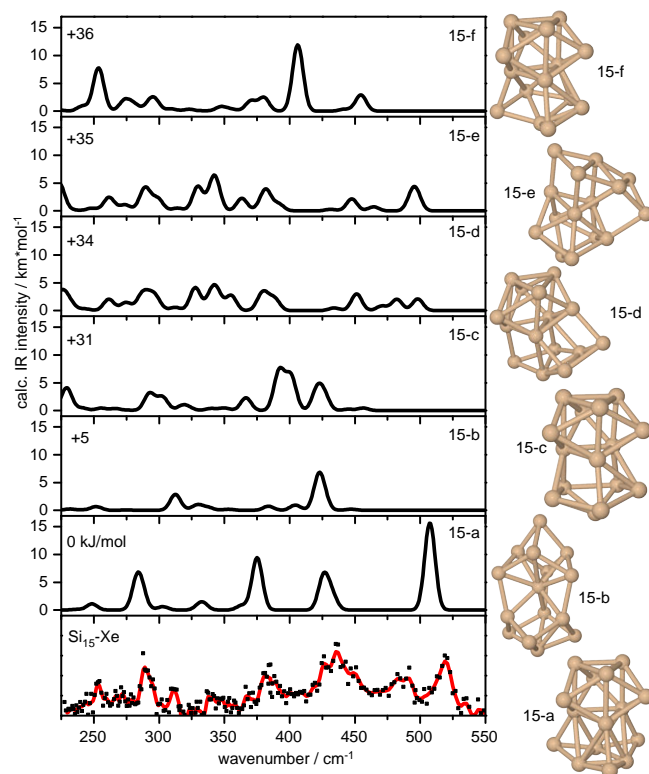


Figure 3.9.: IR-MPD spectrum of xenon-tagged  $\text{Si}_{15}$  clusters compared with linear absorption spectra for several predicted minimum energy structures.

tion at  $422\text{ cm}^{-1}$ , and two weaker bands at  $425$  and  $426\text{ cm}^{-1}$ . Other bands also may have an approximate counterpart in the experimental spectrum. This may be the first evidence for the prediction that for neutral silicon clusters with more than 12 atoms several isomers are present at elevated temperatures [180]. Only a weaker band at  $\sim 485\text{ cm}^{-1}$  has no counterpart in the calculated spectrum and its origin is unclear. It may be due to the presence of the messenger atom, which is not accounted for in the calculations. None of the calculated spectra of higher energy isomers give a better fit to the measured spectrum or explain the additional feature. The identified ground state isomer has a large electric dipole moment of  $2.9\text{ D}$  which may facilitate the formation of the Xe complex. The other cluster sizes forming the messenger complex, however, have calculated dipole moments of only  $0.001\text{ D}$  and  $0.290\text{ D}$ , for  $\text{Si}_8$  and  $\text{Si}_9$ , respectively. Apparently, the dipole moment is not the critical parameter for the complex formation.



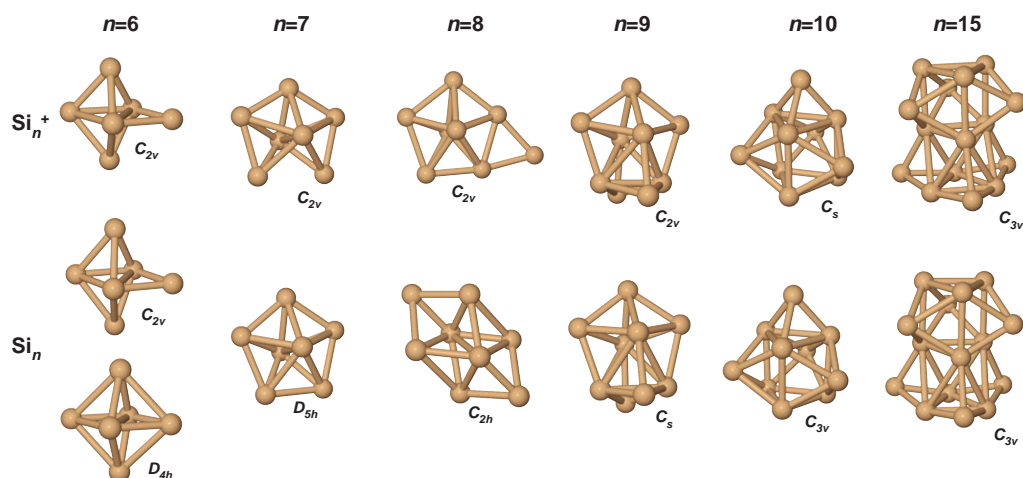


Figure 3.10.: Comparison between the structures determined by gas-phase IR spectroscopy for cationic and neutral silicon clusters with  $n = 6 - 10$  and 15. Approximate symmetries are determined from the atomic geometries calculated without symmetry constraints.

### 3.5. Conclusions

Cluster size-specific vibrational spectra of  $\text{Si}_{6-10}$  and  $\text{Si}_{15}$  have been measured by using two different gas-phase IR spectroscopic methods, IR-MPD of Xe messenger complexes and IR-UV two-color ionization. Comparison with predictions from density functional theory allows assignment of the cluster structures. The identified structures correspond to the lowest energy isomers as predicted at the BP-86 level of theory. The structures of the smaller clusters ( $\text{Si}_{6-9}$ ) are found to be based on the bipyramidal motif.  $\text{Si}_6$  has the structure of a (distorted) tetragonal bipyramid that forms, if capped by two atoms, the  $\text{Si}_8$  structure. The pentagonal bipyramid of  $\text{Si}_7$  forms the base for the  $\text{Si}_9$  cluster. With the exception of  $\text{Si}_8$ , the same growth pattern as for cationic clusters is observed (see Fig. 3.10).

Similar to cationic silicon clusters, the tricapped trigonal prism structure is not found for  $\text{Si}_9$ , but is the fundamental motif for clusters from  $\text{Si}_{10}$  onwards. For  $\text{Si}_8$  a marked difference is observed between the structures of the cation and neutral, as they are built upon the pentagonal vs. tetragonal bipyramidal motif, respectively. This structural change can be rationalized by the bonding character of the HOMO of  $\text{Si}_8$  which relaxes the bipyramidal structure upon ionization. Even though the structures of neutral silicon clusters have been predicted by theory before, this is the first unambiguous experimental confirmation for larger clusters. The presented results provide reference data for theoretical investigations and may allow

for further insights into the charge-state dependence of the clusters' properties in general.

The tunable IR-VUV two photon ionization technique allows for characterization of the cluster structures without the need of a possibly perturbing messenger or host matrix. As many strongly bound clusters have their ionization energies in a range accessible by (tunable) UV lasers, near threshold ionization should be achievable. It is expected that tunable IR-UV two photon ionization will become a more generally applicable method for the investigation of vibrational spectra of neutral clusters. By combining two tunable laser sources, the UV photon energy can be adjusted allowing for vibrational spectroscopy to the very far-IR, the terahertz regime, where other methods reach their limits. Furthermore, the technique should not be limited to low temperatures, as messenger tagging experiments are, and therefore could allow for studying temperature dependent effects over a wide temperature range.

## 4. Charged and neutral magnesium oxide clusters\*

Magnesium oxide is considered as a prototype material of a (simple) metal oxide. In contrast to many other materials, the bulk structure, a cubic NaCl structure, is preserved even at extremely high pressures of up to 227 GPa [181]. Its physical properties, high melting point, high resistance, corrosion resistance, etc. are the reason for its use in many industrial applications, such as for crucibles, insulators in heating elements, or in cements. In the high temperature superconductor  $\text{Bi}_2\text{Sr}_2\text{CaCu}_2\text{O}_x$  (nano-)particles of magnesium oxide are used as pinning centers for the (magnetic) flux to enhance the critical current density [182–187]. Furthermore, MgO plays an important role in chemistry and is used as a support material for (transition) metal catalysts. Whereas the perfect MgO surface is generally unreactive, this changes for defect-rich surfaces. These are active for hydrogenation (transfer) reactions or dehydrogenation [188–190].

In methane based chemistry [191, 192] MgO may also play an important role. Currently, many large-scale chemical processes base on crude oil as raw material, but resources are limited. Methane, the main constituent of natural gas, but which is also a product of fermentation processes, would be an alternative. Because of its biological origin it could be considered as a renewable resource, though it also acts as a greenhouse gas. Efforts are currently underway to develop catalysts, which would allow direct selective functionalisation of methane to ethane or methanol. Up to now, only reactions with the detour via synthesis gas ( $\text{CO} + \text{H}_2$ ) have industrial relevance. Several possible catalysts have been found in the lab for the oxidative coupling of methane to ethene [193, 194], but none has made the step to the large scale process. Selectivity and yield are the limiting factors, as the reaction products, which are more reactive than the methane, react further to  $\text{CO}_x$ . Among the possible candidates is lithium doped magnesium oxide. Lunsford and coworkers found that this system is able to activate methane [195, 196], which is the first step of the catalytic cycle. They proposed a mechanism [196], depicted in

---

\* Parts of this chapter are based on the following publications: *Structural diversity and flexibility of MgO gas phase clusters*, K. Kwapien, M. Sierka, J. Döbler, J. Sauer, M. Haertelt, A. Fielicke, G. Meijer, *Angew. Chem. Int. Ed.* **2011**, 50, 1716.

*Structure determination of neutral MgO clusters – hexagonal nanotubes and cages*, M. Haertelt, A. Fielicke, G. Meijer, K. Kwapien, M. Sierka, and J. Sauer, *Phys. Chem. Chem. Phys.* **2012**, 14, 2849.

Figure 4.1, that assumes  $[\text{Li}^+\text{O}^-]^\bullet$  sites as the active species. In a homolytic reaction methyl radicals,  $\text{CH}_3^\bullet$ , are formed, leaving a surface hydroxy group  $\text{OH}^-$  as an intermediate species. The methyl group is mobile on the surface, and ethane can be formed by coupling with another methyl. The surface hydroxyl group undergoes heterolytic dissociation into a surface  $\text{O}^{2-}$  and a proton. The proton can recombine with another hydroxyl group, leading to water desorption and the formation of an oxygen vacancy  $\text{V}_\text{O}$  on the surface. With gas-phase oxygen molecules and by electron transfer from the  $[\text{Li}^+\text{O}^{2-}]$  sites, the active centers can be regenerated. These original studies were the starting point for further investigations by experiment and theory. The more recent investigations cast doubts on the proposed mechanism, as experiments showed that the Li is not stable on the surface [197], and that the reaction also occurs on bare MgO surfaces and even without any particular catalyst [198]. The selectivity, however, is higher on the lithium doped system. Theory that describes the electronic structure, the defect formation energies, and the reaction pathways is also very challenging as only the most accurate levels of theory for very large supercells or cluster models seem to give results consistent with experiment. Furthermore, the reaction occurs at rather high temperatures, where the surface becomes unstable. Theoretical kinetic studies, which would help to develop a mechanistic understanding of the reaction and which are required to develop an industrial process, are only in agreement with some experiments. The common opinion is that oxygen radical centers,  $\text{O}^-$ ,  $\text{O}_2^-$ ,  $\text{O}_2^{2-}$  and  $\text{O}_3^-$  are important for the reaction [193, 199, 200] and that it involves both gas-phase and surface catalytic reactions [201, 202]. For a recent review summarizing the current knowledge see Ref. [203].

Gas-phase studies on clusters may help to improve the understanding of the methane activation on MgO, as systems with a reduced size can act as model systems and allow for high level calculations. The geometric and electronic structure of the cluster model systems can be experimentally investigated, and their reactions can be studied. Depending on the experimental conditions reactive intermediate species are also accessible. Here, vibrational spectroscopy has been performed on a series of different species, which may be relevant at different steps of the oxidation reaction. The systems covered include neutral  $(\text{MgO})_n$  clusters, whose electronic structure corresponds to that of MgO on a perfect surface and cationic  $(\text{MgO})_n^+$  clusters, which are isoelectronic to the lithium doped magnesium oxide. The influence of charge on the geometric structure of the clusters can thereby be investigated.

As clusters often have very different structures to those observed for the bulk phase, the size range for the transition to the bulk structure is of great importance. For neutral clusters there are indications that instead of bulk cubelike structures,

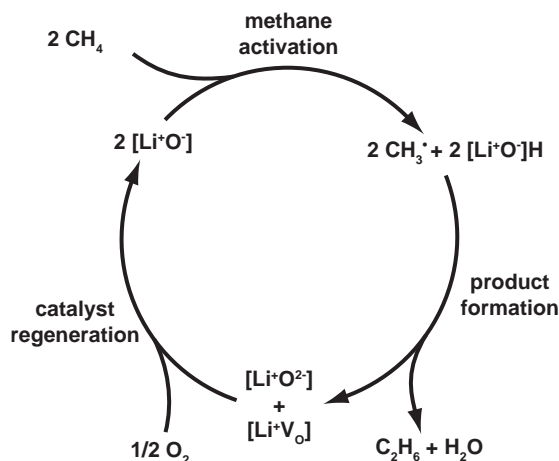


Figure 4.1.: Lunsford mechanism [193] for the oxidative coupling of methane on a lithium doped MgO surface (Figure adapted from Ref. [192]).

hexagonal tubes are formed for smaller  $(\text{MgO})_n$  clusters.

Oxygen rich MgO clusters with  $\text{Mg}_n\text{O}_{n+1}$  are investigated, as these may contain activated (di-)oxygen species, which are presumably the active centers for the methane activation. The reaction with  $\text{CH}_4$  creates hydroxy groups on the surface and model systems for such species have also been investigated by vibrational spectroscopy. Finally, the interaction of the structurally characterized MgO clusters with different small molecules, water, methane and carbon monoxide is studied.

#### 4.1. Stoichiometric $(\text{MgO})_n^{+,0}$ clusters

Nanotubes, rods, or cages are fascinating structural motifs and their electronic, optical or chemical properties may be tuned by changing their aspect ratio [204], adsorption of other molecules [205, 206] or filling [207], and adapted to possible applications, *e.g.*, in nanodevices [208–210]. Elongated structures like nanotubes, or nanorods can be formed, apart from carbon, from many different substances like elemental compounds (including metals), oxides, nitrides, and carbides [211] and also magnesium oxide. Bundles of MgO nanotubes with lengths up to several ten  $\mu\text{m}$  can be made by simple thermal evaporation methods [212–214]. Though the macroscopic shape of these tubes may not easily fit into the picture of a cubic

crystal, on an atomic scale the cubic motif of the bulk MgO in its rocksalt structure is still retained. For nanoscaled clusters, however, we observe a different behavior.

The first experiments on MgO clusters by multiple photon laser ionization mass spectrometry [215] already suggested that, in addition to the cubic motif, tubular structures formed by stacking hexagonal  $(\text{MgO})_3$  units – hexagonal nanotubes – may be present. A number of theoretical studies have followed these experimental investigations, most applying simple ion (pair) potentials [216–220] sometimes in combination with global structure optimization schemes [221–224]. Such simulations applying parameterized potential functions predict two different structural types depending on the ionic charges: a cubic motif for full formal charges and hexagonal tubes and cages [221] for smaller charges. Hexagonal tubes have been identified by a genetic algorithm as the putative global minima for clusters with  $(\text{MgO})_{3k}$ ,  $k=1-5$  [223]. For other cluster compositions more cube-like structures are often predicted but, as yet, there is no common agreement on their structures in the literature. Quantum chemical methods [225–230] in combination with global optimization approaches have, to our knowledge, not yet been systematically applied to neutral MgO clusters of different sizes. Only for the alkaline halide clusters  $(\text{LiF})_n$ , which are assumed to behave similarly to MgO clusters [218], simulated annealing at an *ab initio* level has been performed for  $n=1-8$  [231]. Experimental data to benchmark the theoretical predictions is highly desirable especially for larger systems, but spectroscopic information is, to date, rather limited.

The combination of IR excitation with mass spectrometric detection has been proven to be very successful [53] for determining the structure of strongly bound gas-phase clusters. Obtaining IR spectra of neutral metal oxide clusters remains, however, challenging. Matrix isolation spectroscopy has been used to study very small  $(\text{MgO})$  species, in particular  $\text{OMgO}$  and  $(\text{MgO})_2$  [232]. For larger clusters in the gas phase, starting with  $(\text{MgO})_{15}$ , IR resonance enhanced multiple photon ionization (IR-REMPI) spectra [73] have been reported and very similar IR spectra for all sizes have been found. Because of the vicinity of the observed bands to the surface phonon modes the cubic motif was suggested as being present even at smaller sizes. Quantum calculations were missing at that time, making a definite structural assignment impossible. In such gas-phase experiments the neutral clusters can be investigated without any perturbation from the environment. However, the absorption of several hundred IR photons needed to induce IR-REMPI requires a high IR fluence and the high internal energies necessary for the thermionic electron emission usually lead to broadening and shifting of spectral lines, making the spectra less informative.

For this reason more evolved techniques have been developed, which have, so far, mainly been used to study ionic metal oxide clusters. IR multiple photon dis-

sociation of the cluster itself or the dissociation of more weakly bound messenger complexes has been used to measure vibrational spectra of several metal oxide cluster ions, including vanadium, aluminum, iron or niobium oxides [75, 84, 233–236]. For MgO such studies do not exist yet.

Compared to the experiments on ionic clusters, the mass spectrometric investigation of neutral species requires an additional ionization step. For this, UV single photon ionization is usually used to avoid excessive fragmentation of the clusters. However, direct investigation of neutral metal oxides with such a technique is hampered by the large ionization energies ( $\text{IE} > 8 \text{ eV}$ ) typical for oxygen rich metal oxide clusters, as no ‘simple’ high fluence laser sources are available with a photon energy above 8 eV.

In the following it will be shown that the tunable IR-UV two-color ionization scheme used before to study neutral silicon clusters can also be applied to  $(\text{MgO})_n$  clusters containing between 3 and 16 MgO units. This study closes the gap between the matrix isolation studies for very small MgO clusters and the IR-REMPI investigations on large MgO clusters. The structures of MgO clusters are assigned by comparison with calculated IR spectra for low energy isomers located using an *ab initio* global optimization employing a genetic algorithm. Our approach delivers detailed insights into the structural evolution of small neutral MgO clusters and reveals dramatic structural differences between MgO in the bulk phase and at the nanoscale. In addition, the cationic clusters are studied for  $n=2-10$  by IR-MPD spectroscopy of weakly bound messenger species as this allows investigation of the influence of charge on the cluster structures, and to test the often applied vertical ionization approximation, which assumes a similar structure between cation and neutral cluster.

#### 4.1.1. Cationic clusters\*

##### 4.1.1.1. $(\text{MgO})_n^+$ clusters – IR-MPD spectroscopy of messenger complexes (Ar vs. $\text{O}_2$ )

MgO clusters are particularly stable, and are therefore one of the few systems (besides metal carbide and fullerene clusters), for which IR spectra of the neutral species [73] could be measured by IR-REMPI. Direct multiple photon dissociation of cationic clusters in the IR, which was used successfully in many experiments on vanadium [235, 237] or aluminum oxide clusters [235] is unfeasible for MgO due to the high stability. Instead, the messenger technique is used. However, due to a

\* Major parts of this section have been published: *Structural diversity and flexibility of MgO gas phase clusters*, K. Kwapien, M. Sierka, J. Döbler, J. Sauer, M. Haertelt, A. Fielicke, G. Meijer, *Angew. Chem. Int. Ed.* **2011**, *50*, 1716

mass coincidence between argon (the major isotope with an abundance of 99.6 % has a mass of 40 amu) and a  $^{24}\text{Mg}^{16}\text{O}$  unit, it is not possible to perform such an experiment with magnesium of natural isotopic distribution ( $^{24}\text{Mg}$ : 79%;  $^{25}\text{Mg}$ : 10%;  $^{26}\text{Mg}$ : 11%). Also most other rare gas atoms cause mass coincidences, and more importantly, the formation of complexes under our experimental conditions is expected to be very difficult, *i.e.* for neon. For species that bind stronger deformations of the clusters are more likely.

A mass spectrum obtained using a normal Mg target and 0.5 % oxygen in the helium carrier gas taken in the Berlin setup is shown in Figure 4.2(a). Clusters with different stoichiometries are formed, however, the major peaks can either be assigned to clusters with a one-to-one stoichiometry or to clusters with a single additional oxygen atom. Clusters with an additional magnesium atom can also be observed, but have a much lower intensity.

To circumvent the mass coincidence between the bare clusters and the messenger complexes different special isotopes could, in principle, be used, *i.e.*  $^{18}\text{O}$ ,  $^{36}\text{Ar}$ ,  $^{25}\text{Mg}$ , or  $^{26}\text{Mg}$ . However, the latter has been selected, as various aspects argue against the others.  $^{18}\text{O}$  has, for instance, the same mass as water, which is always present as a contaminant in the carrier gas, but also evaporates from the surfaces in the source chamber. Although in small amounts, hydrogen containing species have been observed and, as can be seen later, spectroscopy on such species was also possible. Another possibility is to use  $^{36}\text{Ar}$ , but this is very expensive (3 €/ml), and more importantly, the cluster signal still smears out due to the isotopic pattern of the Mg itself. Furthermore, mass coincidences between different stoichiometries can occur for larger clusters. The  $^{26}\text{Mg}$  isotope has finally been chosen, as it will also allow in the future experiments on (lithium) doped species. The even mass of this isotope would make it very easy to identify a lithium doped species due its odd mass (92.6 % of the natural abundant lithium has an atomic mass of 7).

As only the outer surface of the target rod is ablated by the laser only a 0.1 mm thick foil of  $^{26}\text{Mg}$  (99.4 %, Oak Ridge National Laboratory, 20×20 mm, 1500 €/target) has been used in the experiment. This is wrapped and glued around a stainless steel carrier rod. To avoid the signal being lost when the laser hits the seam, a sensor was installed that detects it. This has been used to interrupt the Q-switch trigger for the ablation laser and the signal recording when the unusable part of the rod was reached. At the same time the turning speed for the rod was increased, to reduce the down time.

The  $^{26}\text{MgO}$  cluster cation complexes are generated by using a pulse energy of  $\approx 1.5$  mJ (at 532 nm) for the ablation laser and a gas mixture of 1 % oxygen and 5 % argon in helium. A distribution of bare cationic clusters as well as their complexes



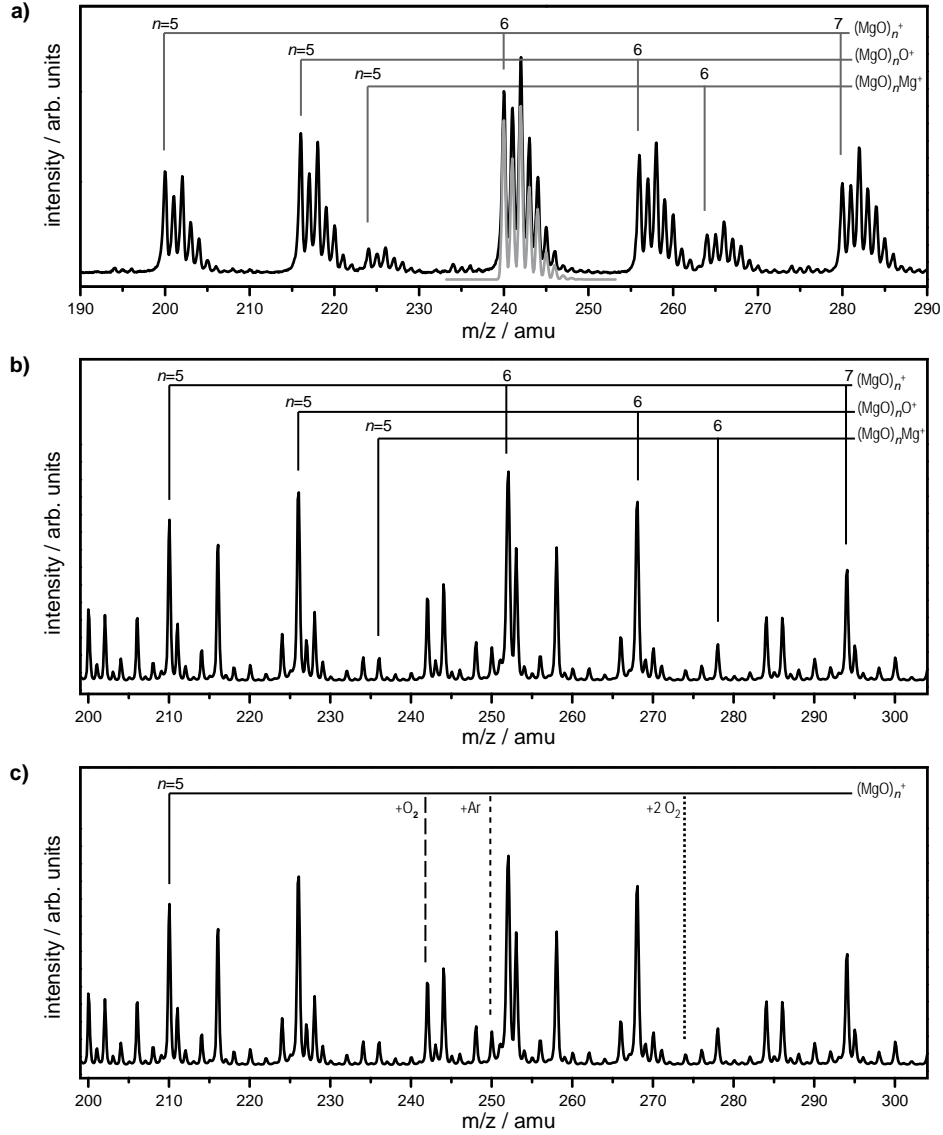


Figure 4.2.: a) Mass spectrum of MgO clusters made by laser ablation of Mg with natural isotopic abundance. In grey the simulated isotopic pattern of  $(\text{MgO})_6^+$ . b) Mass spectrum of MgO clusters made by laser ablation of  $^{26}\text{Mg}$  in an atmosphere containing helium, oxygen, and argon. c) Mass spectrum highlighting the messenger species for  $(\text{MgO})_5$ .

with Ar and O<sub>2</sub> was produced in the source at ambient temperature (30 °C), expanded into vacuum to form a molecular beam and was then analyzed in a reflectron time-of-flight mass spectrometer. A corresponding mass spectrum can be seen in Figure 4.2(b) and (c). Although an isotopically pure target was used, the mass spectrum looks quite complex, but the different species can be unambiguously assigned. The bare clusters are marked in Figure 4.2(b). Clusters are formed with similar compositions and relative intensities as those obtained with the normal Mg rod. The other species formed can be identified as complexes of these clusters with Ar and O<sub>2</sub>. Some of the species have been assigned in Figure 4.2(c). Mainly species containing additional O<sub>2</sub> are observed, and particularly for the smaller sizes, up to 3–4 oxygen molecules can stick to the clusters. The intensities of the Ar complexes is usually much lower than for the O<sub>2</sub> complexes. Species containing both Ar and O<sub>2</sub> are also observed. The presence of different bare cluster sizes and compositions, in combination with the large number of possible complexes is the reason for the complexity of the mass spectra. At lower source temperatures, where complex formation is even more favorable, this becomes even worse and an assignment becomes very challenging.

Relatively low FELIX pulse energies of 4–20 mJ ( $\leq 7$  mJ below 1000 cm<sup>-1</sup>) have been used to record the IR-MPD spectra for the cationic MgO clusters. The absorption spectra have been corrected by the photon fluence.

**Messenger tagging – Ar vs. O<sub>2</sub>.** Several different kinds of messenger atoms (He, Ne, Ar, Kr, Xe) or molecules (H<sub>2</sub>, N<sub>2</sub>) are common. However, a good messenger should interact only weakly with the molecule or cluster studied and should, in principle, be only physisorbed. This could be a problem for cations complexed with heavier rare-gas atoms, but may be even worse for messenger molecules as charge transfer could also occur, leading to a (partly) covalent bonding. Therefore, data obtained using such messengers has to be interpreted with care, taking the possible influence of the messenger into account. For a few cases, e. g. V<sub>4</sub>O<sub>8</sub><sup>+</sup> [75], Nb<sub>2</sub>O<sub>6</sub><sup>+</sup> [233], Ta<sub>4</sub>O<sub>11</sub><sup>+</sup> [239] V<sub>2</sub>O<sub>5</sub><sup>-</sup> [237], and Fe<sub>n</sub>O<sub>m</sub><sup>+</sup> clusters [236], the desorption of O<sub>2</sub> has been used as a messenger. In these examples, however, different chemically bound molecular dioxygen species are distinguished, differing in the amount of charge transferred into the antibonding orbitals of the oxygen molecule (see Figure 4.3). In principle, each of these dioxygen species can be unambiguously identified by the frequency of the O-O stretch. The physisorbed oxygen molecule absorbs around 1550 cm<sup>-1</sup>, while the chemisorbed superoxo species has a characteristic vibration around 1150 cm<sup>-1</sup>. The peroxo species is more difficult to assign, as its band is around 800–900 cm<sup>-1</sup>, where the stretches of metal–oxygen units are also found. The vibration of the free O<sub>2</sub> molecule is not IR active, however, if

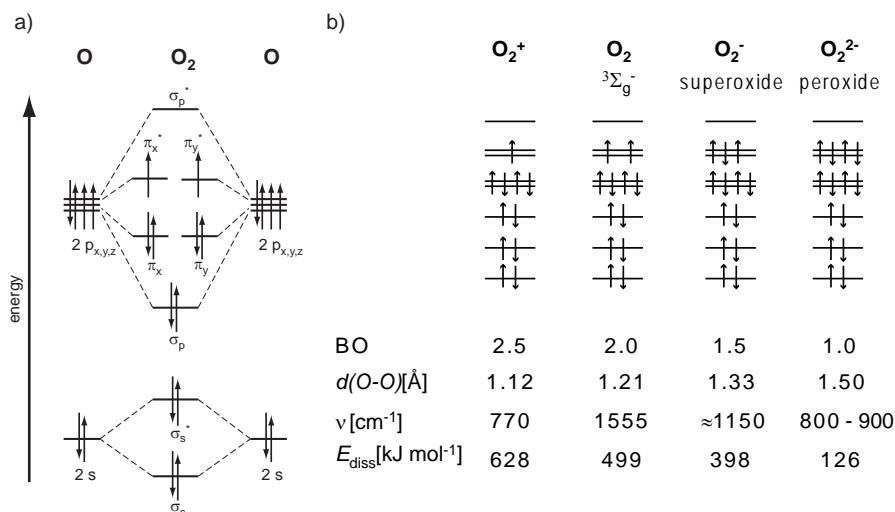


Figure 4.3.: (a) Molecular term scheme of  $\text{O}_2$ . (b) Term schemes of the different dioxygen species, along with their most characteristic properties [bond order (BO), O-O distance ( $d$ ), vibrational frequency ( $\nu$ ), dissociation energy  $E_{\text{diss}}$ ] taken from Ref. [238].

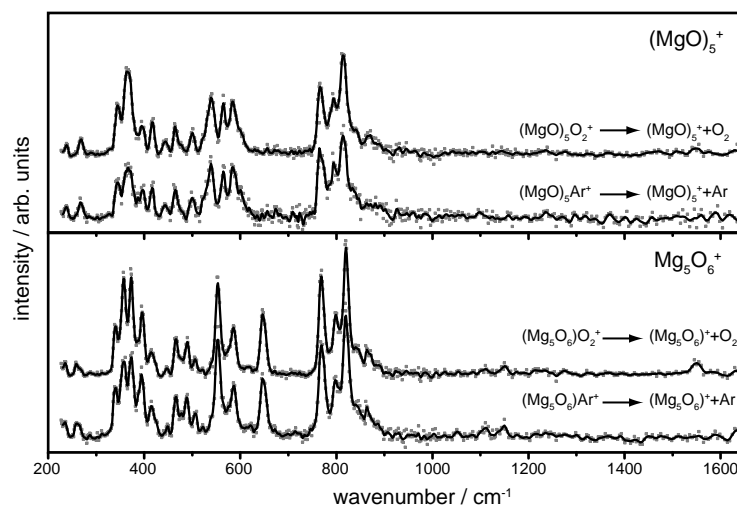


Figure 4.4.: IR-MPD spectra for  $(\text{MgO})_5^+$  and  $\text{Mg}_5\text{O}_6^+$  obtained by tagging with different messengers, Ar and  $\text{O}_2$ .

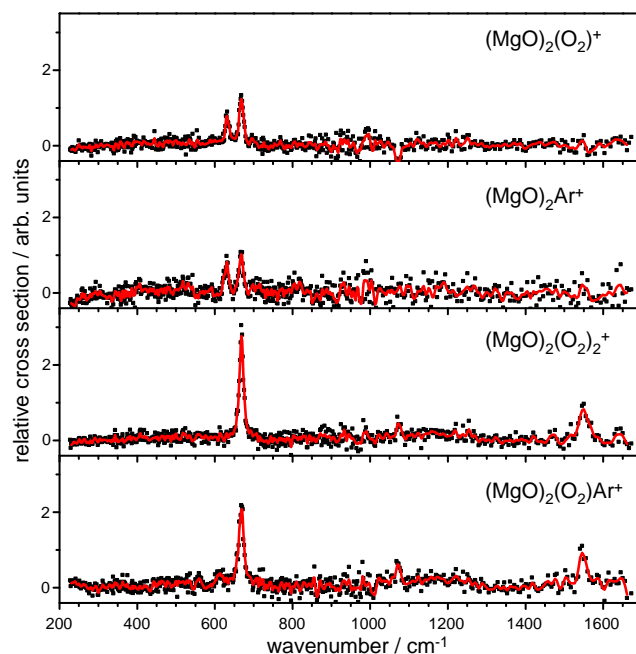


Figure 4.5.: Comparison between the IR-MPD spectra for  $(\text{MgO})_n^+$  clusters obtained with different messenger species.

physisorbed to a cluster it can become weakly IR active. The O-O stretches in  $\text{O}_2^-$  and  $\text{O}_2^{2-}$  can also have only very low IR intensities in some situations, as will be shown later. The superoxo and peroxy species will later play a major role as structural elements in clusters of the composition  $\text{Mg}_n\text{O}_{n+1}$ , discussed in Section 4.2.

For cationic MgO clusters it was possible to compare two different messengers, Ar and  $\text{O}_2$ , for a large number of species. For a given cluster, both messenger spectra hardly deviate. Figure 4.4 shows the comparison of IR-MPD spectra obtained on the Ar and  $\text{O}_2$  complexes for  $(\text{MgO})_5^+$  and  $\text{Mg}_5\text{O}_6^+$  from 200–1650  $\text{cm}^{-1}$ . This range covers a major part of the vibrational fundamentals of the bare clusters, including those for the different dioxygen species and the bending mode of water, at 1650  $\text{cm}^{-1}$ , which also allows such species to be identified.

The similarity between the spectra of Ar and  $\text{O}_2$  complexes shows that the dioxygen molecules are only weakly physisorbed. A similar binding, via charge induced dipole interaction, between the cationic cluster and both messenger species can be rationalized by the rather similar polarizabilities of the Ar atom and the  $\text{O}_2$  molecule. The band observed at 1550  $\text{cm}^{-1}$  for the  $\text{Mg}_5\text{O}_6^+$  cluster can be assigned to the stretching vibration of practically unperturbed  $\text{O}_2$  which becomes weakly IR active for  $\text{O}_2$  bound to the cluster.

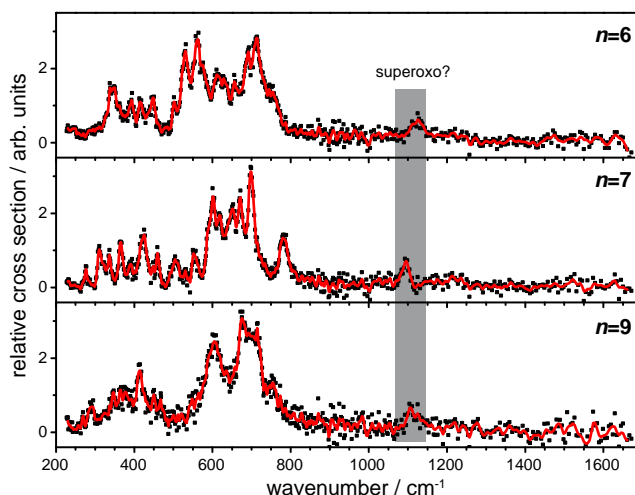


Figure 4.6.: IR-MPD spectra for  $(\text{MgO})_n^+$  clusters obtained by  $\text{O}_2$  tagging. At  $1100 \text{ cm}^{-1}$  an absorption is observed for the clusters sizes shown above, which is an indication for the presence of an  $\text{O}_2^-$  unit in the cluster.

For all cases where a comparison is possible the spectra of Ar and  $\text{O}_2$  complexes are very similar. In addition, no change in the spectra for different messenger coverages are found except for  $(\text{MgO})_2^+$ . Here, the spectra of complexes containing a single or two messengers differ by the presence of an additional band at  $631 \text{ cm}^{-1}$ , irrespective of the kind of messenger, see Fig. 4.5. This can be understood as a change in symmetry; a single messenger reduces the cluster's symmetry from  $D_{2h}$  to  $C_{2v}$  (see discussion below), while complexes with two physisorbed dioxygen molecules or Ar and  $\text{O}_2$  have the higher  $D_{2h}$  symmetry. This is the only example where a significant influence of the messenger on the spectrum has been found. In all following cases the calculations have been performed only for the bare cluster.

For a few sizes,  $(\text{MgO})_6^+$ ,  $(\text{MgO})_7^+$ , and  $(\text{MgO})_9^+$ , a weak absorption around  $1100 \text{ cm}^{-1}$  was also observed, see Figure 4.6. This might be an indication for the presence of a superoxo species that does not originate from the  $\text{O}_2$  messenger itself, as for  $(\text{MgO})_6^+$  for instance, this absorption was also observed in the Ar spectrum (for the larger two species the Ar complex intensity was too low). This means that, at least for a fraction of the clusters produced, a complex with an intact  $\text{O}_2$  unit, *i.e.*  $\text{Mg}_6\text{O}_4(\text{O}_2)^+$ , may have been present.

In the following, only the spectra obtained with the  $\text{O}_2$  messenger are shown as these have a better signal to noise ratio, because of their higher intensity in the beam.

#### 4.1.1.2. Theoretical method\*

DFT calculations have been performed using the TURBOMOLE program package [240]. The global optimizations of cluster structures employed the B3-LYP hybrid exchange-correlation functional [241, 242], triple zeta valence plus polarization (def2-TZVP) basis sets [173, 243] and a hybrid *ab initio* genetic algorithm (HAGA) [244]. To speed up the DFT calculations the multipole accelerated resolution of identity (MARI-J) method [245] along with the def2-TZVP auxiliary basis sets [246] was used. All minima were verified by vibrational analysis. The differences in the zero-point vibrational energies (ZPVE) are negligible and have therefore not been considered. MP2 and CCSD(T) calculations were performed for  $(\text{MgO})_n^+$ ,  $n = 3-4$  and 6, with the same def2-TZVP basis set as the B3-LYP calculations. Initially, MP2 optimizations with TURBOMOLE were performed, followed by CCSD(T) calculations with MOLPRO [247]. Single point calculations at the MP2 structures were carried out for  $n=6$ . CCSD(T) structure optimizations and subsequent numerical frequency calculations were performed for  $n=3-4$ . All frequencies are unscaled.

#### 4.1.1.3. Results and discussion

The measured IR-MPD spectra obtained on the  $\text{O}_2$  messenger complex for  $(\text{MgO})_n^+$  clusters with  $n=2-10$  in the  $200-1000\text{ cm}^{-1}$  range are shown in Figure 4.7 and 4.8, and are compared to the predictions from calculations. The comparison shows that cationic  $(\text{MgO})_n^+$  clusters prefer very open structures, often with low symmetry, quite different to the neutral MgO clusters shown later. The unpaired electron is delocalized over two oxygen atoms in the global minimum structures of  $(\text{MgO})_2^+$ ,  $(\text{MgO})_5^+$ , and  $(\text{MgO})_7^+$ . Removing an electron from the neutral clusters for  $n=3, 4$ , and 6 results in a Jahn-Teller (JT) distortion that leads to the appearance of two or more nearly degenerate low energy states which differ in their spin localization. The information about spin localization is of particular interest for reactivity studies of gas-phase clusters [248].

The smallest ionic cluster  $(\text{MgO})_2^+$  has a ring-structure with  $D_{2h}$  symmetry, and the calculated IR spectrum for pure  $(\text{MgO})_2^+$  is in excellent agreement with the experimental finding for  $(\text{MgO})_2(\text{O}_2)_2^+$ . For  $(\text{MgO})_3^+$  the predicted IR spectrum from DFT calculations does not agree with the measured IR-MPD spectrum. Instead, calculation at the CCSD(T) level are required for a proper description of the system. These calculation show that JT distortion leads to a  $C_{2v}$ -symmetric structure with  $^2B_1$  and  $^2A_1$  states, which are separated by less than  $2\text{ kJ mol}^{-1}$ . For the lowest

\* The calculations have been performed by K. Kwapien, Dr. M. Sierka, and Dr. J. Döbler from the Quantum Chemistry group of the Humboldt University Berlin headed by Prof. J. Sauer within the UniCat collaboration.

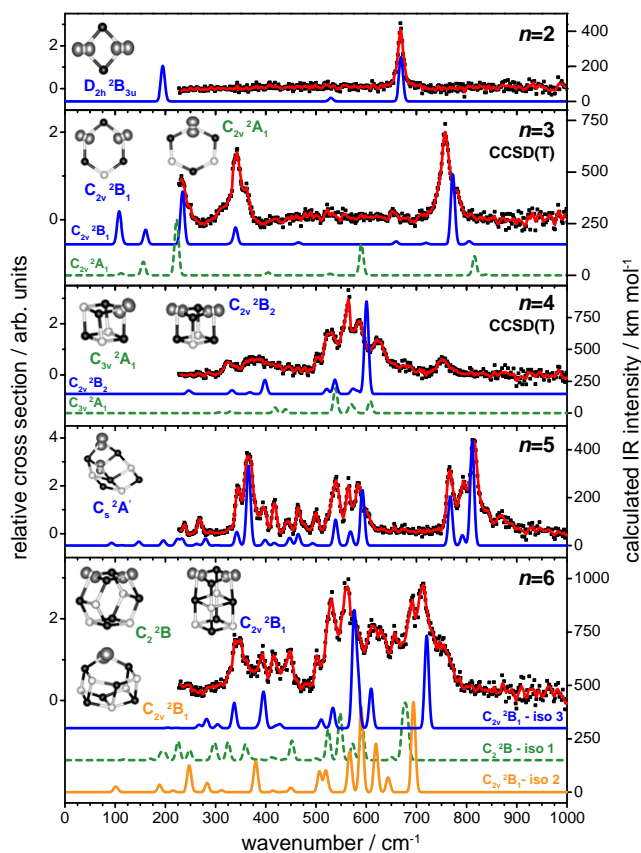


Figure 4.7.: IR-MPD spectra for  $(\text{MgO})_n^+$   $n=2-7$  clusters compared to calculated linear absorption spectra (DFT or CCSD(T)) for the lowest energy structures. The experimental data points (shown in black) are folded with a 5-point running average (solid red line). The calculated theoretical spectra have been smoothed with a Gaussian function with a FWHM of  $8 \text{ cm}^{-1}$ . Oxygen atoms are shown in white, magnesium atoms in black, and the spin density in grey.

energy  $^2\text{B}_1$  state, where the spin density is delocalized over two oxygen sites, the calculated spectrum shows a satisfactory agreement with the IR-MPD spectrum (Figure 4.7). For  $(\text{MgO})_4^+$ , JT distortion leads to  $\text{C}_{2v}$ - and  $\text{C}_{3v}$ -symmetric structures with the lowest energy electronic states  $^2\text{B}_2$  ( $\text{C}_{2v}$ ) and  $^2\text{A}_1$  ( $\text{C}_{3v}$ ) separated only by  $2.2 \text{ kJ mol}^{-1}$ . Figure 4.7 shows that the combined calculated spectra for both isomers would reproduce the experimental one, except for the weak band at about  $750 \text{ cm}^{-1}$ . A band at this frequency could be due to a peroxo species. As the  $\text{O}_2$  molecule was used as the messenger this would indicate a charge transfer from the cluster to the molecule, and a much stronger binding. In this case the  $\text{O}_2$  molecule

Table 4.1.: Relative energies [kJ mol<sup>-1</sup>] of isomers of the (MgO)<sub>6</sub><sup>+</sup> cluster ion (shown in Figure 4.7) with different quantum chemical methods (def2-TZVP basis set).

Method	C <sub>2</sub> <sup>2</sup> B iso-1	C <sub>2v</sub> <sup>2</sup> B <sub>1</sub> iso-2	C <sub>2v</sub> <sup>2</sup> B <sub>1</sub> iso-3
B3-LYP	0.0	25.1	11.8
MP2	9.2	0.0	8.2
CCSD(T)	1.8	3.3	0.0

would no longer be an innocent messenger. However, spectra measured with Ar as the messenger yield an identical spectrum.

Another possible source for this band could be the presence of isomers (such as Mg<sub>4</sub>O<sub>2</sub>(O<sub>2</sub>)<sup>+</sup>) or of a different species with the same mass/charge ratio. For the neutral (MgO)<sub>4</sub> cluster a band at slightly higher wavenumber has been observed and possible isomers have been constructed in order to explain this feature. As will be shown later, species with a stable O<sub>2</sub> unit have been found, however, they are predicted to be very high in energy for the neutral species.

For (MgO)<sub>5</sub><sup>+</sup> excellent agreement between experimental and theoretical spectra is found. Although no scaling was applied to the calculated spectrum, there is a perfect match between measured and predicted band positions. In the 600–740 cm<sup>-1</sup> range, where no absorptions were measured, the theoretical spectrum also has no IR active features. The structure that was found by the global optimization method has not been considered before and is an open sheetlike structure with C<sub>s</sub> symmetry and, as will be shown later, with no resemblance to its neutral counterpart.

The structural assignment of the (MgO)<sub>6</sub><sup>+</sup> cluster ion is more challenging. The global optimization yields three low lying structures with similar energies (see Table 4.1). In fact, different quantum chemical methods predict different energy orderings of the three structures. Figure 4.7 shows that the calculated spectra for all three isomers reproduce some features of the experimental spectrum. A single isomer is not sufficient to explain the experimental observation. This may indicate that the IR-MPD spectrum for the (MgO)<sub>6</sub><sup>+</sup> cluster ion reflects the presence of a mixture of all three isomers. As the experiment was performed with the cluster source at ambient temperature (ca. 30 °C), the population of high-lying isomers as well as an isomerization on the time scale of the experiment cannot be ruled out. Due to the small structural changes required to go from one structure to the other this is even very likely. None of the structures would explain the mode observed at 1100 cm<sup>-1</sup>, and it may also well be that another isomer with a superoxo unit causes this additional feature and possibly contributes to some of the other observed absorptions.

The calculated and experimental spectra for the next larger cluster ion, (MgO)<sub>7</sub><sup>+</sup>,



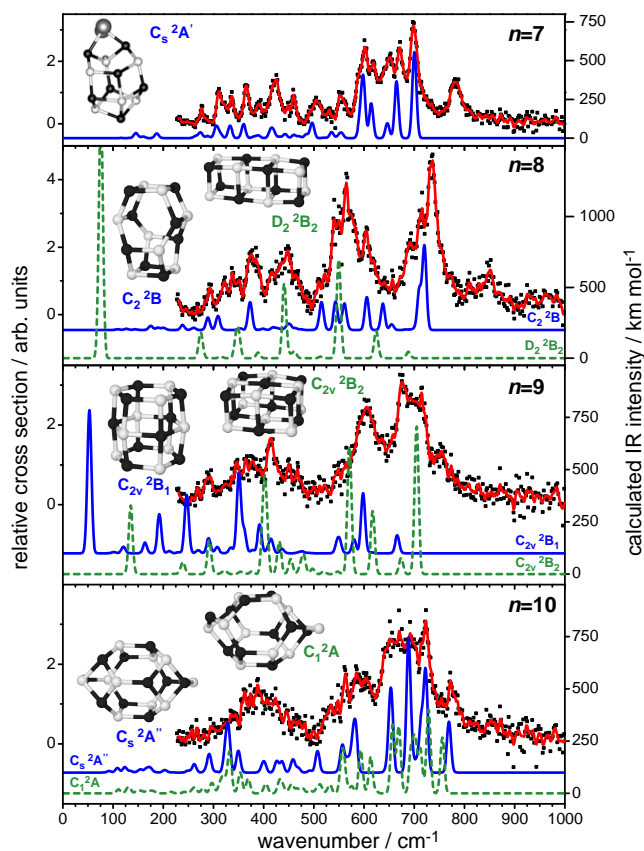


Figure 4.8.: IR-MPD spectra for  $(\text{MgO})_n^+$   $n=7-10$  clusters and comparison with results from DFT calculations.

again shows good agreement (see Figure 4.8). Except for a band at  $780\text{ cm}^{-1}$ , all the features are reproduced in the calculated spectrum, which is a good indication that the structure of the cluster present in the beam has been found.

For the next two larger sizes only preliminary calculations have been performed. For both sizes the two lowest energy structures identified are shown. The structure for  $(\text{MgO})_8^+$  is based on the two-layer hexagonal tube structure of iso-1 of  $(\text{MgO})_6^+$ , while for the  $(\text{MgO})_9^+$  cluster a hexagonal tube consisting of 3 layers of the hexagonal ring structure of  $(\text{MgO})_3^+$  has been identified as the global minimum, similar to many predictions for the neutral counterpart. Surprisingly, cube-based structures are found to be only slightly higher in energy, at  $16.8$  and  $11.9\text{ kJ mol}^{-1}$ , for  $(\text{MgO})_8^+$  and  $(\text{MgO})_9^+$ , respectively. In both cases, most of the experimental spectra are explained by the putative global minimum structures, but a few features are missing in the predicted spectrum, which may indicate the presence of these higher lying isomers.

For  $(\text{MgO})_{10}^+$  the agreement between experiment and theory is again very convincing. The calculations predicts a cage structure with  $C_s$  symmetry in a  $^2A''$  state as the global minimum.

#### 4.1.2. Neutral clusters\*

##### 4.1.2.1. $(\text{MgO})_n$ clusters – IR-UV2CI spectroscopy

The neutral clusters are made, similar to the cationic ones, by laser ablation from the  $^{26}\text{Mg}$  target. 1 % oxygen has been added to the helium carrier gas. The clusters are cooled to  $\sim 100$  K in the thermalization channel attached to the source. The charged species are deflected out of the beam by a voltage applied to the aperture. The remaining neutral cluster distribution is analyzed with the reflectron time-of-flight mass spectrometer by using a unfocussed  $\text{F}_2$  excimer laser (7.87 eV photon energy) for ionization. Small peaks are observed at the positions for the 1:1 stoichiometric magnesium oxide clusters, *e.g.*  $\text{Mg}_n\text{O}_m$  with  $n = m$ , as well as for systems deviating slightly from this stoichiometry, *e.g.*  $n = m + 2, m \pm 1$ , see also Fig. 4.9.

The intensities of the different species measured in the photoionization mass spectrum are determined by the abundance of the neutral species and their ionization efficiencies, which depend on the ionization energies (IE). Experimental values of the IEs for these systems are not available. Therefore, one has to refer here to the calculated IEs for the low lying isomers discussed later. For systems with  $n = m$  they are around 8 eV, see the inset in Fig. 4.9. From this, one might already expect that these clusters will not be very efficiently ionized at the photon energy of the  $\text{F}_2$  laser. Indeed, the small mass spectrometric signals observed qualitatively confirm the calculations of the IEs.

The predicted IEs lie in a narrow range around the photon energy of the  $\text{F}_2$  laser, making the neutral MgO clusters a perfect system to be studied by tunable IR-UV two-color ionization spectroscopy, as applied to neutral silicon clusters. Messenger tagging cannot be used for neutral MgO clusters as there is no convenient UV source for their single photon ionization. Again, the cluster-size specific IR spectra are obtained by recording on alternating shots mass spectra with (intensity  $I$ ) and without FELIX irradiation ( $I_0$ ) and by scanning the IR wavelength. An example for the observed rise in intensity upon resonant absorption of IR light is shown in Figure 4.9. For  $(\text{MgO})_9$ , for example, an intensity increase of a factor of three is observed at  $380\text{ cm}^{-1}$ . Figure 4.9 shows also the competing process to ionization;

\* This section has been published: *Structure determination of neutral MgO clusters – hexagonal nanotubes and cages*, M. Haertelt, A. Fielicke, G. Meijer, K. Kwapien, M. Sierka, and J. Sauer, *Phys. Chem. Chem. Phys.* **2012**, *14*, 2849

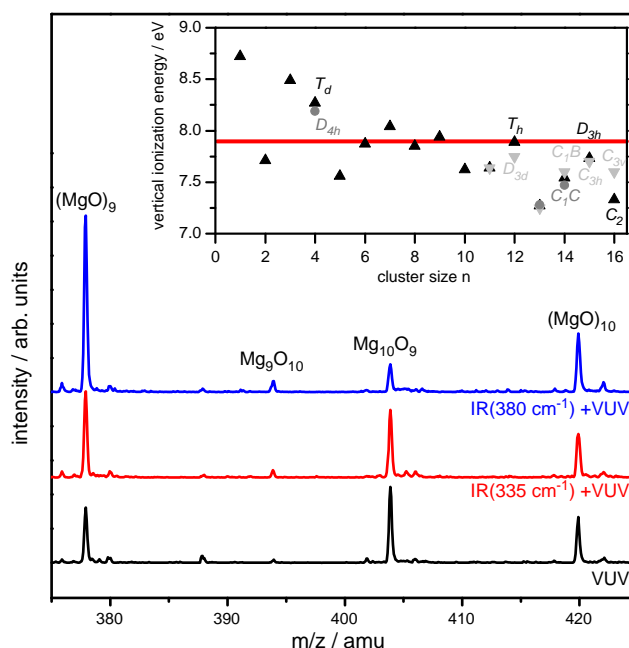


Figure 4.9.: Time-of-flight mass spectra obtained under different ionization conditions. Upon irradiation with just 7.87 eV photons, only weak signals are observed, which significantly increase for strongly bound systems when IR radiation, resonant with a vibrational transition, is added. The inset shows the calculated vertical IEs of the low energy structures obtained from the global optimization. The red line indicates the photon energy of the  $\text{F}_2$  excimer laser (7.87 eV).

more weakly bound species like  $\text{Mg}_{10}\text{O}_9$  tend to be fragmented by the IR radiation, and the neutral fragments formed cannot be detected with the mass spectrometer. The IR absorption spectrum of such species can be recorded by monitoring the depletion of the mass spectrometric signal. Almost all Mg-rich  $\text{Mg}_n\text{O}_m$  species with  $n > m$  show this behavior, while stoichiometric and oxygen rich systems with  $n = m$  and  $m > n$  can be studied with the ionization technique. A FELIX macropulse energy of  $\sim 16$  mJ was used in the whole range, with an IR beam diameter of approximately 1 mm at the aperture. Relative absorption spectra are derived by the procedure described in Section 2.4.2.1.

#### 4.1.2.2. Results and discussion

Vibrational spectra of  $(\text{MgO})_n$  clusters have been measured in the region from 200–1700  $\text{cm}^{-1}$ , to be able to identify any molecular dioxygen species which might be present and how they are bound to the cluster. For all of the  $(\text{MgO})_n$  clusters con-

sidered here, no features above  $1000\text{ cm}^{-1}$  are seen, which makes the presence of physisorbed dioxygen as well as of superoxo species unlikely. This is quite different from the cationic MgO clusters investigated before. There, some of the measured bands have been assigned to isomers containing dioxygen species. Complexes containing intact water molecules can also be ruled out. As no additional structural information is contained in the range above  $1000\text{ cm}^{-1}$ , the experimental spectra are shown only for the range  $200\text{--}1000\text{ cm}^{-1}$ . Comparison is again made to predictions from DFT calculations\* using the B3-LYP functional, the def2-TZVP basis set and the genetic algorithm, as for the cationic clusters. The experimental spectra for the  $(\text{MgO})_n$  clusters with  $n = 3\text{--}16$  together with a comparison to the results of the calculations are shown in Figs. 4.10-4.12. For most sizes very distinct IR spectra have been recorded. In several cases, rather small numbers of bands are found, which can be an indication of rather symmetric structures. For all sizes above  $n > 5$  a very intense band is observed around  $700\text{ cm}^{-1}$ , which seems to be saturated and power broadened. For lower frequencies, saturation effects do not seem to play a major role for the quality of the spectra. The observed bands can be narrower than  $< 10\text{ cm}^{-1}$  (FWHM).

**The hexagonal tubes -  $(\text{MgO})_{3k}$  clusters.** The vibrational spectra for clusters of the  $(\text{MgO})_{3k}$  composition ( $k=1\text{--}5$ ) are shown in Fig. 4.10. Already at the first glance the similarities between the spectra of the different sizes become apparent. This may indicate a similar structural motif for the clusters based on the  $(\text{MgO})_3$  unit. Indeed, previous theoretical studies, initiated by the observation of magic peaks in the mass spectra[215], predicted that the sizes with  $n=3\times k$  should favor hexagonal tube structures formed by stacking  $k$   $(\text{MgO})_3$  hexagons. The global optimization scheme employed here also identifies the hexagonal tubes as the global minima for most of these sizes. Only for  $(\text{MgO})_{3\times 4}$  is a cage-like structure found, lying  $1.8\text{ kJ/mol}$  lower in energy. The calculated linear absorption spectra for these low energy structures and the experimental spectra are compared in Fig. 4.10.

For all sizes the spectrum of the hexagonal ring or tube structure shows a very good match to the experimental spectrum. For the hexagonal ring  $(\text{MgO})_{3\times 1}$  and the small tubes with  $(\text{MgO})_{3\times 2}$  and  $(\text{MgO})_{3\times 3}$  there is little doubt about the assignment, as the calculated spectra of the putative global minima also explain the finer details of the measurements, *e.g.*, the weak band for  $(\text{MgO})_{3\times 2}$  at  $240\text{ cm}^{-1}$ . The isomer we identify for the neutral  $(\text{MgO})_{3\times 2}$  is one of the three low energy isomers found for the cation, but here it is clearly the only structure present in the beam. For the next larger size,  $(\text{MgO})_{3\times 4}$ , a cage with  $T_h$  symmetry is predicted to

\* The calculations have been performed by K. Kwapien, and Dr. M. Sierka from the Quantum Chemistry group of the Humboldt University Berlin headed by Prof. J. Sauer within the UniCat collaboration.

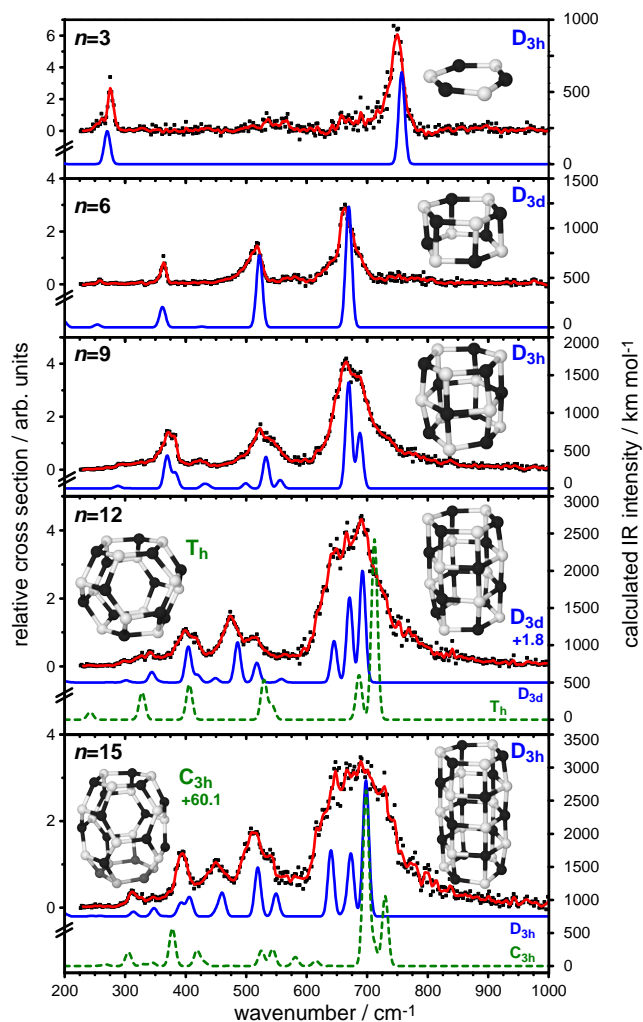


Figure 4.10.: Vibrational spectra of  $(\text{MgO})_{3k}$  clusters with  $k=1-5$  ( $3k=n$ ) and comparison to calculated linear absorption spectra. The measured data points are shown as dots and a five-point-running average (solid red line) is added to guide the eye. The calculated IR spectra are unscaled and have been convoluted using a Gaussian line shape function with a FWHM of  $10 \text{ cm}^{-1}$ . The effect of zero-point vibrational energies (ZPVE) on energetic ordering of different isomers was found to be negligible and was therefore not included. Some of the theoretical spectra are shifted vertically for clarity. Relative energies of different isomers are given in  $\text{kJ/mol}$ .

be lower in energy than the tube, but its spectrum does not fit well with the experimental spectrum, which can be fully explained by the tube structure. Inclusion of zero point vibrational energy differences does not alter the order of the two isomers. The energy difference actually increases slightly from 1.8 to 3.2 kJ/mol. The calculated IEs for the two isomers are 7.89 eV for the cage and 7.75 eV for the tube structure. As the IR spectroscopic technique used here exploits relative enhancements in the ionization efficiency of the systems, it is more sensitive to the isomers with the lower IE. Therefore, the additional presence of the cage isomer cannot be completely ruled out.

For the  $(\text{MgO})_{3 \times 5}$  cluster the hexagonal tube is again the lowest energy structure and its spectrum nicely fits the experimental data. The next higher isomer, energetically separated by 60.1 kJ/mol, is a cage of  $C_{3h}$  symmetry. It has similarities with the cage structure calculated as global minimum of  $(\text{MgO})_{3 \times 4}$  and can be formed by adding an additional hexagonal ring to the  $(\text{MgO})_{3 \times 4}$  cage.

Although the IR spectra for all the tubular structures appear to have many common features, the characteristic vibrations of the tubular structure like concerted movements of the layers, breathing modes or even kinks of the whole tube, are either not IR active, or show only very low IR intensities. The modes of high IR intensities observed in the experiment are strongly delocalized.

**Small non-tubular MgO clusters.** Besides the  $(\text{MgO})_{3k}$  clusters, which adopt perfect hexagonal tube structures the intermediate sizes ( $n \neq 3k$ ) also turn out to have interesting structures, mostly very different to the bulk. The experimental spectra and the comparison to the theoretical predictions for these non-tubular clusters containing up to ten MgO units are shown in Fig. 4.11. Except for the smallest size ( $n=4$ ), the experimental findings can be explained by the calculated IR spectrum of a single isomer, the predicted global minimum.

For  $(\text{MgO})_4$  theory identifies a cube with  $T_d$  symmetry as the global minimum. Of all neutral sizes studied, it is the only one which has a bulk-like structure. The cube has four IR active modes at 328, 532, 566, and 570  $\text{cm}^{-1}$ , which are up to triply degenerate. The two most intense experimental features are reproduced by this structure, but the experimentally observed bands at  $\sim 820 \text{ cm}^{-1}$  and 280  $\text{cm}^{-1}$  can not be explained by this isomer. These bands might be explained by the 8-membered ring isomer of  $D_{4h}$  symmetry, 64.2 kJ/mol above the global minimum. The calculation predicts a vibration at 852  $\text{cm}^{-1}$ , which would partially explain the broad mode around 820  $\text{cm}^{-1}$ . However, the experimental band seems to have a finer structure, with sharper features at 817 and 834  $\text{cm}^{-1}$ , which might indicate the presence of even more isomers.

The O-O stretches of peroxo species are also found around 850  $\text{cm}^{-1}$  and, for

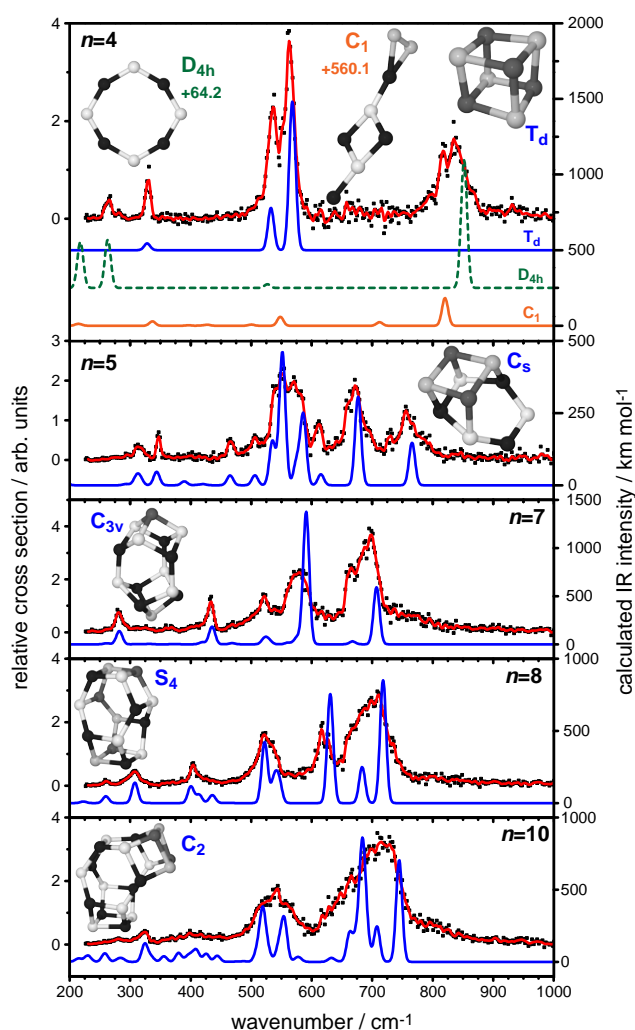


Figure 4.11.: Measured and calculated IR spectra of smaller  $(\text{MgO})_n$  clusters with  $n=4,5,7,8,10$ . Comparison with theory shows that more cage-like structures are observed, and that the hexagonal ring is a main building block in the observed structures.

the cations such species were suspected to be present in the molecular beam. For instance, the  $(\text{MgO})_4^+$  and  $(\text{MgO})_7^+$  clusters had features at such frequencies, which could not be assigned to a specific isomer. In order to assess the possibility that  $\text{O}_2^{-/2-}$  species contribute to the spectrum of  $(\text{MgO})_4$  we have investigated the binding of molecular  $\text{O}_2$  on the  $\text{Mg}_4\text{O}_2$  cluster. Surprisingly, superoxo complexes were found, instead of peroxo complexes. These superoxo complexes are high in energy, but may not easily relax to the global minimum. The spectrum of such a

structure is also shown in Fig. 4.11. The O-O bond distance is 1.36 Å, quite typical for such a species. The superoxo mode is found at 1149 cm<sup>-1</sup> with a calculated IR intensity of only 0.19 km/mol. This is much weaker than for any other feature observed in the experiment, which would explain its absence in the experiment. The other modes are also calculated to have small cross sections. The most intense feature is predicted to be at 820 cm<sup>-1</sup>, the position where the peroxo mode was expected. This position agrees very well with the first sharper peak in the feature at 820 cm<sup>-1</sup>. The weaker mode calculated at 336 cm<sup>-1</sup> may also contribute to the feature seen at 331 cm<sup>-1</sup> in the experiment. A similar superoxo complex would also help to explain the experimental IR spectrum of the (MgO)<sub>7</sub><sup>+</sup> cluster, as this showed absorptions at 780 and 1095 cm<sup>-1</sup>, see Figure 4.6.

The predicted global minimum structure of (MgO)<sub>5</sub> is completely different from that of the cationic cluster. There, an open, book-like structure was observed. For the neutral a more compact structure is found that has both the cubic and the hexagonal ring motif. It can be seen either as being formed by adding a (MgO)<sub>2</sub> unit to the (MgO)<sub>3</sub> hexagonal ring, or by adding a MgO bridge to the (MgO)<sub>4</sub> cluster.

For the larger sizes, the main structural motif is based on the (MgO)<sub>6</sub> cluster. The structure of (MgO)<sub>7</sub> is cage-like with C<sub>3v</sub> symmetry and seems, at first, to have nothing in common with most other structures. However, it can be seen as a (MgO)<sub>6</sub> unit where the hexagons have buckled after adding O and Mg atoms to the two open ends of the tube. For the larger sizes, the (MgO)<sub>6</sub> cluster motif is more evident. The (MgO)<sub>8</sub> cluster, for example, contains two of these units, fused at 90°. Another way to describe the structure is by adding a (MgO)<sub>2</sub> unit to the side of the (MgO)<sub>6</sub> cluster. The structure of (MgO)<sub>10</sub> is also built up by this principle. Its core is formed by a (MgO)<sub>8</sub> cluster that is capped with a (MgO)<sub>2</sub> unit. The symmetry changes from S<sub>4</sub> for (MgO)<sub>8</sub> to C<sub>2</sub> for (MgO)<sub>10</sub>.

The global minima identified in the range up to (MgO)<sub>8</sub> and for the tubes up to k=5 are identical to the predictions for the alkaline halide system LiF [231, 249]. For (LiF)<sub>4</sub> the barrier landscape was also calculated and it was predicted that both the cube and the eight-membered ring could be observed in experiment [231]. It appears that these two isomers are also present in the case of (MgO)<sub>4</sub>, but that here a third isomer may need to be considered.

The most extensive calculations on MgO clusters using a genetic algorithm with a Born-Mayer potential and post-optimization with DFT [223], predicted structures consistent with our findings for all the tubular structures (MgO)<sub>3k</sub> as well for the other sizes up to (MgO)<sub>7</sub>. For (MgO)<sub>8</sub> and (MgO)<sub>10</sub>, however, we identify quite different structures.



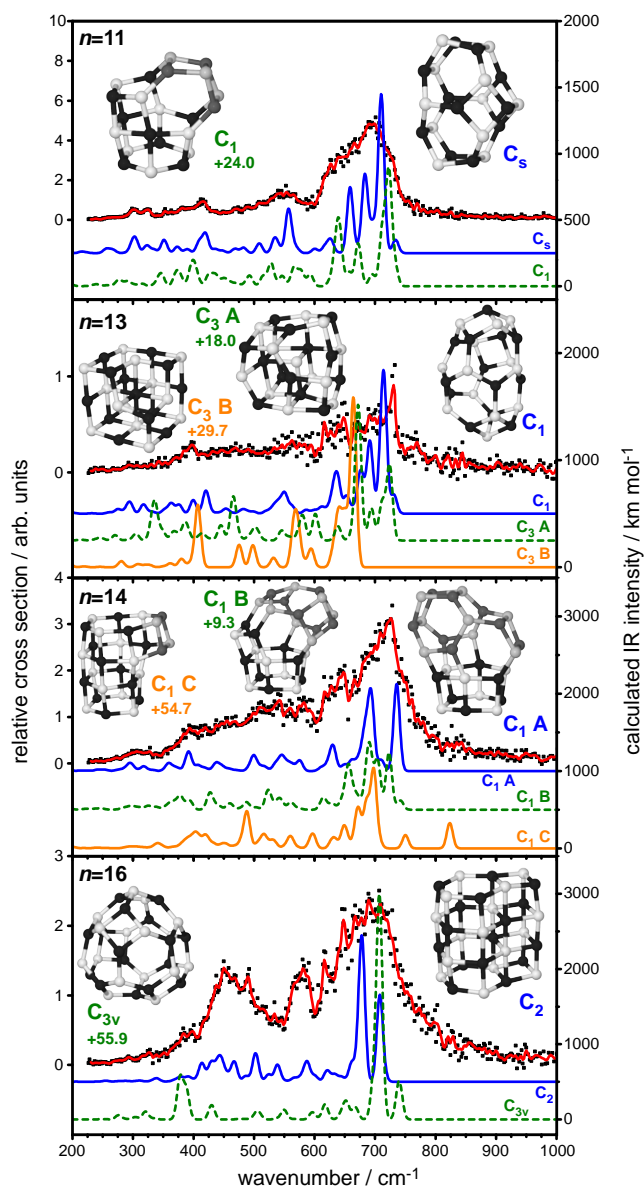


Figure 4.12.: Measured and calculated IR spectra for several isomers of  $(\text{MgO})_{11}$ ,  $(\text{MgO})_{13}$ ,  $(\text{MgO})_{14}$ , and  $(\text{MgO})_{16}$ .

**Large  $(\text{MgO})_n$  clusters ( $n > 10$ ) - between imperfect tubes and cages.** For the perfect hexagonal tubes the quality of the experimental spectra is sufficient to confirm the presence of the putative global minima found by the genetic algorithm up to rather large sizes ( $n = 15$ ). This becomes more difficult for the large non-tubular clusters. The number of bands in the vibrational spectra increases and, presumably due to a lower symmetry, leads to the observation of rather broad absorptions (cf. Fig. 4.12). The potential energy surface for such large species becomes also more complicated with more local minima, which can lie very close in energy, making it more likely that multiple isomers might be observed in the experiment. Additionally, the ionization energy decreases for larger sizes, yielding a significant ionization probability even for colder clusters. This reduces the relative amount of the IR induced enhancement of the ionization efficiency which eventually makes the application of our spectroscopic technique unfeasible with just the  $\text{F}_2$  laser. The  $(\text{MgO})_{13}$  cluster seems to be particularly affected by this problem. The calculated IE for the identified global minimum is only 7.27 eV, 0.6 eV below the photon energy of the ionization laser. This calculation is supported by the high intensity of  $(\text{MgO})_{13}$  observed in the time-of-flight mass spectrum, which is almost a factor of two larger than the neighboring  $(\text{MgO})_{12}$  signal and a factor of three larger than that of  $(\text{MgO})_{14}$ . The calculated IEs of  $(\text{MgO})_{12}$  and  $(\text{MgO})_{14}$  are also significantly higher. Nevertheless, small IR induced increases in the ion intensities are observed, allowing IR spectra to be obtained, albeit with a lower signal-to-noise ratio.

For  $(\text{MgO})_{11}$  the genetic algorithm identifies a cage-like structure of  $C_s$  symmetry that shows some similarity with the  $(\text{MgO})_8$  structure. All the main features in the experimental spectrum can be explained by this structure, in particular the features at about 300, 410, and  $540\text{ cm}^{-1}$ . The broad band at  $700\text{ cm}^{-1}$  is also reproduced by a multiplet of lines. A second isomer, which is closer to a tubular structure, is only 24 kJ/mol higher in energy. Although the agreement of its spectrum with the experiment is not bad, the band positions do not fit as well as those of the global minimum. This becomes especially apparent in the lower frequency part of the spectrum.

For  $(\text{MgO})_{13}$  a cage structure is identified as the putative global minimum. Some of the experimental features are reproduced by the calculated spectrum, but the lower signal-to-noise level precludes a definite structural assignment. The next higher energy structures can be seen as somewhat distorted fragments of the MgO bulk structure. Both are close in energy, at 18 and 29 kJ/mol above the global minimum. Their spectral features could also explain parts of the measured spectrum. Therefore, the presence of these additional isomers cannot be completely ruled out.

The experimental spectrum of  $(\text{MgO})_{14}$  could be explained by the presence of either one of the two lowest energy isomers (**A** and **B**) or a mixture of both, as shown in Fig. 4.12. The supposed minimum structure **A** already explains most of the experimental features, in particular in the 250–600  $\text{cm}^{-1}$  range. All bands have comparable IR intensities and overlap, thereby forming a very broad absorption band with little structure. Only in the 600–750  $\text{cm}^{-1}$  range are sharper features seen. The one at 640  $\text{cm}^{-1}$  could either be explained by the putative global minimum **A**, which would also account for the small drop in the experimental intensity at 600  $\text{cm}^{-1}$ , or by the second lowest structure **B**, which is only 9.3 kJ/mol higher in energy. This isomer might also explain the most intense feature at 700  $\text{cm}^{-1}$ , although the calculated IR intensity does not completely fit. Both isomers have similarities with the  $C_1$  structure of the  $(\text{MgO})_{11}$  cluster. The third lowest structure, isomer **C**, which is 54.7 kJ/mol above the ground-state, does not seem to be observed in the experiment, as the band at 820  $\text{cm}^{-1}$  is missing.

The structure of the putative global minimum for  $(\text{MgO})_{16}$  found by the genetic algorithm contains the hexagonal tube motif of  $(\text{MgO})_{12}$  as well as a cubic stack. Even for such a large size there is still decent agreement between the calculated linear absorption spectrum and the experimental spectrum, although the relative band intensities fit less well. In particular the features at 490 and 590  $\text{cm}^{-1}$  can be explained by this structure. The additional presence of the second lowest isomer, a cage-structure, 55.9 kJ/mol above the minimum, cannot be completely ruled out. The feature at 390  $\text{cm}^{-1}$  and the high-energy shoulder of the 700  $\text{cm}^{-1}$  band might originate from this isomer.

**Comparison to previous IR-REMPI experiments.** For a single size,  $(\text{MgO})_{15}$ , the IR-UV two-color ionization spectrum can be compared to data obtained previously via IR-REMPI[73]. The two experimental spectra are shown in Fig. 4.13 and appear rather different, with the IR-REMPI spectrum lacking any features below 600  $\text{cm}^{-1}$  and showing a significant shift of  $\sim 50 \text{ cm}^{-1}$  for the most intense band. The true shift is probably even larger – the calculation predicts an additional shift of up to 11  $\text{cm}^{-1}$  – as the IR-REMPI spectra were measured using Mg with the natural isotopic distribution ( $^{24}\text{Mg}$ : 79%;  $^{25}\text{Mg}$ : 10%;  $^{26}\text{Mg}$ : 11%), while we used  $^{26}\text{Mg}$ .

While the current experiments give clear evidence that the  $(\text{MgO})_{15}$  cluster has a hexagonal tube structure, the strong similarities between the IR-REMPI spectrum of  $(\text{MgO})_{15}$  as well as those of larger clusters and the phonon spectrum of bulk MgO led to the conclusion that cube-like structures were observed. The lowest energy isomer of  $(\text{MgO})_{15}$  with a cubic sub-structure identified in our calculations is found  $\sim 70 \text{ kJ/mol}$  above the tubular ground-state. At higher temperatures, required for IR-REMPI, the energetic ordering might change but this has not been

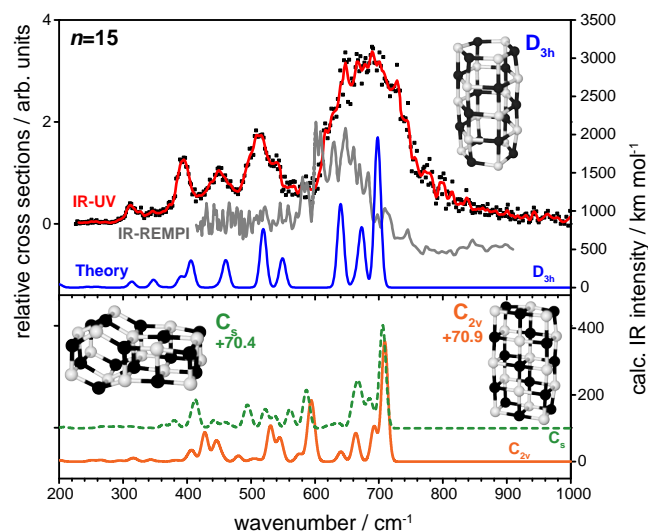


Figure 4.13.: The upper panel shows the comparison of the IR-REMPI spectrum (grey line) of  $(\text{MgO})_{15}$  of natural isotopic distribution taken from Ref. [73], with the IR-UV2CI spectrum of  $(^{26}\text{MgO})_{15}$  and with the calculated spectrum of the hexagonal tube structure of  $(\text{MgO})_{15}$ . The lower panel shows calculated spectra of species, which have a cubic sub-structure.

observed in our calculations. The predicted IR spectrum of that structure, but also other cubic sub-structures, does not fit the IR-REMPI spectrum well, see Figure 4.13. The differences in the experimental spectra may be related to the specifics of the IR-REMPI process. The IR-REMPI spectrum can be significantly affected by (cross-)anharmonicities, leading to large redshifts and changes in the relative IR intensities[90, 250]. Furthermore, the lack of spectral features at lower wavenumbers is more often observed in IR-REMPI spectra[52], as the thermionic emission of an electron requires the absorption of several hundred IR photons, and that cannot be easily fulfilled in the far-IR. In principle, the IR-REMPI spectrum can be modeled [90, 250], but this requires knowledge not only of the linear absorption spectrum but also detailed information on the anharmonicities.

For very large clusters, the appearance of the cubic motif of the MgO bulk can be expected. All previous experiments on MgO clusters showed a considerable change in the mass spectral abundance pattern for larger sizes [73, 215]. Furthermore, starting from  $(\text{MgO})_{21}$  IR bands close to frequencies of the perpendicular and parallel bulk phonon modes have been observed, whereas for the smaller  $(\text{MgO})_{15}$  cluster only a single feature was seen[73]. Theory also predicts the structural change to occur just above the sizes considered here. For the  $(\text{MgO})_{3 \times 6}$  clus-

ter the cubic motif is predicted to be energetically favored over the hexagonal tube structure[223]. Further experimental and theoretical investigations will be necessary to locate the size-range where this transition occurs.

#### 4.1.3. Comparison between neutral and cationic $(\text{MgO})_n$ clusters

A comparison between the structures assigned for small to medium-sized neutral and cationic  $(\text{MgO})_n$  clusters is shown in Figure 4.14. Surprisingly, for both charge states only the  $(\text{MgO})_4$  cluster reflects the cubic bulk structure of MgO. Instead, for all other sizes tubular or cage-like structures are observed as the global minimum. For a few cluster sizes there is evidence that cubic-like structures may be populated under the experimental conditions as minority species. The neutral clusters, which are closed-shell, usually have a high symmetry whereas the cationic clusters are more distorted. As this determination is related to Jahn-Teller-distortion it is not well described within DFT calculations and, for the smallest sizes, only CCSD(T) calculations gave a convincing agreement. For a few cluster sizes, *i.e.*  $(\text{MgO})_5$ ,  $(\text{MgO})_6$ ,  $(\text{MgO})_7$ , and  $(\text{MgO})_{10}$ , significant differences in geometry between the two charge states are observed, meaning that the often applied assumption that cationic and neutral clusters have a similar structure [225] can completely fail.

The differences between the small cluster regime and the bulk are rationalized by a change in the bonding. Previous theoretical investigations [219, 227] showed that small MgO clusters may be bound by ionocovalent bonding. This means part of the charge is not localized on the oxygen atoms, but rather leads to a direct covalent bonding. The non cube-like structures observed here, confirm these predictions.

#### 4.1.4. Conclusions

The geometric structures of  $(\text{MgO})_n$  clusters have been determined for neutral ( $n=3-16$ ) and cationic ( $n=2-10$ ) species by combining results from gas-phase vibrational spectroscopy and predictions from DFT calculations. For the cationic species IR-MPD spectroscopy using Ar and  $\text{O}_2$  as the messenger species has been performed, allowing for a direct comparison of the two messenger species. For the neutral clusters a tunable IR-UV two-color ionization technique was employed.

Neutral and cationic magnesium oxide clusters exhibit structures very different from the geometry of the simple cubic MgO bulk phase, with the only exception of  $(\text{MgO})_4$ . The combination of gas-phase IR spectroscopy and density functional theory calculations revealed unambiguously that the hexagonal ring is the fundamental building block for most neutral MgO clusters. Hexagonal tubes or rings are formed by clusters of  $(\text{MgO})_{3k}$  composition with  $k=1-5$ , while the intermediate

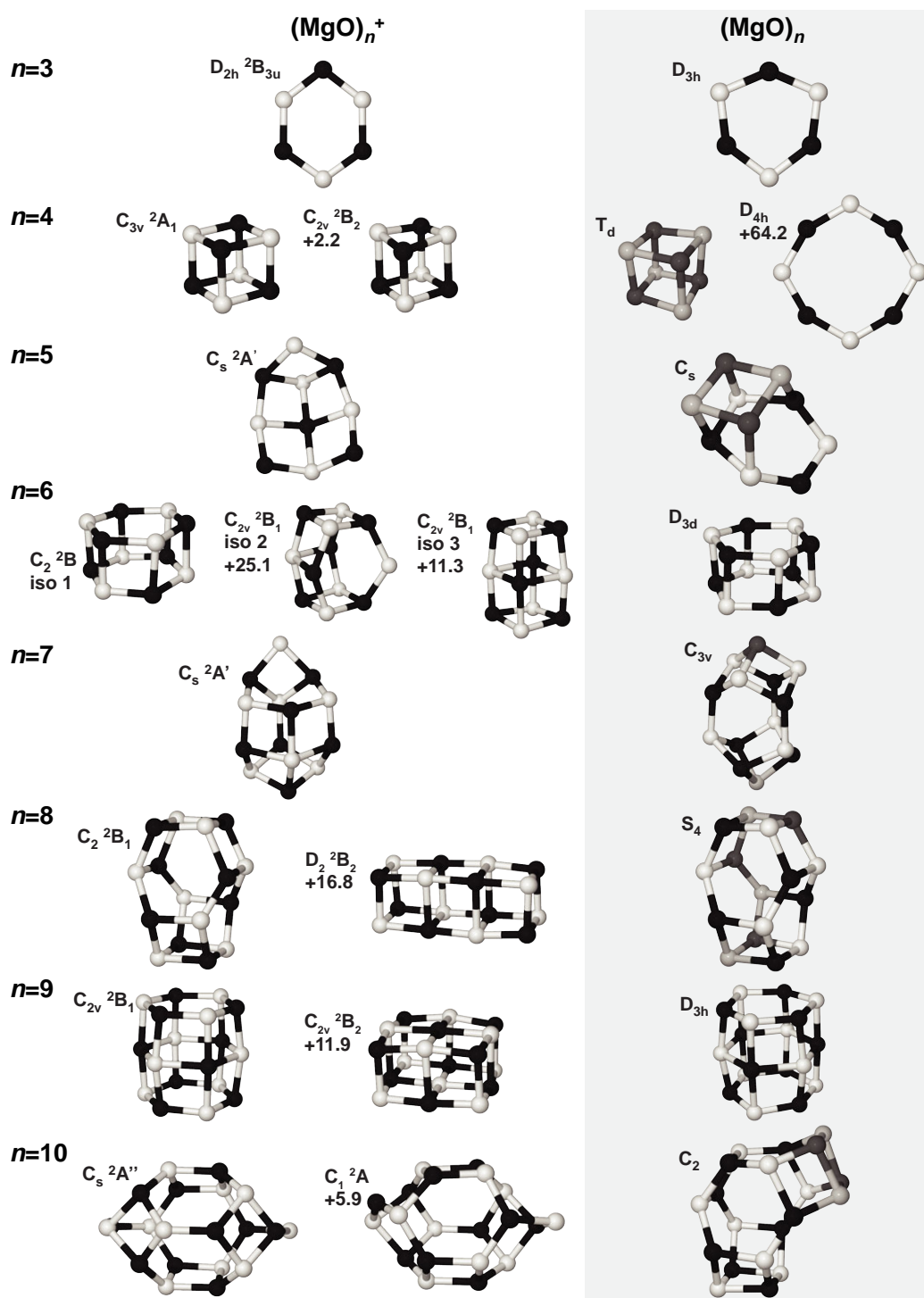


Figure 4.14.: Comparison between the identified structures for cationic and neutral (MgO) $_n$  clusters.

sizes prefer cage like structures, though these cages also incorporate the hexagonal ring motif. The structural transition towards the bulk-like cubic nano-crystals was not observed in the size range investigated here. The cubic  $(\text{MgO})_4$  cluster is the only size with a global minimum structure close to the bulk geometry, however, for this size higher lying isomers also need to be considered to fully explain the experimental spectrum. For the  $(\text{MgO})_{13}$  cluster, the second and third lowest energy structures appear like distorted fragments of the bulk and some evidence for their presence was found, but the cage-like global minimum structure largely explains the experimental spectrum.

The cations, on the other hand, usually have more open structures with low symmetry, leading to very complex IR spectra. For the  $(\text{MgO})_5^+$ ,  $(\text{MgO})_7^+$ , and  $(\text{MgO})_{10}^+$  cluster ions an excellent agreement between experiment and theory has been found, proving the presence of structures, which are different to the neutral structures. These large structural differences show that the assumption of similar structural motifs for cations and neutrals can completely fail for such ‘simple’ systems as MgO clusters. For the  $(\text{MgO})_4^+$  and  $(\text{MgO})_6^+$  clusters the small energy differences between different low-energy isomers and the similarities between the calculated IR spectra prevents unequivocal structure assignment.

## 4.2. Activation of molecular oxygen in MgO clusters

Surfaces of non-reducible metal oxides like MgO or  $\text{Al}_2\text{O}_3$  are often used as support for (metal) catalysts, but can also show on their own high reactivity. The active species are defect centers, such as kinks, steps or vacancies. Important active species for oxidation reactions are activated dioxygen, *i.e.* superoxo ( $\text{O}_2^-$ ) or peroxy ( $\text{O}_2^{2-}$ ), and the  $\text{O}^-$  radical species. The superoxo [251–253] and  $\text{O}^-$  [254] species can be experimentally observed by electron spin resonance (EPR) spectroscopy, and have been detected for MgO powder samples. However, the detailed structural characterization of powder samples is challenging. Inverse catalysts, (perfect) thin oxide films on a metal support, can be prepared under better controlled conditions. Interestingly, such systems can also show very high low-temperature reactivity. A monolayer of FeO(111) on a Pt(111) support, for instance, was found to be highly reactive for CO oxidation [255, 256]. In order for the reaction to occur, the film is initially enriched with oxygen, approaching the formal stoichiometry  $\text{FeO}_x$  ( $x \approx 1.8$ – $1.9$ ). Theoretical modeling showed that extra oxygen is molecularly chemisorbed to the surface. Two electrons are transferred from the oxide/metal substrate and the adsorbed oxygen becomes negatively charged, forming a peroxy species  $\text{O}_2^{2-}$ , which is important in order to understand the mechanism of the CO oxidation reaction. Experimentally, the peroxy species is not detectable by EPR.

Theoretical investigations have shown that the charge transfer itself is not limited to FeO, but rather seems to be generally observed and depends on film thickness and the support. A similar charge transfer mediated oxygen activation has been predicted for few monolayer thick MgO films on Ag(100) [257] and Mo(100) [258], but for both of these cases only a single electron is transferred, leading to a superoxo species. Recently, the presence of the superoxo species was confirmed experimentally by EPR measurements of a MgO film on Mo(001) [259]. Another activated species, the  $O^-$  radical, has also been observed in thin MgO films [260].

Charge transfer processes can also be studied for model systems with further reduced dimensionality. Fragments of the surface, clusters, can be studied in the gas phase and the charge transfer from the surface is mimicked by changing the charge state of the particle.  $Mg_nO_{n+1}$  clusters can model the thin film, as for such systems the excess oxygen may be present in the form of a dioxygen species. These species can be probed by their characteristic IR absorptions. In addition, the structure of the 'film', here a  $Mg_nO_{n-1}$  cluster, can also be studied by vibrational spectroscopy, whereas on the surface often only single sites are experimentally accessible. In the following, cationic, neutral, and anionic  $Mg_nO_{n+1}$  clusters are investigated using a combination of several gas-phase IR spectroscopy methods and quantum chemistry to elucidate the effect of charge on the binding of the extra oxygen.

#### 4.2.1. Experimental

In the previous section 1:1 stoichiometric cationic and neutral clusters have been discussed. But clusters deviating from the 'perfect' stoichiometry are also made in the cluster source at the same time. Clusters with an additional oxygen atom, for instance, were particular intense in the mass spectra obtained for cationic clusters, see Figure 4.2, but were of low intensity in the mass spectra for the neutrals (Figure 4.9). In contrast to magnesium rich species such species were not mentioned in previous experimental studies on neutral MgO clusters [73, 215]. This is most likely because of the mass overlaps between larger clusters when using natural abundance magnesium. The use of the isotopical enriched  $^{26}\text{Mg}$  target allows us to observe such species.

The same IR spectroscopy methods as applied before can be used to obtain IR spectra of these clusters. For cations IR-MPD spectroscopy of the Ar and  $O_2$  messenger species is employed. As discussed before, no differences are observed between the two messengers (see also Figure 4.4) and, because of the more favorable intensities, here we show only spectra obtained on the  $O_2$  complexes. The neutrals are studied by IR-UV2CI spectroscopy. The low intensities of the neutral  $Mg_nO_{n+1}$  species can not be explained by very high IEs, as IR-UV2CI spectroscopy is only possible for systems with an IE just above the photon energy of the ionization laser.



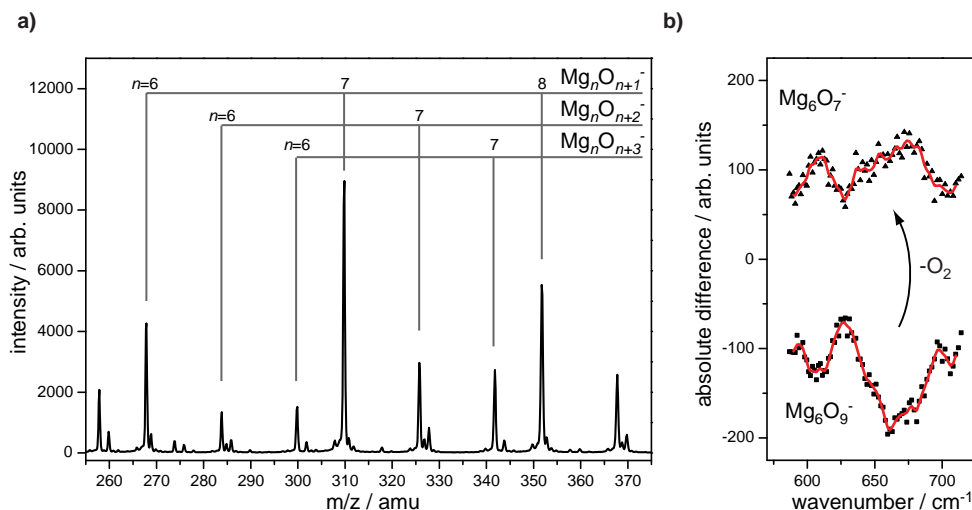


Figure 4.15.: a) Mass spectrum of MgO cluster anions and assignment of the most intense species observed. b) Difference spectra for  $Mg_6O_7^-$  and  $Mg_6O_9^-$  obtained by comparing the mass spectrometric signals with and without IR radiation. The loss in the  $Mg_6O_9^-$  channel is almost completely accounted for by the growth up in the  $Mg_6O_7^-$  channel.

Anionic magnesium oxide clusters can also be produced with the source, by adding 1 % oxygen to the helium carrier gas with the source at room-temperature. For detection, the voltages in the ToF-MS are reversed. Under these conditions intense signals for  $Mg_nO_{n+1}^-$  clusters, or clusters containing even more oxygen atoms can be observed, see Figure 4.15(a). We did not observe argon complexes, however, upon irradiation with the IR light from FELIX using a macropulse energy of 1.5–18 mJ fragmentation of some of the species in the molecular beam is observed. Figure 4.15 shows the difference spectra with and without FELIX radiation obtained on the  $Mg_6O_9^-$  and  $Mg_6O_7^-$  species. For the  $Mg_6O_9^-$  species a loss in the mass spectrum with FELIX is observed, simultaneously the  $Mg_6O_7^-$  mirrors the change, and increases its intensity. This can be explained by the loss of an  $O_2$  from  $Mg_6O_9^-$ . As for the MgO cations, molecular oxygen acts as a messenger species. An identical loss channel has also been observed for  $V_2O_7^-$  [237]. Unfortunately, such a good quantitative match between the fragmenting and product species can not be observed for all of the species in the mass spectrum. Presumably, this is because the normal fluctuations of the cluster signal masks the small increases due to the fragmentation of the larger cluster. However, other cooling channels (including electron detachment and the formation of other neutral fragments) can also compete with the  $O_2$  loss. Strictly speaking, the IR spectra obtained are for the  $Mg_nO_{n+3}^-$  anions.

#### 4.2.2. Results and discussion

Vibrational spectra in the 200–1700  $\text{cm}^{-1}$  range are measured for  $\text{Mg}_n\text{O}_{n+1}$  cluster cations, neutrals and anions with  $n=6-9$  and for cations and neutrals for  $n=4,5$ . The spectral range includes vibrational modes of the bare clusters as well as of dioxygen species. The latter are found, depending on the kind of dioxygen species (compare Figure 4.3(b)) between 800–900, at  $\sim 1150$ , or 1550  $\text{cm}^{-1}$ , indicating the presence of peroxy, superoxy, or physisorbed oxygen species, respectively.

For clusters measured via messenger tagging using  $\text{O}_2$ , *i.e.* cations and (presumably) anions, two different dioxygen species can play a role, a (chemisorbed) dioxygen species embedded in the cluster, and a physisorbed  $\text{O}_2$  messenger. This leads for  $\text{Mg}_5\text{O}_6^+$ , for instance, (see Figure 4.4) to the observation of an absorption at 1550  $\text{cm}^{-1}$ , indicating a physisorbed oxygen molecule in the initial  $\text{Mg}_5\text{O}_8^+$  complex. For  $\text{Mg}_6\text{O}_7^+$  and  $\text{Mg}_7\text{O}_8^+$  such an absorption is also observed. As this feature is not reproduced in the argon spectrum, it can be attributed completely to the  $\text{O}_2$  messenger. For anionic clusters one would also expect to observe such a physisorbed  $\text{O}_2$  mode. However, for none of the cluster sizes shown in the following is an absorption at such a frequency observed. It could be that the IR cross section (the free  $\text{O}_2$  stretch is not IR active) in the anionic complex is just too weak to be observable in the experiment. As no other absorptions are seen in this spectral region and it only contains information on the messenger species employed, the spectra in the following are shown only up to 1200  $\text{cm}^{-1}$ .

More significant for the cluster structure than the stretch region of the free O-O is the wavelength range for a superoxy complex ( $\approx 1150 \text{ cm}^{-1}$ ). For  $\text{Mg}_7\text{O}_8^+$  and  $\text{Mg}_8\text{O}_9^+$  a weak absorption at such a frequency is observed, see upper panels in Figs. 4.18 and 4.19. It does not stem from the messenger species, but rather from a chemisorbed dioxygen species in the cluster itself. Absorption at such a frequency is not seen for any of the other charge states. For several species, absorption in the spectral range of peroxy vibrations, 800–900  $\text{cm}^{-1}$ , is observed, but this range overlaps with the bare cluster modes, and an assignment to such a mode is only possible by comparison with calculations.

For further assignments, all species are compared to predictions from calculations\*. Similar to the  $(\text{MgO})_n^{+,0}$  clusters studied before, DFT has been employed using TURBOMOLE and the B3-LYP functional with the def2-TZVP basis-set. For cations and neutrals the global minimum structure is identified by using a genetic algorithm, whereas for the anions for most sizes† a series of (distorted) minimum

\* The calculations for cations and neutrals have been performed by K. Kwapien and Dr. M. Sierka from the Quantum Chemistry group of the Humboldt University Berlin headed by Prof. J. Sauer within the UniCat collaboration.

† The calculations for  $\text{Mg}_9\text{O}_{10}^-$  have also been performed by the group of Prof. J. Sauer and employed their genetic algorithm.

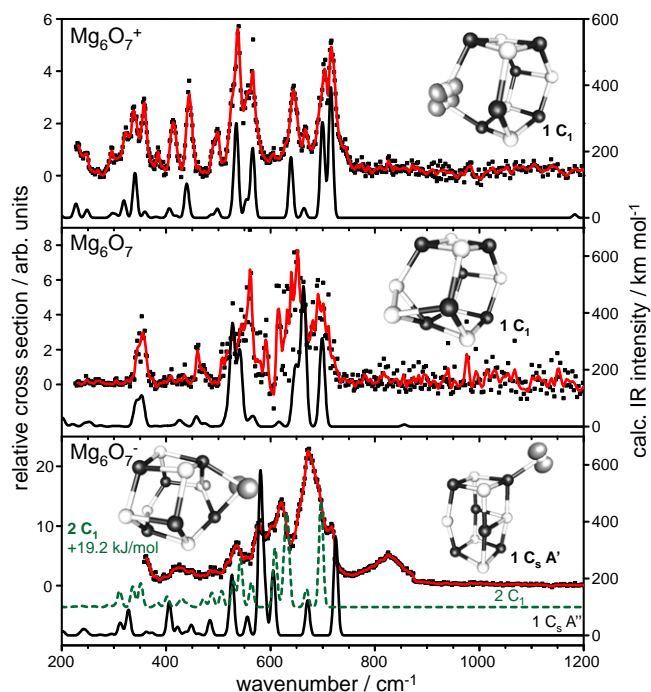


Figure 4.16.: Vibrational spectra of  $\text{Mg}_6\text{O}_7^{+,0,-}$  clusters and comparison to the calculated linear absorption spectra of the best fitting isomers. The comparison to other isomers can be found in the Appendix. The measured data points are shown as dots and a five-point-running average (solid red line) is added to guide the eye. Some of the predicted spectra are offset for clarity. Oxygen is shown in white, magnesium in black and the spin density in grey.

structures of the cations and neutrals have been used as the starting geometries. For convenience, the comparison here is limited to the isomers agreeing best with the experimental results. With two exceptions, these are also the identified lowest energy structures. For all sizes and charge states the comparison to other low energy isomers can be found in the Appendix.

#### 4.2.2.1. The observation of different oxygen species using the example of $\text{Mg}_6\text{O}_7$

For the cationic and neutral  $\text{Mg}_6\text{O}_7$  clusters the genetic algorithm identifies structures very similar to the ones observed for the  $(\text{MgO})_6^{+,0}$  clusters. For the neutral  $(\text{MgO})_6$  an unambiguous assignment of a two-layered hexagonal tube was possible, whereas for the cation this structure was one of three competing structures. The oxygen rich cationic and neutral clusters also have this structural motif, see

Figure 4.16. For both species, a single oxygen in the hexagonal tube is replaced by a dioxygen unit and the cluster slightly readapts. The agreement for the predicted IR spectra and the experimental IR-MPD and IR-UV2CI spectra for the cation and neutral, respectively, is very good. Other high energy isomers fit the experiment less well, see Figures A.1 and A.5. Although the structure look quite similar, the type of dioxygen species in the cluster is different.

In the cation, the oxygen ligand is bridging two metal atoms ( $\mu^2$ ) and each Mg atom forms only a single O-Mg bond ( $\eta^1$ ), whereas in the neutral it is bridging three metal atoms ( $\mu^3$ ), and one of the Mg atom is bound to both oxygen atoms (O-Mg-O) ( $\eta^2$ ). The bonds can therefore be described as  $\mu^2(\eta^1:\eta^1)$  for the cation and  $\mu^3(\eta^1:\eta^2:\eta^1)$  for the neutral. The O-O distances in the two assigned structures also differ. For the  $\text{Mg}_6\text{O}_7$  structures we get 1.33 Å for the cation and 1.52 Å for the neutral, with associated vibrations at 1193 and 856  $\text{cm}^{-1}$ . These are very characteristic values for superoxo and peroxy species (see Fig. 4.3(b)). Table 4.2 shows the coordination of the dioxygen ligand, the O-O bond distance and the IR frequency and intensity of the associated O-O stretch mode for all of the cationic and neutral cluster structures discussed. The IR intensities of the O-O stretches for the structures of  $\text{Mg}_6\text{O}_7^+$  and  $\text{Mg}_6\text{O}_7$  are relatively weak, with intensities of 10.5 and 7.1  $\text{km mol}^{-1}$ , compared to the other normal modes, many of which have values of a few hundred  $\text{km mol}^{-1}$ . The large differences in relative intensities between the O-O stretches and the other modes make it hard to observe these characteristic features even in the calculated spectra and also explain their absence or bare visibility in experiment. Although the dioxygen species for  $\text{Mg}_6\text{O}_7^{+,0}$  can not be directly experimentally confirmed here, the structural assignment is unambiguous as the rest of the IR spectrum is nicely reproduced in intensity and position. For  $\text{Mg}_6\text{O}_7^+$  experiments on methane complexes, see section 4.3.4, also show that when higher IR intensities are used the superoxo mode should be observable (compare Fig. 4.30).

For the  $\text{Mg}_6\text{O}_7^-$  anion isomers containing a dioxygen species are found very high in energy. Instead, structures with a dissociated oxygen molecule are energetically favored. The structure giving the best agreement with the experimental spectrum is the second lowest one  $2C_1$  (+19.2 kJ/mol). Most parts of the experimental spectrum can be assigned to this structure, although band positions do not match perfectly. A frequency scaling factor of 0.97 would give better agreement. Still the agreement is surprisingly good taking the problems of DFT with anions into account. Other, *e.g.* wave function based methods are in principle available, but using the same method for all charge states has the advantage that the comparison between them may be more reliable (provided that it does not completely fails for one charge state). The structure assigned to  $\text{Mg}_6\text{O}_7^-$  is again based on the hexagonal tube. The dioxygen species found in the cation and the neutral is

Table 4.2.: Coordination of the dioxygen species in the neutral and cationic clusters along with the calculated O-O bond distances, IR frequencies and intensities.

Charge	$\text{Mg}_n\text{O}_{n+1}$	Isomer	Coordination of the $\text{O}_2$ ligand	O-O stretch		O-O distance
				frequency	intensity	
	n			$\text{cm}^{-1}$	$\text{km mol}^{-1}$	$\text{\AA}$
+1	4	1 $\text{C}_1$	$\mu^2(\eta^1:\eta^1)$	1153	14.8	1.34
	5	1 $\text{C}_s$	$\mu^2(\eta^1:\eta^1)$	1221.6	0.4	1.33
	6	1 $\text{C}_1$	$\mu^2(\eta^1:\eta^1)$	1182.9	10.5	1.33
	7	1 $\text{C}_s$	$\mu^2(\eta^1:\eta^1)$	1224.6	0.85	1.33
	8	1 $\text{C}_1^*$	$\mu^3(\eta^1:\eta^2:\eta^1)$	1192.7	6.0	1.33
		2 $\text{C}_1^*$	$\mu^3(\eta^1:\eta^2:\eta^1)$	1177.7	12.0	1.34
		3 $\text{C}_1$	$\mu^2(\eta^1:\eta^1)$	1166.7	15.7	1.34
		4 $\text{C}_1^*$	$\mu^2(\eta^1:\eta^1)$	1170.4	4.6	1.34
	9	1 $\text{C}_1$	$\mu^2(\eta^1:\eta^1)$	1203.4	1.6	1.33
		2 $\text{C}_1$	$\mu^2(\eta^1:\eta^1)$	1191.1	8	1.33
0	4	1 $\text{C}_s$	$\mu^3(\eta^1:\eta^1:\eta^1)$	843.4	8	1.51
		2 $\text{C}_s$	$\mu^3(\eta^1:\eta^2:\eta^1)$	853.8	1.52	1.52
		3 $\text{C}_{2v}$	$\mu^2(\eta^2:\eta^2)$	788.0	15.0	1.58
	5	1 $\text{C}_s$	$\mu^3(\eta^1:\eta^2:\eta^1)$	824.4	20.2	1.54
		2 $\text{C}_s$	$\mu^2(\eta^2:\eta^2)$	807.4	29.8	1.57
		3 $\text{C}_s$	$\mu^4(\eta^1:\eta^1:\eta^1:\eta^1)$	836.4	3.1	1.52
	6	1 $\text{C}_1$	$\mu^3(\eta^1:\eta^2:\eta^1)$	856.1	7.1	1.52
	7	1 $\text{C}_1$	$\mu^3(\eta^1:\eta^2:\eta^1)$	860	5.9	1.52
	8	1 $\text{C}_1$	$\mu^3(\eta^1:\eta^2:\eta^1)$	859.4	13.1	1.53
	9	1 $\text{C}_1$	$\mu^3(\eta^1:\eta^2:\eta^1)$	862	8	1.52
		2 $\text{C}_1$	$\mu^3(\eta^1:\eta^1:\eta^1)$	893.1	24.4	1.51

\* See Appendix for structures and IR spectra.

dissociated, and a single oxygen atom is bridging one of the hexagonal rings. The lowest energy structure 1 $\text{C}_s$  is also quite similar, it differs mainly by the fact that the hexagonal ring is squeezed, and a cube-like structure is obtained, with the oxygen atom coordinated to a single magnesium atom. This structure could explain parts of the experimental spectrum which are poorly explained by isomer 2 $\text{C}_1$ . Only a feature at  $800\text{ cm}^{-1}$  cannot be explained by these two structures. A sheet-like structure found 56 kJ/mol higher in energy has a vibrational mode in this range (see Figure A.9). However, the predicted frequency of this band is a bit too low and, furthermore, the experimental feature is much wider than any other mode measured. Some other cluster sizes and compositions, such as  $\text{Mg}_8\text{O}_9^-$ ,  $\text{Mg}_9\text{O}_{10}^-$ , but also  $(\text{MgO})_7^+$  and  $(\text{MgO})_4$  have similar features. For the latter cluster size an isomer very high in energy has been used to explain it. An additional isomer, which is also for  $\text{Mg}_6\text{O}_7^-$  the most likely source of this feature, could only be a minor-

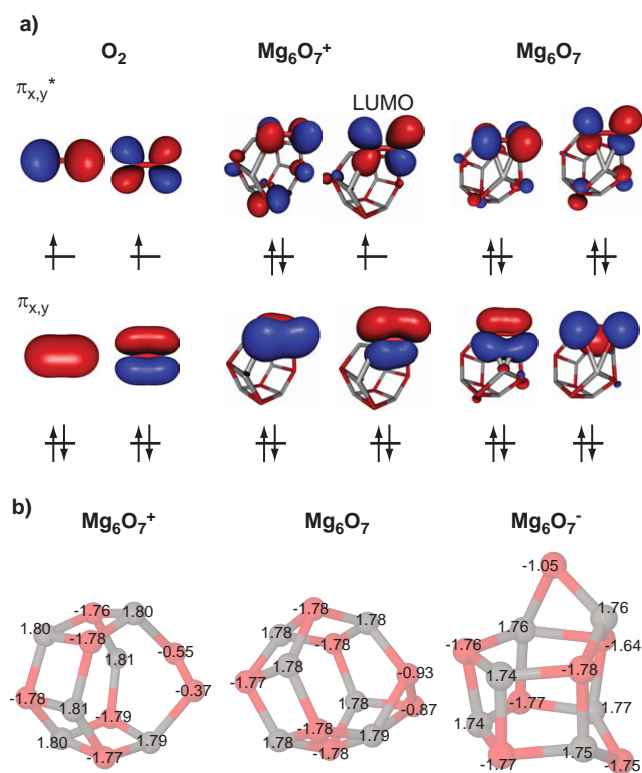


Figure 4.17.: a) Orbitals of  $Mg_6O_7^{+0}$  in comparison to the orbitals of  $O_2$ . Upon going from the cation to the neutral the LUMO, a  $\pi^*$  orbital, gets filled, reducing the bonding in the dioxygen species. b) Charge distribution in the  $Mg_6O_7$  clusters derived by a natural population analysis.

ity species, as the rest of the spectrum is completely reproduced by the identified structures.

**Charge distribution and molecular orbitals of  $Mg_6O_7$ .** The observation of a superoxo species for the  $Mg_6O_7^{+}$  cation, a peroxo for the neutral and dissociated oxygen for the anion can be understood by assuming a  $Mg_6O_5$  cluster as the basic structure. In the fully ionic bulk each Mg provides two electrons and is formally in a +2 state, whereas the oxygen is in a -2 state. In a cation, the underlying  $Mg_6O_5$  cluster would therefore have one excess electron that can be transferred to the dioxygen ligand. The electronic configuration of free molecular oxygen in the ground state is a  $\sigma_s^2\sigma_s^{*2}\sigma_p^2\pi_x^2\pi_y^2\pi_x^{*1}\pi_y^{*1}$  configuration, see Figure 4.3(a). An additional electron would be transferred into the antibonding  $\pi_x^*$  orbital, forming

a superoxo species, that becomes chemically bound. In the neutral two excess electrons are transferred to the dioxygen, filling both the  $\pi_x^*$  and  $\pi_y^*$  orbitals and leading to a peroxo species  $O_2^{2-}$  (see also Figure 4.3(b)). A third electron as present for an anionic species can not be easily accommodated by the dioxygen species, as both antibonding  $\pi^*$  orbitals are fully occupied. Instead, the dioxygen species dissociates if one more electron is provided, leading to  $O^{2-} + O^-$ . This means one of the oxygens is in its most stable oxidation state. This explanation is supported by the calculated charge distribution obtained by a natural population analysis, as shown in Figure 4.17(b). The underlying  $Mg_6O_5$  cluster has almost full formal charges of +1.8 for magnesium and -1.8 for oxygen, independent of the total charge state of the cluster. The dioxygen species carries only a single negative charge in the cation and two negative charges in the neutral cluster, in both cases almost equally distributed between the two oxygen atoms. In the anion, the natural population analysis shows the formation of  $O^{2-} + O^-$ . Previous calculations usually considered only Mulliken charges [225, 226, 230, 261] and give fractional charges with values between 1 and 1.5. The natural population analysis seems to give the more physical answers.

The molecular orbitals of the dioxygen species are only slightly perturbed in the clusters and are almost identical to the ones found for free  $O_2$ . In Figure 4.17 the  $\pi_{x,y}^{(*)}$  orbitals of  $O_2$  are compared to the orbitals of  $Mg_6O_7^{+,0}$ . Similar bonding  $\pi_{x,y}$  orbitals can also be identified in  $Mg_6O_7^+$ . The  $\pi_x^*$  orbital, which gets populated in the superoxo species is also found in the cationic cluster. The LUMO of the cation is the  $\pi_y^*$  orbital. Assuming the correct energetic ordering of the unoccupied states, this means that upon electron attachment this state becomes populated. A weakening of the O-O bond is expected. The structure observed here in the experiment for the neutral should be a direct consequence of this process, as the structural difference between the two species is small. A confirmation of this picture is given by the molecular orbitals of the neutral species.

#### 4.2.2.2. (Di-)oxygen species in larger MgO clusters – $Mg_7O_8$ , $Mg_8O_9$ and $Mg_9O_{10}$

The picture of  $O_2$  activation is not only valid for a single cluster size, but seems to hold for all smaller and medium-sized MgO clusters. To confirm this, the experimental vibrational spectra are compared to predicted IR spectra for the assigned structures for  $Mg_7O_8^{+,0,-}$ ,  $Mg_8O_9^{+,0,-}$ , and  $Mg_9O_{10}^{+,0,-}$  in Figures 4.18, 4.19 and 4.20, respectively.

For the  $Mg_7O_8^{+,0,-}$  cluster again very similar structures to those of the corresponding 1:1 stoichiometric clusters are identified in the calculations as the global minima. For all charge states these are cage-like structures, which are structurally

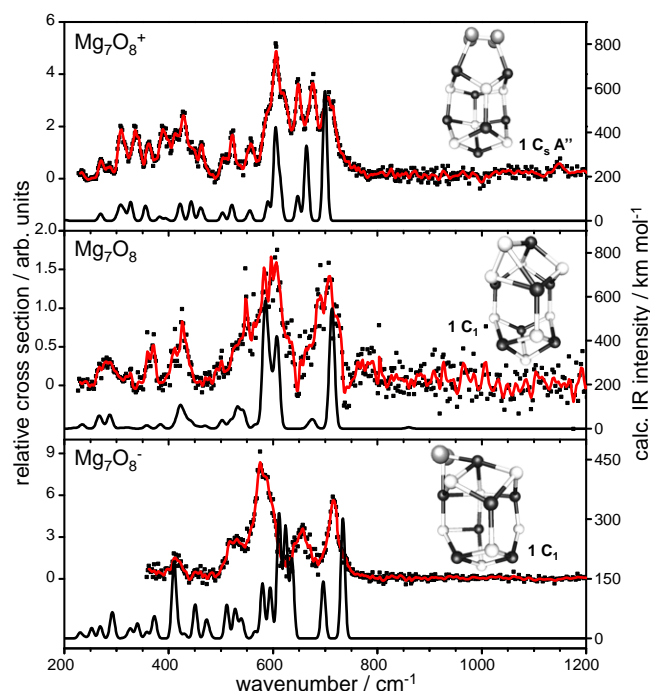


Figure 4.18.: Vibrational spectra of  $\text{Mg}_7\text{O}_8^{+,0,-}$  clusters and comparison to the calculated linear absorption spectra of the best fitting isomers.

very similar and require only small rearrangements when going from one to the other. The agreement between experimental and predicted IR spectra is very good, with the exception of the anion. For this size the overall pattern fits, but some modes would require significant shifts and a single scaling factor is not sufficient. For all charge states only the predicted global minima show good agreement between simulated and experimental spectra. For the neutral, the second lowest energy structure, 0.6 kJ/mol higher in energy, may also be considered (see Figure A.6 in the Appendix) as it has an IR spectrum similar to the ground state. The structures differ only in the position of the dioxygen species.

The (di-)oxygen species found for the different charge states are in a similar coordination as for  $\text{Mg}_6\text{O}_7$ . The dioxygen is found for the cation in a  $\mu^2(\eta^1:\eta^1)$  and the neutral in a  $\mu^3(\eta^1:\eta^2:\eta^1)$  coordination, see Table 4.2. The O-O distances for the cationic and neutral structure reveal that again superoxo and peroxy are present in the cation and neutral, respectively. In contrast to  $\text{Mg}_6\text{O}_7^+$  the superoxo mode in  $\text{Mg}_7\text{O}_8^+$  is also observed in the experiment at  $1147\text{ cm}^{-1}$ . The prediction from the (unscaled) DFT calculation of  $1224\text{ cm}^{-1}$  is, however, too high, see Table 4.2. A scaling factor of 0.94 would give better agreement for this mode, but would also lead to a worse description in the far-IR, where a scaling factor of one gives good



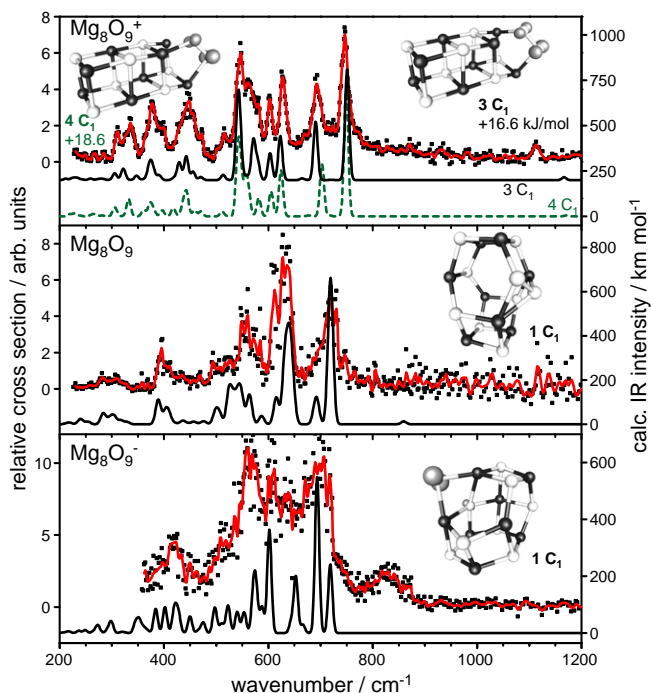


Figure 4.19.: Vibrational spectra of  $\text{Mg}_8\text{O}_9^{+,0,-}$  clusters and comparison to the calculated linear absorption spectra of the best fitting isomers.

agreement. This is also seen for other oxide clusters [84]. The peroxo mode for the neutral  $\text{Mg}_7\text{O}_8$  cluster, predicted at  $860\text{ cm}^{-1}$ , is not observed in the experiment, but, again, it is calculated to have a very low intensity.

For  $\text{Mg}_8\text{O}_9^+$  the putative global minimum obtained from the genetic algorithm is not observed in the experiment. The two lowest energy structures are two distorted versions of the  $(\text{MgO})_8^{+,0}$  structure, in which two hexagonal tube  $(\text{MgO})_6$  units are fused at  $90^\circ$  (see Figure A.3). Instead, we assign the spectrum to one of the next higher energy isomers  $3\text{C}_1$  or  $4\text{C}_1$ , that are 16.6 and 18.6 kJ/mol higher in energy, respectively. Their structures resemble fragments of the bulk, being  $(2 \times 2 \times 4)$  cubes, in which one of the corner oxygen atoms is replaced by a dioxygen unit. In particular, their two highest vibrational modes are very characteristic in the experimental spectrum and the lower energy structures clearly do not contribute significantly to this part of the spectrum. The failure of B3-LYP in predicting the ground state cannot be easily explained here, but it does not seem to be a messenger effect. The binding of argon to these different isomers does not change the energetic ordering nor is the binding strength dramatically different. For the physisorption of  $\text{O}_2$  similar energetics are also expected. For all four low-energy structures considered only superoxo species are found, and as for the  $\text{Mg}_7\text{O}_8^+$  clus-

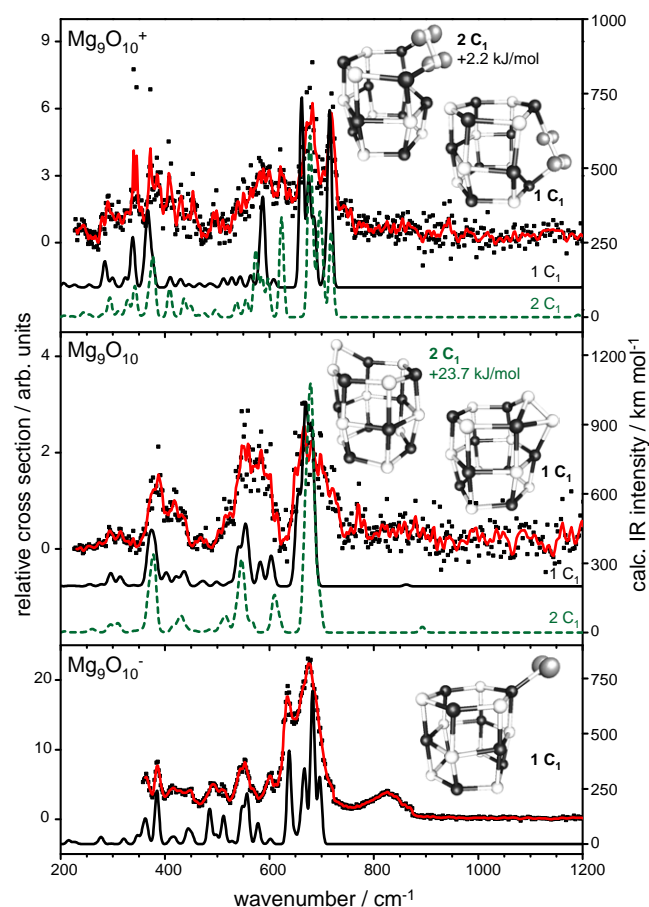


Figure 4.20.: Vibrational spectra of  $\text{Mg}_9\text{O}_{10}^{+,0,-}$  clusters and comparison to the calculated linear absorption spectra of the best fitting isomers.

ter the experimental frequency of this mode is lower than in the predictions.

The putative global minimum structure for  $\text{Mg}_8\text{O}_9$  is similar to the structure of the  $(\text{MgO})_8^{+,0}$  clusters and the calculated lowest energy structure for the cation. The predicted IR spectrum agrees well with the measured one, and the match to other isomers (Figure A.7) is less convincing. Again, a peroxo species is identified for the neutral structure.

The structural change observed when going to the anion is more dramatic. Whereas the structures of cation and neutral are based upon a  $(2 \times 2 \times 4)$  cube-like structure, the anion is more similar to a  $(2 \times 3 \times 3)$  cube, in which one of the corner magnesium atoms is missing. The  $\text{O}^-$  is found in a bridge position, similar to  $\text{Mg}_7\text{O}_8^-$  and the second lowest energy structure of  $\text{Mg}_6\text{O}_7^-$ . In contrast to the smaller sizes, no scaling factor is required to fit the experimental spectrum.

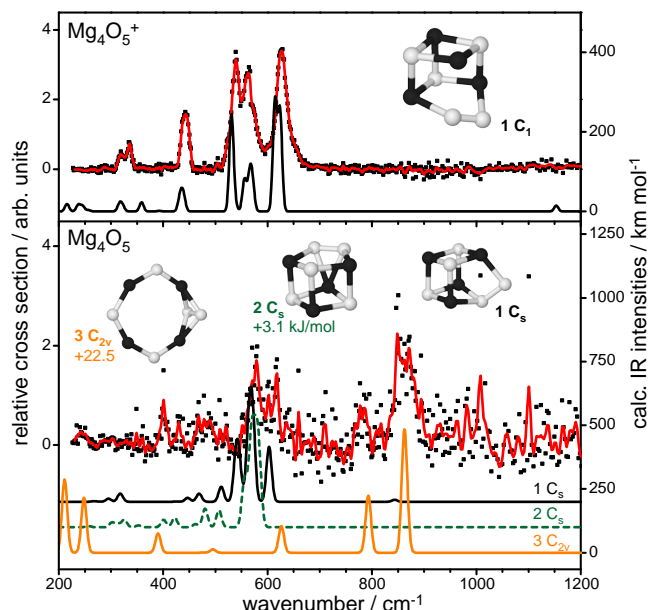


Figure 4.21.: Vibrational spectra of  $\text{Mg}_4\text{O}_5^{+,0}$  clusters and comparison to the calculated linear absorption spectra of the best fitting isomers.

The largest cluster size for which experimental spectra for all three charge states are available is the  $\text{Mg}_9\text{O}_{10}$  cluster. The neutral and cationic ( $\text{MgO}$ )<sub>9</sub> cluster have both been assigned to a hexagonal tube structure. This structural motif is also present in the cluster with an additional oxygen atom. Figure 4.20 shows the comparison between measured IR spectra and spectra computed for the two lowest energy structures. For both charge states, either isomer could explain the IR-MPD and IR-UV2CI spectra. Each of the isomers contains either a superoxo species or a peroxo species for the cation and neutral, respectively. The structural change when going to the anion is small. The structure giving the best agreement to the experimental spectrum is the predicted ground state, in which the additional oxygen atom is bound to a single magnesium atom of a hexagonal tube structure. Similar to the lowest energy structure of  $\text{Mg}_6\text{O}_7^-$ , the additional oxygen atom carries a charge of -1. A scaling of the calculated frequencies is not required.

The good agreement between measured and predicted spectrum for the anions of the largest two cluster sizes demonstrates that by measuring the depletion of the  $\text{Mg}_n\text{O}_{n+3}^-$  species we were probing the structures of the  $\text{Mg}_n\text{O}_{n+1}^-$  clusters and that the  $\text{O}_2$  messenger was only weakly physisorbed.

#### 4.2.2.3. Cationic and neutral cluster containing 4 and 5 Mg atoms

For cluster containing four and five Mg atoms the comparison can only be made for the cation and neutral species. The measured IR spectra of  $\text{Mg}_4\text{O}_5$  and  $\text{Mg}_5\text{O}_6$  are shown in Figures 4.21 and 4.22 along with the predictions from calculations. For  $\text{Mg}_4\text{O}_5^+$  and  $\text{Mg}_5\text{O}_6^+$  the structures are based on the cube and the sheet-like structures of  $(\text{MgO})_4$  and  $(\text{MgO})_5$ , respectively. Unambiguous agreement between experiment and theory is found. The interpretation for the neutrals is less clear, since for  $\text{Mg}_4\text{O}_5$  three different isomers, all containing a peroxo species, have to be considered to explain the experimental spectrum. Two different structural motifs are identified for the low energy structures, both can be derived from the isomers of the  $(\text{MgO})_4$  cluster. From the cube, which is the global minimum of the neutral  $(\text{MgO})_4$ , the  $1C_s$  and  $2C_s$  structures are formed by exchanging an O atom for an  $\text{O}_2$ . The structure  $3C_{2v}$  is based on a different isomer observed for  $(\text{MgO})_4$ , an 8-membered ring, again, with a single oxygen atom replaced by  $\text{O}_2$ . The  $1C_s$  and  $2C_s$  isomers have strong absorption bands around  $600\text{ cm}^{-1}$ , where the experimental spectrum shows a broad feature, and either isomer would explain this part of the spectrum. However, the additional features at  $400$ ,  $780$ , and  $880\text{ cm}^{-1}$  are not due to these isomers. The  $3C_{2v}$  structure does have absorptions at these positions and would therefore explain the missing parts. The  $3C_{2v}$  structure is the only one with very intense vibrations above  $800\text{ cm}^{-1}$  with the O-O vibration located at  $788\text{ cm}^{-1}$ . The predicted energy of this isomer is  $22\text{ kJ/mol}$  above the ground state. For the  $(\text{MgO})_4$  cluster the energy difference between the two isomers was even higher,  $64\text{ kJ/mol}$ . Similar to the  $(\text{MgO})_4$  cluster several isomers need to be considered to explain all details of the experimental spectrum for  $\text{Mg}_4\text{O}_5$ .

The IR-UV2CI spectrum of  $\text{Mg}_5\text{O}_6$  shows a series of weak bands between  $280$  and  $340\text{ cm}^{-1}$ , a broad one centered at  $\approx 590\text{ cm}^{-1}$ , and two intense features at  $687$  and  $731\text{ cm}^{-1}$ . This double feature around  $700\text{ cm}^{-1}$  is very characteristic and can help to assign the structure observed in the experiment. The two lowest energy structures,  $1C_s$  and  $2C_s$ , do not have two bands in this range. The next isomer  $3C_s$ ,  $18\text{ kJ/mol}$  above the minimum has such characteristic modes, predicted at  $692$  and  $720\text{ cm}^{-1}$ , almost exactly at the experimental position. The broad absorption around  $590\text{ cm}^{-1}$  can also be explained by a series of peaks predicted in this range, though the intensities do not completely agree. This isomer also explains the small features seen below  $400\text{ cm}^{-1}$ . As the spectroscopic technique employed here is more sensitive to the isomer with the lower ionization energy, the observation of a higher energy isomer is not entirely surprising. The predicted energy difference is even below that of the isomers considered for the  $\text{Mg}_4\text{O}_5$  cluster. For the  $(\text{MgO})_n$  clusters such a behavior was also observed for the  $(\text{MgO})_{12}$  cluster and was discussed there in more detail.

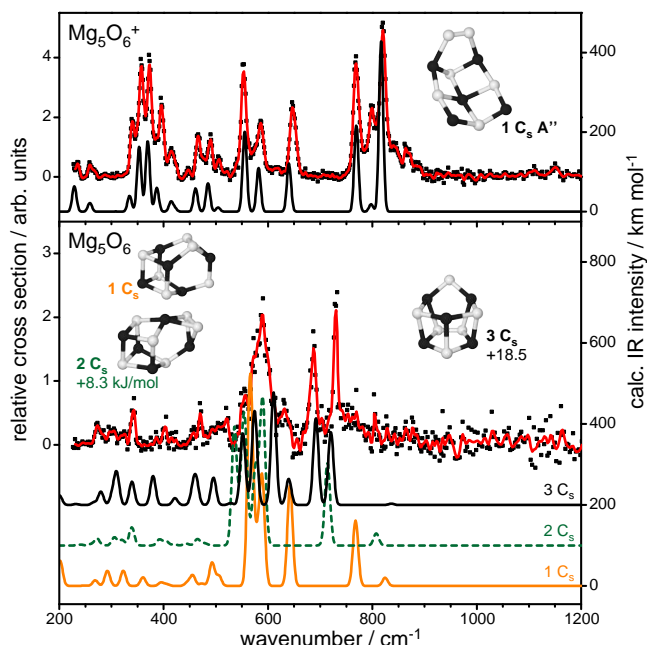


Figure 4.22.: Vibrational spectra of  $\text{Mg}_5\text{O}_6^{+,0}$  clusters and comparison to the calculated linear absorption spectra of lowest energy structures.

The observation of superoxo and peroxy species for cations and neutrals, respectively, also holds for these two systems. The charge transfer into the dioxygen unit therefore seems to be valid in general for small and medium-sized  $\text{Mg}_n\text{O}_{n+1}$  clusters.

#### 4.2.2.4. Comparison to surface studies

The superoxo species identified for the cationic clusters can be compared to thin film results. The theoretical predictions for  $\text{O}_2$  adsorbed on  $\text{MgO}/\text{Ag}$  also predicted a superoxo species in  $\mu^2(\eta^1:\eta^1)$  configuration and a O-O bond distance of 1.32 Å [257], and 1.35 Å for  $\text{MgO}$  on  $\text{Mo}$  [259]. These results agree very well with our gas-phase results obtained for the cationic species. For all experimentally observed structures, a  $\mu^2(\eta^1:\eta^1)$  coordination is found and the calculated O-O distances are 1.33–1.34 Å.

#### 4.2.3. Conclusion

In the gas phase, cationic and neutral  $\text{MgO}$  clusters of the composition  $\text{Mg}_n\text{O}_{n+1}$  contain stable dioxygen species demonstrated by combining predictions from theory and experiments using two different IR spectroscopic methods.

Depending on the cluster charge state different dioxygen species are identified. For the cations superoxo  $\text{O}_2^-$  species have been found, whereas for the neutrals peroxo species  $\text{O}_2^{2-}$  form, determined by the calculated O-O bond distances in the clusters of 1.3 and 1.5 Å, respectively. The weak IR intensities for the O-O vibrations make their direct experimental observation difficult. However, based on the vibrational fingerprint of the MgO framework the full structure of the cluster and thereby also the type of dioxygen species can be unambiguously determined. In anionic clusters the dioxygen unit is broken apart to accommodate the additional charge.

A natural population analysis for the  $\text{Mg}_n\text{O}_m$  clusters found that the Mg and the O atoms (except for the dioxygen ones) have almost full formal charges of  $\pm 1.8$ , very close to the bulk value of  $\pm 2$ . In the case of a cation the underlying  $\text{Mg}_n\text{O}_{n-1}^+$  cluster carries a single excess electron, which is transferred to the  $\text{O}_2$  species into one of the antibonding  $\pi^*$  orbitals. Adding a further electron, which is equivalent to neutralizing, adds a second electron to the other antibonding orbital, forming  $\text{O}_2^{2-}$ , and further weakens the O-O bond. The dioxygen cannot accommodate any additional charge, hence for the anionic clusters an  $\text{O}^{2-}$  and an  $\text{O}^-$  species are formed.

The structures observed for these clusters are only slightly modified versions of the structures observed for 1:1 stoichiometric clusters and, in general, one of the oxygen atoms is replaced by a dioxygen unit and the cluster slightly rearranges.

Similar charge transfer processes can be induced by growing thin films on appropriate supports or by deposition of clusters onto a metal oxide surface [258] or alkali atoms on MgO powders [262]. Whereas the experimental observation of activated species is very challenging in surface science, on the free cluster the 'transfer' of up to three electrons towards  $\text{O}_2$  can be investigated. These results may help to get a better understanding of activated oxygen species on surfaces and how to tune the electron transfer.

### 4.3. Ligand complexes of MgO - CO, CH<sub>4</sub>, H<sub>2</sub>O

In the previous sections the structures of bare MgO clusters were investigated, but IR spectroscopy also allows the interaction of these clusters with different ligands to be probed.

Using suitable ligands, one may obtain information on the charge distribution in the cluster and thereby probe its electronic structure. CO is often used in such experiments. This may help to understand real catalysts, as the structures of activated short-lived intermediates can be frozen out during the expansion of the molecular beam. Cooling during the expansion reduces the cluster's internal en-

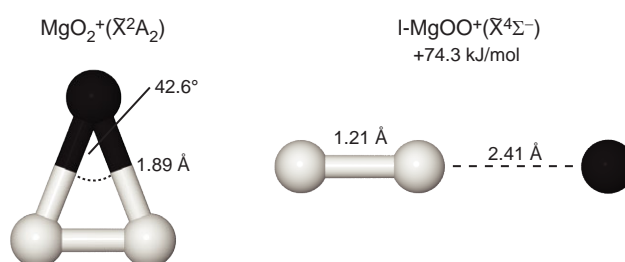


Figure 4.23.: Equilibrium geometries for  $\text{MgO}_2^+$  taken from Ref. [267].

ergy and traps these species behind reaction barriers. The interaction of MgO cluster with methane is therefore particularly interesting, as it would allow a better understanding of the methane activation observed for lithium doped MgO surfaces. Another interesting species is water, as it is present under real reaction conditions and may alter the catalytic properties. Water enters the reaction process either as a contaminant in the reaction gases or can be a side product of the chemical reaction itself.

In the following, the interaction of  $\text{O}_2$  and  $\text{H}_2\text{O}$  with the simplest model system of a defective MgO surface, the  $\text{MgO}_2^+$  species, are investigated first. Afterwards, hydroxylated MgO clusters are compared to bare clusters. Finally the interaction of MgO clusters with methane and CO is briefly discussed.

#### 4.3.1. $\text{O}_2$ and $\text{H}_2\text{O}$ complexes of the magnesium superoxide cation $\text{MgO}_2^+$

The metal-ion superoxide  $\text{MgO}_2^+$  molecule may be considered to be the simplest model system of an active species of a magnesium oxide surface. Whereas the perfect surface is not reactive, such a defect center may be able to catalyze oxidation reactions. Besides its model character for a surface site, the molecule itself is important in atmospheric chemistry. Magnesium is among the major components of meteorites, and large quantities are injected into the atmosphere when they burn up. Most of the material is ionic, and the ion/neutral ratio for magnesium is among the largest of any element [263, 264]. The magnesium atoms undergo a rich chemistry with the residual gas in the atmosphere, most importantly with oxygen (including ozone) and water. Several studies have been devoted to investigate the structure of the  $\text{MgO}_2^+$  ion [265–267] and its reactions [264, 268, 269].

Two equilibrium geometries have been determined for  $\text{MgO}_2^+$ , a triangular one with a O-Mg-O angle of  $42.6^\circ$  with a strong ionic character,  $\text{Mg}^{2+}\text{O}_2^-$ , and a linear one  $\text{l-MgOO}^+$  (see Fig. 4.23). The latter is best described as a  $\text{Mg}^+$  interacting with a free oxygen molecule [267]. The linear molecule is currently thought to be only

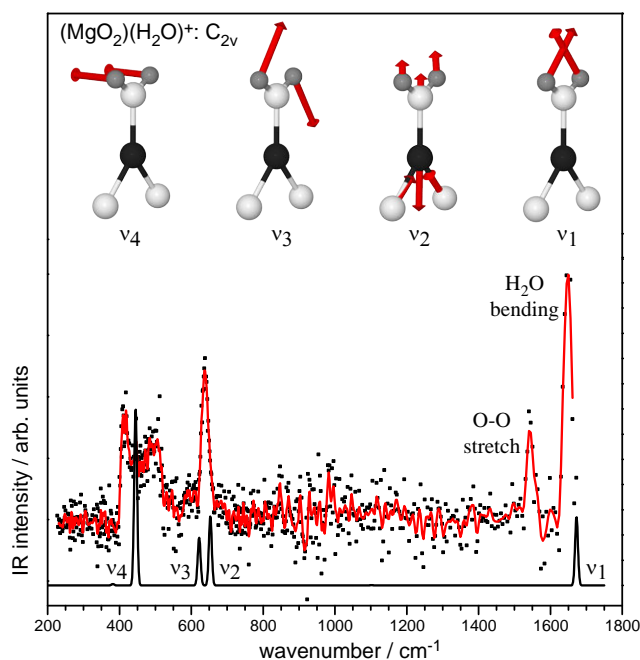


Figure 4.24.: IR-MPD spectrum measured for the  $\text{MgO}_2^+$  water complex and comparison to the predicted spectrum obtained from a DFT calculation. The modes are illustrated for the most intense features in the spectrum.

a minority species. In the following, two complexes with  $\text{MgO}_2^+$  are discussed, a  $\text{MgO}_2^+$ -water and a  $\text{MgO}_2^+$ -dioxygen species. Both complexes may also form in the atmosphere.

Complexes of  $\text{MgO}_2^+$  with water and dioxygen can be produced in the cluster source simultaneously with all other cationic MgO clusters studied before. Whereas the formation of the dioxygen containing species is not very surprising and has been used in the spectroscopy of the larger clusters, the formation of the water complex is more so, as water is not directly added in the cluster formation process. However, very small amounts may enter through the carrier gas, or come from the surfaces of the cluster source and the target rod.

Depending on the kind of interaction, one may distinguish between physisorption or chemisorption of the ligand. Physisorbed species are usually only weakly bound and the absorption of a single IR photon may be sufficient to dissociate the complex. A shift in the frequencies of the ligand's vibrational modes can provide information about charge transfers and the local environment of the ligand. Electric fields, for instance, may lead to deformations of the ligand.



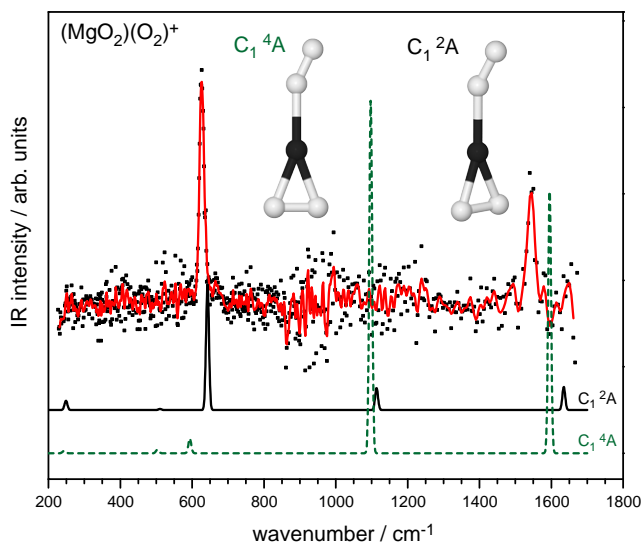


Figure 4.25.: IR-MPD spectrum of the  $\text{MgO}_2^+$  dioxygen complex in comparison to the predictions from a DFT calculation. Doublet and quartet state are isoenergetic.

Ligands that have undergone a reaction may be more strongly bound making direct dissociation of the complex more difficult. Such reaction products are identified by the absence of the vibrational frequencies of the reactant and the appearance of bands for the product species, *e.g.* CO (CO stretch:  $2170\text{ cm}^{-1}$ ) and  $\text{CO}_2$  (Absorptions at:  $667, 1333, 2349\text{ cm}^{-1}$ ). Species that can not be directly dissociated by single photon absorption are again studied using more loosely bound messengers.

Spectra for the water and dioxygen complexes have been measured via the messenger species  $(\text{MgO}_2)(\text{H}_2\text{O})(\text{O}_2)^+$  and  $(\text{MgO}_2)(\text{O}_2)\text{Ar}^+$  simultaneously with the other cationic MgO clusters, as described before\*. The spectra obtained are shown in Figures 4.24 and 4.25 for the  $200\text{--}1700\text{ cm}^{-1}$  range.

An assignment of the  $(\text{MgO}_2)(\text{H}_2\text{O})(\text{O}_2)^+$  species, with a mass of 108, is only possible by its IR spectrum, as there is a mass coincidence with  $(\text{Mg}_2\text{O})\text{Ar}^+$ . The spectrum obtained for the species at this mass shows three sharp peaks. The two at highest frequencies ( $1648$  and  $1544\text{ cm}^{-1}$ ) can unambiguously be assigned to the water bending mode and the stretch vibration of unperturbed  $\text{O}_2$ , respectively. Therefore, a composition of  $(\text{Mg}_2\text{O})\text{Ar}^+$  can be ruled out. The amount of depletion observed for the water bending mode  $\delta(\text{H}_2\text{O})$  was 50 %, which means that the water complex forms a major fraction of the clusters contributing to this mass peak.

\*  $^{26}\text{Mg}$  has been used in this experiment.

The depletion in this range may not be saturated (5 dB attenuation was used in this range). While the O-O stretch for the physisorbed O<sub>2</sub> is almost unshifted, the interaction with the water seems to be stronger, as  $\delta(\text{H}_2\text{O})$  is blue shifted by  $\approx 50 \text{ cm}^{-1}$  with respect to free water ( $1595 \text{ cm}^{-1}$ ).

DFT calculations on the B3-LYP level using the same def2-TZVP basis set as before (see section 4.1.1.2) have been used in order to calculate the geometry of the complex. The predicted IR spectrum for such a species is shown along with the experiment. Displacements for the normal modes corresponding to the most intense absorptions are also shown. The superoxo unit and the water ligand are both found within the same plane. The experimentally observed vibrations can be assigned to the water bending mode predicted at  $1680 \text{ cm}^{-1}$  ( $\nu_1$ ), a stretch between the  $\text{MgO}_2^+$  and  $\text{H}_2\text{O}$  ( $\nu_2$ ), and the two frustrated rotations of the water molecule ( $\nu_3$  and  $\nu_4$ ).

The charge distribution of  $(\text{MgO}_2)(\text{H}_2\text{O})^+$  has been calculated using a natural population analysis, which indicates a charge close to a formal +2 oxidation state for the Mg atom (1.83) and a single negative charge on the superoxo-type dioxygen species, distributed almost equally between the two oxygen atoms (both -0.43). The polar character of the  $\text{MgO}_2^+$  molecule explains the strong blueshift of the water bending mode. In a DFT model calculation, water bound to  $\text{Mg}^+$  and  $\text{Mg}^{2+}$  has been considered and the frequencies of the water bending modes have been calculated. For  $\text{Mg}^+$  the calculation predicts a shift to  $1650 \text{ cm}^{-1}$  (compared to the calculated position for free  $\text{H}_2\text{O}$  of  $1616 \text{ cm}^{-1}$ ) while for  $\text{Mg}^{2+}$  it shifts to  $1681 \text{ cm}^{-1}$ . The value obtained for  $\text{MgO}_2^+$ , at  $1672 \text{ cm}^{-1}$ , is closer to the one of  $\text{Mg}^{2+}$ . This suggests that the  $\text{H}_2\text{O}$  coordination in both species is similar and is probably dominated by the electrostatic interaction. This blueshift of the water bending mode by an increased electrostatic potential has also been observed previously. The position of the water bending mode has been determined for vanadium cluster cations [270] complexed with 1–3 water molecules. The strongest blueshift, of almost  $30 \text{ cm}^{-1}$ , has been observed for the smallest cluster considered,  $\text{V}_3^+$ , which should also have the strongest field. The blueshift drops then for the larger clusters reaching the value for free water at a cluster size of 9 atoms. The calculated binding energy between the  $\text{MgO}_2^+$  cluster and water, calculated by  $E_{\text{bind}} = -E_{\text{ZPVE}}((\text{MgO}_2)(\text{H}_2\text{O})^+) + E_{\text{ZPVE}}(\text{MgO}_2^+) + E_{\text{ZPVE}}(\text{H}_2\text{O})$ , is 2.37 eV. This is stronger than the binding in  $\text{Mg}^+ \cdot \text{H}_2\text{O}$ , which has been determined before to be 1.40 eV [271].

The second species investigated is  $(\text{MgO}_2^+)(\text{O}_2)\text{Ar}^+$ . It contains, besides the superoxo species, a physisorbed dioxygen that can be unambiguously identified by the O-O stretch vibration at  $1543 \text{ cm}^{-1}$ . The superoxo stretch on the other hand is not directly observed in the vibrational spectrum. Around  $1200 \text{ cm}^{-1}$  no absorp-

tions are seen. The calculations for this system are more demanding, as the superoxo and the physisorbed dioxygen are both open-shell systems, that carry a spin. These can either be oriented parallel or antiparallel leading to a quartet or doublet state, respectively. Both possible configurations have been calculated using DFT and they are isoenergetic. However, the IR spectra predicted using DFT are rather different. Although the band positions are almost the same the intensities are significantly different. Unfortunately standard DFT may not be capable in properly handling such systems as open-shell systems with electrons having spins in different spatial orbitals cannot be described with single-determinant wave functions [272]. This failure is revealed for the doublet state by a high spin contamination ( $s(s+1)=1.77$ ). The outcome of the frequency calculation may therefore not be completely correct. But the agreement between experimental and predicted band intensity pattern indicate that the doublet state is the one observed in experiment. Only tiny structural differences are seen between both states. The quartet is almost planar (the perfectly planar one is 0.80 eV higher in energy) in contrast to the doublet, for which the physisorbed oxygen rotates out of the molecular plane. Surprisingly, no further fragmentation of the  $(\text{MgO}_2)(\text{O}_2)^+$  cluster is observed experimentally. This is an indication for it being a very stable complex, despite the fact that one of the dioxygen units is only physisorbed. The binding energy calculated by DFT for the physisorbed  $\text{O}_2$  is 1.67 eV, which seems to be surprisingly high. However, assuming that the interaction is based on a charged induced dipole between the Mg ion ( $q=1.87 e$ , taken from natural population analysis) and the polarizable  $\text{O}_2$  ( $\alpha=1.5689 \times 10^{-24} \text{ cm}^3$ ) the binding energy can be calculated by  $E_{\text{pot}} = -(\alpha q^2) / ((4\pi\epsilon_0)^2 R^4)$ , using the distance between the Mg and the center of mass of the dioxygen from the DFT calculation ( $R=2.6 \text{ \AA}$ ). The calculated value of 1.6 eV, is almost identical to the binding energy obtained by DFT.

For both species the O-Mg-O angle in the metal ion superoxide complex (with  $\text{H}_2\text{O}$ :  $41.5^\circ$ ; doublet with  $\text{O}_2$ :  $42.1^\circ$ ) is very close to the one of free  $\text{MgO}_2^+$  ( $42.5^\circ$ ) [267]. The effect of the ligands on the structure of the molecule itself is negligible.

The  $(\text{MgO}_2)(\text{H}_2\text{O})^+$  complex is the only  $\text{H}_2\text{O}$  containing complex of a MgO cluster for which the water bending mode was observed. In other experiments where water has been added intentionally under single collision conditions by crossing the free MgO cluster beam with another molecular beam that contains water (see chapter 2.4) complexes with single water molecules have been prepared. For all water complexes of  $(\text{MgO})_n^+$  and  $\text{Mg}_n\text{O}_{n+1}^+$  clusters prepared by this method the water bending mode was not observed. Complexes that contain more water can be prepared by using the reaction valve attached to the cooling channel. Unfortunately, under these conditions a very large number of water ligands stick to the clusters, leading to very complex mass spectra, which make an assignment for

larger systems very challenging. For one of the smallest systems  $(\text{MgO})_2^+$  this was still possible, and for the complex with 2–4 water ligands the water bending mode reappears (not shown). This may be taken as evidence for the dissociation of the first water molecule(s). However, further experiments are needed in order to determine the cause of this effect, which will require the controlled preparation of complexes with multiple water ligands, for example by increasing the vapor pressure of water by heating to increase the water density achievable for the single collision experiment. Additional insights into the complexes formed may be given by investigating the OH stretch region, which also allows hydroxy species to be probed. This may allow the study of the dissociation of water as well as solvation effects for MgO clusters.

#### 4.3.2. Hydroxylation of $\text{Mg}_n\text{O}_m^+$

Several experimental and theoretical studies have shown that water heterolytically dissociates on MgO surfaces. This may lead to surface modifications and thereby could poison a catalyst based on MgO. On perfect (100) surfaces individual water molecules are stable, however, upon water multilayer formation on the surface their dissociation may occur [273] and would explain the origin of the brucite mineral  $(\text{Mg}(\text{OH})_2)$ . Defect sites such as kinks, steps, edges, and color centers are, on the other hand, capable of dissociating individual water molecules [274–277]. In the process, two species are formed,  $\text{OH}^-$  and  $\text{H}^+$ . The first is considered to be found in a dangling position. The latter interacts with a surface oxygen atom, forming a hydroxy group via protonation. There is also evidence from theory, in agreement with earlier experiments, suggesting that MgO surfaces can heterolytically dissociate  $\text{H}_2$ , again leading to the formation of hydroxyl species [278–280]. Although cluster models are often used in the theoretical treatment of these surface reaction problems, studies on free clusters do not exist. In the following, IR spectroscopic information for cationic hydroxylated MgO clusters are shown and the structural changes upon single hydrogen attachment are discussed.

Besides the water complex for the  $\text{MgO}_2^+$  species, water contamination in the experiment also leads to other hydrogen containing species. Presumably, water is dissociated in a plasma reaction initiated by the laser ablation, which allows the formation of species that contain single hydrogen atoms. These may lead to hydroxy species, similar to the ones observed on surfaces following (heterolytic) water dissociation.

Species containing hydrogen are easily recognized in the experiment, as all other components have even masses. IR spectra for such species are again obtained by messenger tagging with  $\text{O}_2$ . The formation of messenger complexes in sufficient intensities was possible for  $(\text{MgO})_n\text{H}^+$  clusters with  $n=2-6$  and  $\text{Mg}_m\text{O}_{m+1}\text{H}^+$  clus-

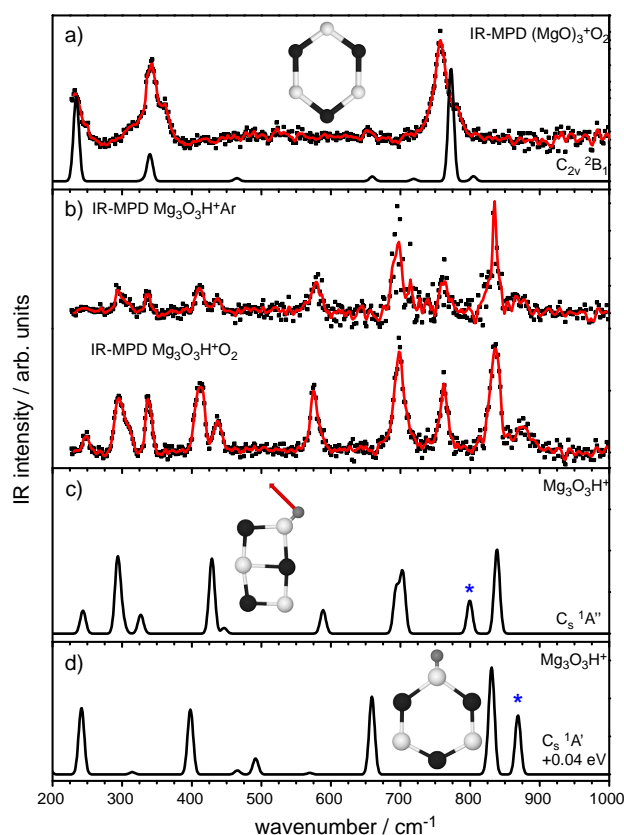


Figure 4.26.: IR-MPD spectrum of  $\text{Mg}_3\text{O}_3^+$  (a) in comparison to the one of  $\text{Mg}_3\text{O}_3\text{H}^+$  obtained for the Ar and  $\text{O}_2$  messenger complexes (b). (c) and (d) show IR spectra for two predicted isomers. The red arrow in (c) shows the type of vibration, a bending mode of the OH, that is marked with an asterisk in the calculated spectrum.

ters with  $m=4,5$ . For a single cluster size,  $\text{Mg}_3\text{O}_3\text{H}^+$ , the formation of messenger complexes with  $\text{O}_2$  and Ar was possible, and, as before, their IR spectra are identical (Fig. 4.26(b)).

The spectra for the hydrogen containing species can be compared to those for the bare clusters, and an example is shown for the cluster containing 3 MgO units in Fig. 4.26. In general, the number of IR active modes seem to be much larger for the hydrogen containing clusters, indicating a lowered symmetry. For  $(\text{MgO})_3^+$  a slightly distorted hexagonal ring was identified as the global minimum. For the  $(\text{MgO})_3\text{H}^+$  cluster such an isomer is slightly higher in energy\* (see Fig. 4.26 (d)) and an isomer with a rectangular shape with the hydrogen atom bound to

\* Parts of these calculations have been performed by K. Kwapien and Dr. M. Sierka from the Quantum Chemistry group of the Humboldt University Berlin headed by Prof. J. Sauer.

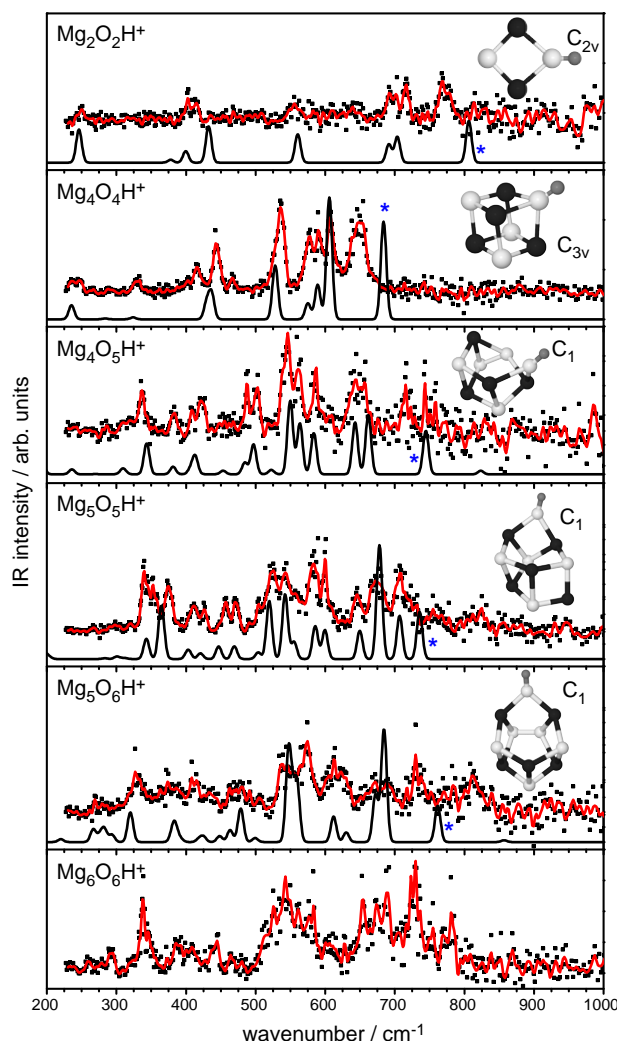


Figure 4.27.: IR-MPD spectra for  $\text{Mg}_n\text{O}_m\text{H}^+$  cluster in comparison with results from DFT calculations. Asterisks mark the bending mode of the OH.

one of the corner oxygen atoms fits the experiment better (Fig. 4.26(c)). Only the OH bending mode (marked by an asterisk) is predicted too high in frequency ( $763\text{ cm}^{-1}$  experimentally vs.  $800\text{ cm}^{-1}$  theoretically). For all other cluster sizes considered, the frequency of this mode is also calculated to be too high compared to the experiment, presumably due to anharmonicities.

The IR-MPD spectra for the other cluster sizes in comparison to the spectra from DFT calculations (except for  $n=6$ ) are shown in Figure 4.27. For most sizes, a decent agreement between prediction and experiment is found and a single isomer is always sufficient to explain the experimental spectrum. The structures identi-

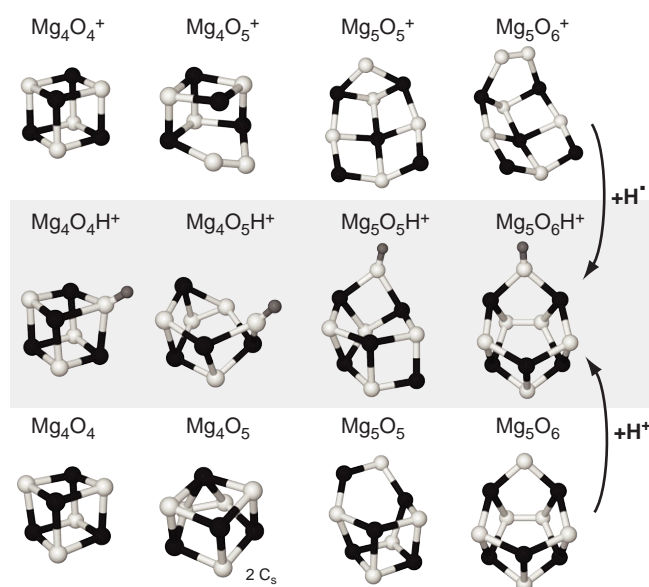


Figure 4.28.: Influence of the composition on the structure for clusters containing 4 and 5 Mg atoms, and possible formation mechanism via hydrogen attachment from a homolytic ( $H^\bullet$ ) or heterolytic ( $H^+$ ) dissociation of water, to the cationic or neutral bare cluster, respectively.

fied are very similar to the ones for the bare cluster for  $Mg_2O_2H^+$ ,  $Mg_4O_4H^+$  and  $Mg_4O_5H^+$ . For the largest size, however, larger deformations are observed. In contrast to the bulk, the hydroxy group is always incorporated into the cluster and no dangling OH species are found. In  $Mg_nO_{n+1}^+$  the hydrogen and the dioxygen species are spatially separated. As an additional electron is provided by the hydrogen, the type of the dioxygen species changes and instead of a superoxo, a peroxy species is found.

To illustrate the effect of different compositions, the structures of clusters containing 4 and 5 Mg atoms are compared in Figure 4.28. This allows also to discuss the two ways how conceptionally the OH species can be formed. Either  $H^+$  (from a heterolytic dissociation of  $H_2O$ :  $H_2O \longrightarrow OH^- + H^+$ ) is added to the neutral cluster, or the  $H^\bullet$  radical (from a homolytic dissociation:  $H_2O \longrightarrow OH^\bullet + H^\bullet$ ) is added to the cationic cluster.

Both pictures would explain the structure observed for  $(MgO)_4H^+$ , as the cube structure observed for both charge states is hardly perturbed. Adding another oxygen atom to the two clusters without the hydrogen, a five-membered ring is formed, but one side still keeps its rectangular shape. Upon hydrogen attachment this also breaks apart. However, the structural change for the neutral seems to be

smaller (three different isomers have been identified in the experiment for  $\text{Mg}_4\text{O}_5$ , only the second lowest energy one is shown here). For the  $\text{MgO}$  clusters containing five Mg atoms, the structural changes cannot be explained by radical attachment to the bare cationic cluster. The differences to the neutral structures are much smaller. The structures observed in our experiment can be better rationalized by a heterolytic dissociation process, similar to the one observed on surfaces.

#### 4.3.3. CO on cationic $\text{MgO}$ clusters

The interaction between carbon monoxide and bulk  $\text{MgO}$ , in the form of perfect crystals [281], thin films [282, 283] and powders [284], has been studied for a long time, as it is a sensitive probe of the surface electronic structure. On  $\text{MgO}$  surfaces the CO binds via the carbon atom to the magnesium atom by an almost purely electrostatic interaction [285]. This is different to metal surfaces, where the two major competing interactions are  $\sigma$  donation from the CO to the metal and  $\pi$  back-donation from the metal d-orbitals to the CO.

In an electric field CO can be polarized. When a positive charge approaches the C site it attracts electron density from the oxygen. This makes the bond more covalent and thereby shortens the bond length leading to an increase of the CO stretching frequency  $\nu(\text{CO})$ . The position of  $\nu(\text{CO})$  can therefore be used as a probe of the formal oxidation state of the Mg atoms out of the perfect ionic surface, and for the coordination of the magnesium atoms on defect sites [286, 287].

In the following, the position of the CO stretch frequency is measured as a function of composition and cluster size for  $\text{Mg}_n\text{O}_{n+1}^+$  clusters in the gas phase. This provides a test of the assumption of a pure electrostatic interaction with CO for clusters. For metal cluster such an approach was used to study cluster size dependent charge transfer processes and binding geometries, but also molecular versus dissociative chemisorption [288–292].

To form complexes of cationic  $\text{MgO}$  clusters with CO, cationic  $\text{MgO}$  clusters are prepared, in similar way to the earlier experiments, but without adding argon to the carrier gas. In a second step, the clusters are complexed with CO by introducing  $^{13}\text{CO}$  into the reaction valve attached to the cooling channel. Complexes of the type  $(^{26}\text{Mg}_n\text{O}_{n+1})(^{13}\text{CO})^+$  with  $n=6\text{--}20$  are made.  $^{13}\text{CO}$  has been used in the experiment as odd numbered masses are easier to distinguish in the mass spectra and, more importantly, because the C-O stretch frequency shifts to lower frequencies for the heavier carbon isotope. A large blueshift is expected for such cationic systems that could shift the band position for  $^{12}\text{CO}$  out of the range of the fundamental of FELIX (lower limit  $\approx 4.5 \mu\text{m} = 2222 \text{ cm}^{-1}$ ). Higher frequencies can be obtained using the third harmonic, but only at the expense of the laser fluence. The drawback of using this isotope is that complexes composed out of two CO



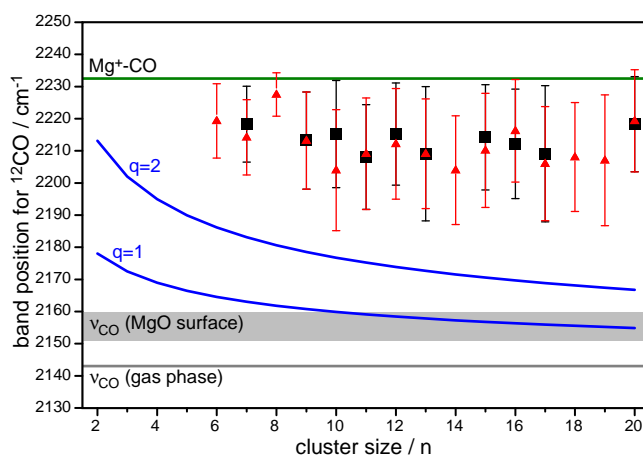


Figure 4.29.:  $\nu(\text{CO})$  for CO absorbed on  $\text{Mg}_n\text{O}_m^+$  clusters (black squares:  $(\text{MgO})_n^+$ ; red triangles:  $\text{Mg}_n\text{O}_{n+1}^+$ ). The peak positions are determined by least-squares fit to a Gaussian peak shape. The error bars represent the standard deviation ( $\sigma$ ) of the fit. An additional error, a (constant) shift of  $\pm 20 \text{ cm}^{-1}$  needs to be added due to the wavelength calibration. The measurements, which have been performed on  $^{13}\text{CO}$ , have been scaled to  $^{12}\text{CO}$ . Grey lines and shadings show  $\nu(\text{CO})$  for gas-phase CO and CO adsorbed on MgO surfaces. Blue lines correspond to predictions for an electrostatic model. In green, prediction for  $\nu(\text{CO})$  from DFT calculation for  $\text{Mg}^+$  interacting with CO.

molecules and a  $(\text{MgO})_n^+$  cluster have the same mass as the oxygen rich cluster of the type  $\text{Mg}_{n+1}\text{O}_{n+2}^+$ .

The CO itself acts as the messenger for the absorption, and spectra are obtained by observing the depletion of the CO complex. Spectra have been measured in the range  $1950\text{--}2250 \text{ cm}^{-1}$ , with a FELIX power of  $16\text{--}32 \text{ mJ/pulse}$ . The maximum depletion observed was only 40 %. The observed  $\nu(\text{CO})$  band positions as function of the cluster size are plotted in Figure 4.29. For an easier comparison with CO band positions observed on surfaces, the band positions for  $^{13}\text{CO}$  has been rescaled to  $^{12}\text{CO}$  by  $\nu(^{12}\text{CO}) = \nu(^{13}\text{CO}) \cdot \sqrt{\mu(^{13}\text{CO})/\mu(^{12}\text{CO})} = 1.02273\nu(^{13}\text{CO})$ .

The experimentally determined band position for the CO stretch frequency shows no strong dependence on the size or composition of the cluster. For all, a large blueshift (approx.  $70 \text{ cm}^{-1}$ ) with respect to the free value of  $2143 \text{ cm}^{-1}$  [293] is observed. This is greater than that observed on perfect surfaces ( $2151 \text{ cm}^{-1}$  from Ref. [281]), smoke particles ( $2156 \text{ cm}^{-1}$  from Ref. [284]), or thin films ( $2160 \text{ cm}^{-1}$  from Ref. [283]) shown in grey in Fig. 4.29.

The insensitivity of  $\nu(\text{CO})$  on cluster size and composition is an indication for a similar CO bonding mechanism on all complexes. This behavior poses the ques-

tion how much the electrostatic field could shift the mode in the cluster size range considered here. For the metal cluster CO interaction a very simple model has been developed which separately treats electrostatic interaction and  $\pi$  back-donation [288]. Only the first needs to be considered here. The model assumes that the CO experiences the electrostatic field  $E \propto q/R^2$  from the charged cluster which is approximated by a conducting sphere with a charge  $+q$ . The distance  $R$  between the center of sphere and the center of the CO bond is given by  $R = r_{\text{CL}} + r_{\text{C}} + r_{\text{C-O}}/2$  (covalence radius of carbon:  $r_{\text{C}} \approx 1.3$  bohr, CO bond distance:  $r_{\text{C-O}} = 2.18$  bohr). The radius of the cluster or the conducting sphere  $r_{\text{CL}}$ , is approximated by the Wigner-Seitz radius  $r_{\text{ws}}$  (for MgO:  $\approx 3.11$  bohr) and the number of atoms  $n$  in the cluster,  $r_{\text{CL}} \approx r_{\text{ws}} n^{1/3}$ . The band position of the CO stretch frequency is calculated to be

$$\nu_{\text{CO}} = \nu_{\text{free}} + \Delta\nu = 2143 \text{ cm}^{-1} + 1395 \text{ cm}^{-1} \cdot E/\text{a.u.} \quad (4.1)$$

The band positions calculated as a function of cluster size are plotted as blue lines in Fig. 4.29 for two possible charges,  $q=1$  and 2. As can be seen, the model significantly underestimates the shift. This is presumably mainly due to the assumption of a conducting sphere, which is a very poor assumption for an ionically bound cluster. The charge will be more localized in a MgO cluster compared to a metal like system. The Mg and O atoms in the cluster have almost their full formal charges, the local ‘environment’ that the CO experiences has therefore a much higher electric field, which varies less with cluster size. The size of the shift is limited by charge redistribution and/or shielding by the  $\text{O}^{2-}$  giving a net charge of  $+1$ . Despite this disagreement, the simple model shows that in the considered cluster size range a small but observable size-dependent shift should be present.

In a previous investigation, the effects of the presence of a point charge or a proton on the CO stretch frequency were compared [294]. For sufficiently large distances ( $>1.5$  Å), both models give the same shift. Only for smaller distances, were deviations observed, mainly because of coupling of the C-H and C-O vibrations. The C-O bond strength is, however, completely different, because of covalent contributions. As for the  $\text{MgO}_2^+$ -water complex, the interaction between  $\text{Mg}^+$  and  $\text{Mg}^{2+}$  with CO was calculated using DFT. For the free CO molecule the B3-LYP functional and the def2-TZVP basis set predicts  $\nu_{\text{CO}} = 2211 \text{ cm}^{-1}$ . The comparison with the experimental gas-phase value gives a scaling factor of 0.968. Using this scaling, the predicted frequencies for  $\text{Mg}^+$  and  $\text{Mg}^{2+}$  CO complexes are 2232 and  $2296 \text{ cm}^{-1}$ , respectively. The first value is only slightly higher than that measured for CO on the clusters, the difference may be due to an additional shielding of the charge by nearby  $\text{O}^{2-}$  species. A complex of the type Mg-OC can be ruled out by this model, as a redshift of the CO stretch frequency with respect to the gas-phase value is predicted for such species. More detailed calculations, treating the

cluster-CO interaction properly, should be able to explain the behavior of  $\nu_{\text{CO}}$  for MgO clusters.

#### 4.3.4. Methane on MgO

Chemistry based on methane is a topic of ongoing interest [191, 192], as methane is stored in large quantities on earth in the form of natural gas, mine gas in coal deposits, or in the deep sea as methane hydrate. Methane is also formed in many geological and biological processes, if methane could be used in chemical processes it would help to reduce the human dependence on oil. The (direct) conversion of methane into methanol, or longer alkanes would therefore be desirable. This, however, is difficult due to the intrinsic properties of methane [192], *i.e.* low electron affinity, high ionization energy, no dipole moment and low polarizability. The first reaction step for such a conversion would require breaking a non-activated C-H bond, but this demands high energies. An industrial relevant catalyst for this process has not yet been found.

Most candidates for a catalyst are based on transition metals [295], and only in 2006 was the first main group metal oxide species, the  $\text{MgO}^+$  cation [296], found which is capable of activating methane and other small alkanes [297]. These findings initiated theoretical studies on larger clusters [248] investigating their ability for C-H bond activation. These showed that larger clusters are also capable of activating longer alkanes, *e.g.*  $(\text{MgO})_2^+$  abstracts hydrogen from propane, but not from methane. A systematic experimental study looking for methane activation of larger cationic clusters of different size and composition is missing.

Here, we have studied the vibrational spectra of the complexes between methane and  $(\text{MgO})_n^+$  and  $\text{Mg}_m\text{O}_{m+1}^+$  clusters with  $n=4-12$  and  $m=1-15$  in the range of the infrared active  $t_2$  modes of free methane ( $\nu_4$ , at  $1306\text{ cm}^{-1}$  for  $^{12}\text{CH}_4$ ). For experimental reasons, to avoid mass coincidences between  $^{12}\text{CH}_4$  and O, the study is performed using  $^{13}\text{CH}_4$ . Due to the small effect of substituting  $^{12}\text{C}$  by  $^{13}\text{C}$  on the reduced masses, the vibrational frequencies in  $^{13}\text{CH}_4$  shift only slightly compared to  $^{12}\text{CH}_4$  ( $-8\text{ cm}^{-1}$  for  $\nu_4$ ) [298].

For all cluster sizes depletion spectra are measured on the methane complexes in the  $900-1450\text{ cm}^{-1}$  range. An example for the  $\text{Mg}_6\text{O}_7^+$  cluster is shown in Figure 4.30(a). A similar band splitting for all cluster sizes is measured, suggesting a similar binding motif for all cluster sizes. A signal increase for the bare clusters is observed simultaneously with the depletion of the methane complex. The methane seems to be only physisorbed under our experimental conditions. The species observed in the mass spectra give also no hint for any CH activation, as the formation of  $\text{Mg}_n\text{O}_m\text{H}^+$  via hydrogen abstraction from  $\text{CH}_4$  is not observed.

The interaction between the clusters and methane appears to be purely electro-

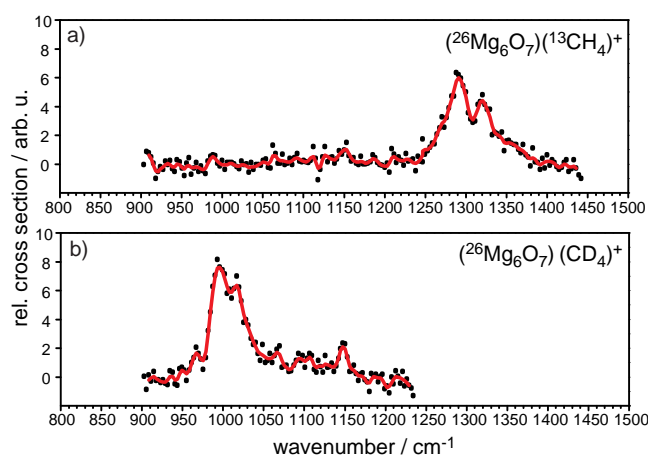


Figure 4.30.: Measured IR-MPD spectra of methane  $\text{Mg}_6\text{O}_7^+$  complexes for  $^{13}\text{CH}_4$  (upper panel) and  $\text{CD}_4$  (lower panel) in the range of the deformation mode  $\nu_4$  of the methane. The difference in band position is due to the different reduced masses. The splitting, however, is identical for both. The additional mode at  $1150\text{ cm}^{-1}$  is due the superoxo mode of  $\text{Mg}_6\text{O}_7^+$ , see also section 4.2.

static. The nature of the bands can be confirmed by experiments using  $\text{CD}_4$ . For the heavier hydrogen isotope the deformation mode should shift to the red (gas phase  $\text{CD}_4$ :  $1029\text{ cm}^{-1}$  [299]). Despite this shift, the pattern of the IR spectrum should remain identical. For all cluster sizes under investigation, see example in Figure 4.30(b), this shift is observed\*. If other species are present, the pattern is expected to change more dramatically.

Even if  $\text{CH}_4$  binds only via electrostatic interactions, the lowering of the band degeneracy could, in principle, be used to determine the binding geometry. Unfortunately, the splitting observed here is not sufficiently resolved, to allow this. Nevertheless, the experimental results confirm the previous theoretical predictions for  $(\text{MgO})_{4-7}^+$  clusters [248], as larger MgO clusters seem unable to activate methane. In addition, it has been shown that oxygen rich MgO cluster of the type  $\text{Mg}_n\text{O}_{n+1}^+$  are also unreactive towards methane.

\* The additional band in the spectrum for  $\text{CD}_4$  (and much weaker in the  $^{13}\text{CH}_4$  spectrum) is due to the superoxo species in the  $\text{Mg}_6\text{O}_7^+$  complex. In the previous experiment, using Ar/ $\text{O}_2$  messenger tagging to study the structure of the bare cluster, this mode was not observed for  $\text{Mg}_6\text{O}_7^+$ . The larger IR fluence for the current experiment allows its detection.

## 4.4. Summary and outlook

MgO clusters have been studied by vibrational spectroscopy and comparison to predictions from quantum chemical calculations. For cationic and neutral MgO clusters with equal numbers of oxygen and magnesium atoms structures which are quite different to the bulk phase have been found. These structures are used as the starting geometry to investigate the influence of dioxy species, as found in oxygen rich MgO clusters. Depending on the charge state of the cluster different activated oxygen species can be formed. Cationic  $\text{Mg}_n\text{O}_{n+1}$  clusters contain a superoxo species, in contrast to neutral clusters which incorporate a peroxo species, while for anions it dissociates to  $\text{O}^-$  and  $\text{O}^{2-}$ . All three activated oxygen species may be important in the oxidative coupling of methane. As a first step in investigating the reactivity of the systems, the interaction of the cationic clusters with methane has been probed. For 1:1 stoichiometric and oxygen rich clusters only physisorption of the methane has been found, with no hints for any methane activation. This might be an indication that, at least in the gas phase, the superoxo species found in larger MgO clusters is not sufficiently reactive to activate methane. Further reactivity studies should focus on the peroxo or oxygen radical species of the neutrals and anions, respectively. Another possibility to tune the active center might be to use cationic hydrogen containing species,  $\text{Mg}_n\text{O}_{n+1}\text{H}^+$ . For these, the addition of the hydrogen changes the activated dioxygen species from superoxo to peroxo. The experiments also showed that the observed structures can be rationalized via heterolytic dissociation of water or hydrogen. Intact water has only been found on a single cationic cluster size,  $\text{MgO}_2^+$ , for all other sizes and stoichiometries of cations studied there are indications that the first water molecule dissociates. Future studies should also focus on metal rich MgO clusters, which have already been investigated by vibrational spectroscopy (not shown here), but where agreement to quantum chemical calculations is still missing. Such species would model oxygen vacancy sites,  $\text{V}_\text{O}$ , of surfaces (see Fig. 4.1). Another possibility to tune the reactivity is by doping with other metals and such experiments should be possible using the newly set up dual target cluster source mentioned in Chapter 2.



## 5. Action spectroscopy of anions – Metal and metal-carbon clusters\*

Several kinds of experimental methods have been developed to study the geometric and electronic structure of neutral and (singly) charged gas-phase nanoparticles. The insights obtained in these studies may lead to a better understanding of the size and charge dependence of the physical and chemical properties of these clusters and their evolution to the bulk. Here, we will focus on singly negatively charged transition metal (TM) clusters.

Previously, ion mobility measurements, electron diffraction on trapped ions, or photoelectron spectroscopy (PES) in combination with quantum-chemical calculations have been used to determine the structure of anionic TM clusters. In particular, gold cluster anions have been studied intensively [20, 23, 38, 39, 300, 301]. So far, most other metal cluster anions have been studied mainly by PES [40, 41], another variant of action spectroscopy. As anion PES probes transitions between *electronic* states of anionic and neutral clusters a detailed theoretical description of both charge states is, in principle, required. This can hamper a definite structural assignment. Direct information about the geometries of the species involved in these studies are therefore highly desirable. Vibrationally resolved PES can provide additional insights into the *geometric* structure, but there are only very few examples for TM clusters larger than the trimers, *i.e.*,  $\text{Au}_{4,6}^-$  [302] and  $\text{Nb}_8^-$  [303]. Infrared absorption spectroscopy provides a more direct approach to the vibrational spectra. By measuring the position and IR absorption strength of the cluster vibrations, the bonds between the atoms in the cluster are probed directly and theoretically tractable information on the structure of the cluster is thus obtained.

For the investigation of strongly bound neutral clusters in the gas phase several methods to obtain vibrational spectra have been developed, including the messenger tagging technique, tunable IR-UV two-color ionization, or IR resonant enhanced multiple photon ionization (IR-REMPI) [51, 52].

IR spectroscopic techniques using messenger tagging similar to those used for

---

\* Parts of this chapter have been published in: *Structure Determination of Anionic Metal Clusters via Infrared Resonance Enhanced Multiple Photon Electron Detachment Spectroscopy*, M. Haertelt, V.J.F. Lapoutre, J.M. Bakker, B. Redlich, D.J. Harding, A. Fielicke, and G. Meijer, *J. Phys. Chem. Lett.* **2011**, 2, 1720.

neutral clusters have also provided a wealth of structural information for cationic clusters. For anionic metal clusters on the other hand, no IR spectra have been recorded so far, in part because tagging of anionic clusters with rare gas atoms is considerably more difficult. Moreover, the fundamental vibrations of bare metal clusters often have low IR intensities and are found in the far-IR region, typically below  $500\text{ cm}^{-1}$ , where the photon energy is only a few tens of meV. The absorption of many IR photons is required to induce fragmentation or ionization (electron detachment) of the anionic clusters, which can only be achieved using high intensity IR light sources.

To date, only free electron lasers combine a wide tuning range in the far-IR with a sufficiently high intensity. The temporal structure of the radiation emitted by IR-FELs based on normal conducting linear accelerators enables repeated cycling of the molecules or clusters through an absorption and subsequent internal energy redistribution process, avoiding the ‘anharmonicity bottleneck’, thereby resonantly heating them on a  $\mu\text{s}$  time-scale [304]. For neutral fullerenes, for example, the absorption of several hundred IR photons by a single cluster has been observed in IR-REMPI experiments [51].

While IR-REMPI spectroscopy is limited to clusters of refractory materials for which ionization is favored over fragmentation, this is different for many anionic metal clusters, as their electron affinity is clearly lower than the bond dissociation energy. Therefore, for anionic clusters (multiple photon) electron detachment offers the possibility to measure their vibrational spectra. While such a technique has been recently applied to obtain mid-IR spectra of  $\text{SF}_5^-$  [305],  $\text{C}_{60}^-$  [306], and  $\text{C}_{76}^{2-}$  [307], these experiments relied on mass selected and trapped ions for which the electron detachment can be sensitively probed by electron scavengers or, in case of  $\text{C}_{76}^{2-}$ , the appearance of the singly charged anion. By storing all of the ions in an ion trap, the signal intensity could be improved by extending the interaction time with the IR-FEL radiation over several macro-pulses. The much lower photon energy in the vibrational fingerprint region of TM clusters anions prevented the application of such a technique to these systems.

Here we report the extension of multiple photon electron detachment spectroscopy to the far-IR and to TM metal clusters anions and their adducts. Their spectra have been recorded by monitoring the depletion of the anion population directly in a molecular beam induced by IR Resonance Enhanced Multiple Photon Electron Detachment (IR-REMPED). This process has been observed in an experiment where the cluster beam crosses the IR laser beam inside the optical cavity of a Free Electron Laser. As the clusters are passing freely through the interaction region with the far-IR radiation and as their IR absorption cross-sections are at least an order of magnitude lower than for the systems studied previously, the



demands on the far-IR fluence (in J/cm<sup>2</sup>, integrated over the interaction time) are significantly increased.

The demands on IR fluence can be fulfilled by the Free Electron Laser for IntraCavity Experiments, FELICE, which is designed for such experiments and provides – inside the cavity – approximately a hundred times more energy in a single micropulse compared to the Free Electron Laser for Infrared eXperiments, FELIX, which is part of the same facility at the FOM Institute Rijnhuizen in the Netherlands.

Initially, experiments have been performed on the metal carbide clusters as these species can be produced under similar conditions as the pure metal clusters but in higher intensities, having absorptions at higher frequencies. This was essential for optimizing the experimental procedures.

To prove the feasibility of this spectroscopic method tantalum carbide clusters have been investigated across most of the possible tuning range of this new FEL. In order to understand the excitation mechanism and to show the prospects offered by this new technique, anion photoelectron spectroscopy (PES) has also been performed on the same systems. The knowledge of the geometric structure determined by IR-REMPED assists in the interpretation of the observed PES spectra.

In a second step, we aimed to measure spectra of bare metal clusters. Niobium clusters are, besides gold, among the best studied systems [308–313]. Niobium clusters with a single or two carbon atoms have been used to further optimize the setup and to improve the sensitivity of the detection. Such systems already have many of the characteristics of the bare metal cluster, *i.e.* low IR absorption cross sections, but have absorptions over a wider wavelength range. The measured spectra nicely demonstrate the capabilities of the technique, and IR modes have been observed down to the low photon energy tuning limit. With such an optimized setup, spectroscopy on the bare niobium cluster became possible. These results are discussed towards the end of the chapter.

## 5.1. The Free Electron Laser for Intra-Cavity Experiments and the molecular beam setup

The required fluence for the IR-REMPED experiments is obtained at a new beam-line which is part of the Free Electron Laser for Infrared eXperiments (FELIX) user facility at the FOM Institute Rijnhuizen, where the experiments were performed. The Free Electron Laser for IntraCavity Experiments, FELICE, has an extended optical cavity that can host user experiments, which allows the full pulse energy available inside the optical cavity to be used. The IR pulse energies that can be provided with such a configuration are up to a factor of 100 larger compared to

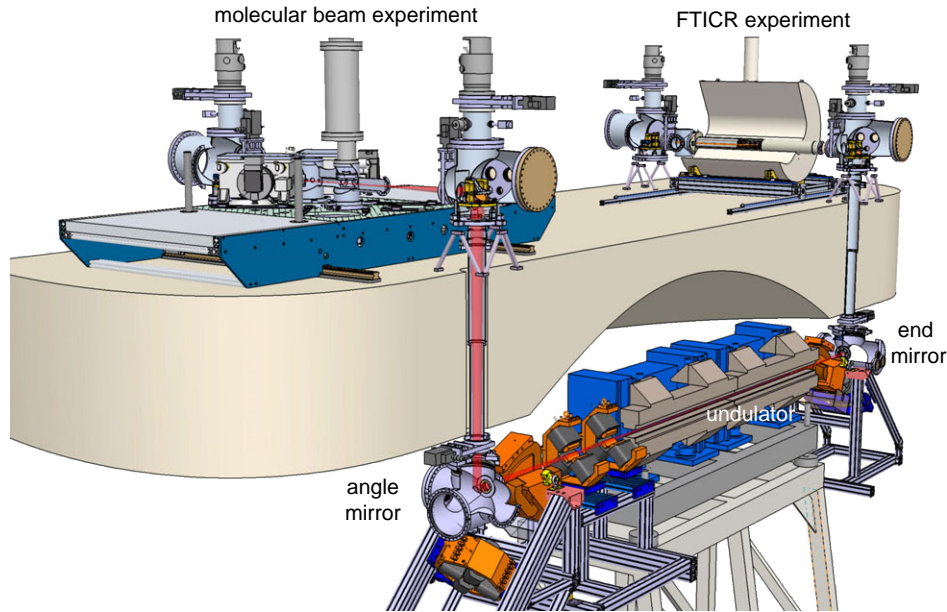


Figure 5.1.: Artist's view of the Free Electron Laser for IntraCavity Experiments, FELICE. The setup in the front is the molecular beam machine, used for the experiments.

what is available from the conventional FELIX FELs.

To accommodate two experimental stations and to allow (restricted) permanent access during operation the cavity has been designed as two 4-mirror resonators each with a total length of 9 m. This allows parts of the optical beamlines and the experiments to be placed in a separate experimental hall above the FEL vault, see Figure 5.1. By using interchangeable mirrors in the FEL vault it is possible to flip between the two possible cavity configurations. In Fig. 5.1 the mirror configuration used for the molecular beam setup is shown. The setup is installed in the 2-m section between the last two mirrors of the cavity. The optical beam has a secondary hard focus in the center between these two mirrors. The beam is near-Gaussian and characterized by a Rayleigh range ( $z_R$ ) of 55 mm. The IR beam waist,  $\omega$ , is wavelength,  $\lambda$ , dependent and in the focus ( $z=0$ :  $\omega_0$ ) is given by  $\omega_0[\text{mm}] = \sqrt{z_R \lambda / \pi} = 0.13 \sqrt{\lambda[\mu\text{m}]}$ . At a distance  $z$  from the focus the waist size becomes

$$\omega(z) = \omega_0 \sqrt{1 + (z/z_R)^2}. \quad (5.1)$$

A small fraction of the light is coupled out through a hole ( $r_{\text{hole}}=0.5$  mm) in the center of one of the end mirrors to allow wavelength calibration and power

measurement. The fraction  $\eta$  of the outcoupled pulse energy  $P_{meas}$  at the mirror position ( $z=1$  m) can then be used to estimate the intra-cavity pulse energy  $P$ .

$$P = \int I(r, z) dA = \int I_0 \exp(-2 \frac{r^2}{(\omega(z))^2}) 2\pi dr \quad (5.2)$$

$$\eta = \frac{P_{meas}}{P} = \frac{\int_0^{r_{hole}} I(r, z) dA}{\int_0^\infty I(r, z) dA} = 1 - e^{-2 \frac{r_{hole}^2}{\omega(z)^2}} \quad (5.3)$$

The molecular beam setup used in the experiments has been equipped with a laser ablation cluster source and a reflectron time-of-flight (ToF) mass spectrometer (mass resolution  $m/\Delta m \approx 1700$ ). The space-fixed IR beam runs in the horizontal plane and crosses the molecular beam at an angle of  $35^\circ$  in the center of the extraction region of the mass spectrometer. The IR beam is only 400 mm above the lab floor to keep the cavity length as short as possible. To overlap the molecular and the IR beams the whole molecular beam setup can be moved vertically under computer control. Furthermore, the setup can also be translated along the laser axis by up to 300 mm from the focus, which allows the power density to be changed by a factor of 40.

Other ways to change the power density are to change the length of the electron macropulse, or to change the cavity detuning. For the latter, the length of the cavity is shortened by multiples  $n$  of the wavelength  $\lambda$  from the synchronous value for which the round trip time of a IR (micro-)pulse exactly matches the repetition rate of the electron pulses. On successive roundtrips the electron pulses experience a larger optical field already at the beginning of the undulator. With increasing cavity detuning this decreases the bandwidth and lowers the total pulse energy. By leaving the cavity detuning  $n\lambda$  constant when changing the wavelength, the bandwidth is kept almost constant over the whole wavelength range reachable for a certain electron beam energy (see Refs. [92, 314] for more details).

The optical pulse of FELICE has a structure similar to that of FELIX, a macropulse with a typical duration of  $\approx 5 \mu s$ , consisting of picosecond-long micropulses at a 1 ns interval. However, because of the intra-cavity design the clusters interact with each micropulse twice, as it travels to and from the end mirror. The optical pulse at the interaction point therefore consists of two pulse trains that are shifted from 0 to 0.5 ns with respect to each other depending on the position along the laser axis. This can be used to double the available micropulse energy or to effectively double the micropulse repetition rate.

The FELICE beamline is not completely independent from the other two FELs. Major parts of the electron beamline, *i.e.* the electron gun and the two accelerators are shared (see also Fig 2.4(b)). These parts have been laid-out for an interleaved operation, which means that only every other electron macropulse is sent to the

Table 5.1.: Characteristics of the FELICE free electron laser as used in the current experiment.

Wavenumber range	120-2500 cm <sup>-1</sup>
Energy per macropulse	0.5–5 J
Macropulse length	4-6 $\mu$ s
Macropulse repetition rate	5,10 Hz
Energy per micropulse	0.1-1 mJ
Relative spectral bandwidth	0.2-1 % FWHM

FELICE undulator. The electron beam energy used for FELIX and FELICE can be different. A third accelerator adds more flexibility on the settings available for FELICE and is required to achieve very short wavelengths. An overview of the FELICE specifications is shown in Table 5.1. More details on FELICE and other possibilities (sources and detectors) offered by the molecular beam setup can be found in Ref. [315].

## 5.2. IR Resonance Enhanced Multiple Photon Electron Detachment spectroscopy – Experimental

IR resonance enhanced multiple photon electron detachment spectroscopy is a very similar technique to IR-REMPI. In IR-REMPI a neutral, initially cold, cluster is resonantly heated by the absorption of very many IR photons, see also section 2.2.2. This internal energy can be released by three different mechanisms: (i) by IR emission (ii) by fragmentation or (iii) by thermionic electron emission, which ionizes the cluster. The dominant process depends on the internal energy and the cluster properties. For niobium clusters the ionization (IEs) and the bond dissociation energies (BDEs) are shown in Figure 5.2. For clusters with  $n > 3$ , the BDEs are larger than the IEs, whereas this is different for very small ones and also changes again for larger ones. For clusters for which the IE is smaller, a dominant energy release channel at sufficient internal energy will be ionization of the cluster. This is employed in the IR-REMPI experiments.

Ionization of the neutral cluster requires considerably higher internal energies than ionization of an anionic cluster. For niobium clusters the binding energies of the electron in the anionic clusters (the electron affinity, EA) is clearly lower than the ionization energy. It is also much smaller than the BDE, so it is expected that electron detachment is the dominant energy release channel. This is employed in IR-REMPED spectroscopy. As most TM clusters have EAs much lower than their BDEs it should be a very general method, whereas IR-REMPI is only applicable to a limited number of refractory metals.

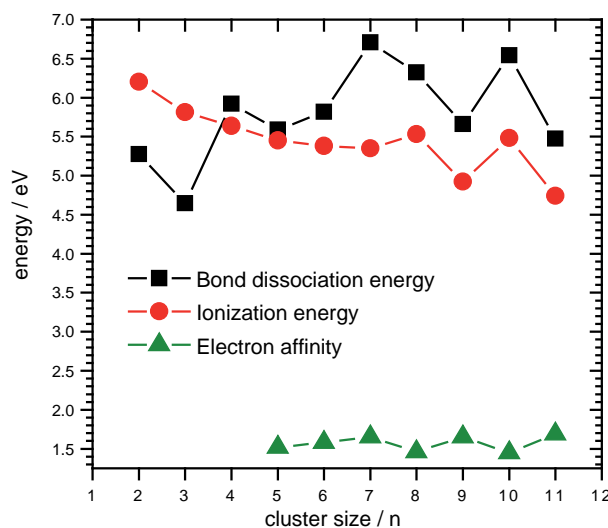


Figure 5.2.: Properties of  $\text{Nb}_n$  clusters, taken from Refs. [309, 316, 317].

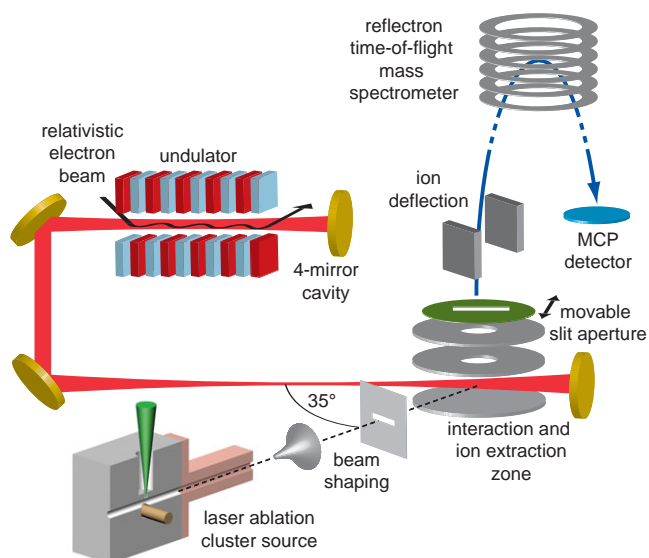


Figure 5.3.: Scheme of the experimental setup. The clusters are made in a pulsed laser ablation cluster source. The molecular beam is shaped with a skimmer and a slit aperture and crosses the FELICE beam axis under  $35^\circ$ . To detect only the ions that have been irradiated by FELICE a movable aperture is used to reduce the acceptance of the mass spectrometer.

In IR-REMPI the initial species is a neutral cluster, upon IR photon absorption and subsequent thermionic electron emission a cationic cluster is formed, which can be very sensitively detected by mass spectrometry. If the cluster is out of resonance, no absorption will occur and no ions will be produced, making IR-REMPI a background free method. IR-REMPED on the other hand starts with singly negatively charged clusters, which are detected with a ToF mass spectrometer. Upon resonant absorption of IR light a cluster may be sufficiently heated to emit an electron by thermionic emission, leading to a neutral cluster and a depletion of the initial ion intensity. In a molecular beam, where no mass selection is used, the electron cannot be used to monitor the absorption, as its origin is unclear. The only possibility to detect the detachment, is by monitoring the ion abundance. IR-REMPED becomes a depletion method. Therefore, the cluster beam experiment runs at twice the repetition rate of FELICE and mass spectra are taken on alternate shots with and without FELICE. Analysis of the relative ion intensity in the two mass spectra and its IR wavelength-dependence allows the construction of a mass-specific depletion spectrum.

The setup used in the IR-REMPED experiment is quite similar to the ones used for the other FELIX experiments. The scheme in Figure 5.3 shows the major parts. In a laser ablation cluster source the (anionic) TM clusters are produced in the expansion of a short helium gas pulse seeded with methane (0.025 % for  $Ta_nC_m^-$  and 0.1 % for  $Nb_nC_m^-$  clusters). The cluster size distribution can be analyzed in a reflectron ToF mass spectrometer. In contrast to the experiments using the FELIX setup it is not possible to overlap the ion and IR beams in a collinear configuration. Instead, they have to cross under an angle. To increase the interaction time, the angle has been kept as small as possible, which is for the current setup  $35^\circ$ . This increases the interaction time by more than 70 % compared to an interaction under  $90^\circ$ . The setup has been designed such that both beams cross in the center of the extraction region of the mass spectrometer. As the vacuum system of the experiment cannot be separated from that of the FEL during operation, a differential pumping stage has been added between cluster source and mass spectrometer. As a consequence of the crossed beam setup and the finite FELICE beam size, only a small fraction of the ions in the molecular beam are exposed to a sufficient IR fluence to induce REMPED.

In the focus, the IR beam waist ranges from 0.3 to 1.2 mm for light of 2500 and  $120\text{ cm}^{-1}$ , respectively, the limits of the covered wavelength range. In the first experiments on the  $Ta_nC_m^-$  clusters the experiments have been performed with a constant distance of the interaction point of molecular and IR beam of two Rayleigh ranges from the focus. This increases the IR beam size to 1.2–4.1 mm for the 2500– $200\text{ cm}^{-1}$  range studied for this system. For the later experiments on clusters con-

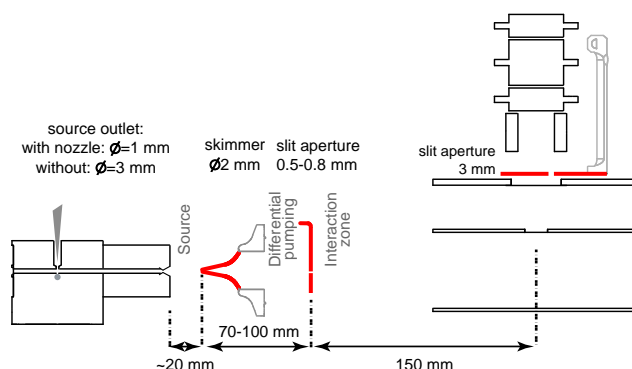


Figure 5.4.: Typical distances and sizes of the different apertures (in red) used to shape the beam.

taining niobium a different approach has been pursued. To make use of the full macropulse duration of FELICE, which is typically  $4-6 \mu\text{s}$ , the experiment has been performed out of the focus of the IR beam. Clusters, made in the expansion of a helium gas pulse, typically have a beam speed of  $\approx 1.6 \text{ mm}/\mu\text{s}$ . By adjusting the FELICE waist to a diameter of  $\approx 4 \text{ mm}$  in each of the individual scan ranges the interaction time becomes more than  $4 \mu\text{s}$ .

As IR-REMPED relies on the measurement of a depletion signal, the detection volume has to be restricted to those ions that have been irradiated by the full pulse. This was achieved by inserting a slit aperture behind the extraction region of the mass spectrometer (with  $3 \text{ mm}$  width) positioned  $\approx 4 \text{ mm}$  downstream of the IR beam axis and by switching the extraction voltages on just after the end of the IR pulse. The spatial extent of the molecular beam in the vertical direction was also shaped by a combination of a skimmer and a slit aperture (see Figures 5.3 and 5.4). The beam shaping and the cluster source were constantly improved, which allowed the molecular beam height to be reduced from  $\approx 6 \text{ mm}$  in the first experiments on  $\text{Ta}_n\text{C}_m^-$ , to  $\approx 4 \text{ mm}$  and  $\approx 2.5 \text{ mm}$  for  $\text{Nb}_n^-$  and  $\text{Nb}_n\text{C}_m^-$ , respectively.

The imperfect overlap between IR and molecular beam and the different ion trajectories through the IR beam (which changes the integrated IR intensity the cluster experiences) mean that the depletion observed is not constant over a peak (for a certain mass to charge ratio) in the ToF mass spectrum. Figure 5.5 shows the depletion observed for  $\text{Nb}_6\text{C}^-$  at  $220 \text{ cm}^{-1}$  as function of the height of the setup with respect to the IR beam and digitizer channel number corresponding to the position in the ToF peak. Depletion by  $60 \%$  can be obtained on the latter part of the ToF peak for a  $2.5 \text{ mm}$  high packet with an optimized vertical overlap. This corresponds to the convolution of the  $\approx 2.5 \text{ mm}$  high molecular beam and the  $4 \text{ mm}$  IR beam size, but is also influenced by the aperture in the mass spectrometer.

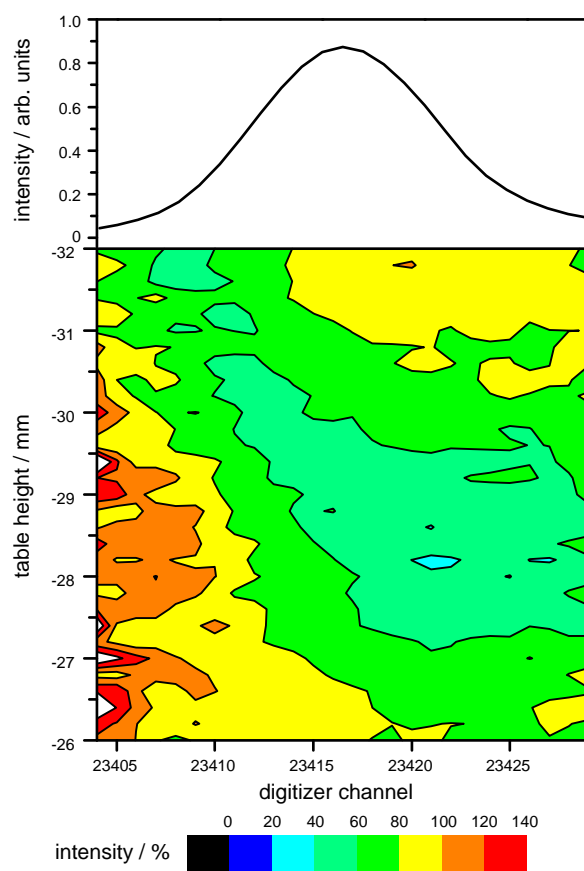


Figure 5.5.: Depletion spectrum for  $\text{Nb}_6\text{C}^-$  at  $220\text{ cm}^{-1}$  as function of the vertical overlap (table height) and position in the ToF spectrum. The maximum depletion is only observed for those ions, that arrive later at the detector.

More depletion can only be achieved by further reducing the molecular beam size. This, however, leads to too little ion counts and requires a (currently) too high stability of the beam overlap. For this reason a further narrowing of the beam size was not feasible. In the analysis of the depletion spectra the poor overlap was considered by using only parts of the ToF peak for the construction of the depletion spectra. Construction of spectra showing relative cross sections, as done for the FELIX experiments, is not straightforward and requires the assumption of an overlap factor, which is not constant, and even changes over the measurement time. Therefore, only depletion spectra are shown in the following.

The overlap between IR and molecular beam and the detected molecular packet was always very carefully adjusted. After identification of an absorption for a single system the depletion signal was maximized by scanning the vertical overlap



and the position of the aperture in the mass spectrometer, while leaving the timing for the high voltage pulses for the extraction plates unchanged. While optimizing the aperture position it was also necessary to adjust the voltages for the deflection plates in order to bend the ion trajectories onto the MCP detector. Changing the distance to the focus, and therefore the IR intensity, required a reoptimization of all of the parameters.

### 5.3. $\text{Ta}_n\text{C}_m^-$ cluster anions

#### 5.3.1. IR-REMPED spectra

IR-REMPED spectra for a large number of  $\text{Ta}_n\text{C}_m^-$  clusters with  $n=3-5$  and  $m=1-4$  have been measured simultaneously in the  $200-2500\text{ cm}^{-1}$  range. For a few selected cluster sizes, which vary in the amount of metal in the cluster ( $\text{Ta}_{3-5}\text{C}^-$ ) and in the amount of carbon ( $\text{Ta}_3\text{C}_{1-4}^-$ ), these spectra are shown in Figures 5.7 and 5.8, respectively. Several different FELICE settings have been used in order to cover the complete wavelength range. The depletion spectra obtained with different settings are shown in the Figures in different colors. The estimated IR fluence at the interaction point between IR and molecular beam is shown in Figure 5.6 and was calculated by using the outcoupled fraction of the IR beam, the position of the interaction point with respect to the focus and equation 5.3. The IR fluence used varies dramatically between  $2$  and  $60\text{ J/cm}^2$ . The spectral range covers metal-metal vibrations, which are typically found below  $400\text{ cm}^{-1}$ , metal-carbon vibrations between  $500-700\text{ cm}^{-1}$  and carbon-carbon vibrations  $>1000\text{ cm}^{-1}$ .

The effect of the fluence on the depletion spectra was studied in the  $300-800\text{ cm}^{-1}$  range. Spectra obtained using two laser fluences differing by one order of magnitude are shown in the Figures. For the  $\text{Ta}_3\text{C}^-$  cluster dramatic differences in the depletion spectra are observed. At the lower fluence only a single peak is observed in the IR-REMPED spectrum (blue line) while an extremely broad absorption is observed at high fluence (red line). For other cluster sizes, the differences are smaller. In general, the absorptions become broader with higher fluence. In some cases, additional bands can be observed, *e.g.* for  $\text{Ta}_4\text{C}^-$  and  $\text{Ta}_3\text{C}_4^-$  at  $314$  and  $358\text{ cm}^{-1}$ , respectively. A systematic study of the fluence dependence was not successful as changing the fluence by moving the setup or changing the cavity detuning also changes the bandwidth or the beam overlap simultaneously.

**$\text{Ta}_n\text{C}^-$  cluster.** For  $\text{Ta}_3\text{C}^-$  the IR-REMPED spectrum obtained at low IR fluence shows only a single absorption at  $703\text{ cm}^{-1}$ . At higher IR intensities two additional features are observed to the red, with their maxima at  $526$  and  $607\text{ cm}^{-1}$ . To the blue a uniform absorption is seen with no clear maxima. The spectrum for  $\text{Ta}_4\text{C}^-$

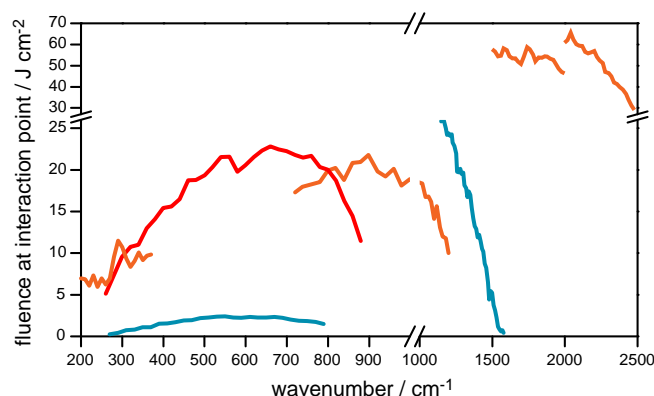


Figure 5.6.: Lower estimate for the FELICE fluence at the interaction point between molecular and IR beam used to measure the IR-REMPED spectra for  $\text{Ta}_n\text{C}_m^-$  cluster. The color coding corresponds to the one used in the IR-REMPED spectra shown later.

shows a large number of peaks over the entire spectrum. The band positions are given in Table 5.3. The modes above  $800\text{ cm}^{-1}$  are surprising, as this is much higher than expected for metal-carbon vibrational fundamentals. For this cluster size the broad absorption is also observed, but appears at higher wavenumber, as it starts only at  $1500\text{ cm}^{-1}$ . The  $\text{Ta}_5\text{C}^-$  cluster has fewer bands than  $\text{Ta}_4\text{C}^-$ , and they are exclusively found in the mid- and far-IR, below  $800\text{ cm}^{-1}$ . Several bands are observed in the  $200\text{--}300\text{ cm}^{-1}$  range, and two sharper features appear at  $610$  and  $678\text{ cm}^{-1}$ . The broad band usually seen at higher wavenumber is shifted even further to the blue and starts only at  $2000\text{ cm}^{-1}$ . Its intensity is much lower than for the previous two cluster sizes.

**$\text{Ta}_3\text{C}_m^-$  cluster.** The spectra for the  $\text{Ta}_3\text{C}_m^-$  clusters differ significantly in the amount of spectral information that can be obtained. For the  $\text{Ta}_3\text{C}_2^-$  cluster clear bands are seen at  $482$ ,  $561$ ,  $670$ , and  $263\text{ cm}^{-1}$ . At higher wavenumber a broader background emerges.

The  $\text{Ta}_3\text{C}_3^-$  absorbs over the entire wavelength range. No distinct features are present. For the far-IR setting, the signal drops by 30 % and in the other scan ranges by at least 50 % in the mass spectra taken with the IR radiation. Similar behavior, with depletion even up to 90 %, has also been seen for some other cluster sizes, which are not shown here, including  $\text{Ta}_4\text{C}_4^-$ ,  $\text{Ta}_4\text{C}_6^-$ ,  $\text{Ta}_5\text{C}_3^-$ , and  $\text{Ta}_5\text{C}_5^-$ .

Adding a carbon atom, forming  $\text{Ta}_3\text{C}_4^-$ , results in an IR spectrum with clear absorption bands at  $220$ ,  $358$ ,  $463$ ,  $547$ ,  $606$ ,  $689$ ,  $789$ , and  $1621\text{ cm}^{-1}$ .

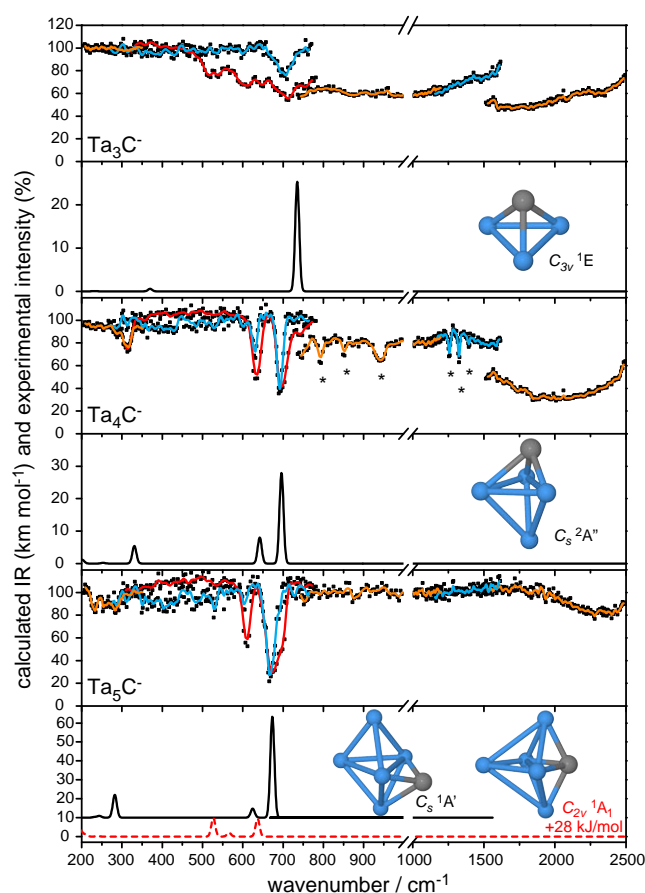


Figure 5.7.: IR-REMPED spectra for  $\text{Ta}_n\text{C}_m^-$  cluster with  $n=3-5$  in comparison with calculated IR spectra from DFT calculations. The experimental data points (shown as black dots) have been folded with a 5-point running average (colored solid lines). The different color coding represent different FELICE settings, and the color is the same as in Figure 5.6, which shows the corresponding IR fluence. Combination modes for  $\text{Ta}_4\text{C}^-$  are marked by asterisks.

### 5.3.2. Photoelectron spectra

Photoelectron spectra have been measured with the velocity map imaging setup described in chapter 2.4 using photon energies of 2.33 and 3.49 eV. The clusters have been made under similar, but not identical conditions to those used in the IR-REMPED experiments. Instead of mixing methane into the carrier gas, which also produces  $\text{Ta}_n\text{C}_m\text{H}_{1,2,\dots}^-$  clusters, methane has been introduced by the reaction valve installed on top of the reaction/cooling channel in the time between ablation laser

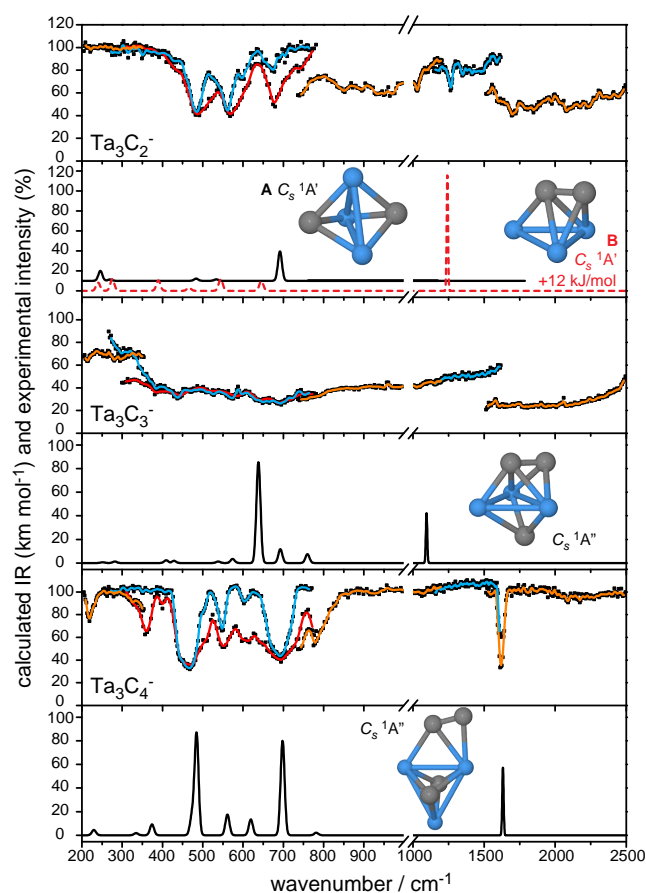


Figure 5.8.: IR-REMPED depletion spectra for  $\text{Ta}_3\text{C}_m^-$  cluster with  $m=2-4$ .

shots. Methane reacts to form a carbide surface on the Ta target and the formation of hydrogen containing cluster species was strongly suppressed. It is important to minimize the intensity of these species as they would contribute to the PES spectra as the mass resolution at the point of photodetachment is not sufficient for full separation of the heavy tantalum carbide clusters and those containing hydrogen. The PES setup was optimized on the Ir atom, which was also used for calibration.

The measured images have been analyzed with the method described previously for  $\text{Ir}^-$  (see section 2.4.1.4). Briefly, the images have been centered and converted to polar coordinates. Afterwards an image reconstruction using the polar onion peeling program described in Ref. [118] was applied. In the following, we neglect the angular information contained in the images and focus on the measured electron binding energies.

Spectra have been taken at two different photon energies. The ones measured

with 532 nm light (2.33 eV) allow to determine the vertical detachment energies more accurately, which we define by the maximum of the first major feature. These values are shown in Table 5.2. The spectra correspond well with the ones measured at 3.49 eV photon energy (355 nm). Only the latter are shown in Figure 5.9, as they show more than a single feature. For  $\text{Ta}_5\text{C}^-$  the PES spectra measured with the two photon energies show a less sharp onset; as it is observed more clearly in the 532 nm spectrum this is also shown for this cluster size.

The vertical detachment energies for the investigated  $\text{Ta}_n\text{C}_m^-$  clusters are between 1.33 and 2.02 eV. No clear size dependent trend for the VDE for the mono-carbide cluster is observed.

Table 5.2.: Comparison of the vertical detachment energies of  $\text{Ta}_n\text{C}_m^-$  cluster from calculations using different DFT methods and experimental values.

size	isomer	TPSS	PBE0	Experiment
$\text{Ta}_3\text{C}^-$	$\text{C}_{3v} \ ^1\text{E}$	1.04	1.22	1.51
$\text{Ta}_3\text{C}_2^-$	<b>A</b> $\text{C}_s \ ^1\text{A}'$	0.69	0.75	1.33
	<b>B</b> $\text{C}_s \ ^1\text{A}'$	1.22	1.26	
$\text{Ta}_3\text{C}_3^-$	$\text{C}_s \ ^1\text{A}''$	0.88	0.92	1.55
$\text{Ta}_3\text{C}_4^-$	$\text{C}_s \ ^1\text{A}''$	1.69	1.69	2.02
$\text{Ta}_4\text{C}^-$	$\text{C}_s \ ^2\text{A}''$	1.03	1.12	1.35
$\text{Ta}_5\text{C}^-$	$\text{C}_s \ ^1\text{A}'$	1.33	1.37	1.69(1.36)
	$\text{C}_{2v} \ ^1\text{A}_1$	1.22	1.16	

### 5.3.3. Theoretical method\*

Density functional theory has been used to determine and calculate the vibrational spectra, the vertical detachment energies (VDE) and the density of states (DOS) of low-energy isomers of  $\text{Ta}_n\text{C}_m^-$ .

The potential energy landscape of the  $\text{Ta}_n\text{C}_m^-$  clusters was explored [318] using a basin hopping (BH) Monte Carlo simulation [319] at the DFT level. A home-made program interfaces with TURBOMOLE V6.2 [320, 321] which is used to perform the DFT local optimizations required at each Monte Carlo step [318]. These used Becke's exchange [170] and Perdew's correlation GGA functionals (B-P86) [171] and the def2-SVP basis sets and effective core potentials (ECP) [172, 322, 323] and the resolution of identity (RI) approximation [246, 324].

The lowest energy structures found by BH were then reoptimized in a range of spin multiplicities using two different functionals. The meta-generalized gradient functional of Tao, Perdew, Staroverov, and Scuseria (TPSS) [325] together with

\* Calculations have been performed by Dan J. Harding from the Fritz-Haber-Institut.

balanced triple- $\zeta$  valence basis sets including polarization functions (def2-TZVP) [243] (and ECP for Ta [323]) and RI approximation were chosen, as this combination was previously found to provide a good description for clusters of tantalum [326]. The second method makes use of the hybrid functional of Perdew, Burke and Ernzerhof (PBE0) [327, 328] which contains 25 % exact exchange and uses the larger def2-QZVPP basis set. Initially the calculations were performed without symmetry constraints, subsequently the highest possible symmetry group has been applied.

DFT calculations on anionic systems often suffer from unbound electrons. This is due to the self-interaction error, where self-interaction terms do not cancel exactly in DFT [329], unlike in Hartree-Fock (HF). This is observed for some of the cluster sizes studied here, too. A general solution for this problem has not yet been found [330, 331]. We use the energy difference of the self-consistent-field calculations ( $\Delta$ SCF) for the anions and neutrals to determine the VDEs and move the DOS to match the HOMO to the VDE.

#### 5.3.4. Discussion

The energetic order of the predicted local minima from the BH algorithm have been investigated with the TPSS and PBE0 functional. For all cluster sizes studied here the same putative global minimum structures have been identified with both methods. Their calculated harmonic frequencies are also very similar. The frequencies from TPSS calculations do not require scaling while the PBE0 frequencies match better if scaled by 0.95. Because of the similarity of the vibrational spectra, the IR-REMPED spectra are only compared to the TPSS calculations. The harmonic frequencies have been folded with Gaussian functions with a width of  $10\text{ cm}^{-1}$  FWHM.

The VDEs predicted by the two methods at the anion geometry are also very close. The DOS, however, shows clear differences for some cluster sizes. The most pronounced differences are seen for the  $\text{Ta}_3\text{C}_4^-$  cluster. For this single cluster size the different results will be discussed. At the moment, the PES spectra will be compared to the PBE0 results only, which is expected to give the most reliable results, because of the hybrid origin of the functional and the very large basis set employed. The DOSs have been shifted to match the highest occupied molecular orbital  $\epsilon_{\text{HOMO}}$  to the calculated VDE plus a constant shift of 0.3 eV, which gives a better match to the experiment ( $\epsilon_{\text{HOMO}} + \text{VDE} + 0.3\text{ eV}$ ).

**$\text{Ta}_3\text{C}^-$ .** For the  $\text{Ta}_3\text{C}^-$  cluster an equilateral triangle with a hollow site carbon atom 3-fold coordinated is found by the BH algorithm as the putative minimum structure. The cluster has  $C_{3v}$  symmetry and a  $^1\text{E}$  electronic state. The calculation

at the TPSS level predicts a single intense band at  $735\text{ cm}^{-1}$ , which is very close to the experimental value (see Figure 5.7). The vertical detachment energy is calculated to be 1.22 and 1.03 eV for PBE0 and TPSS, respectively. The PBE0 value is  $\approx 0.3$  eV below the experimental value of 1.52. This shift has already been considered for the DOS. In Fig. 5.9 the DOS is compared to the measured one, and good agreement is found. All three experimentally observed features are reproduced and almost perfect match in the positions is found.

Previous work on the bare tantalum trimer cluster anion by PES in conjunction with DFT identified the same arrangement of Ta atoms, with  $D_{3h}$  symmetry and a  $^5\text{A}'$  electronic state. A VDE of 1.40 was measured [332]. The  $\text{Ta}_3\text{O}^-$  cluster has a slightly higher electron affinity of 1.58 eV [333, 334]. For this cluster it was even possible to achieve vibrational resolution [333]. In combination with theory a planar structure with an oxygen bridging two atoms of the  $\text{Ta}_3^-$  triangle structure was discussed.

For the neutral  $\text{Ta}_3\text{C}$  cluster photoionization efficiency (PIE) measurements in combination with theory identified a similar structure to ours, but with a lower symmetry, as the carbon is only in a bridging position [335].

**$\text{Ta}_4\text{C}^-$ .** The three lowest frequency modes in the IR-REMPED spectrum of  $\text{Ta}_4\text{C}^-$  are found at 314, 632, and  $694\text{ cm}^{-1}$ . These modes can be assigned to a  $\text{Ta}_4^-$  tetrahedron ( $\text{C}_s$ ,  $^2\text{A}''$ ) in which the carbon is still bound to three Ta atoms on a hollow-site but is significantly shifted off to one side. The calculated IR frequencies agree within  $20\text{ cm}^{-1}$  with the experimental findings, as can be seen in Table 5.3. Bands above  $700\text{ cm}^{-1}$  cannot easily be explained by this isomer. Modes are observed up to very high frequencies of  $1395\text{ cm}^{-1}$ . This is probably too high for fundamental vibrational modes of a cluster that contains only a single carbon atom. Bands above  $700\text{ cm}^{-1}$  are therefore assigned to overtone and combination bands. As the cluster has  $\text{C}_s$  symmetry any combination mode would be IR allowed. However, only some of them are sufficiently intense to be observed. Table 5.3 shows a possible assignment. All experimental bands are slightly red shifted. The bands at  $795\text{ cm}^{-1}$  and  $853\text{ cm}^{-1}$  may be explained by a combination with a band at  $\approx 165\text{ cm}^{-1}$ , which agrees well with two almost degenerate calculated modes at 161 and  $162\text{ cm}^{-1}$ .

A VDE of 1.35 eV was determined from the PES spectrum. The predicted VDE from the PBE0 calculation is 0.23 eV lower, and the TPSS value 0.33 eV. The (shifted) DOS in Fig. 5.9 again agrees well with the measurement. In particular the gap between transition X and A is nicely reproduced.

For the neutral a similar structure has been assigned in Ref. [335].

Table 5.3.: Calculated IR modes at TPSS level and experimental position of the bands for  $\text{Ta}_4\text{C}^-$ . Modes above  $700\text{ cm}^{-1}$  can be assigned to overtones of the fundamental vibrational modes.

mode	sym.	theory		experiment	
		wavenumb.	abs.cross.sec.	wavenumb.	assign.
		$\text{cm}^{-1}$	$\text{km mol}^{-1}$	$\text{cm}^{-1}$	
1	$A'$	117.71	0.32		
2	$A''$	128.92	0.67		
3	$A'$	160.98	0.91		
4	$A''$	162.16	1.15		
5	$A'$	201.34	1.13		
6	$A'$	253.15	0.21		
7	$A'$	330.38	5.40	314	$\nu_7$
8	$A''$	642.23	8.04	631	$\nu_8$
9	$A'$	696.14	27.63	694	$\nu_9$
				795	$(\nu_{3,4} + \nu_8)$
				853	$(\nu_{3,4} + \nu_9)$
				942	$\nu_7 + \nu_8$
				1261	$2\nu_8$
				1325	$\nu_8 + \nu_9$
				1395	$2\nu_9$

**$\text{Ta}_5\text{C}^-$ .** For  $\text{Ta}_5\text{C}^-$  two structures very close in energy have been identified by the BH algorithm. For both, the underlying  $\text{Ta}_5$  metal cluster structure is a triangular bipyramid. For the putative global minimum a smaller deformation by carbon addition is observed. The carbon binds to one of the Ta faces, and forms a  $C_s$   $^1A'$  structure. The second lowest energy structure ( $C_{2v}$ ,  $^1A_1$ ) is 28 kJ/mol higher in energy in the TPSS calculations. In contrast to the previous isomer the carbon binds to four Ta atoms, which requires a stronger deformation as it binds to a butterfly motif of the bipyramid. It can also be seen as a distorted octahedron with one (metal) atom replaced by a carbon. The IR-REMPED spectrum can be well explained by the first isomer. Only a very weak feature at  $529\text{ cm}^{-1}$  might be assigned to the second isomer.

The assumption of a second isomer is supported by the PES spectrum. This cluster size was the only one for which a (weaker) transition at lower binding energy was observed. Two different VDE can be determined from this which are 1.36 and 1.69 eV, for transitions  $X'$  and  $X$ , respectively. All major features, and, in particular transition  $X$ , can be fully explained by the lower energy structure. The second isomer, however, would explain transition  $X'$ . Both experiments therefore suggest that, in addition to the lowest energy structure, a second isomer with a much lower abundance is present in both experiments.



Both structures have been considered before for the neutral cluster. Calculations predict very similar ionization energies for both structures, both in agreement with PIE measurements [336].

**$\text{Ta}_3\text{C}_4^-$ .** A well resolved IR spectrum with a large number of features is observed for the  $\text{Ta}_3\text{C}_4^-$  cluster. In particular the very intense bands at 463, 689  $\text{cm}^{-1}$ , and the 1621  $\text{cm}^{-1}$  mode are very characteristic. Our calculations suggest a  $C_s$   $^1A'$  structure as the global minimum. This structure contains a triangular bipyramid, whose apexes are formed by two carbon atoms. A  $\text{C}_2$  unit bridges one of the Ta-Ta edges. Carbon-carbon stretch vibrations have characteristic frequencies, and the calculation predicts the stretch at 1632  $\text{cm}^{-1}$ . This agrees very well with the experimental value of 1621  $\text{cm}^{-1}$ . Two other very intense features are predicted at 485 and 696  $\text{cm}^{-1}$  agreeing nicely with the experiment. The other experimentally observed modes are also reproduced by this isomer. The calculated DOS at the PBE0 level shows a good match to the photoelectron spectrum. As for the other cluster sizes the calculated VDE is 0.3 eV too low.

The PES spectrum shows only two transitions in the energy range investigated. The calculated DOS however, predicts a third one. This feature is predicted by PBE0 at very high electron binding energies where the sensitivity of the VMI spectrometer decreases. Depending on the applied DFT method the position of this transition varies a lot. In Fig. 5.10 the calculated DOS for this cluster structure using the two methods described previously is compared to the experiment. All are only shifted to match  $\epsilon_{\text{HOMO}}$  to the calculated VDE. The results from TPSS and PBE0 agree well for the first two transitions. The position of the third one, however, is at lower electron binding energy for the TPSS spectrum. The experiment clearly gives no evidence for a transition at this energy. From comparison of the IR-REMPED and PES experimental results, PBE0 appears to provide the best description of the ground and electronic structure of TaC anions.

**$\text{Ta}_3\text{C}_2^-$ .** For  $\text{Ta}_3\text{C}_2^-$  a triangular bipyramid structure **A** ( $C_s$ ,  $^1A'$ ) with the carbon atoms forming the apexes is found to be lowest in energy. This structure has only two intense IR modes, and only the higher one at 691  $\text{cm}^{-1}$  is seen in the experiment. The other experimental modes are not really explained by this isomer. For the second lowest energy structure **B** ( $C_s$ ,  $^1A'$ ) the two carbon atoms form a C-C bond and are found on a single face of the tantalum triangle. This structure has also only one intense mode, which is the C-C stretch. The position is calculated to be 1242  $\text{cm}^{-1}$ , which nicely agrees with a mode at 1263  $\text{cm}^{-1}$  in the experiment. Unfortunately this structure is also not able to explain the other missing features.

The PES spectrum of  $\text{Ta}_3\text{C}_2^-$  has a sharp onset in comparison to the  $\text{Ta}_5\text{C}^-$  cluster.

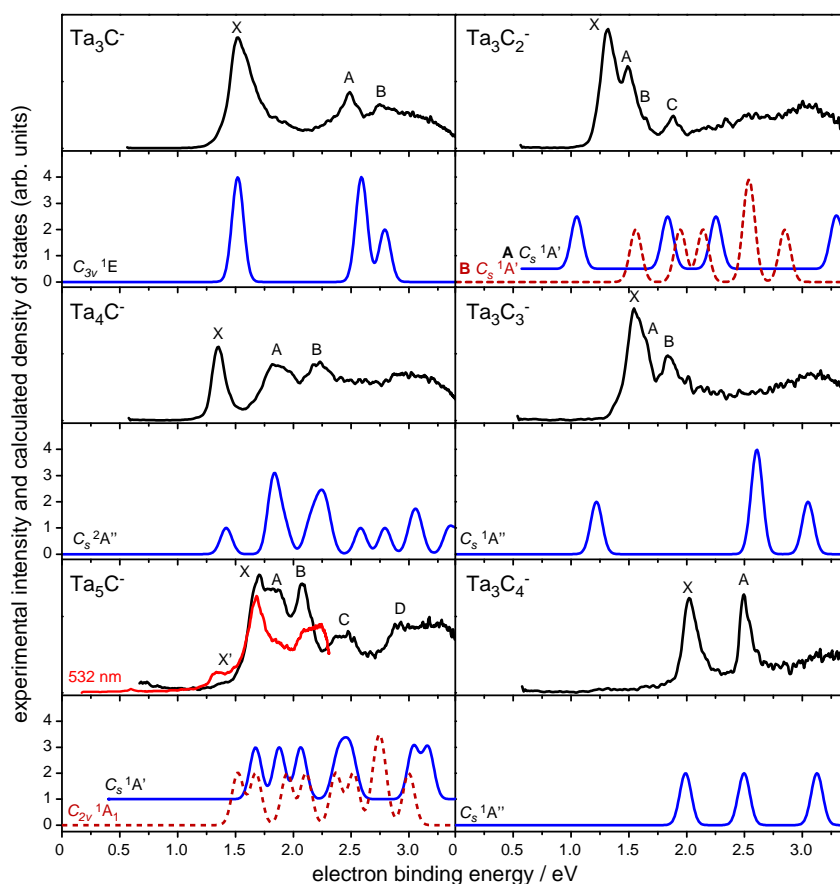


Figure 5.9.: Photoelectron spectra of  $Ta_n C_m^-$  clusters obtained with 355 nm light (and 532 nm for  $Ta_5 C^-$ ) and comparison to the (shifted) density of states for the same structures as in Figs. 5.7 and 5.8. Some spectra have been vertically shifted for clarity. The calculated spectra were folded with a Gaussian linewidth function of 0.1 eV FWHM.

The VDE from experiment is 1.33 eV. The PBE0 calculations give values of 0.75 and 1.26 eV for isomer **A** and **B**, respectively. Whereas the first seems to be too low (even including the additional offset of 0.3 eV seen for the other sizes), the latter, is a little bit too high. Isomer **B**, however, may fit to transition B marked in Figure 5.9. The large difference in the VDE for **A**, and the fact that no earlier onset in the PES spectrum is observed, allows this isomer to be excluded from contributing to the PES spectrum. Its presence in the IR-REMPED experiment cannot be completely ruled out. The experience with the setup used for the PES experiments shows that it is rather difficult to detect anions with low electron affinities (which means either they are not formed, or they do not survive into the detection region). The limit

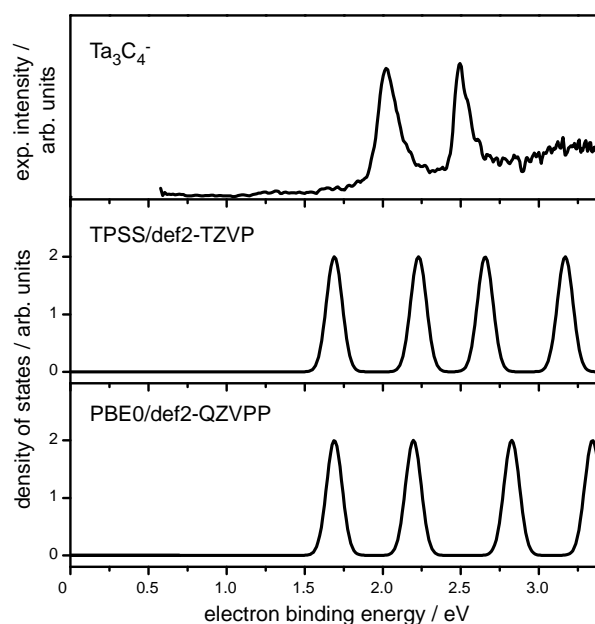


Figure 5.10.: Comparison of the experimental PES spectrum of  $\text{Ta}_3\text{C}_4^-$  to the calculated DOS for two different DFT methods. The DOS is shifted only by the difference of  $\epsilon_{\text{HOMO}}$  and VDE.

is somewhere around 1 eV. As this isomer has a EA in that range, it is possible that it was present in the PES experiment, but not detected. It is not clear whether the source used in the IR-REMPED setup has the same characteristics, but given the similarities in the design, similar behavior would be expected. However, even the presence of both isomers is not sufficient to explain the experimental results. Another isomer seems to be required, but could not be identified. None of the other isomers found explain the IR-REMPED spectrum.

Previous studies on neutral  $\text{Ta}_3\text{C}_2$  clusters by PIE assigned the triangular bipyramid structure [335] for the neutral and cationic clusters. This structure also seems to be present, together with other isomers, for the anion.

The formation of C-C bonds, even if only for a minor isomer, for such a small amount of carbon is very surprising. Investigations on neutral tantalum and niobium carbide clusters suggested such isomers only for a metal/carbon ratio of  $\leq 1$  [336, 337].

$\text{Ta}_3\text{C}_3^-$ . The IR-REMPED spectrum of  $\text{Ta}_3\text{C}_3^-$  does not allow the assignment of a certain structure to the spectrum, as only a very broad absorption is seen. The reason for such featureless spectra is unclear, but possible reasons will be discussed for the  $\text{Nb}_8\text{C}_{12}^-$  clusters, for which a similar behavior is observed.

Nevertheless, the calculated IR spectrum of the lowest energy structure ( $C_s, {}^1A''$ ) identified by the BH is shown along with the experiment. Similar to the other clusters containing three tantalum atoms, the underlying metal cluster has a triangular shape. The three carbons bind in a similar way as before, as the carbons bind to the two faces of the triangle. On one of the faces a C-C species similar to that seen in isomer **B** of  $Ta_3C_2^-$  is formed.

In contrast to the IR spectrum, the PES spectrum is better resolved. A VDE of 1.55 eV is measured, and three features are observed in the spectrum. The calculated VDE of structure  $C_s, {}^1A''$  (0.92 eV) is significantly lower than the experimental value. Additionally, the calculated DOS is a poor match to the experimental PES. This suggests that this isomer is not present in our experiments. So far, it has not been possible to assign an isomer for this cluster size.

## 5.4. From niobium mono- and di-carbide clusters to bare metal clusters

### 5.4.1. IR-REMPED spectroscopy of $\text{Nb}_n\text{C}_{1,2}^-$

IR-REMPED spectra for niobium mono- and di-carbide clusters  $\text{Nb}_n\text{C}_{1,2}$  with  $n=3-12$  have been measured in the  $120-1000\text{ cm}^{-1}$  range covering the metal-metal and metal-carbon vibrations. The spectra are shown Figures 5.12, 5.14 and 5.15. All of the spectra show the direct depletion not corrected for variations of the IR fluence over the scanning range. In order to assess the relative intensity of the bands observed in experiment the IR fluence used in the different ranges is shown in Fig. 5.11.

For many systems well-resolved bands are observed with widths as narrow as  $10\text{ cm}^{-1}$ . These widths are not limited by the bandwidth of the IR radiation, which was typically 0.3 % FWHM of the central frequency, but rather by the multiple photon excitation process [304]. Even for such large systems as  $\text{Nb}_{11}\text{C}^-$  very distinct features are seen and only the  $\text{Nb}_8\text{C}_{1,2}^-$  clusters have almost constant absorption over the entire wavelength range studied. Similar to the  $\text{Ta}_n\text{C}_m^-$  clusters the spectra of some sizes seem to suffer more from the appearance of overtone and combination modes, and show in the mid-IR broad often featureless absorptions. In particular, the dicarbide clusters seem to be affected by this, with the exception of the  $\text{Nb}_9\text{C}_2^-$ , which has three distinct features around  $700\text{ cm}^{-1}$ .

The amount of depletion observed for the narrower features can be as high as 60 % and bands are observed even at very low photon energies. The band of  $\text{Nb}_6\text{C}_2^-$  at  $127\text{ cm}^{-1}$  shows depletion by more than 30 %. For  $\text{Nb}_6\text{C}^-$  the onset of a band at even lower photon energy is seen, see Fig. 5.14.

Three different FELICE electron beam energy settings have been employed to cover the entire wavelength range and are illustrated by the different color coding in the figures. The setting used for the mid-IR range ( $400-1000\text{ cm}^{-1}$ ) has been further split into three regions for the measurements, which differ by the distance of the interaction point from the focus and by the cavity detuning, which had to be reduced in order to reach the highest wavenumber. The estimated intra-cavity fluence is shown in Fig. 5.11. Although differences in the fluence are observed, the measured depletion spectra fit together well.

Measurements performed using different FELICE settings, or the same but on another day, can be strongly affected by different overlaps or different IR beam properties (bandwidth, chirps,...) as can be seen for the setting used in the  $200-400\text{ cm}^{-1}$  range. Although from the estimated intra-cavity fluence at the interaction point the setting can compete with the  $120-320\text{ cm}^{-1}$  setting, which overlaps for major parts of the spectral range (compare Fig. 5.11), the spectra compare less

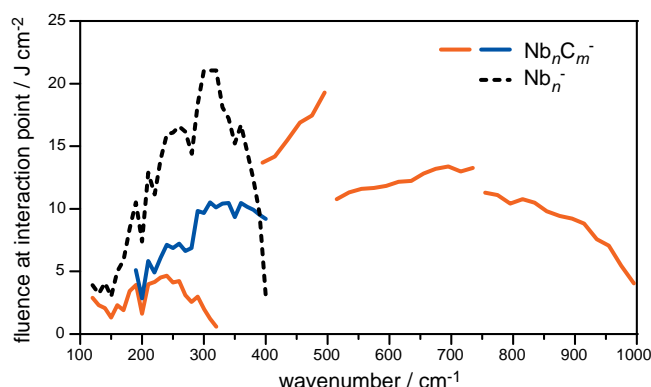


Figure 5.11.: Lower estimate for the FELICE fluence at the point of interaction between the molecular and the IR beam. Solid lines are for  $\text{Nb}_n\text{C}_m^-$  and the dashed line for  $\text{Nb}_n^-$  clusters. The pulse energy was measured with a powerhead in air. Therefore, the measured power might be much lower in the far-IR than the real one due to absorptions in air.

well\*

The depletion spectra are again compared to the IR spectra from DFT calculations<sup>†</sup>. A similar approach to that used for the tantalum carbide clusters was used, with the TPSS functional [325], the def2-TZVP basis sets [243] and ECPs for niobium [323]. As before, low energy structures were initially identified using a basin-hopping Monte Carlo algorithm. For more details see section 5.3.3. Calculations were initially performed without symmetry constraints, subsequently, the higher symmetries were investigated. The calculated harmonic frequencies are scaled by a factor of 0.95 and are folded with a Gaussian linewidth function of  $10\text{ cm}^{-1}$  FWHM.

In the following, a particular focus will be on the underlying metal cluster structure, to learn how the added carbon atom influences the metal cluster structure.

**$\text{Nb}_3\text{C}^-$ .** The IR-REMPED spectrum of  $\text{Nb}_3\text{C}^-$  (Figure 5.12) shows sharp bands at  $215, 311, 598, 732$  and  $821\text{ cm}^{-1}$ . The three central features may be explained by the  $\text{C}_s\ ^3\text{A}''$  isomer, in which the Nb atoms form an isosceles triangle with the carbon atom bound to the Nb face. For this structure the calculations predicts intense absorptions at  $269, 532$ , and  $670\text{ cm}^{-1}$ . The spectral pattern seems to match the experimental one, except that the (rescaled) calculated frequencies are all too low. Using a different scaling factor of 1.06 for the calculated frequencies would give better agreement, but lower frequency modes seem to require larger scaling, which

\* In the  $120\text{--}320\text{ cm}^{-1}$  range only FELICE was in operation.<sup>†</sup> Calculations have been performed by Dr. D. J. Harding from the Fritz-Haber-Institut.

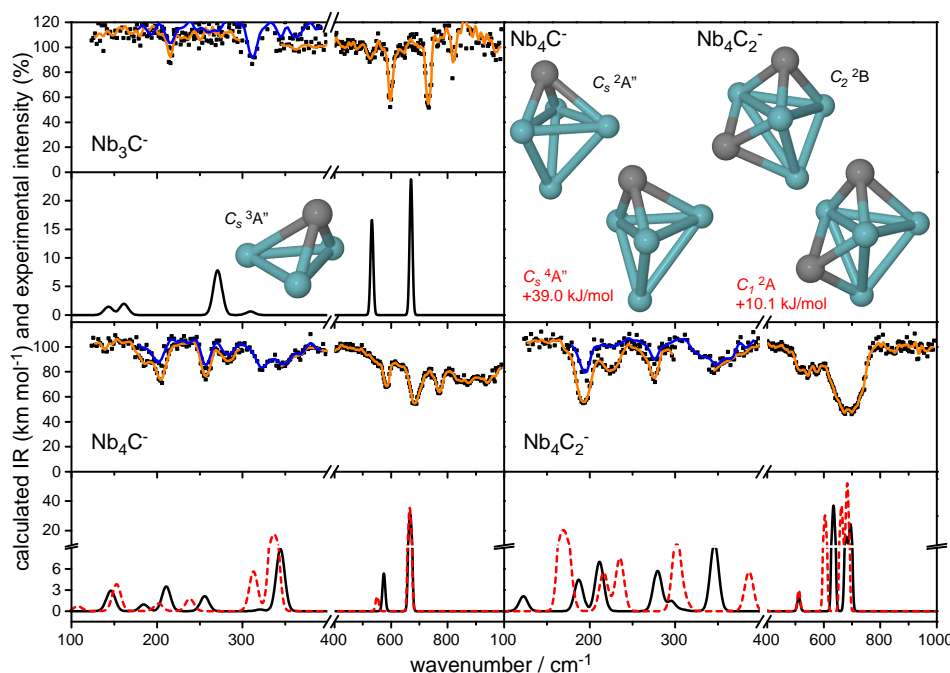


Figure 5.12.: IR-REMPED depletion spectra for  $\text{Nb}_3\text{C}^-$  and the  $\text{Nb}_4\text{C}_{1,2}^-$  clusters in comparison to calculated spectra from DFT. The experimental data points are shown as black dots and are folded with a 5-point running average (colored solid lines). The different color coding for the smoothed spectra represent different FELICE settings. The fluence at the interaction point can be found in Fig. 5.11. The calculated (scaled) theoretical spectra have been broadened with a Gaussian function of FWHM of  $10\text{ cm}^{-1}$ .

would also help to explain the  $215\text{ cm}^{-1}$  mode. This is the only cluster size for which an up-scaling of the calculated frequencies gives a better agreement. None of the other isomers gives a better agreement to the experimental spectrum. The band at  $821\text{ cm}^{-1}$  cannot be explained by this or other isomers, and is presumably due to a combination mode. Such combination modes have been already observed for the  $\text{Ta}_n\text{C}_m^-$  clusters, and will be discussed for the  $\text{Nb}_n\text{C}_{1,2}^-$  clusters using the example of the  $\text{Nb}_6\text{C}^-$  cluster.

The observed cluster structure can be compared to the structure observed for the bare  $\text{Nb}_3^-$ , the  $\text{Nb}_3\text{O}^-$ , and the neutral  $\text{Nb}_3\text{C}$ , which have previously been studied experimentally and theoretically (compare Fig. 5.13). The underlying  $\text{Nb}_3^-$  substructure in the  $\text{Nb}_3\text{C}^-$  cluster is very similar to the one assigned to the bare  $\text{Nb}_3^-$  by combining PES and DFT calculations [338]. An open-shell isosceles triangle structure with  $C_{2v}$  symmetry and  $^3\text{A}_2$  state has been identified in that experiment.

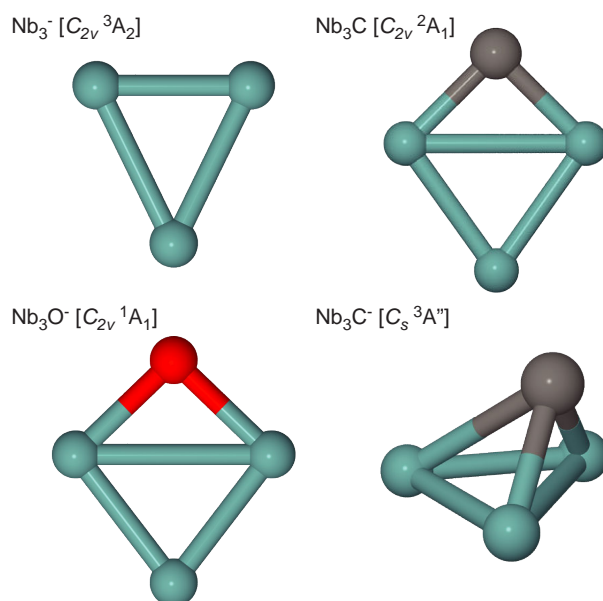


Figure 5.13.: Structures assigned for  $\text{Nb}_3^-$  [338],  $\text{Nb}_3\text{O}^-$  [338],  $\text{Nb}_3\text{C}$  [339], and  $\text{Nb}_3\text{C}^-$  clusters based on results from PES, PIE, or IR-REMPED spectroscopy.

The major difference between the  $\text{Nb}_3^-$  and  $\text{Nb}_3\text{C}^-$  is the difference in the angle between the two equal sides of the isosceles triangle, which increases from  $52^\circ$  to  $72^\circ$  following the addition of the carbon atom. A similar structure has also been considered for the  $\text{Nb}_3\text{O}^-$  cluster [338]. However, a planar structure with a bridging oxygen was found to be lower in energy and also showed better agreement to the PES experiment. Such a structure has been considered for the  $\text{Nb}_3\text{C}^-$ , but it is 88 kJ/mol higher in energy and does not explain the experimental spectrum. For the neutral  $\text{Nb}_3\text{C}$ , a photoionization efficiency experiment (PIE) gave indications that the planar isomer is experimentally observed and was also found lowest in energy [339].

**$\text{Nb}_4\text{C}_{1,2}^-$ .** For the  $\text{Nb}_4\text{C}_{1,2}^-$  clusters whole series of bands are observed. The narrower features are seen for the monocarbide cluster. The BH algorithm identifies structures with a tetrahedron for the underlying metal cluster for both cluster sizes. The carbon atoms always bind to the Nb faces. The two lowest energy species for  $\text{Nb}_4\text{C}^-$  have similar geometric structures with  $C_s$  symmetry, but different spin states. The doublet is predicted lower in energy than the quartet, and fits the experiment better. A good match between experimental and calculated spectrum is found with respect to the band positions, only the observed intensities do not



agree perfectly. The highest frequency mode is not explained by the fundamental vibrations and is presumably a combination mode.

In the  $\text{Nb}_4\text{C}_2^-$  cluster the two carbon atoms bind to separate faces of the tetrahedral niobium cluster. The two isomers shown in Fig. 5.12 are both doublet states and are energetically separated by only 10 kJ/mol. The comparison between the experimental spectrum and the calculated spectra shows that the putative ground state  $\text{C}_2$   $^2\text{B}$  structure matches the experiment better. All of the bands around  $700\text{ cm}^{-1}$  are nicely reproduced, and combination modes do not have to be considered. The second isomer is not needed to explain the experimental spectrum. The PIE experiment of Ref. [339] assigns a similar structure for the neutral  $\text{Nb}_4\text{C}$  ( $\text{C}_s$ ,  $^1\text{A}'$ ), whereas for the  $\text{Nb}_4\text{C}_2$  cluster a small structural change is observed, as they determined a  $\text{C}_{2v}$   $^1\text{A}_1$  structure from their PIE spectrum. In our case the structure is slightly twisted. However, there is a disagreement in the literature over the structure of the neutral, as another experiment studying the reaction of ethene with niobium clusters identified the twisted structure [340].

**$\text{Nb}_5\text{C}_{1,2}^-$ .** For  $\text{Nb}_5\text{C}^-$  the IR-REMPED spectrum shows narrow bands at 198, 231, 299, 324,  $599\text{ cm}^{-1}$ , and a broader asymmetric band around  $650\text{ cm}^{-1}$ , which can be fitted with two Gaussian functions, centered at 651 and  $683\text{ cm}^{-1}$ . The lowest-energy structure identified by the BH approach used in the current study is a trigonal bipyramid structure  $\text{C}_s$   $^1\text{A}'$  with the carbon bound to a Nb face. The calculated IR spectrum has intense features at 202, 226, 303, 316, 593 and  $655\text{ cm}^{-1}$ . These match the experimental frequencies very well. The only absorption band not properly described is the one at  $683\text{ cm}^{-1}$ . As all of the other experimental absorptions are explained, if another isomer is responsible for this absorption it should have essentially a single intense band at this position. Such a structure could not be identified, suggesting the band has a different origin. A combination of the  $593\text{ cm}^{-1}$  mode and a band predicted at  $110\text{ cm}^{-1}$  would be a possible explanation.

For the neutral, PIE measurements identified the same structure ( $\text{C}_1$ ,  $^2\text{A}$ ) [337]. Clusters containing five niobium atoms and more can also be compared to the bare neutral niobium clusters, where IR-MPD spectroscopy has been performed [308]. Both, IR-MPD and PIE measurements found for  $\text{Nb}_5$  [337] the same trigonal bipyramid ( $\text{C}_{2v}$ ,  $^2\text{B}_1$ ).

The IR-REMPED spectrum of  $\text{Nb}_5\text{C}_2^-$  shows bands less well separated from each other compared to the  $\text{Nb}_5\text{C}^-$ , but still single peaks can be observed. The predicted IR spectrum for the doubly capped trigonal bipyramid structure ( $\text{C}_s$ ,  $^1\text{A}'$ ) also looks more complex and nicely fits the experimental one. It is also the lowest energy structure that was identified in our calculations. For the neutral  $\text{Nb}_5\text{C}_2$  a different

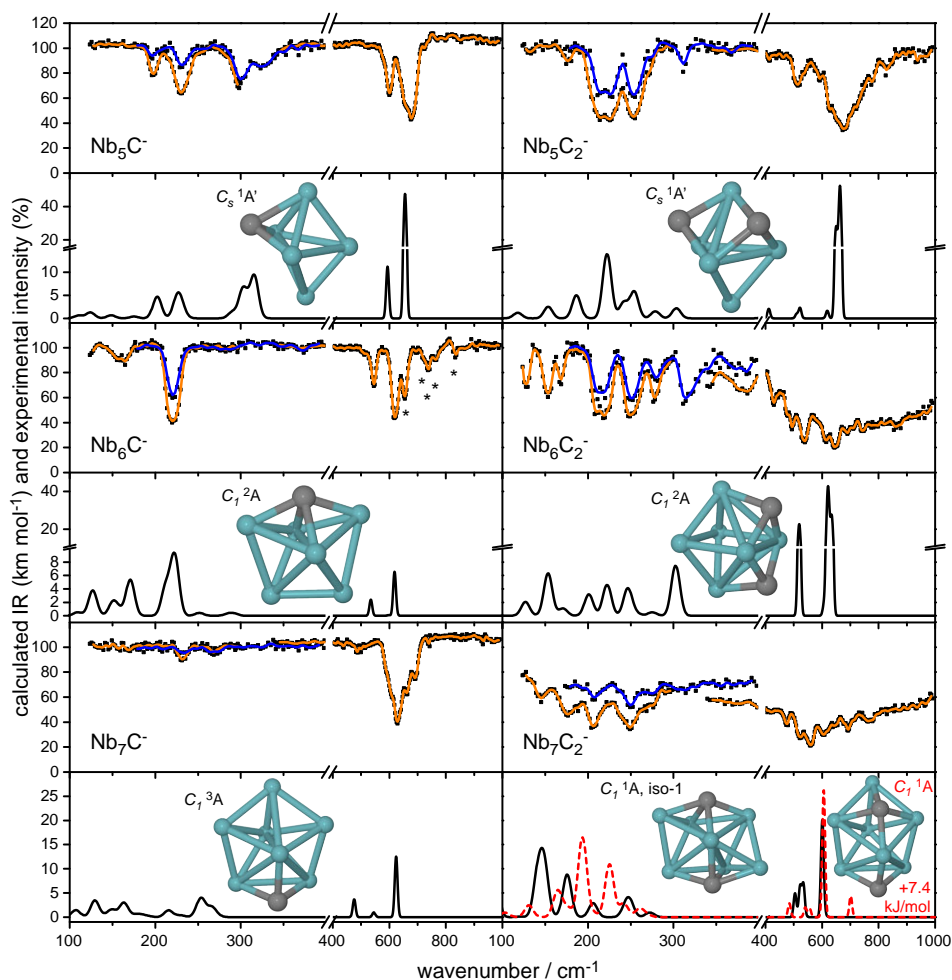


Figure 5.14.: IR-REMPED depletion spectra for  $\text{Nb}_n\text{C}_{1,2}^-$  clusters with  $n=5-7$  and comparison to calculated spectra from DFT calculations. Combination modes for  $\text{Nb}_6\text{C}^-$  are marked by asterisks.

structure has been assigned based on PIE in which the underlying  $\text{Nb}_5$  cluster [337] forms an oblate trigonal bipyramid. In contrast to the structure of the anion, the carbons are bound to four Nb atoms as they bind to the two butterfly motifs of the oblate trigonal bipyramid ( $C_{2v}$ ,  $^2B_1$ ). The same structure was also assigned by ethene reactivity studies Ref. [340]. In the case of the anion, such a structure is 29 kJ/mol higher in energy and does not fit the experimental spectrum.

**$\text{Nb}_6\text{C}_{1,2}^-$ .** For  $\text{Nb}_6\text{C}^-$  only a few modes are observed below  $500\text{ cm}^{-1}$ . Among them is the lowest frequency mode identified so far by IR-REMPED, which appears just at the lower limit of the tuning range of FELICE at  $124\text{ cm}^{-1}$ . In contrast

to the low number of modes in the far-IR, a relatively large number of well resolved bands is observed between 500–1000  $\text{cm}^{-1}$ .

The calculations predict a distorted pentagonal bipyramid (DPBP) in a  $^2A$  state as the global minimum structure, in which the atoms in the five-membered ring are not in a plane. The structure has  $C_1$  symmetry, but the distortion from  $C_2$  is very small. Below 650  $\text{cm}^{-1}$  all of the features in the measured IR-REMPED spectrum of  $\text{Nb}_6\text{C}^-$  are reproduced by the calculated harmonic IR spectrum for this structure. An almost perfect match in the positions is observed, as can be seen in Table 5.4, showing the experimental band positions, calculated frequencies, and IR intensities. The three highest energy bands between 530 and 620  $\text{cm}^{-1}$  correspond to Nb–C stretch vibrations of the 4-fold bound carbon atom:  $\nu_{14}$ ,  $\nu_{15}$  in the plane of the five-membered ring and  $\nu_{13}$  out of this plane. However, the additional bands above 650  $\text{cm}^{-1}$  cannot be explained by the harmonic spectrum. These are marked by an asterisk in Fig. 5.14 and the band positions are given in Table 5.4. These may be rationalized by at least two different explanations: (i) other isomers or (ii) combination bands. In particular the mode at 655  $\text{cm}^{-1}$ , which is rather intense might come from another isomer. The third lowest isomer (not shown) has one very intense absorption close to that position, but the structure is 66 kJ/mol above the global minimum. Furthermore, by using the same scaling factor as before, this mode would shift from 664 to 630  $\text{cm}^{-1}$ . This is 24  $\text{cm}^{-1}$  below the observed experimental feature. For all other bands deviation of less than 10  $\text{cm}^{-1}$  between calculated and experimental values have been observed for this cluster size. Metal–carbon vibrations at even higher frequencies, required to explain all of the other features, are uncommon, which makes it unlikely that these bands are due to other isomers. Therefore, combination modes are the more likely reason for these features. The low symmetry makes any combination IR allowed, which makes a definite assignment difficult. Several different combinations would be possible, some are shown in Table 5.4. All combination modes are red-shifted with respect to the sum of the vibrational fundamentals by about 2–15  $\text{cm}^{-1}$ . The feature at 655  $\text{cm}^{-1}$  is particularly intense. Presumably, this  $\nu_{13} + \nu_2$  combination borrows intensity from the mode at 621  $\text{cm}^{-1}$  by a Fermi resonance.

Other experimental information on  $\text{Nb}_6\text{C}$  and also all other larger clusters is sparse, as only the neutral clusters have been studied with photoionization efficiency spectroscopy [341], but no structural assignments have been made. However, comparison to the structure of the neutral  $\text{Nb}_6$  cluster is possible. For this cluster, the IR-MPD spectrum has been assigned to a dimer-capped rhombus [308], similar to the metal core observed in  $\text{Nb}_6\text{C}^-$ . The carbon binds centrally to the rhombus, and gets incorporated in the cluster. This is the first cluster size where a four-fold coordination to the Nb has been observed.

Table 5.4.: Calculated linear IR absorption spectrum for the global minimum structure of  $\text{Nb}_6\text{C}^-$  with rescaled frequencies and IR absorption cross sections, compared to the experimental band positions. For the bands observed above the range of the calculated vibrational fundamentals tentative assignments as combination modes have been made.

mode	calc. resc. wavenumber $\text{cm}^{-1}$	calc. IR intensity $\text{km mol}^{-1}$	exp. wavenumber $\text{cm}^{-1}$	suggested assignment
$\nu_1$	109.2	0.5		
$\nu_2$	126.6	2.1		
$\nu_3$	127.3	1.7	$\leq 124$	
$\nu_4$	150.5	2.0	155	
$\nu_5$	157.5	0.8		
$\nu_6$	170.8	5.4	165	
$\nu_7$	212.0	4.1		
$\nu_8$	222.4	8.4	221	
$\nu_9$	225.7	0.6		
$\nu_{10}$	251.6	0.4		
$\nu_{11}$	285.0	0.3		
$\nu_{12}$	292.2	0.3		
$\nu_{13}$	534.9	2.4	544	
$\nu_{14}$	596.7	0.1		
$\nu_{15}$	618.2	6.6	621	
			655	$\nu_{13} + \nu_2$
			726	$\nu_{15} + \nu_1$
			739	$\nu_{15} + \nu_{2,3}$
			764	$\nu_{15} + \nu_4$ or $\nu_{13} + \nu_{8,9}$
			834	$\nu_{15} + \nu_8$ or $\nu_{13} + \nu_{12}$

The number of photons necessary to detach the electron from the cluster at  $124 \text{ cm}^{-1}$ , a photon energy of only 15 meV, can be estimated from the calculated VDE, which is 0.98 eV. This means that more than 60 photons have to be absorbed to reach the detachment energy when starting from a cold cluster. A simple thermionic emission model following Ref. [342] gives a similar number of photons that need to be absorbed at  $124 \text{ cm}^{-1}$  to reach a rate constant of  $2 \cdot 10^4 \text{ s}^{-1}$  for electron ejection, which corresponds to the lower limit to achieve detachment within the time window of the experiment.

Below  $400 \text{ cm}^{-1}$  the IR-REMPED spectrum of  $\text{Nb}_6\text{C}_2^-$  shows bands at 128, 153, 169, 209, 222, 252, 279, and  $313^* \text{ cm}^{-1}$ . These band positions are perfectly matched by the calculated vibrational spectrum of the tetragonal-square bipyramid structure (or octahedron), having the two carbon atoms bound to adjacent Nb faces.

\* Neglecting the shoulder to the blue

The calculation gives IR allowed frequencies at 127, 153, 171, 208, 222, 246, 275, and  $302\text{ cm}^{-1}$ . Above the  $302\text{ cm}^{-1}$  mode, a very broad, but structured, absorption starts, which presumably originates from combination modes.

The structure observed for the metal-subcluster is quite different to the one with a single carbon. This structure is similar to the one predicted as the global minimum for the neutral  $\text{Nb}_6$ , though this was not observed in the IR-MPD experiment [308].

The two structural motifs observed for the underlying  $\text{Nb}_6^-$  cluster also compete for the bare cluster. Depending on the applied theoretical method, the dimer-capped rhombus, the distorted octahedron, or a distorted triangular prism, is predicted as the global minimum [343]. Earlier investigations using PES and DFT, assigned the dimer-capped rhombus for the  $\text{Nb}_6^-$  cluster [344, 345].

**$\text{Nb}_7\text{C}_{1,2}^-$ .** The IR-REMPED spectrum of  $\text{Nb}_7\text{C}^-$  in Figure 5.14 is somehow special, as only a single absorption centered at  $629\text{ cm}^{-1}$  having a progression to the blue (and less pronounced to the red) is observed. The BH algorithm identifies a pentagonal bipyramid structural motif in a triplet electronic state, with the carbon bound to a Nb face. This structure has only one intense absorption, which is at the experimentally measured position. The sidebands observed seem to originate from several different combination bands including the intense absorption.

For  $\text{Nb}_7\text{C}_2^-$  the vibrational spectrum shows broad but structured absorption over the whole wavelength range covered. Below  $400\text{ cm}^{-1}$  the maxima for the depletion are seen at 145, 176, 206, 250 and  $270\text{ cm}^{-1}$ . Two different singlet structures are predicted by the BH differing by only  $7.4\text{ kJ/mol}$ . One is based on the structure of the  $\text{Nb}_6\text{C}^-$  structure, capped by a (four-fold coordinated) carbon and a Nb atom, whereas the other, higher energy, one is based more on the  $\text{Nb}_7\text{C}^-$  structure. At first glance, the second lowest energy structure seems to match the experiment better. However, a closer look at the frequency reveals that it is not the case. For the lowest energy structure the calculated band positions for the most dominant peaks are at 148, 175, 206, 248, and  $272\text{ cm}^{-1}$ . For the second lowest one these are at 131, 164, 165, 193, 225, and  $241\text{ cm}^{-1}$ . The former seem to agree better with the experiment. The disagreement in intensity is caused by the change in the fluence, which increases significantly from 150 to  $250\text{ cm}^{-1}$ , compare Fig. 5.11. A more detailed look at the intensities for the  $\text{Nb}_5\text{C}_2^-$  and  $\text{Nb}_6\text{C}_2^-$  clusters reveals the same behavior. This is the inherent disadvantage of using only non-normalized depletion spectra, as intensities do not necessarily reflect real IR absorption cross sections.

The  $\text{Nb}_7\text{C}^-$  cluster has (presumably) a similar geometry as the bare  $\text{Nb}_7^-$  cluster, which was assigned to a (distorted) pentagonal bipyramid by PES and DFT [344,

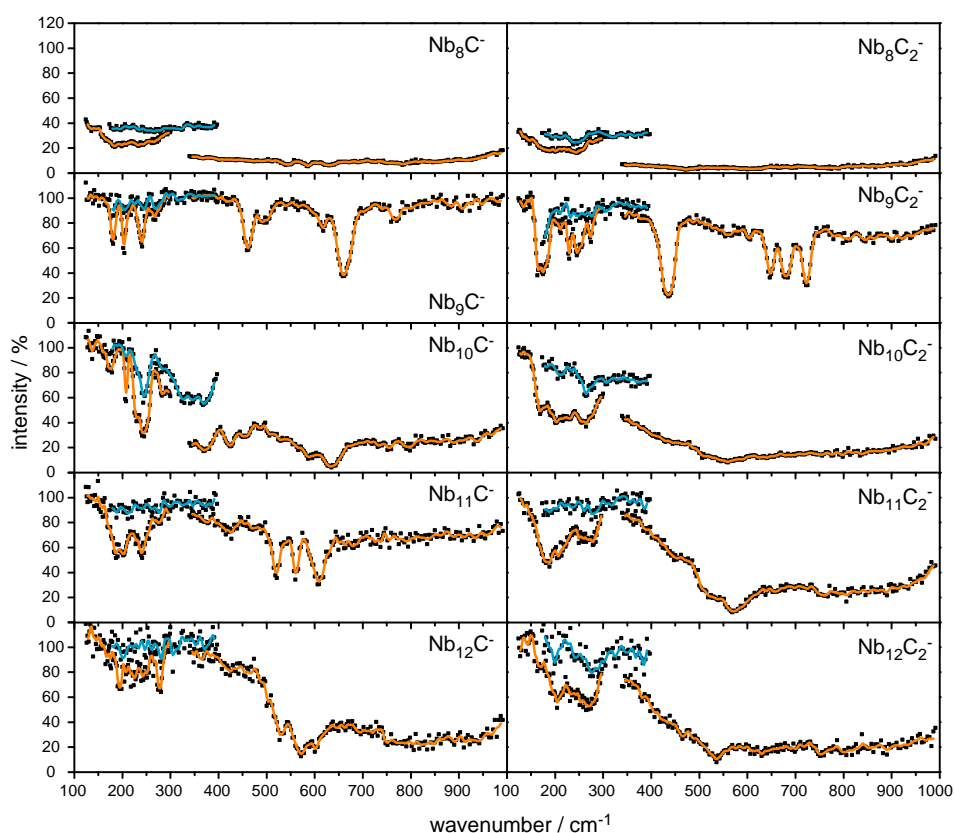


Figure 5.15.: IR-REMPED spectra of larger  $\text{Nb}_n\text{C}_{1,2}^-$  clusters with  $n=8-12$ .

345], as well as predicted purely by theory [346]. Surprisingly, the structure of  $\text{Nb}_7\text{C}_2^-$  shows the largest deformation by carbon addition, despite its large (metal) cluster size.

**$\text{Nb}_n\text{C}_{1,2}^-$  with  $n=8-12$ .** The IR-REMPED depletion spectra for  $\text{Nb}_n\text{C}_{1,2}^-$  clusters with  $n=8-12$  are shown in Fig. 5.15. The quality of the spectra varies strongly with cluster size despite being measured at the same time. For  $\text{Nb}_8\text{C}_{1,2}^-$  almost constant absorption is seen over the entire wavelength range, while  $\text{Nb}_9\text{C}_{1,2}^-$  and  $\text{Nb}_{11}\text{C}_1^-$  clusters have well resolved spectra. The large amount of depletion for the  $\text{Nb}_8\text{C}_m^-$  clusters, which goes down at least by 60 % and in some parts of the spectrum by almost 100 %, cannot be easily explained. Something similar has been observed for  $\text{Ta}_3\text{C}_3^-$ , though the depletion was less, in particular in the far-IR. A possible explanation by overtone and combination bands seems unlikely.

The density of vibrational states at low wavenumber is usually small, which makes it rather complicated to form a sufficiently large number of combination

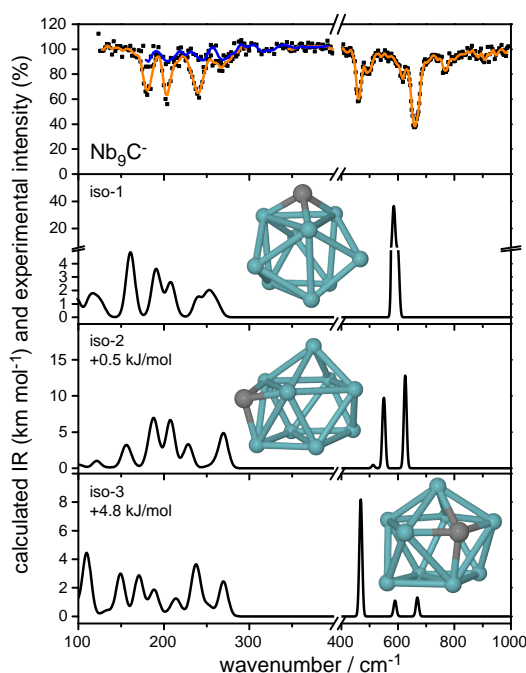


Figure 5.16.: IR-REMPED depletion spectrum of  $\text{Nb}_9\text{C}^-$  and comparison to calculated vibrational spectra for several low energy isomers.

modes. Therefore, in the far-IR, usually structured spectra are observed, and even for the largest cluster sizes studied (compare Fig. 5.15), for which the number of vibrational modes increases, single features can be resolved. Only in the mid-IR broad absorptions evolve.

A single low frequency mode can, in principle, significantly increase the vibrational density of states, allowing clusters even with lower internal energy to absorb photons of any frequency. However, the large amount of depletion would mean that *all* of the  $\text{Nb}_n\text{C}_m^-$  clusters leaving the source are already in the quasi-continuum region (see Section 2.2.2), which seems unlikely. Another reason could be a lower EA, that would require a lower number of photons to be absorbed to achieve thermionic emission. For  $\text{Ta}_3\text{C}_3^-$ , which also shows such constant depletion, it was found that it has a similar EA to the other tantalum carbide clusters studied. Recently, it has been reported that the IR field intensities available with FELICE are sufficient to tunnel ionize metastable xenon atoms in a single micropulse [347]. As tunneling ionization does not require resonant absorption of (IR) light, this might also explain the broad absorption observed. Currently, testing this hypothesis is not simple.

For the large  $\text{Nb}_n\text{C}_{1,2}^-$  clusters, calculations have been performed for a single

size,  $\text{Nb}_9\text{C}^-$ . The BH algorithm identifies several low energy isomers, very close in energy. The calculated vibrational spectra of the three lowest ones are compared to the experiment in Fig. 5.16. Despite the simplicity of the experimental spectrum, the agreement with any of the calculated ones is not very convincing. None really explains the experimental spectrum, and a closer look at the frequencies reveals larger differences between experimental and predicted band positions. Other high energy structures do not provide a better match to the experiment. More calculations are required in order to locate the structure observed in the experiment.

#### 5.4.2. IR-REMPED spectroscopy of $\text{Nb}_n^-$ clusters

The successful application of IR-REMPED to niobium mono- and dicarbide clusters in the far-IR made it also feasible to investigate the bare Nb clusters. It was not possible to form the bare and the monocarbide clusters simultaneously in sufficient intensities, as the former were almost completely absent after addition of the methane (0.1 %) to the carrier gas. However, leaving all other source parameters the same and switching over to pure helium shifts the cluster distribution from the monocarbides to the bare clusters. As the amount of methane was so small the change of the molecular beam speed is negligible, which means a preoptimized setup using the niobium monocarbides should also guarantee good spatial and temporal overlap with the IR beam for the bare clusters. Indeed this procedure turned out to work well.

IR-REMPED spectra for  $\text{Nb}_n^-$  clusters with  $n=7-16$  have been measured in the  $120-400\text{ cm}^{-1}$  range\* with a setup that was optimized before on the monocarbide clusters (Figure 5.17). For niobium and niobium carbide clusters the experiment was performed at the same distance from the focus for this wavelength range. However, the macropulse energy for the experiment on the bare clusters was much higher, as can be seen in Fig. 5.11.

Despite the much higher IR fluence the amount of depletion observed for the bare metal clusters is low (Fig. 5.17). The maximum amount of depletion is observed for  $\text{Nb}_{16}^-$  and is only 30 %. This is, in part, due to the larger molecular beam size used for the bare Nb clusters, which had a diameter of 4 mm compared to the 2.5 mm in the case of the niobium carbides. In general, the depletion is even weaker and only very few features are seen in the spectra.

For the three smallest cluster sizes, composed out of 7–9 niobium atoms, no obvious depletion is observed in the spectra, despite the fact that they had significant intensities in the mass spectra. The next larger cluster,  $\text{Nb}_{10}^-$  shows the most detailed spectrum, with two sharp bands at  $201$  and  $239\text{ cm}^{-1}$ . The width of the

\* The interleaved operation of FELIX and FELICE was not used for this setting.



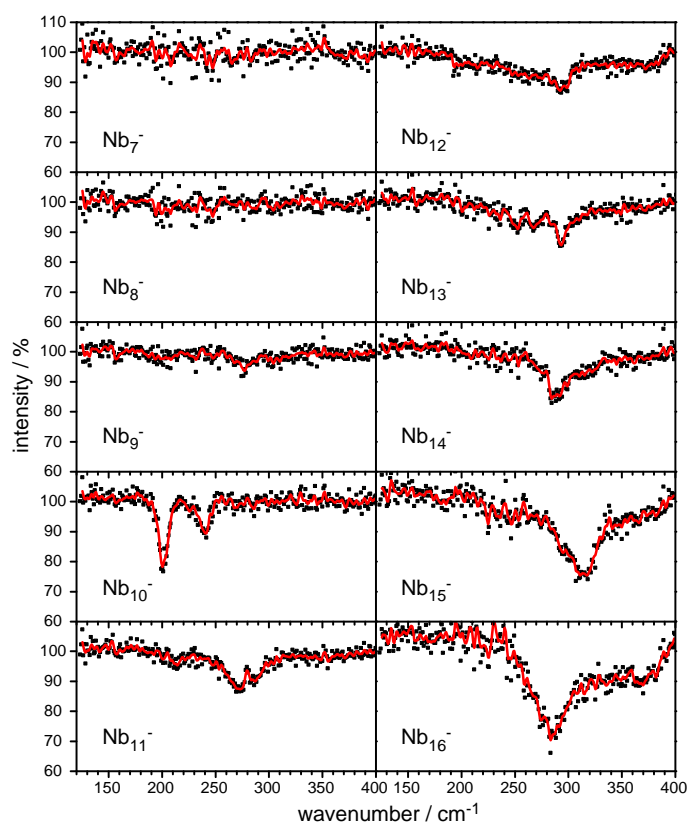


Figure 5.17.: IR-REMPED depletion spectra of  $\text{Nb}_n^-$  clusters with  $n=7-16$ .

first is only  $10 \text{ cm}^{-1}$  FWHM. For  $\text{Nb}_{11}^-$  two clear features are observed with maximum absorption at  $271$  and  $285 \text{ cm}^{-1}$ . For the larger sizes with  $n=12-16$  a broader absorption around  $300 \text{ cm}^{-1}$  evolves.

This seems, at first, a bit surprising and may indicate that structural assignments would be impossible. However, an IR-MPD experiment using Ar messenger tagging also found only a small number of absorptions for larger  $\text{Nb}_n$  and  $\text{Nb}_n^+$  clusters. This seems to be characteristic of larger niobium clusters, containing 15–17 atoms, and may be an indication for very symmetric structures. For the  $\text{Nb}_{15}$  cluster the IR-MPD\* and IR-REMPED spectra for all charge states are compared in Figure 5.18. For all three spectra a very intense absorption around  $315 \text{ cm}^{-1}$  is seen.

**$\text{Nb}_{10}^-$ .** The  $\text{Nb}_{10}$  cluster has already been studied extensively by theory in different charge states and a bicapped square antiprism (BCSA) has been predicted

\* Spectra for the cationic and neutral  $\text{Nb}_{15}$  cluster have been provided by Dr. A. Fielicke

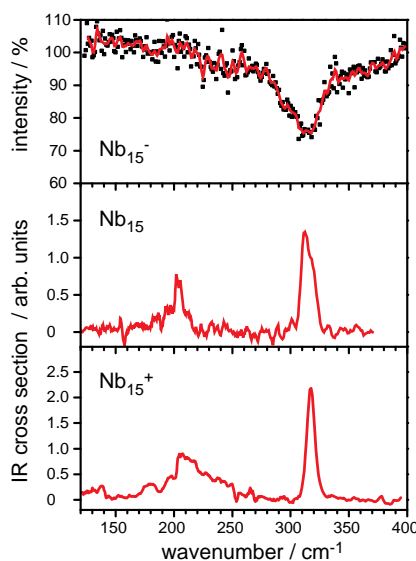


Figure 5.18.: Comparison of the vibrational spectra of the  $\text{Nb}_{15}$  cluster for different charge states.

as the ground state structure [311–313]. In a more recent theoretical investigation for  $\text{Nb}_n$  ( $n=9\text{--}12$ ) clusters IR spectra for neutral, anionic and cationic clusters have been reported [348]. In a comment to this article, the experimental IR-MPD spectra have been reported by Fielicke and Meijer [349], which confirm the predictions for cationic and neutral clusters, with the exception of the  $\text{Nb}_{12}$  cluster. For  $\text{Nb}_{10}$  both cationic and neutral cluster have the perfect BCSA structure with  $D_4$  symmetry, in the  $^2\text{A}_1$  and  $^1\text{A}_1$  electronic state for the cation and neutral, respectively.

The same structure with  $D_4$  symmetry in the  $^2\text{A}_1$  electronic state has now been considered also for the anionic cluster. Using the same theoretical approach as for the niobium carbide clusters, *i.e.* the TPSS functional, the def2-TZVP basis set and effective core potential for niobium, the IR spectrum has been calculated\*.

The calculated spectrum is shown in Fig. 5.19(a) and agrees well with the measured IR-REMPED spectrum. This good agreement supports a previous hypothesis based on the sharp transitions observed in photoelectron spectra for the  $\text{Nb}_{10}^-$  cluster [309, 310], typically indicative for electronic shell closing in the neutral [309]. Figure 5.19(b) compares the calculated density of states of the  $\text{Nb}_{10}$  cluster in the distorted bicapped antiprism structure to the photoelectron spectrum reported in Ref. [310], which had not previously been compared to theory. This experimental spectrum is slightly better resolved than the one reported in Ref. [309]. However, the major features are observed in both experimental spectra and are

\* Calculations have been performed by Dr. A. Fielicke from the Fritz-Haber-Institut

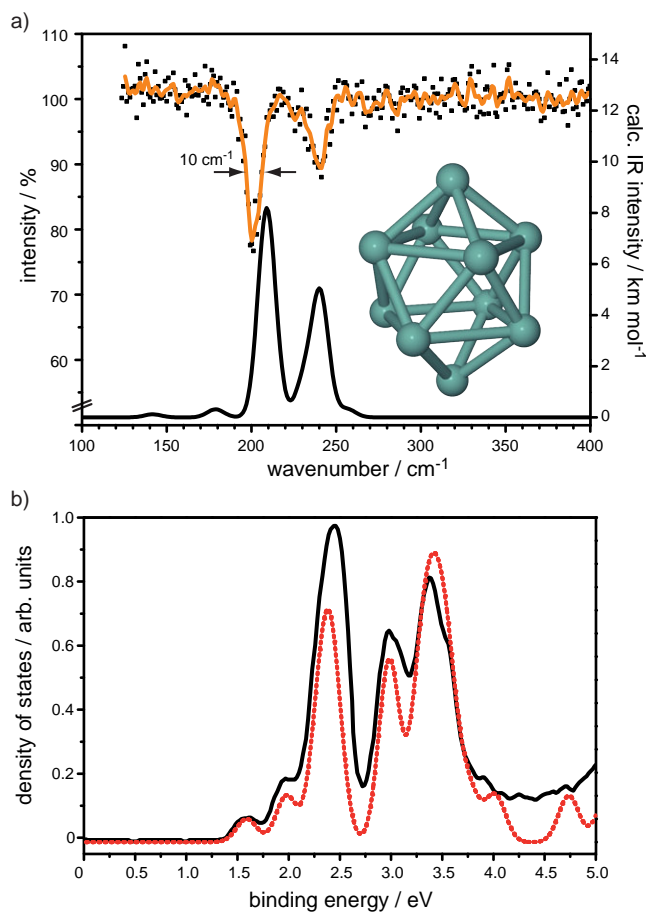


Figure 5.19.: (a) Comparison of the IR-REMPED spectrum of  $\text{Nb}_{10}^-$  with the calculated linear IR absorption spectrum of the ground state structure. (b) Comparison of the experimental PES spectrum (solid black line) [310] and the calculated density of states of the structure assigned by IR-REMPED spectroscopy (dashed red line). The calculated spectrum was folded with a Gaussian linewidth function of 0.25 eV FWHM.

reproduced by the calculation. The calculated vertical detachment energy (VDE) is 1.49 eV and compares well with the experimental value of 1.46 eV [309].

Similar to  $\text{Nb}_6\text{C}^-$  the required number of IR photons required for electron detachment can be estimated. For the low frequency mode of  $\text{Nb}_{10}^-$  60 photons need to be absorbed, a similar number as for the  $\text{Nb}_6\text{C}^-$  cluster. Although a multiple photon process was used to detect the absorption, the calculated linear IR intensities give, in these cases, a good indication for the relative intensities of the experimental depletion bands. The differences in the degree of depletion between  $\text{Nb}_6\text{C}^-$  and  $\text{Nb}_{10}^-$  arise, at least in part, from varied experimental conditions, but

may also reflect the 0.5 eV difference in the electron binding energies. The features observed for  $\text{Nb}_{10}^-$ , and the  $\text{Nb}_n\text{C}_{1,2}^-$  clusters have calculated IR intensities of 2–8 km mol<sup>-1</sup>, which is comparable to other neutral and cationic metal clusters previously studied with rare-gas tagging [56, 308].

## 5.5. Conclusions

The first experiments on negatively charged cluster ions using the intra-cavity molecular beam setup at FELICE are presented. Metal carbide and bare metal cluster anions have been studied by IR-REMPED spectroscopy in the mid and far-IR directly in a molecular beam. Well resolved bands have been observed over almost the complete wavelength tuning range of FELICE, reaching from weak fundamental metal-metal vibrations at the low photon energy limit of FELICE to combination modes at frequencies as high as 1400 cm<sup>-1</sup>.

The measured IR spectra have been compared to the results from DFT calculations, which allowed a structural assignment for many of the investigated species. The tantalum and niobium mono- and dicarbide clusters have structures similar to the ones of the bare metal clusters. On most sizes the carbon atoms bind to the metal cluster faces. Indications for carbon-carbon bonds in carbide clusters with only two carbon atoms, *i.e.*  $\text{Ta}_3\text{C}_2^-$ , have also been found.

Additional measurements on the tantalum carbide clusters, studying their photoelectron spectra, have been performed. The vertical electron detachment energies determined from these experiments give no clear indication on the range of detachment energies that is required for the application of IR-REMPED spectroscopy.

For the clusters whose structures could be unambiguously assigned by their IR-REMPED spectra, the calculated electronic DOS of the anions at the PBE0 level shows a very good match to the measured PES spectra.

IR-REMPED spectra have also been measured for bare niobium clusters. These spectra are the first far-IR spectra for TM cluster anions. For a single cluster size,  $\text{Nb}_{10}^-$ , it has been shown that the spectra offer sufficient quality to allow for structural assignment. For large Nb clusters, the comparison with the vibrational spectra for their neutral and cationic counterparts shows that very similar spectra for all charge states are observed.

## 5.6. Outlook

The results presented show that electron detachment by multiple photon excitation is possible even for the weak IR bands of transition metal clusters and it opens up a

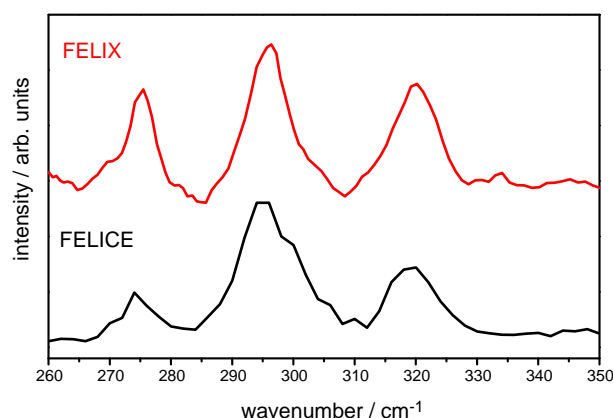


Figure 5.20.: Comparison of the vibrational spectra for  $\text{Nb}_{13}$  measured via argon tagging using FELIX and the IR-REMPI spectrum measured with FELICE [350].

new way to investigate metal cluster anions. IR-REMPED spectroscopy is expected to be applicable to a wide range of anionic metal clusters, as their electron affinity will generally be lower than the bond dissociation energy. Thus, IR spectroscopic methods are now available to determine the structure of isolated gas-phase metal clusters in their cationic, neutral, and anionic states.

Other experiments requiring a very high IR fluence will also be possible in the future with FELICE. Among those is IR-REMPI spectroscopy of bare neutral metal clusters. The number of absorbed IR photons required to observe ionization is significantly higher, as the IE is usually much larger than the EA for TM metal clusters. As the detection of the ionization process in IR-REMPI is essentially background free, this simplifies the experiment and the fluence dependence can be studied more easily, *e.g.* by changing the interaction time with the IR radiation by changing the molecular beam speed. Initial experiments showed that IR-REMPI for neutral niobium clusters is indeed possible and the spectrum of  $\text{Nb}_{13}$  is shown in Figure 5.20\*.

The high intensities and long wavelength of the radiation of FELICE may also allow for tunneling ionization within a single micropulse for some (charged) clusters and molecules. As the radiation is linearly polarized, photoelectron holography and diffraction would then be possible. Initial experiments could here confirm the creation of high harmonics, made by tunneling and recombination of the photoelectrons, and should even be possible with *tightly* focussed light from a normal

\* The results have been measured in collaboration with V.J.F. Lapoutre and Dr. J.M. Bakker from the FOM Institute Rijnhuizen, and will be part of the PhD thesis of V.J.F. Lapoutre.

(hole-coupled) IR-FEL.

## 6. Summary and concluding remarks

Gas-phase vibrational spectroscopy allows the geometric and electronic structure of clusters to be probed. This information can be used to obtain a deeper understanding of more complex systems, such as surfaces. In the research described here two directions have been followed. First, the extension or development of new techniques to study systems which were not previously accessible. Secondly, the application of available methods to a particular substance (here MgO clusters), to get a deeper insight into its properties. In the following the outcome of the research is summarized, followed by a perspective for future research directions.

### 6.1. Summary

In **chapter 3** a tunable IR-UV two-color ionization method was presented, which allows a wider range of neutral clusters to be studied. The method is based on a technique which has been used before in the mid-IR range, and is extended here to the far-IR. Neutral silicon clusters,  $\text{Si}_n$  with  $n=6,7,9$ , and 10, have been studied with this method. We have attempted to test our assumptions about the excitation mechanism. For a single cluster size,  $n=9$ , IR multiple photon dissociation spectroscopy of a messenger tagged cluster could also be applied, allowing a direct comparison of the two methods.

By combination of the two methods, it was possible to study silicon clusters of a broader size range, which allowed theoretical predictions for the structures of small silicon clusters and their growth pattern to be investigated. The results support previous theoretical predictions. It could be shown that smaller clusters,  $n=6-9$ , are based on bipyramidal motifs and only for  $n \geq 10$  is a tricapped trigonal prism motif found.

In the next chapter, **chapter 4**, magnesium oxide clusters are studied using several variants of IR multiple photon dissociation spectroscopy and the tunable IR-UV two-color ionization method. This system may play an important role in catalysis as, when doped appropriately, it is able to activate methane. This is the key step in the direct conversion of methane to more valuable products, which would reduce mankind's demand for oil. Within the cluster of excellence UniCat several research groups focussed on (doped) magnesium oxide. The gas-phase studies

undertaken here focused on several model systems for active centers, but also on reactive intermediates. These results allow testing and improvement of the theoretical modeling, and may thereby also have relevance for other studies, *e.g.* on extended MgO systems.

Initially, MgO clusters with the same number of oxygen and magnesium have been studied in the cationic and neutral charge states. The experimental spectra in combination with theoretical calculations provided by the Sauer group within the UniCat collaboration allowed the structures of these clusters to be determined. Surprisingly, these are quite different from the bulk structure. For neutral clusters, for instance, hexagonal tubes have been found for clusters of the composition  $(\text{MgO})_{3 \times k}$  with  $k=1-5$ . The other cluster sizes investigated are also based on the hexagonal ring motif and form cage-like structures. In contrast to the neutral clusters, the cations form more open structures.

In a second step, oxygen rich MgO clusters, *i.e.*  $\text{Mg}_n\text{O}_{n+1}$ , have been studied in their cationic, neutral, and anionic charge states. In these clusters dioxygen species can be present, which may be an active center, and have indeed been experimentally observed. Depending on the charge state of the cluster, superoxo, peroxy, or dissociated dioxygen have been found, for cation, neutral, and anion, respectively. These activated dioxygen species differ by the occupation of the antibonding  $\pi^*$  orbitals of the  $\text{O}_2$ . By changing the charge state of the cluster this occupation can be modified.

Another possibility to change the type of active center or the type of dioxygen species is by adding a single hydrogen atom. For cationic oxygen rich clusters it has been seen that, instead of a superoxo, a peroxy species is present in the cluster. The electron contributed by the hydrogen is transferred to the dioxygen. This is important for other reactivity studies, as it may make it more straightforward to investigate the reactivity of the peroxy unit, because charged clusters are more easily handled experimentally.

Reactions of cationic MgO clusters with carbon monoxide, water and methane have also been studied. For methane and CO indications have been found that both are only adsorbed molecularly on stoichiometric and oxygen rich clusters. For CO this was expected, as CO is often used to study the electronic structure of surfaces, including clusters. On cationic MgO clusters a strong blueshift of the CO stretching frequency has been observed, which is almost constant and independent of cluster composition and size. The results on the methane show that larger cationic clusters do not seem to be able to activate methane.

The reaction with water is important, as water would be formed in a catalytic process involving methane. This could, in principle, change and even poison the active centers. Intact water has only been found on one of the smallest clusters



studied,  $\text{MgO}_2^+$ . On all other cluster sizes investigated the first water molecule seems to dissociate.

In the last chapter, **chapter 5**, IR resonant enhanced multiple photon electron detachment spectroscopy (IR-REMPED) is presented and applied to transition-metal (carbide) cluster anions in a molecular beam using the intra-cavity free electron laser FELICE. These are the first experiments on charged clusters using this new FEL. For transition metal cluster anions no IR spectroscopy method was, to date, available to study their structure. This was due to a combination of difficulties in preparing their rare gas complexes, their low IR cross sections and the low photon energy in the vibrational fingerprint region of these systems.

In a proof-of-principle experiment tantalum carbide cluster anions have been studied and their IR spectra have been measured over a very wide wavelength range,  $200\text{--}2500\text{ cm}^{-1}$ , which covers almost the whole range available with this new FEL. Absorptions have been seen over the complete range, which could only be explained by assuming overtone and combination modes of the vibrational fundamentals, which are in the far-IR for metal-metal vibrations. Structural assignment has been performed by comparison with DFT calculations. In addition, anion photoelectron spectra have been taken for the same systems. This method is frequently used to study anionic systems, but often suffers from poor description of anions by theory. Now, the results from IR spectroscopy, PES, and theory can be combined and directly compared. Furthermore, information on the electron binding energy gives important information on how much energy needs to be pumped into the systems by the IR light for IR-REMPED to occur.

In a second step the sensitivity of the method has been increased, using niobium clusters with a single or two carbons to allow spectroscopy at even lower IR photon energy. This finally allowed the IR spectra of bare niobium cluster anions to be measured, which are also the first IR spectra for anionic transition metal clusters.

## 6.2. Perspectives for future research

The two very generally applicable vibrational spectroscopy methods, tunable IR-UV two-color ionization and IR resonance enhanced multiple photon electron detachment may have significant impact on the field of mass-selective IR spectroscopy of gas-phase species because of their versatility.

The two-color ionization method allows neutral clusters to be studied without a possible perturbation from a messenger, which is normally used to study such systems. Complex formation, which can also be very demanding, is not longer required. By using tunable UV radiation it should be possible to further extend the spectral wavelength range to even lower IR photon energy and more species.

The number of required IR photons, which has a direct influence on the width of the absorption bands, can also be reduced by a corresponding increase in the UV photon energy. This should lead to better resolved IR spectra. Temperature dependent effects on the spectra should be accessible with this method.

IR resonance enhanced multiple photon electron detachment spectroscopy on the other hand allows to study the geometric structure of (transition metal) cluster anions, which can be different from those of their neutral or cationic counterparts. This could provide theory with benchmark data for cluster anions, which may allow to improve their modeling, which is at least at DFT level, sometimes still questionable.

The properties of clusters often vary drastically with cluster size. Until now, it was often only possible to investigate a single aspect or property. By combining several experimental methods which probe the geometry and electronic structure more information can be obtained, which will allow for a deeper understanding. The electronic structure of clusters can be studied with various methods, *e.g.* photoelectron spectroscopy, UV-VIS spectroscopy, or X-ray absorption spectroscopy to study core levels. The interpretation and detailed understanding of these spectra benefits dramatically from knowing what the geometry is. A step into this direction has already been made in this thesis by combining IR-REMPED and photoelectron spectroscopy.

Similar studies could provide interesting insights also for MgO clusters. As their structures are now precisely known, more details of their electronic structure, which governs the reactivity of these systems, could be investigated by, for instance, optical spectroscopy. This however, has to be done in the VUV range. By selective doping, *e.g.* with transition metal atoms, it should also be possible to tune these properties. Such species can now be produced with the new dual-target source developed.

## A. Low energy isomers for $\text{Mg}_n\text{O}_{n+1}^{+,0,-}$ clusters

$\text{Mg}_n\text{O}_{n+1}^+$  clusters

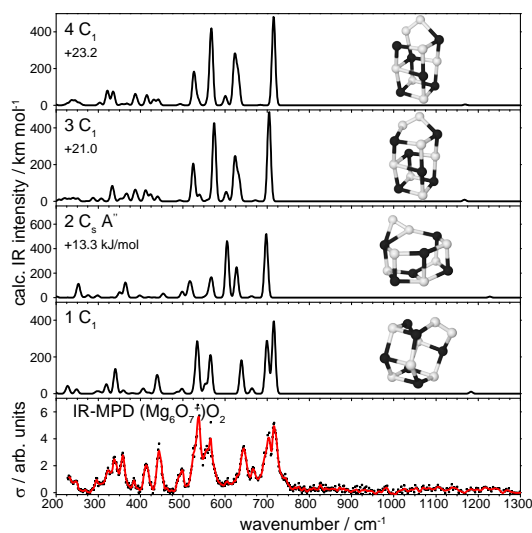


Figure A.1.: Vibrational spectra of  $\text{Mg}_6\text{O}_7^+$  clusters and comparison to the calculated linear absorption spectra of several low energy structures.

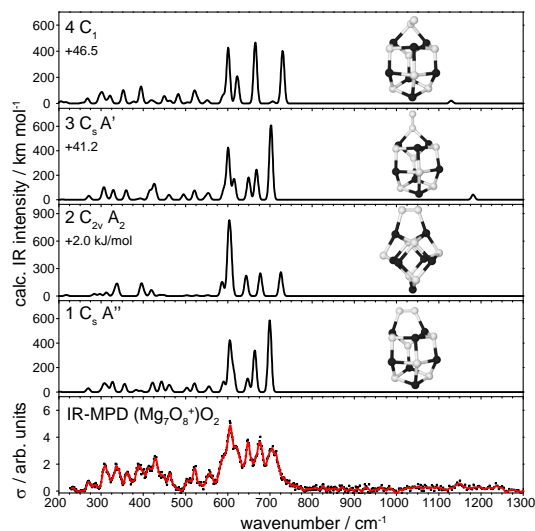


Figure A.2.: Vibrational spectra of  $\text{Mg}_7\text{O}_8^+$  clusters and comparison to the calculated linear absorption spectra of several low energy structures.

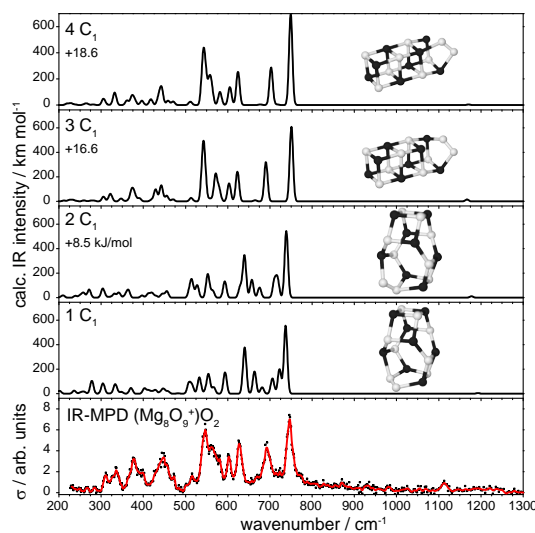


Figure A.3.: Vibrational spectra of  $\text{Mg}_8\text{O}_9^+$  clusters and comparison to the calculated linear absorption spectra of several low energy structures.

## Mg<sub>n</sub>O<sub>n+1</sub> clusters

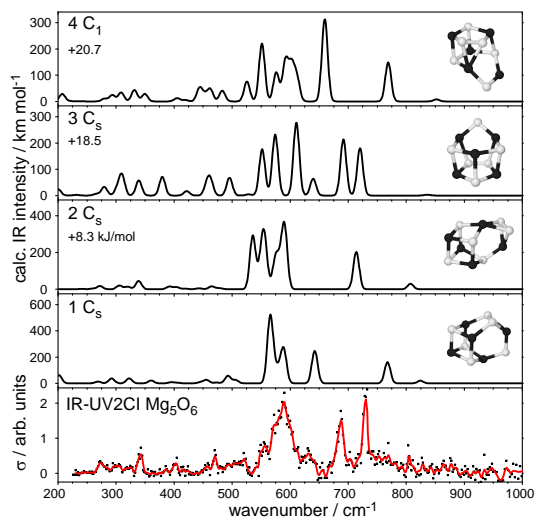


Figure A.4.: Vibrational spectra of Mg<sub>5</sub>O<sub>6</sub> clusters and comparison to the calculated linear absorption spectra of several low energy structures.

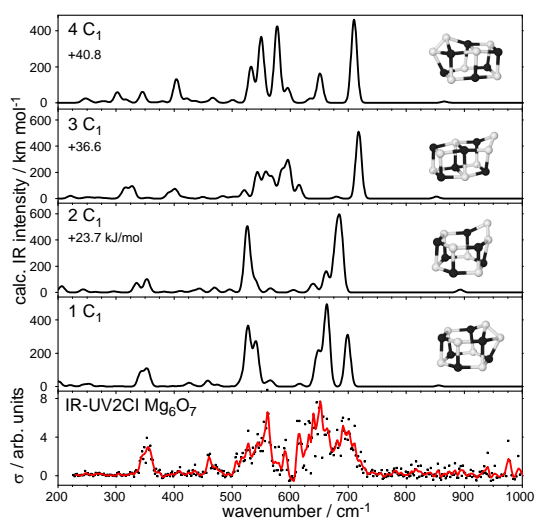


Figure A.5.: Vibrational spectra of Mg<sub>6</sub>O<sub>7</sub> clusters and comparison to the calculated linear absorption spectra of several low energy structures.

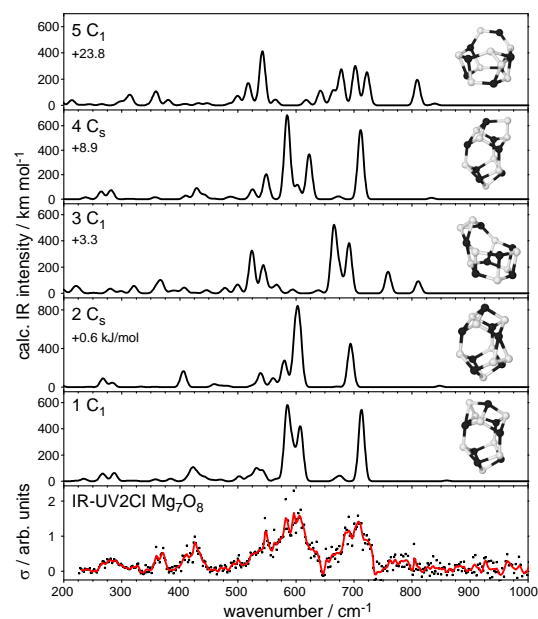


Figure A.6.: Vibrational spectra of  $\text{Mg}_7\text{O}_8$  clusters and comparison to the calculated linear absorption spectra of several low energy structures.

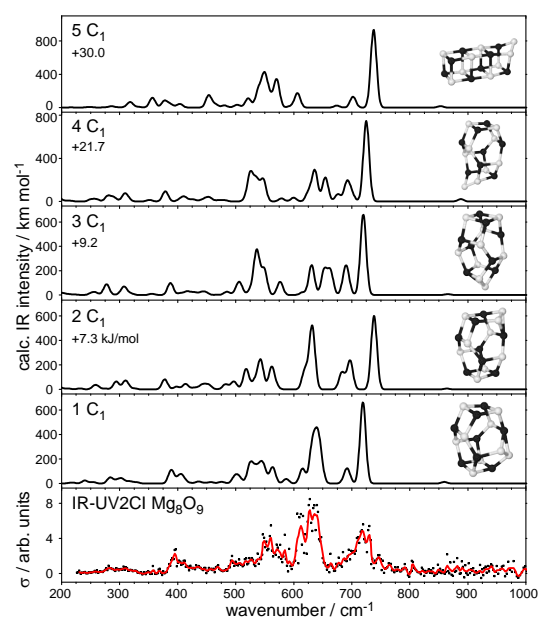


Figure A.7.: Vibrational spectra of  $\text{Mg}_8\text{O}_9$  clusters and comparison to the calculated linear absorption spectra of several low energy structures.

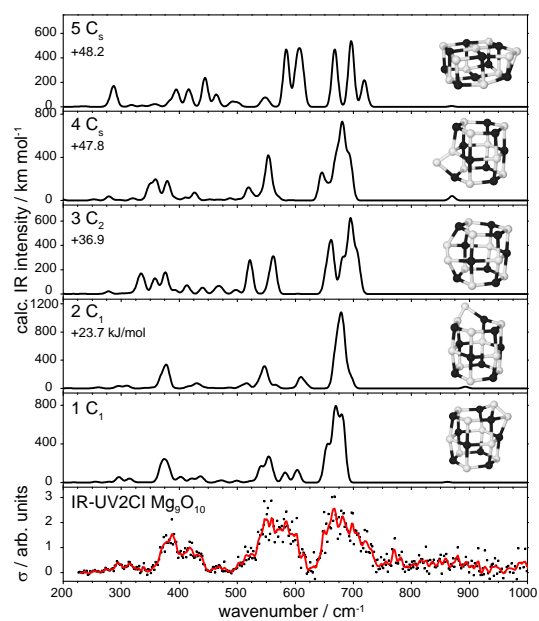


Figure A.8.: Vibrational spectra of  $\text{Mg}_9\text{O}_{10}$  clusters and comparison to the calculated linear absorption spectra of several low energy structures.

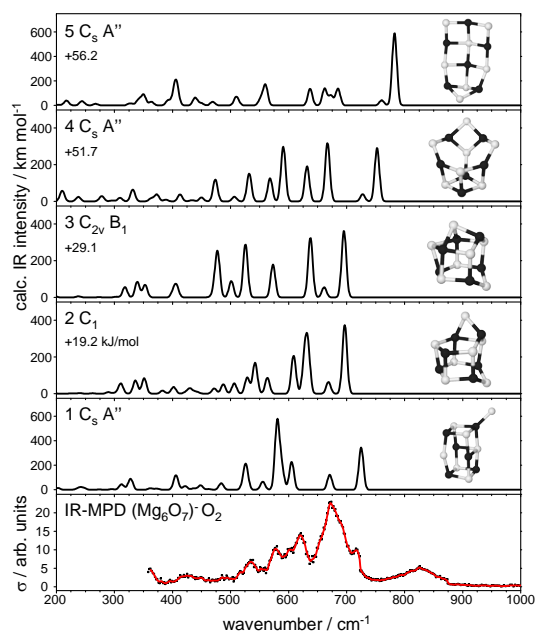
$\text{Mg}_n\text{O}_{n+1}^-$  clusters

Figure A.9.: Vibrational spectra of  $\text{Mg}_6\text{O}_7^-$  clusters and comparison to the calculated linear absorption spectra of several low energy structures.



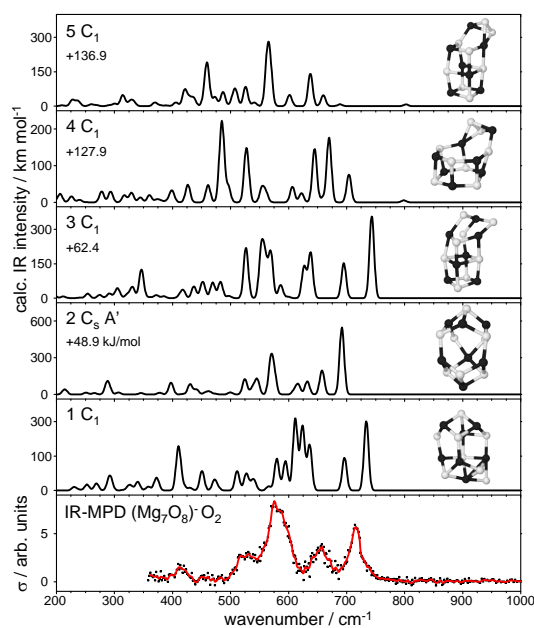


Figure A.10.: Vibrational spectra of  $\text{Mg}_7\text{O}_8^-$  clusters and comparison to the calculated linear absorption spectra of several low energy structures.

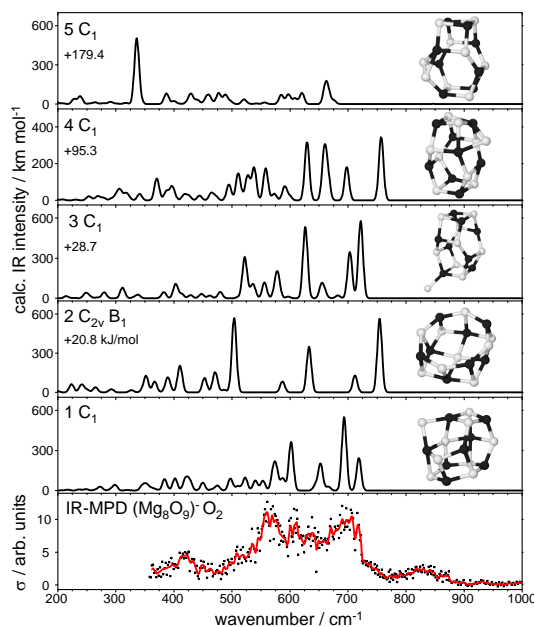


Figure A.11.: Vibrational spectra of  $\text{Mg}_8\text{O}_9^-$  clusters and comparison to the calculated linear absorption spectra of several low energy structures.

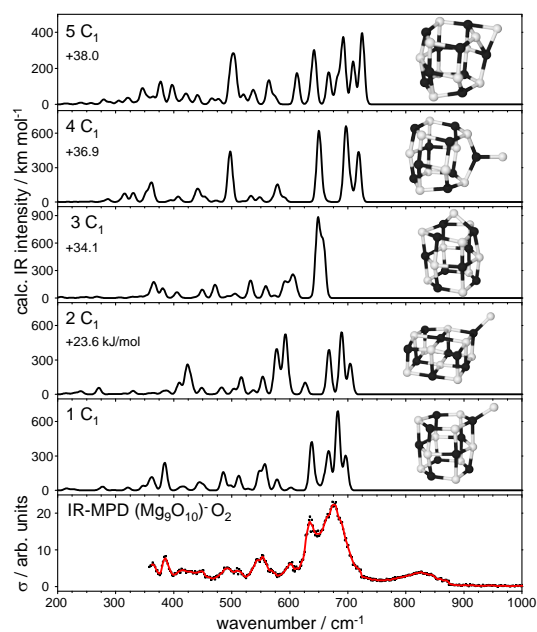


Figure A.12.: Vibrational spectra of  $\text{Mg}_9\text{O}_{10}^-$  clusters and comparison to the calculated linear absorption spectra of several low energy structures.

## Bibliography

- [1] W. A. de Heer. The physics of simple metal-clusters - Experimental aspects and simple-models. *Rev. Mod. Phys.* **65** (1993) 611.
- [2] G. Ertl and H. J. Freund. Catalysis and surface science. *Phys. Today* **52** (1999) 32.
- [3] N. Nilius, T. Risse, S. Schauermaun, S. Shaikhutdinov, M. Sterrer, and H. J. Freund. Model studies in catalysis. *Top. Catal.* **54** (2011) 4.
- [4] M. Haruta, T. Kobayashi, H. Sano, and N. Yamada. Novel gold catalysts for the oxidation of carbon-monoxide at a temperature far below 0 °C. *Chem. Lett.* **16** (1987) 405.
- [5] M. Haruta. Size- and support-dependency in the catalysis of gold. *Catal. Today* **36** (1997) 153.
- [6] F. Boccuzzi, A. Chiorino, M. Manzoli, P. Lu, T. Akita, S. Ichikawa, and M. Haruta. Au/TiO<sub>2</sub> nanosized samples: A catalytic, TEM, and FTIR study of the effect of calcination temperature on the CO oxidation. *J. Catal.* **202** (2001) 256.
- [7] L. M. Molina and B. Hammer. Theoretical study of CO oxidation on Au nanoparticles supported by MgO(100). *Phys. Rev. B* **69** (2004) 155424.
- [8] M. S. Chen and D. W. Goodman. The structure of catalytically active gold on titania. *Science* **306** (2004) 252.
- [9] N. Lopez, T. V. W. Janssens, B. S. Clausen, Y. Xu, M. Mavrikakis, T. Bligaard, and J. K. Norskov. On the origin of the catalytic activity of gold nanoparticles for low-temperature CO oxidation. *J. Catal.* **223** (2004) 232.
- [10] B. Yoon, H. Häkkinen, U. Landman, A. S. Wörz, J. M. Antonietti, S. Abbet, K. Judai, and U. Heiz. Charging effects on bonding and catalyzed oxidation of CO on Au<sub>8</sub> clusters on MgO. *Science* **307** (2005) 403.
- [11] M. Chen and D. W. Goodman. Catalytically active gold: From nanoparticles to ultrathin films. *Acc. Chem. Res.* **39** (2006) 739.

- [12] M. Chen, Y. Cai, Z. Yan, and D. W. Goodman. On the origin of the unique properties of supported Au nanoparticles. *J. Am. Chem. Soc.* **128** (2006) 6341.
- [13] S. Laursen and S. Linic. Oxidation catalysis by oxide-supported Au nanostructures: The role of supports and the effect of external conditions. *Phys. Rev. Lett.* **97** (2006) 026101.
- [14] X. Lin, B. Yang, H. M. Benia, P. Myrach, M. Yulikov, A. Aumer, M. A. Brown, M. Sterrer, O. Bondarchuk, E. Kieseritzky, J. Rocker, T. Risse, H. J. Gao, N. Nilius, and H. J. Freund. Charge-mediated adsorption behavior of CO on MgO-supported Au clusters. *J. Am. Chem. Soc.* **132** (2010) 7745.
- [15] A. Sanchez, S. Abbet, U. Heiz, W. D. Schneider, H. Häkkinen, R. N. Barnett, and U. Landman. When gold is not noble: Nanoscale gold catalysts. *J. Phys. Chem. A* **103** (1999) 9573.
- [16] G. Pacchioni, L. Giordano, and M. Baistrocchi. Charging of metal atoms on ultrathin MgO/Mo(100) films. *Phys. Rev. Lett.* **94** (2005) 226104.
- [17] C. Harding, V. Habibpour, S. Kunz, A. N. S. Farnbacher, U. Heiz, B. Yoon, and U. Landman. Control and manipulation of gold nanocatalysis: Effects of metal oxide support thickness and composition. *J. Am. Chem. Soc.* **131** (2009) 538.
- [18] M. E. Vaida, T. M. Bernhardt, C. Barth, F. Esch, U. Heiz, and U. Landman. Ultrathin magnesia films as support for molecules and metal clusters: Tuning reactivity by thickness and composition. *Phys. Status Solidi B* **247** (2010) 1001.
- [19] R. R. Hudgins, M. Imai, M. F. Jarrold, and P. Dugourd. High-resolution ion mobility measurements for silicon cluster anions and cations. *J. Chem. Phys.* **111** (1999) 7865.
- [20] D. Schooss, P. Weis, O. Hampe, and M. M. Kappes. Determining the size-dependent structure of ligand-free gold-cluster ions. *Philos. Trans. R. Soc. London, Ser. A* **368** (2010) 1211.
- [21] M. Maier-Borst, D. B. Cameron, M. Rokni, and J. H. Parks. Electron diffraction of trapped cluster ions. *Phys. Rev. A* **59** (1999) R3162.
- [22] D. Schooss, M. N. Blom, J. H. Parks, B. von Issendorff, H. Haberland, and M. M. Kappes. The structures of  $\text{Ag}_{55}^{+}$  and  $\text{Ag}_{55}^{-}$ : Trapped ion electron diffraction and density functional theory. *Nano Lett.* **5** (2005) 1972.

- [23] A. Lechtken, C. Neiss, J. Stairs, and D. Schooss. Comparative study of the structures of copper, silver, and gold icosamers: Influence of metal type and charge state. *J. Chem. Phys.* **129** (2008) 154304.
- [24] P. Gruene, D. M. Rayner, B. Redlich, A. F. G. van der Meer, J. T. Lyon, G. Meijer, and A. Fielicke. Structures of neutral Au<sub>7</sub>, Au<sub>19</sub>, and Au<sub>20</sub> clusters in the gas phase. *Science* **321** (2008) 674.
- [25] W. T. Wallace and R. L. Whetten. Coadsorption of CO and O<sub>2</sub> on selected gold clusters: Evidence for efficient room-temperature CO<sub>2</sub> generation. *J. Am. Chem. Soc.* **124** (2002) 7499.
- [26] L. D. Socaciu, J. Hagen, T. M. Bernhardt, L. Wöste, U. Heiz, H. Häkkinen, and U. Landman. Catalytic CO oxidation by free Au<sub>2</sub><sup>-</sup>: Experiment and theory. *J. Am. Chem. Soc.* **125** (2003) 10437.
- [27] D. Stolcic, M. Fischer, G. Ganteför, Y. D. Kim, Q. Sun, and P. Jena. Direct observation of key reaction intermediates on gold clusters. *J. Am. Chem. Soc.* **125** (2003) 2848.
- [28] A. P. Woodham, G. Meijer, and A. Fielicke. Activation of molecular oxygen by anionic gold clusters. *Angew. Chem., Int. Ed.* **51** (2012) 4444.
- [29] L. M. Molina and B. Hammer. The activity of the tetrahedral Au<sub>20</sub> cluster: charging and impurity effects. *J. Catal.* **233** (2005) 399.
- [30] M. Sterrer, M. Yulikov, E. Fischbach, M. Heyde, H. P. Rust, G. Pacchioni, T. Risse, and H. J. Freund. Interaction of gold clusters with color centers on MgO(001) films. *Angew. Chem., Int. Ed.* **45** (2006) 2630.
- [31] K. R. Asmis, G. Santambrogio, M. Brummer, and J. Sauer. Polyhedral vanadium oxide cages: Infrared spectra of cluster anions and size-induced d electron localization. *Angew. Chem., Int. Ed.* **44** (2005) 3122.
- [32] H. Häkkinen, W. Abbet, A. Sanchez, U. Heiz, and U. Landman. Structural, electronic, and impurity-doping effects in nanoscale chemistry: Supported gold nanoclusters. *Angew. Chem., Int. Ed.* **42** (2003) 1297.
- [33] S. S. Lee, C. Y. Fan, T. P. Wu, and S. L. Anderson. CO oxidation on Au<sub>n</sub>/TiO<sub>2</sub> catalysts produced by size-selected cluster deposition. *J. Am. Chem. Soc.* **126** (2004) 5682.
- [34] R. Casaes, R. Provencal, J. Paul, and R. J. Saykally. High resolution pulsed infrared cavity ringdown spectroscopy: Application to laser ablated carbon clusters. *J. Chem. Phys.* **116** (2002) 6640.

- [35] M. D. Morse, J. B. Hopkins, P. R. R. Langridge-Smith, and R. E. Smalley. Spectroscopic studies of the jet-cooled copper trimer. *J. Chem. Phys.* **79** (1983) 5316.
- [36] P. J. Brucat, L. S. Zheng, C. L. Pettiette, S. Yang, and R. E. Smalley. Metal cluster ion photofragmentation. *J. Chem. Phys.* **84** (1986) 3078.
- [37] M. F. Jarrold and K. M. Creegan. Photodissociation of copper clusters,  $\text{Cu}_n^+$  ( $n=3-8$ ), in the 370–710 nm wavelength region. *Int. J. Mass Spectrom. Ion Processes* **102** (1990) 161.
- [38] H. Häkkinen, B. Yoon, U. Landman, X. Li, H. J. Zhai, and L. S. Wang. On the electronic and atomic structures of small  $\text{Au}_n^-$  ( $n=4-14$ ) clusters: A photoelectron spectroscopy and density-functional study. *J. Phys. Chem. A* **107** (2003) 6168.
- [39] J. Li, X. Li, H. J. Zhai, and L. S. Wang.  $\text{Au}_{20}$ : A tetrahedral cluster. *Science* **299** (2003) 864.
- [40] B. von Issendorff and O. Cheshnovsky. Metal to insulator transitions in clusters. *Annu. Rev. Phys. Chem.* **56** (2005) 549.
- [41] D. M. Neumark. Slow electron velocity-map imaging of negative ions: Applications to spectroscopy and dynamics. *J. Phys. Chem. A* **112** (2008) 13287.
- [42] K. Hansen, R. Müller, P. Brockhaus, E. E. B. Campbell, and I. V. Hertel. Resonant two-photon ionisation spectroscopy of  $\text{C}_{60}$ . *Z. Phys. D: At., Mol. Clusters* **42** (1997) 153.
- [43] J. T. Lau, J. Rittmann, V. Zamudio-Bayer, M. Vogel, K. Hirsch, P. Klar, F. Lofink, T. Möller, and B. von Issendorff. Size dependence of L(2,3) branching ratio and 2p core-hole screening in X-Ray absorption of metal clusters. *Phys. Rev. Lett.* **101** (2008) 153401.
- [44] J. T. Lau, K. Hirsch, P. Klar, A. Langenberg, F. Lofink, R. Richter, J. Rittmann, M. Vogel, V. Zamudio-Bayer, T. Möller, and B. von Issendorff. X-ray spectroscopy reveals high symmetry and electronic shell structure of transition-metal-doped silicon clusters. *Phys. Rev. A* **79** (2009) 053201.
- [45] K. Hirsch, J. T. Lau, P. Klar, A. Langenberg, J. Probst, J. Rittmann, M. Vogel, V. Zamudio-Bayer, T. Möller, and B. von Issendorff. X-ray spectroscopy on size-selected clusters in an ion trap: From the molecular limit to bulk properties. *J. Phys. B: At., Mol. Opt. Phys.* **42** (2009) 154029.

- [46] J. T. Lau, M. Vogel, A. Langenberg, K. Hirsch, J. Rittmann, V. Zamudio-Bayer, T. Möller, and B. von Issendorff. Highest occupied molecular orbital-lowest unoccupied molecular orbital gaps of doped silicon clusters from core level spectroscopy. *J. Chem. Phys.* **134** (2011) 041102.
- [47] M. Vogel, C. Kasigkeit, K. Hirsch, A. Langenberg, J. Rittmann, V. Zamudio-Bayer, A. Kulesza, R. Mitric, T. Möller, B. von Issendorff, and J. T. Lau. 2p core-level binding energies of size-selected free silicon clusters: Chemical shifts and cluster structure. *Phys. Rev. B* **85** (2012) 195454.
- [48] S. Peredkov, M. Neeb, W. Eberhardt, J. Meyer, M. Tombers, H. Kampschulte, and G. Niedner-Schatteburg. Spin and orbital magnetic moments of free nanoparticles. *Phys. Rev. Lett.* **107** (2011) 233401.
- [49] M. Niemeyer, K. Hirsch, V. Zamudio-Bayer, A. Langenberg, M. Vogel, M. Kossick, C. Ebrecht, K. Egashira, A. Terasaki, T. Möller, B. von Issendorff, and J. T. Lau. Spin coupling and orbital angular momentum quenching in free iron clusters. *Phys. Rev. Lett.* **108** (2012) 057201.
- [50] M. B. Knickelbein. Reactions of transition metal clusters with small molecules. *Annu. Rev. Phys. Chem.* **50** (1999) 79.
- [51] G. von Helden, I. Holleman, G. M. H. Knippels, A. F. G. van der Meer, and G. Meijer. Infrared resonance enhanced multiphoton ionization of fullerenes. *Phys. Rev. Lett.* **79** (1997) 5234.
- [52] G. von Helden, D. van Heijnsbergen, and G. Meijer. Resonant ionization using IR light: A new tool to study the spectroscopy and dynamics of gas-phase molecules and clusters. *J. Phys. Chem. A* **107** (2003) 1671.
- [53] K. Asmis, A. Fielicke, G. von Helden, and G. Meijer. *Atomic Clusters: From Gas Phase to Deposited (The Chemical Physics of Solid Surfaces)*, volume 12. Elsevier Science (2007). ISBN 0444527567.
- [54] M. Okumura, L. I. Yeh, C. S., J. D. Myers, and Y. T. Lee. Infrared-spectra of the cluster ions  $\text{H}_7\text{O}_3^+ \cdot \text{H}_2$  and  $\text{H}_9\text{O}_4^+ \cdot \text{H}_2$ . *J. Chem. Phys.* **85** (1986) 2328.
- [55] J. T. Lyon, P. Gruene, A. Fielicke, G. Meijer, E. Janssens, P. Claes, and P. Lievens. Structures of silicon cluster cations in the gas phase. *J. Am. Chem. Soc.* **131** (2009) 1115.
- [56] A. Fielicke, A. Kirilyuk, C. Ratsch, J. Behler, M. Scheffler, G. von Helden, and G. Meijer. Structure determination of isolated metal clusters via far-infrared spectroscopy. *Phys. Rev. Lett.* **93** (2004) 023401.

- [57] U. Boesl and W. J. Knott. Negative ions, mass selection, and photoelectrons. *Mass Spectrom. Rev.* **17** (1998) 275.
- [58] M. W. Siegel, R. J. Celotta, J. L. Hall, J. Levine, and R. A. Bennett. Molecular photodetachment spectrometry. I. The electron affinity of nitric oxide and the molecular constants of  $\text{NO}^-$ . *Phys. Rev. A* **6** (1972) 607.
- [59] L. A. Posey, M. J. Deluca, and M. A. Johnson. Demonstration of a pulsed photoelectron spectrometer on mass-selected negative ions:  $\text{O}^-$ ,  $\text{O}_2^-$ , and  $\text{O}_4^-$ . *Chem. Phys. Lett.* **131** (1986) 170.
- [60] P. Kruit and F. H. Read. Magnetic-field parallelizer for  $2\pi$  electronspectrometer and electron-image magnifier. *J. Phys. E: Sci. Instrum.* **16** (1983) 313.
- [61] O. Cheshnovsky, S. H. Yang, C. L. Pettiette, M. J. Craycraft, and R. E. Smalley. Magnetic time-of-flight photoelectron spectrometer for mass-selected negative cluster ions. *Rev. Sci. Instrum.* **58** (1987) 2131.
- [62] T. N. Kitsopoulos, I. M. Waller, J. G. Loeser, and D. M. Neumark. High-resolution threshold photodetachment spectroscopy of negative-ions. *Chem. Phys. Lett.* **159** (1989) 300.
- [63] A. T. J. B. Eppink and D. H. Parker. Velocity map imaging of ions and electrons using electrostatic lenses: Application in photoelectron and photofragment ion imaging of molecular oxygen. *Rev. Sci. Instrum.* **68** (1997) 3477.
- [64] S. J. Cavanagh, S. T. Gibson, M. N. Gale, C. J. Dedman, E. H. Roberts, and B. R. Lewis. High-resolution velocity-map-imaging photoelectron spectroscopy of the  $\text{O}^-$  photodetachment fine-structure transitions. *Phys. Rev. A* **76** (2007) 052708.
- [65] For general overview of VMI and comparison of different inversion methods see: B. Whitaker, editor. *Imaging in Molecular Dynamics: Technology and Applications*. Cambridge University Press (2003). ISBN 0521810590.
- [66] J. Cooper and R. N. Zare. Angular distribution of photoelectrons. *J. Chem. Phys.* **48** (1968) 942.
- [67] W. Demtröder. *Atoms, molecules and photons: An introduction to atomic-, molecular-, and quantum-physics*. Springer, Berlin London (2006). ISBN 3540206310.
- [68] D. Wales. *Energy landscapes*. Cambridge University Press, Cambridge, UK New York (2003). ISBN 0521814154.



- [69] P. Bernath. *Spectra of atoms and molecules*. Oxford University Press, New York (2005). ISBN 0195177592.
- [70] P. M. Morse. Diatomic molecules according to the wave mechanics. II. Vibrational levels. *Phys. Rev.* **34** (1929) 57.
- [71] D. E. Cooper, C. M. Klimcak, and J. E. Wessel. Ion dip spectroscopy - A new technique of multi-photon ionization spectroscopy applied to  $I_2$ . *Phys. Rev. Lett.* **46** (1981) 324.
- [72] M. Putter, G. von Helden, and G. Meijer. Mass selective infrared spectroscopy using a free electron laser. *Chem. Phys. Lett.* **258** (1996) 118.
- [73] D. van Heijnsbergen, G. von Helden, G. Meijer, and M. A. Duncan. Infrared resonance-enhanced multiphoton ionization spectroscopy of magnesium oxide clusters. *J. Chem. Phys.* **116** (2002) 2400.
- [74] M. B. Knickelbein. Photodissociation spectroscopy of  $Cu_3$ ,  $Cu_3Ar$ , and  $Cu_3Kr$ . *J. Chem. Phys.* **100** (1994) 4729.
- [75] K. R. Asmis, M. Brümmer, C. Kaposta, G. Santambrogio, G. von Helden, G. Meijer, K. Rademann, and L. Wöste. Mass-selected infrared photodissociation spectroscopy of  $V_4O_{10}^+$ . *Phys. Chem. Chem. Phys.* **4** (2002) 1101.
- [76] B. A. Collings, K. Athanassenas, D. Lacombe, D. M. Rayner, and P. A. Hackett. Optical-absorption spectra of  $Au_7$ ,  $Au_9$ ,  $Au_{11}$  and  $Au_{13}$  and their cations - Gold clusters with 6, 7, 8, 9, 10, 11, 12, and 13 s-electrons. *J. Chem. Phys.* **101** (1994) 3506.
- [77] B. A. Collings, K. Athanassenas, D. M. Rayner, and P. A. Hackett. Optical spectroscopy of  $Ag_7$ ,  $Ag_9^+$ , and  $Ag_9$  - A test of the photodepletion method. *Chem. Phys. Lett.* **227** (1994) 490.
- [78] S. Minemoto, A. Terasaki, and T. Kondow. Electronic structures of cobalt cluster cations: Photodissociation spectroscopy of  $Co_n^+Ar$  ( $n=3-5$ ) in the visible to near-infrared range. *J. Chem. Phys.* **104** (1996) 5770.
- [79] S. Minemoto, A. Terasaki, and T. Kondow. Electronic and geometric structures of vanadium cluster ions;  $V_n^+$  ( $n=3-5$ ), studied by optical absorption spectroscopy. *J. Electron Spectrosc. Relat. Phenom.* **106** (2000) 171.
- [80] J. M. Antonietti, A. Chatelain, and S. Fedrigo. Ultraviolet-visible photodissociation spectra of  $V_n^+Xe$  ( $n=5-8$ ) cluster complex cations. *J. Chem. Phys.* **114** (2001) 2981.

- [81] S. Gilb, K. Jacobsen, D. Schooss, F. Furche, R. Ahlrichs, and M. M. Kappes. Electronic photodissociation spectroscopy of  $\text{Au}_n^- \cdot \text{Xe}$  ( $n=7-11$ ) versus time-dependent density functional theory prediction. *J. Chem. Phys.* **121** (2004) 4619.
- [82] J. M. Antonietti, F. Conus, A. Chatelain, and S. Fedrigo. Photodissociation spectra of cationic xenon-silicon cluster complexes  $\text{Si}_n^+ \text{Xe}$  ( $n=2-13$ ). *Phys. Rev. B* **68** (2003) 035420.
- [83] A. Fielicke, G. von Helden, and G. Meijer. Far-infrared spectroscopy of isolated transition metal clusters. *Eur. Phys. J. D* **34** (2005) 83.
- [84] K. R. Asmis and J. Sauer. Mass-selective vibrational spectroscopy of vanadium oxide cluster ions. *Mass Spectrom. Rev.* **26** (2007) 542.
- [85] W. Haynes, editor. *CRC Handbook of Chemistry and Physics, 92nd Edition*. CRC Press (2011). ISBN 1439855110.
- [86] J. G. Black, E. Yablonovitch, N. Bloembergen, and S. Mukamel. Collisionless multiphoton dissociation of  $\text{SF}_6$  - Statistical thermodynamic process. *Phys. Rev. Lett.* **38** (1977) 1131.
- [87] S. E. Stein and B. Rabinovitch. Accurate evaluation of internal energy-level sums and densities including anharmonic oscillators and hindered rotors. *J. Chem. Phys.* **58** (1973) 2438.
- [88] J. M. L. Martin, J. ElYazal, and J. P. Francois. Structure and vibrational spectrum of some polycyclic aromatic compounds studied by density functional theory .1. Naphthalene, azulene, phenanthrene, and anthracene. *J. Phys. Chem.* **100** (1996) 15358.
- [89] P. M. Felker and A. H. Zewail. Dynamics of intramolecular vibrational-energy redistribution (IVR). 2. Excess energy-dependence. *J. Chem. Phys.* **82** (1985) 2975.
- [90] J. Oomens, A. G. G. M. Tielens, B. G. Sartakov, G. von Helden, and G. Meijer. Laboratory infrared spectroscopy of cationic polycyclic aromatic hydrocarbon molecules. *Astrophys. J.* **591** (2003) 968.
- [91] A. Bekkerman, E. Kolodney, G. von Helden, B. Sartakov, D. van Heijnsbergen, and G. Meijer. Infrared multiphoton ionization of superhot  $\text{C}_{60}$ : Experiment and model calculations. *J. Chem. Phys.* **124** (2006) 184312.
- [92] G. M. H. Knippels. *The Short-Pulse Free-Electron-Laser: Manipulation of the Gain Medium*. Ph.D. thesis, Vrije Universiteit, Amsterdam (1996).

- [93] B. W. J. McNeil and N. R. Thompson. X-ray free-electron lasers. *Nature Photon.* **4** (2010) 814.
- [94] J. Ullrich, A. Rudenko, and R. Moshhammer. Free-electron lasers: New avenues in molecular physics and photochemistry. *Annu. Rev. Phys. Chem.* **63** (2012) 635.
- [95] T. C. Marshall. *Free Electron Lasers*. Macmillan USA (1985). ISBN 0029486203.
- [96] H. Onuki and P. Elleaume, editors. *Undulators, Wigglers and Their Applications*. CRC Press (2002). ISBN 0415280400.
- [97] W. B. Colson, E. D. Johnson, M. J. Kelley, and H. A. Schwettman. Putting free-electron lasers to work. *Phys. Today* **55** (2002) 35.
- [98] Z. R. Huang and K. J. Kim. Review of x-ray free-electron laser theory. *Phys. Rev. ST Accel. Beams* **10** (2007) 034801.
- [99] D. Oepts, A. F. G. van der Meer, and P. W. van Amersfoort. The Free-Electron-Laser User Facility Felix. *Infrared Phys. Technol.* **36** (1995) 297.
- [100] Detailed descriptions of the Berlin and FELIX setups (including the vacuum systems) and details on IR-MPD using the second setup can be found in: Philipp Grüne. *Structure and Reactivity of Metal and Semiconductor Clusters in the Gas Phase*. Ph.D. thesis, Technische Universität Berlin (2009).
- [101] M. Yamashita and J. B. Fenn. Electrospray ion-source - Another variation on the free-jet theme. *J. Phys. Chem.* **88** (1984) 4451.
- [102] J. Ho, K. M. Ervin, and W. C. Lineberger. Photoelectron-spectroscopy of metal cluster anions -  $\text{Cu}_n^-$ ,  $\text{Ag}_n^-$ , and  $\text{Au}_n^-$ . *J. Chem. Phys.* **93** (1990) 6987.
- [103] G. Ganteför, H. R. Siekmann, H. O. Lutz, and K. H. Meiwes-Broer. Pure metal and metal-doped rare-gas clusters grown in a pulsed-arc cluster ion-source. *Chem. Phys. Lett.* **165** (1990) 293.
- [104] T. G. Dietz, M. A. Duncan, D. E. Powers, and R. E. Smalley. Laser production of supersonic metal cluster beams. *J. Chem. Phys.* **74** (1981) 6511.
- [105] D. E. Powers, S. G. Hansen, M. E. Geusic, A. C. Puiiu, J. B. Hopkins, T. G. Dietz, M. A. Duncan, P. R. R. Langridge-Smith, and R. E. Smalley. Supersonic metal cluster beams - Laser photo-ionization studies of  $\text{Cu}_2$ . *J. Phys. Chem.* **86** (1982) 2556.

- [106] V. E. Bondybey and J. H. English. Laser-induced fluorescence of metal-clusters produced by laser vaporization - Gas-phase spectrum of  $\text{Pb}_2$ . *J. Chem. Phys.* **74** (1981) 6978.
- [107] M. A. Duncan. Invited review article: Laser vaporization cluster sources. *Rev. Sci. Instrum.* **83** (2012) 041101.
- [108] A. Y. Vorobyev and C. L. Guo. Reflection of femtosecond laser light in multiple pulse ablation of metals. *J. Appl. Phys.* **110** (2011) 043102.
- [109] S. Nonose, Y. Sone, K. Onodera, S. Susdo, and K. Kaya. Structure and reactivity of bimetallic  $\text{Co}_n\text{V}_m$  clusters. *J. Phys. Chem.* **94** (1990) 2744.
- [110] W. Bouwen, P. Thoen, F. Vanhoutte, S. Bouckaert, F. Despa, H. Weidele, R. E. Silverans, and P. Lievens. Production of bimetallic clusters by a dual-target dual-laser vaporization source. *Rev. Sci. Instrum.* **71** (2000) 54.
- [111] R. L. Wagner, W. D. Vann, and A. W. Castleman, Jr. A technique for efficiently generating bimetallic clusters. *Rev. Sci. Instrum.* **68** (1997) 3010.
- [112] T. Hihara, S. Pokrant, and J. A. Becker. Magnetic moments and chemical bonding in isolated  $\text{Bi}_N\text{Co}_M$  clusters. *Chem. Phys. Lett.* **294** (1998) 357.
- [113] M. Turra, B. Waldschmidt, B. Kaiser, and R. Schäfer. An improved time-of-flight method for cluster deposition and ion-scattering experiments. *Rev. Sci. Instrum.* **79** (2008) 013905.
- [114] D. Banser, M. Schnell, J. U. Grabow, E. J. Cocinero, A. Lesarri, and J. L. Alonso. The internuclear potential, electronic structure, and chemical bond of tellurium selenide. *Angew. Chem., Int. Ed.* **44** (2005) 6311.
- [115] W. C. Wiley and I. H. McLaren. Time-of-flight mass spectrometer with improved resolution. *Rev. Sci. Instrum.* **26** (1955) 1150.
- [116] B. A. Mamyrin. Laser-assisted reflectron time-of-flight mass-spectrometry. *Int. J. Mass Spectrom. Ion Processes* **131** (1994) 1.
- [117] A. Schweizer, J. M. Weber, S. Gilb, H. Schneider, D. Schooss, and M. M. Kappes. Electronic photodissociation spectroscopy of  $\text{Au}_4^+ \cdot \text{Ar}_n$ ,  $n=0-4$ : Experiment and theory. *J. Chem. Phys.* **119** (2003) 3699.
- [118] G. M. Roberts, J. L. Nixon, J. Lecointre, E. Wrede, and J. R. R. Verlet. Toward real-time charged-particle image reconstruction using polar onion-peeling. *Rev. Sci. Instrum.* **80** (2009) 053104.

- [119] <http://www.dur.ac.uk/chemistry/lsd/groups/j.r.r.verlet/research/-clusters/pop/>.
- [120] T. A. M. Van Kleef. Structure and Zeeman effect in the spectrum of the iridium atom, Ir I. *Physica* **23** (1957) 843.
- [121] C. S. Feigerle, R. R. Corderman, S. V. Bobashev, and W. C. Lineberger. Binding-energies and structure of transition-metal negative-ions. *J. Chem. Phys.* **74** (1981) 1580.
- [122] J. Thøgersen, M. Scheer, L. D. Steele, H. K. Haugen, and W. P. Wijesundera. Two-photon detachment of negative ions via magnetic dipole transitions. *Phys. Rev. Lett.* **76** (1996) 2870.
- [123] R. C. Bilodeau, M. Scheer, H. K. Haugen, and R. L. Brooks. Near-threshold laser spectroscopy of iridium and platinum negative ions: Electron affinities and the threshold law. *Phys. Rev. A* **61** (1999) 012505.
- [124] Jordan TOF Products, Inc., see [www.rmjordan.com](http://www.rmjordan.com).
- [125] W. R. Gentra and C. F. Giese. 10-microsecond pulsed molecular-beam source and a fast ionization detector. *Rev. Sci. Instrum.* **49** (1978) 595.
- [126] D. J. Harding, C. Kerpel, G. Meijer, and A. Fielicke. Activated methane on small cationic platinum clusters. *Angew. Chem., Int. Ed.* **51** (2012) 817.
- [127] G. E. Moore. Cramming more components onto integrated circuits. *Electronics* **38** (1965) 114.
- [128] M. Haselman and S. Hauck. The future of integrated circuits: A survey of nanoelectronics. *Proc. IEEE* **98** (2010) 11.
- [129] D. Vuillaume. Molecular nanoelectronics. *Proc. IEEE* **98** (2010) 2111.
- [130] R. I. Bahar, D. Hammerstrom, J. Harlow, J. Joyner, William H., C. Lau, D. Marculescu, A. Orailoglu, and M. Pedram. Architectures for silicon nanoelectronics and beyond. *Computer* **40** (2007) 25.
- [131] K. M. Ho, A. A. Shvartsburg, B. C. Pan, Z. Y. Lu, C. Z. Wang, J. G. Wacker, J. L. Fye, and M. F. Jarrold. Structures of medium-sized silicon clusters. *Nature* **392** (1998) 582.
- [132] B. Liu, Z. Y. Lu, B. C. Pan, C. Z. Wang, K. M. Ho, A. A. Shvartsburg, and M. F. Jarrold. Ionization of medium-sized silicon clusters and the geometries of the cations. *J. Chem. Phys.* **109** (1998) 9401.

- [133] P. Garcia-Fernandez, J. E. Boggs, and J. F. Stanton. Ab initio simulation of the vibrationally resolved photoelectron spectrum of  $\text{Si}_3^-$ . *J. Chem. Phys.* **126** (2007) 074305.
- [134] Y. Achiba, M. Kohno, M. Ohara, S. Suzuki, and H. Shiromaru. Electron detachment spectroscopic study on carbon and silicon cluster anions. *J. Electron Spectrosc. Relat. Phenom.* **142** (2005) 231.
- [135] C. S. Xu, T. R. Taylor, G. R. Burton, and D. M. Neumark. Vibrationally resolved photoelectron spectroscopy of silicon cluster anions  $\text{Si}_n^-$  ( $n=3-7$ ). *J. Chem. Phys.* **108** (1998) 1395.
- [136] J. Müller, B. Liu, A. A. Shvartsburg, S. Ogut, J. R. Chelikowsky, K. W. M. Siu, K. M. Ho, and G. Ganteför. Spectroscopic evidence for the tricapped trigonal prism structure of semiconductor clusters. *Phys. Rev. Lett.* **85** (2000) 1666.
- [137] M. A. Hoffmann, G. Wrigge, B. von Issendorff, J. Müller, G. Ganteför, and H. Haberland. Ultraviolet photoelectron spectroscopy of  $\text{Si}_4^-$  to  $\text{Si}_{1000}^-$ . *Eur. Phys. J. D* **16** (2001) 9.
- [138] G. Meloni, M. J. Ferguson, S. M. Sheehan, and D. M. Neumark. Probing structural transitions of nanosize silicon clusters via anion photoelectron spectroscopy at 7.9 eV. *Chem. Phys. Lett.* **399** (2004) 389.
- [139] S. J. Peppernick, K. D. D. Gunaratne, S. G. Sayres, and A. W. Castleman, Jr. Photoelectron imaging of small silicon cluster anions,  $\text{Si}_n^-$  ( $n=2-7$ ). *J. Chem. Phys.* **132** (2010) 044302.
- [140] K. Raghavachari. Theoretical study of small silicon clusters - Equilibrium geometries and electronic-structures of  $\text{Si}_{2-7}$ ,  $\text{Si}_{10}$ . *J. Chem. Phys.* **84** (1986) 5672.
- [141] P. Ballone, W. Andreoni, R. Car, and M. Parrinello. Equilibrium structures and finite temperature properties of silicon microclusters from ab initio molecular-dynamics calculations. *Phys. Rev. Lett.* **60** (1988) 271.
- [142] K. Raghavachari and C. M. Rohlfing. Bonding and stabilities of small silicon clusters - A theoretical-study of  $\text{Si}_7$ - $\text{Si}_{10}$ . *J. Chem. Phys.* **89** (1988) 2219.
- [143] W. von Niessen and V. G. Zakrzewski. Complex electron-affinity processes and ionization in the clusters  $\text{Si}_3$ - $\text{Si}_{10}$ . *J. Chem. Phys.* **98** (1993) 1271.
- [144] B. X. Li, P. L. Cao, and X. Y. Zhou. Electronic and geometric structures of  $\text{Si}_n^-$  and  $\text{Si}_n^+$  ( $n=2-10$ ) clusters and in comparison with  $\text{Si}_n$ . *Phys. Status Solidi B* **238** (2003) 11.

- [145] J. C. Yang, W. G. Xu, and W. S. Xiao. The small silicon clusters Si, ( $n=2-10$ ) and their anions: Structures, thermochemistry, and electron affinities. *J. Mol. Struct. THEOCHEM* **719** (2005) 89.
- [146] S. Nigam, C. Majumder, and S. K. Kulshreshtha. Structural and electronic properties of Si<sub>n</sub>, Si<sub>n</sub><sup>-</sup>, and PSi<sub>n-1</sub> clusters ( $2 \leq n \leq 13$ ): Theoretical investigation based on ab initio molecular orbital theory. *J. Chem. Phys.* **125** (2006) 074303.
- [147] U. Röthlisberger, W. Andreoni, and M. Parrinello. Structure of nanoscale silicon clusters. *Phys. Rev. Lett.* **72** (1994) 665.
- [148] A. Tekin and B. Hartke. Global geometry optimization of silicon clusters employing empirical potentials, density functionals, and ab initio calculations. *J. Theor. Comput. Chem.* **4** (2005) 1119.
- [149] S. Goedecker, W. Hellmann, and T. Lenosky. Global minimum determination of the Born-Oppenheimer surface within density functional theory. *Phys. Rev. Lett.* **95** (2005) 055501.
- [150] S. De, S. A. Ghasemi, A. Willand, L. Genovese, D. Kanhere, and S. Goedecker. The effect of ionization on the global minima of small and medium sized silicon and magnesium clusters. *J. Chem. Phys.* **134** (2011) 124302.
- [151] K. D. Rinnen and M. L. Mandich. Spectroscopy of neutral silicon clusters, Si<sub>18</sub>-Si<sub>41</sub> - Spectra are remarkably size independent. *Phys. Rev. Lett.* **69** (1992) 1823.
- [152] Q. S. Ran, R. W. Schmude, M. Miller, and K. A. Gingerich. Mass-spectrometric investigation of the thermodynamic properties of the Si<sub>5</sub> molecule. *Chem. Phys. Lett.* **230** (1994) 337.
- [153] K. A. Gingerich, Q. S. Ran, and R. W. Schmude. Mass spectrometric investigation of the thermodynamic properties of the Si<sub>6</sub> molecule. *Chem. Phys. Lett.* **256** (1996) 274.
- [154] G. Meloni and K. A. Gingerich. Thermodynamic investigation of the Si<sub>7</sub> and Si<sub>8</sub> clusters by Knudsen cell mass spectrometry. *J. Chem. Phys.* **115** (2001) 5470.
- [155] K. Fuke, K. Tsukamoto, F. Misaizu, and M. Sanekata. Near-threshold photoionization of silicon clusters in the 248-146 nm region - Ionization-potentials for Si<sub>n</sub>. *J. Chem. Phys.* **99** (1993) 7807.

- [156] O. Kostko, S. R. Leone, M. A. Duncan, and M. Ahmed. Determination of ionization energies of small silicon clusters with vacuum ultraviolet radiation. *J. Phys. Chem. A* **114** (2010) 3176.
- [157] E. C. Honea, A. Ogura, C. A. Murray, C. A., K. Raghavachari, W. O. Sprenger, M. F. Jarrold, and W. L. Brown. Raman-spectra of size-selected silicon clusters and comparison with calculated structures. *Nature* **366** (1993) 42.
- [158] S. Li, R. J. Vanzee, W. Weltner, and K. Raghavachari. Si<sub>3</sub>–Si<sub>7</sub> - Experimental and theoretical infrared-spectra. *Chem. Phys. Lett.* **243** (1995) 275.
- [159] E. C. Honea, A. Ogura, D. R. Peale, C. Felix, C. A. Murray, K. Raghavachari, W. O. Sprenger, M. F. Jarrold, and W. L. Brown. Structures and coalescence behavior of size-selected silicon nanoclusters studied by surface-plasmon-polariton enhanced Raman spectroscopy. *J. Chem. Phys.* **110** (1999) 12161.
- [160] P. Gruene, A. Fielicke, G. Meijer, E. Janssens, V. T. Ngan, M. T. Nguyen, and P. Lievens. Tuning the geometric structure by doping silicon clusters. *ChemPhysChem* **9** (2008) 703.
- [161] R. Gehrke, P. Gruene, A. Fielicke, G. Meijer, and K. Reuter. Nature of Ar bonding to small Co<sub>n</sub><sup>+</sup> clusters and its effect on the structure determination by far-infrared absorption spectroscopy. *J. Chem. Phys.* 034306.
- [162] H. K. Woo, P. Wang, K. C. Lau, X. Xing, C. Chang, and C. Y. Ng. State-selected and state-to-state photoionization study of trichloroethene using the two-color infrared-vacuum ultraviolet scheme. *J. Chem. Phys.* **119** (2003) 9333.
- [163] S. A. Krasnokutski, Y. X. Lei, J. S. Lee, and D. S. Yang. Pulsed-field ionization photoelectron and IR-UV resonant photoionization spectroscopy of Al-thymine. *J. Chem. Phys.* **129** (2008) 124309.
- [164] C. J. Sansonetti, J. Reader, and K. Vogler. Precision measurement of wavelengths emitted by a molecular fluorine laser at 157 nm. *Appl. Optics* **40** (2001) 1974.
- [165] D. J. Trevor, D. M. Cox, K. C. Reichmann, R. O. Brickman, and A. Kaldor. Ionizing laser intensity dependence of the silicon cluster photoionization mass-spectrum. *J. Phys. Chem.* **91** (1987) 2598.
- [166] M. B. Knickelbein and W. J. C. Menezes. Metal cluster-rare gas van der Waals complexes - Nb<sub>n</sub>Ar<sub>m</sub> and Fe<sub>n</sub>Kr<sub>m</sub>. *Chem. Phys. Lett.* **184** (1991) 433.



- [167] V. N. Bagratashvili, V. S. Letokhov, A. A. Makarov, and E. A. Ryabov. Multiple photon IR laser photophysics and photochemistry. iii. *Laser Chem.* **4** (1984) 171.
- [168] A. S. Sudbø, P. A. Schulz, D. J. Krajnovich, Y. T. Lee, and Y. R. Shen. Photoionization study of multiphoton-excited SF<sub>6</sub> in a molecular beam. *Opt. Lett.* **4** (1979) 219.
- [169] M.J. Frisch, et al. Gaussian 03, revision C.02; Gaussian, Inc.: Wallingford, CT, 2004.
- [170] A. D. Becke. Density-functional exchange-energy approximation with correct asymptotic-behavior. *Phys. Rev. A* **38** (1988) 3098.
- [171] J. P. Perdew. Density-functional approximation for the correlation-energy of the inhomogeneous electron-gas. *Phys. Rev. B* **33** (1986) 8822.
- [172] A. Schäfer, H. Horn, and R. Ahlrichs. Fully optimized contracted Gaussian-basis sets for atoms Li to Kr. *J. Chem. Phys.* **97** (1992) 2571.
- [173] A. Schäfer, C. Huber, and R. Ahlrichs. Fully optimized contracted Gaussian-basis sets of triple zeta valence quality for atoms Li to Kr. *J. Chem. Phys.* **100** (1994) 5829.
- [174] G. S. Icking-Konert, H. Handschuh, P. S. Bechthold, G. Ganteför, B. Kessler, and W. Eberhardt. Vibrationally resolved photoelectron spectra of annealed C<sub>n</sub><sup>-</sup> and Si<sub>n</sub><sup>-</sup> clusters. *Surf. Rev. Lett.* **3** (1996) 483.
- [175] C. Y. Zhao and K. Balasubramanian. Geometries and spectroscopic properties of silicon clusters (Si<sub>5</sub>, Si<sub>5</sub><sup>+</sup>, Si<sub>5</sub><sup>-</sup>, Si<sub>6</sub>, Si<sub>6</sub><sup>+</sup>, and Si<sub>6</sub><sup>-</sup>). *J. Chem. Phys.* **116** (2002) 3690.
- [176] A. D. Zdetsis. Fluxional and aromatic behavior in small magic silicon clusters: A full ab initio study of Si<sub>n</sub>, Si<sub>n</sub><sup>1-</sup>, Si<sub>n</sub><sup>2-</sup>, and Si<sub>n</sub><sup>1+</sup>, n=6, 10 clusters. *J. Chem. Phys.* **127** (2007) 014314.
- [177] P. Karamanis, D. Zhang-Negrerie, and C. Pouchan. A critical analysis of the performance of conventional ab initio and DFT methods in the computation of Si<sub>6</sub> ground state. *Chem. Phys.* **331** (2007) 417.
- [178] K. Raghavachari and C. M. Rohlfing. Structures of Si<sub>10</sub> - Are there conventionally bonded low-energy isomers. *Chem. Phys. Lett.* **198** (1992) 521.

- [179] X. L. Zhu and X. C. Zeng. Structures and stabilities of small silicon clusters: Ab initio molecular-orbital calculations of Si<sub>7</sub>–Si<sub>11</sub>. *J. Chem. Phys.* **118** (2003) 3558.
- [180] W. Hellmann, R. G. Hennig, S. Goedecker, C. J. Umrigar, B. Delley, and T. Lenosky. Questioning the existence of a unique ground-state structure for Si clusters. *Phys. Rev. B* **75** (2007) 085411.
- [181] T. S. Duffy, R. J. Hemley, and H. K. Mao. Equation of state and shear-strength at multimegabar pressures - magnesium-oxide to 227GPa. *Phys. Rev. Lett.* **74** (1995) 1371.
- [182] S. L. Huang, D. DewHughes, D. N. Zheng, and R. Jenkins. Effects of MgO addition on phase evolution and flux pinning of Bi-2212/Ag tapes fabricated by electrophoretic deposition and partial-melting processing. *Supercond. Sci. Technol.* **9** (1996) 368.
- [183] W. H. Wei, Y. G. Sun, J. Schwartz, K. Goretta, U. Balachandran, and A. Bhargava. Preparation and properties of nanosize TiO<sub>2</sub> and MgO-doped Bi<sub>2</sub>Sr<sub>2</sub>CaCu<sub>2</sub>O<sub>x</sub> tapes. *IEEE T. Appl. Supercon.* **7** (1997) 1556.
- [184] W. Wei, J. Schwartz, K. C. Goretta, U. Balachandran, and A. Bhargava. Effects of nanosize MgO additions to bulk Bi<sub>2.1</sub>Sr<sub>1.7</sub>CaCu<sub>2</sub>O<sub>x</sub>. *Physica C* **298** (1998) 279.
- [185] K. Christova, A. Manov, J. Nyhus, U. Thisted, O. Herstad, S. E. Foss, K. N. Haugen, and K. Fossheim. Bi<sub>2</sub>Sr<sub>2</sub>CaCu<sub>2</sub>O<sub>x</sub> bulk superconductor with MgO particles embedded. *J. Alloys Compd.* **340** (2002) 1.
- [186] B. R. Ni, K. Asayama, and S. Kiyuna. Relationship between MgO particles addition and critical current density in Bi-2212 thick film grown on oxidized Ni substrate. *Physica C* **372** (2002) 1868.
- [187] A. Iluyshechkin, I. E. Agranovski, I. S. Altman, N. Racha, and M. Choi. Distribution of MgO nanoparticles in Bi-2212/Ag tapes and their effect on the superconducting properties. *Supercond. Sci. Technol.* **18** (2005) 1123.
- [188] M. A. Aramendia, V. Borau, C. Jimenez, J. M. Marinas, A. Porras, and F. J. Urbano. Magnesium oxides as basic catalysts for organic processes - study of the dehydrogenation-dehydration of 2-propanol. *J. Catal.* **161** (1996) 829.
- [189] G. Szöllösi and M. Bartok. Vapour-phase heterogeneous catalytic transfer hydrogenation of alkyl methyl ketones on MgO: Prevention of the deactivation of MgO in the presence of carbon tetrachloride. *Appl. Catal., A* **169** (1998) 263.

- [190] G. Szöllösi and M. Bartok. Catalytic transfer hydrogenation of 2-butanone on MgO. New active surface sites generated by treatment with chloroform. *Catal. Lett.* **59** (1999) 179.
- [191] J. H. Lunsford. Catalytic conversion of methane to more useful chemicals and fuels: a challenge for the 21st century. *Catal. Today* **63** (2000) 165.
- [192] H. Schwarz. Chemistry with methane: Concepts rather than recipes. *Angew. Chem., Int. Ed.* **50** (2011) 10096.
- [193] J. H. Lunsford. The catalytic oxidative coupling of methane. *Angew. Chem., Int. Ed. Engl.* **34** (1995) 970.
- [194] E. V. Kondrotenko and M. Baerns. in *Handbook of Heterogeneous Catalysis*, (Eds.: G. Ertl, H. Knözinger, F. Schüth, and J. Weitkamp). Wiley-VCH (2008). ISBN 3527312412.
- [195] T. Ito and J. H. Lunsford. Synthesis of ethylene and ethane by partial oxidation of methane over lithium-doped magnesium-oxide. *Nature* **314** (1985) 721.
- [196] T. Ito, J. X. Wang, C. H. Lin, and J. H. Lunsford. Oxidative dimerization of methane over a lithium-promoted magnesium-oxide catalyst. *J. Am. Chem. Soc.* **107** (1985) 5062.
- [197] S. J. Korf, J. A. Roos, N. A. Debruijn, J. G. van Ommen, and J. R. H. Ross. Lithium chemistry of lithium doped magnesium-oxide catalysts used in the oxidative coupling of methane. *Appl. Catal.* **58** (1990) 131.
- [198] D. J. C. Yates and N. E. Zlotin. Blank reactor corrections in studies of the oxidative dehydrogenation of methane. *J. Catal.* **111** (1988) 317.
- [199] J. X. Wang and J. H. Lunsford. Characterization of  $[\text{Li}^+\text{O}^-]$  centers in lithium-doped MgO catalysts. *J. Phys. Chem.* **90** (1986) 5883.
- [200] P. J. Gellings and H. J. M. Bouwmeester. Solid state aspects of oxidation catalysis. *Catal. Today* **58** (2000) 1.
- [201] L. M. Aparicio, S. A. Rossini, D. G. Sanfilippo, J. E. Rekoske, A. A. Trevino, and J. A. Dumesic. Microkinetic analysis of methane dimerization reaction. *Ind. Eng. Chem. Res.* **30** (1991) 2114.
- [202] J. Sun, J. W. Thybaut, and G. B. Marin. Microkinetics of methane oxidative coupling. *Catal. Today* **137** (2008) 90.

- [203] S. Arndt, G. Laugel, S. Levchenko, R. Horn, M. Baerns, M. Scheffler, R. Schlögl, and R. Schomäcker. A critical assessment of Li/MgO-based catalysts for the oxidative coupling of methane. *Catal. Rev. - Sci. Eng.* **53** (2011) 424.
- [204] J. A. Fagan, J. R. Simpson, B. J. Bauer, S. H. D. Lacerda, M. L. Becker, J. Chun, K. B. Migler, A. R. H. Walker, and E. K. Hobbie. Length-dependent optical effects in single-wall carbon nanotubes. *J. Am. Chem. Soc.* **129** (2007) 10607.
- [205] J. Kong, N. R. Franklin, C. W. Zhou, M. G. Chapline, S. Peng, K. J. Cho, and H. J. Dai. Nanotube molecular wires as chemical sensors. *Science* **287** (2000) 622.
- [206] P. G. Collins, K. Bradley, M. Ishigami, and A. Zettl. Extreme oxygen sensitivity of electronic properties of carbon nanotubes. *Science* **287** (2000) 1801.
- [207] K. Komatsu, M. Murata, and Y. Murata. Encapsulation of molecular hydrogen in fullerene C<sub>60</sub> by organic synthesis. *Science* **307** (2005) 238.
- [208] Y. B. Li, Y. Bando, D. Golberg, and Z. W. Liu. Ga-filled single-crystalline MgO nanotube: Wide-temperature range nanothermometer. *Appl. Phys. Lett.* **83** (2003) 999.
- [209] M. S. Arnold, P. Avouris, Z. W. Pan, and Z. L. Wang. Field-effect transistors based on single semiconducting oxide nanobelts. *J. Phys. Chem. B* **107** (2003) 659.
- [210] G. X. Wang, J. S. Park, M. S. Park, and X. L. Gou. Synthesis and high gas sensitivity of tin oxide nanotubes. *Sens. Actuators, B* **131** (2008) 313.
- [211] C. N. R. Rao, F. L. Deepak, G. Gundiah, and A. Govindaraj. Inorganic nanowires. *Prog. Solid State Chem.* **31** (2003) 5.
- [212] P. D. Yang and C. M. Lieber. Nanostructured high-temperature superconductors: Creation of strong-pinning columnar defects in nanorod/superconductor composites. *J. Mater. Res.* **12** (1997) 2981.
- [213] J. Zhan, Y. Bando, J. Hu, and D. Golberg. Bulk synthesis of single-crystalline magnesium oxide nanotubes. *Inorg. Chem.* **43** (2004) 2462.
- [214] Q. Yang, J. Sha, L. Wang, Y. Wang, X. Ma, J. Wang, and D. Yang. Synthesis of MgO nanotube bundles. *Nanotechnology* **15** (2004) 1004.
- [215] P. J. Ziemann and A. W. Castleman, Jr. Stabilities and structures of gas-phase MgO clusters. *J. Chem. Phys.* **94** (1991) 718.

- [216] T. M. Köhler, H. P. Gail, and E. Sedlmayr. MgO dust nucleation in M-stars: Calculation of cluster properties and nucleation rates. *Astron. Astrophys.* **320** (1997) 553.
- [217] E. de la Puente, A. Aguado, A. Ayuela, and J. M. Lopez. Structural and electronic properties of small neutral  $(\text{MgO})_n$  clusters. *Phys. Rev. B* **56** (1997) 7607.
- [218] M. Wilson. Stability of small MgO nanotube clusters: Predictions of a transferable ionic potential model. *J. Phys. Chem. B* **101** (1997) 4917.
- [219] F. Calvo. Crossover between ionic-covalent bonding and pure ionic bonding in magnesium oxide clusters. *Phys. Rev. B* **67** (2003) 161403.
- [220] J. S. Bhatt and I. J. Ford. Investigation of MgO as a candidate for the primary nucleating dust species around M stars. *Mon. Not. R. Astron. Soc.* **382** (2007) 291.
- [221] C. Roberts and R. L. Johnston. Investigation of the structures of MgO clusters using a genetic algorithm. *Phys. Chem. Chem. Phys.* **3** (2001) 5024.
- [222] J. Carrasco, F. Illas, and S. T. Bromley. Ultralow-density nanocage-based metal-oxide polymorphs. *Phys. Rev. Lett.* **99** (2007) 235502.
- [223] R. B. Dong, X. S. Chen, X. F. Wang, and W. Lu. Structural transition of hexagonal tube to rocksalt for  $(\text{MgO})_{(3n)}$ ,  $2 \leq n \leq 10$ . *J. Chem. Phys.* **129** (2008) 044705.
- [224] Y. Zhang, H. S. Chen, B. X. Liu, C. R. Zhang, X. F. Li, and Y. C. Wang. Melting of  $(\text{MgO})_n$  ( $n=18, 21$ , and  $24$ ) clusters simulated by molecular dynamics. *J. Chem. Phys.* **132** (2010) 194304.
- [225] J. M. Recio, R. Pandey, A. Ayuela, and A. B. Kunz. Molecular-orbital calculations on  $(\text{MgO})_n$  and  $(\text{MgO})_n^+$  clusters ( $n=1-13$ ). *J. Chem. Phys.* **98** (1993) 4783.
- [226] M. J. Malliavin and C. Coudray. Ab initio calculations on  $(\text{MgO})_n$ ,  $(\text{CaO})_n$ , and  $(\text{NaCl})_n$  clusters ( $n=1-6$ ). *J. Chem. Phys.* **106** (1997) 2323.
- [227] G. Bilalbegovic. Structural and electronic properties of MgO nanotube clusters. *Phys. Rev. B* **70** (2004) 045407.
- [228] A. Jain, V. Kumar, M. Sluiter, and Y. Kawazoe. First principles studies of magnesium oxide clusters by parallelized Tohoku University mixed-basis program TOMBO. *Comput. Mater. Sci.* **36** (2006) 171.

- [229] L. Chen, C. Xu, and X. F. Zhang. DFT calculations of vibrational spectra and nonlinear optical properties for MgO nanotube clusters. *J. Mol. Struct. THEOCHEM* **863** (2008) 55.
- [230] L. Chen, C. Xu, X. F. Zhang, C. A. Cheng, and T. Zhou. Size dependent structural and electronic properties of MgO nanotube clusters. *Int. J. Quantum Chem.* **109** (2009) 349.
- [231] K. Doll, J. C. Schön, and M. Jansen. Ab initio energy landscape of LiF clusters. *J. Chem. Phys.* **133** (2010) 024107.
- [232] L. Andrews and J. T. Yustein. Reaction of pulsed-laser evaporated magnesium atoms with oxygen - Infrared-spectra of linear OMgO and MgOMgO in solid argon. *J. Phys. Chem.* **97** (1993) 12700.
- [233] A. Fielicke, G. Meijer, and G. von Helden. Infrared spectroscopy of niobium oxide cluster cations in a molecular beam: Identifying the cluster structures. *J. Am. Chem. Soc.* **125** (2003) 3659.
- [234] K. R. Asmis, G. Meijer, M. Brümmer, C. Kaposta, G. Santambrogio, L. Wöste, and J. Sauer. Gas phase infrared spectroscopy of mono- and divanadium oxide cluster cations. *J. Chem. Phys.* **120** (2004) 6461.
- [235] M. Sierka, J. Döbler, J. Sauer, G. Santambrogio, M. Brümmer, L. Wöste, E. Janssens, G. Meijer, and K. R. Asmis. Unexpected structures of aluminum oxide clusters in the gas phase. *Angew. Chem., Int. Ed.* **46** (2007) 3372.
- [236] A. Kirilyuk, A. Fielicke, K. Demyk, G. von Helden, G. Meijer, and T. Rasing. Ferrimagnetic cage-like  $\text{Fe}_4\text{O}_6$  cluster: Structure determination from infrared dissociation spectroscopy. *Phys. Rev. B* **82** (2010) 020405.
- [237] G. Santambrogio, M. Brümmer, L. Wöste, J. Döbler, M. Sierka, J. Sauer, G. Meijer, and K. R. Asmis. Gas phase vibrational spectroscopy of mass-selected vanadium oxide anions. *Phys. Chem. Chem. Phys.* **10** (2008) 3992.
- [238] A. F. Holleman, E. Wiberg, and N. Wiberg. *Lehrbuch der Anorganischen Chemie*. Gruyter (1995). ISBN 3110126419.
- [239] A. Fielicke, G. Meijer, and G. von Helden. Infrared multiple photon dissociation spectroscopy of transition metal oxide cluster cations - Comparison of group Vb (V, Nb, Ta) metal oxide clusters. *Eur. Phys. J. D* **24** (2003) 69.
- [240] TURBOMOLE V6.3 2011, a development of University of Karlsruhe and Forschungszentrum Karlsruhe GmbH, 1989-2007, TURBOMOLE GmbH,

since 2007; available from  
<http://www.turbomole.com>.

- [241] A. D. Becke. Density-functional thermochemistry. 3. The role of exact exchange. *J. Chem. Phys.* **98** (1993) 5648.
- [242] C. T. Lee, W. T. Yang, and R. G. Parr. Development of the Colle-Salvetti correlation-energy formula into a functional of the electron-density. *Phys. Rev. B* **37** (1988) 785.
- [243] F. Weigend and R. Ahlrichs. Balanced basis sets of split valence, triple zeta valence and quadruple zeta valence quality for H to Rn: Design and assessment of accuracy. *Phys. Chem. Chem. Phys.* **7** (2005) 3297.
- [244] M. Sierka. Synergy between theory and experiment in structure resolution of low-dimensional oxides. *Prog. Surf. Sci.* **85** (2010) 398.
- [245] M. Sierka, A. Hogekamp, and R. Ahlrichs. Fast evaluation of the Coulomb potential for electron densities using multipole accelerated resolution of identity approximation. *J. Chem. Phys.* **118** (2003) 9136.
- [246] K. Eichkorn, F. Weigend, O. Treutler, and R. Ahlrichs. Auxiliary basis sets for main row atoms and transition metals and their use to approximate Coulomb potentials. *Theor. Chem. Acc.* **97** (1997) 119.
- [247] MOLPRO, version 2008.1, a package of ab initio programs, H.-J. Werner, P. J. Knowles, R. Lindh, F. R. Manby, M. Schütz et al., see <http://www.molpro.net>.
- [248] K. Kwapien, M. Sierka, J. Döbler, and J. Sauer. Reactions of H<sub>2</sub>, CH<sub>4</sub>, C<sub>2</sub>H<sub>6</sub>, and C<sub>3</sub>H<sub>8</sub> with [(MgO)<sub>n</sub>]<sup>+</sup> clusters studied by density functional theory. *ChemCatChem* **2** (2010) 819.
- [249] C. Ochsenfeld and R. Ahlrichs. An ab-initio investigation of structure and energetics of clusters K<sub>n</sub>Cl<sub>n</sub> and Li<sub>n</sub>F<sub>n</sub>. *Ber. Bunsen. Phys. Chem.* **98** (1994) 34.
- [250] G. von Helden, I. Holleman, G. Meijer, and B. Sartakov. Excitation of C<sub>60</sub> using a chirped free electron laser. *Opt. Express* **4** (1999) 46.
- [251] J. H. Lunsford and J. P. Jayne. Electron paramagnetic resonance of oxygen on ZnO and ultraviolet-irradiated MgO. *J. Chem. Phys.* **44** (1966) 1487.
- [252] A. J. Tench and P. Holroyd. Identification of O<sub>2</sub><sup>-</sup> adsorbed on magnesium oxide. *Chem. Commun.* **1** (1968) 471.

- [253] D. Cordischi, V. Indovina, and M. Occhiuzzi. Thermal-stability and chemical reactivity of  $(\text{O}_2^-)_s$  species adsorbed on MgO surfaces. *J. Chem. Soc., Faraday Trans. I* **74** (1978) 456.
- [254] W. B. Williamson, J. H. Lunsford, and Z. Naccache. The EPR spectrum of  $\text{O}^-$  on magnesium oxide. *Chem. Phys. Lett.* **9** (1971) 33.
- [255] Y. N. Sun, Z. H. Qin, M. Lewandowski, E. Carrasco, M. Sterrer, S. Shaikhutdinov, and H. J. Freund. Monolayer iron oxide film on platinum promotes low temperature CO oxidation. *J. Catal.* **266** (2009) 359.
- [256] Y. N. Sun, L. Giordano, J. Goniakowski, M. Lewandowski, Z. H. Qin, C. Noguera, S. Shaikhutdinov, G. Pacchioni, and H. J. Freund. The interplay between structure and CO oxidation catalysis on metal-supported ultrathin oxide films. *Angew. Chem., Int. Ed.* **49** (2010) 4418.
- [257] A. Hellman, S. Klacar, and H. Grönbeck. Low temperature CO oxidation over supported ultrathin MgO films. *J. Am. Chem. Soc.* **131** (2009) 16636.
- [258] P. Frondelius, H. Häkkinen, and K. Honkala. Adsorption and activation of  $\text{O}_2$  at Au chains on MgO/Mo thin films. *Phys. Chem. Chem. Phys.* **12** (2010) 1483.
- [259] A. Gonchar, T. Risse, H. J. Freund, L. Giordano, C. Di Valentin, and G. Pacchioni. Activation of oxygen on MgO:  $\text{O}_2^-$  radical ion formation on thin, metal-supported MgO(001) films. *Angew. Chem., Int. Ed.* **50** (2011) 2635.
- [260] A. Gonchar. *Defect chemistry of single crystalline MgO (001) films*. Ph.D. thesis, Freie Universität Berlin (2011).
- [261] C. Coudray and G. Blaise. Some size-dependent electronic properties in charged MgO clusters. *Eur. Phys. J. D* **27** (2003) 115.
- [262] F. Napoli, M. Chiesa, E. Giamello, G. Preda, C. Di Valentin, and G. Pacchioni. Formation of superoxo species by interaction of  $\text{O}_2$  with Na atoms deposited on MgO powders: A combined continuous-wave EPR (CW-EPR), hyperfine sublevel correlation (HYSCORE) and DFT study. *Chem.–Eur. J.* **16** (2010) 6776.
- [263] T. Vondrak, J. M. C. Plane, S. Broadley, and D. Janches. A chemical model of meteoric ablation. *Atmos. Chem. Phys.* **8** (2008) 7015.
- [264] J. M. C. Plane and C. L. Whalley. A new model for magnesium chemistry in the upper atmosphere. *J. Phys. Chem. A* **116** (2012) 6240.



- [265] M. Sodupe and C. W. Bauschlicher. The bonding in the low-lying states of  $\text{MgO}_2^+$ . *Chem. Phys. Lett.* **203** (1993) 215.
- [266] J. Chen, T. H. Wong, and P. D. Kleiber. Photodissociation spectroscopy of  $\text{MgO}_2^+$ . *J. Chem. Phys.* **109** (1998) 8311.
- [267] O. Yazidi, A. Ben Houria, Z. Ben Lakhdar, M. L. Senent, and M. Hochlaf. Electronic structure and spectroscopy of the  $\text{MgO}_2^+$  cation. *Chem. Phys.* **348** (2008) 215.
- [268] J. M. C. Plane and M. Helmer. Laboratory study of the reactions  $\text{Mg}+\text{O}_3$  and  $\text{MgO}+\text{O}_3$  - Implications for the chemistry of magnesium in the upper atmosphere. *Faraday Discuss.* **100** (1995) 411.
- [269] B. S. Jursic. Complete basis set investigation of the formation of the magnesium cation through magnesium atom interactions with molecular oxygen cation in gas phase. *J. Mol. Struct. THEOCHEM* **530** (2000) 59.
- [270] T. D. Jaeger, A. Fielicke, G. von Helden, G. Meijer, and M. A. Duncan. Infrared spectroscopy of water adsorption on vanadium cluster cations ( $\text{V}_x^+$ ;  $x=3-18$ ). *Chem. Phys. Lett.* **392** (2004) 409.
- [271] Y. Inokuchi, K. Ohshimo, F. Misaizu, and N. Nishi. Infrared photodissociation spectroscopy of  $[\text{Mg} \cdot (\text{H}_2\text{O})(1-4)]^+$  and  $[\text{Mg} \cdot (\text{H}_2\text{O})(1-4) \cdot \text{Ar}]^+$ . *J. Phys. Chem. A* **108** (2004) 5034.
- [272] C. J. Cramer. *Essentials of Computational Chemistry: Theories and Models*. Wiley (2004). ISBN 0470091827.
- [273] M. A. Johnson, E. V. Stefanovich, T. N. Truong, J. Gunster, and D. W. Goodman. Dissociation of water at the  $\text{MgO}(100)$ -water interface: Comparison of theory with experiment. *J. Phys. Chem. B* **103** (1999) 3391.
- [274] J. L. Anchell and A. C. Hess.  $\text{H}_2\text{O}$  dissociation at low-coordinated sites on  $(\text{MgO})_n$  clusters,  $n=4,8$ . *J. Phys. Chem.* **100** (1996) 18317.
- [275] A. L. Almeida, J. B. L. Martins, C. A. Taft, E. Longo, and W. A. Lester. Ab initio and semiempirical studies of the adsorption and dissociation of water on pure, defective, and doped  $\text{MgO}$  (001) surfaces. *J. Chem. Phys.* **109** (1998) 3671.
- [276] D. M. Murphy, R. D. Farley, I. J. Purnell, C. C. Rowlands, A. R. Yacob, M. C. Paganini, and E. Giamello. Surface defect sites formed on partially and fully dehydrated  $\text{MgO}$ : An EPR/ENDOR study. *J. Phys. Chem. B* **103** (1999) 1944.

- [277] C. M. Wang, Y. D. Wang, J. Dong, S. Liu, and Z. K. Xie. Structure sensitivity of double bond isomerization of butene over MgO surfaces: A periodic DFT study. *Comp. Theor. Chem.* **974** (2011) 52.
- [278] T. Ito, T. Murakami, and T. Tokuda. Isotopic study of hydrogen adsorption on magnesium-oxide powders. *J. Chem. Soc., Faraday Trans. I* **79** (1983) 913.
- [279] T. Ito, M. Kuramoto, M. Yoshioka, and T. Tokuda. Active-sites for hydrogen adsorption on magnesium-oxide. *J. Phys. Chem.* **87** (1983) 4411.
- [280] D. Ricci, C. Di Valentin, G. Pacchioni, P. V. Sushko, A. L. Shluger, and E. Giannelis. Paramagnetic defect centers at the MgO surface. An alternative model to oxygen vacancies. *J. Am. Chem. Soc.* **125** (2003) 738.
- [281] J. Heidberg, M. Kandel, D. Meine, and U. Wildt. The monolayer CO adsorbed on MgO(100) detected by polarization infrared-spectroscopy. *Surf. Sci.* **331** (1995) 1467.
- [282] Z. Dohnalek, G. A. Kimmel, S. A. Joyce, P. Ayotte, R. S. Smith, and B. D. Kay. Physisorption of CO on the MgO(100) surface. *J. Phys. Chem. B* **105** (2001) 3747.
- [283] M. Sterrer, T. Risse, and H. J. Freund. Low temperature infrared spectra of CO adsorbed on the surface of MgO(001) thin films. *Surf. Sci.* **596** (2005) 222.
- [284] L. Marchese, S. Coluccia, G. Martra, and A. Zecchina. Dynamic and static interactions in CO layers adsorbed on MgO smoke (100) facelets - A FTIR and HRTEM study. *Surf. Sci.* **269** (1992) 135.
- [285] G. Pacchioni, G. Cogliandro, and P. S. Bagus. Molecular-orbital cluster model study of bonding and vibrations of CO adsorbed on MgO surface. *Int. J. Quantum Chem.* **42** (1992) 1115.
- [286] A. G. Pelmenchikov, G. Morosi, A. Gamba, and S. Coluccia. A check of quantum-chemical molecular models of adsorption on oxides against experimental infrared data. *J. Phys. Chem.* **99** (1995) 15018.
- [287] Y. J. Xu, J. Q. Li, Y. F. Zhang, and W. K. Chen. CO adsorption on MgO(001) surface with oxygen vacancy and its low-coordinated surface sites: embedded cluster model density functional study employing charge self-consistent technique. *Surf. Sci.* **525** (2003) 13.
- [288] A. Fielicke, G. von Helden, G. Meijer, D. B. Pedersen, B. Simard, and D. M. Rayner. Size and charge effects on the binding of CO to late transition metal clusters. *J. Chem. Phys.* **124** (2006) 194305.

- [289] P. Gruene, A. Fielicke, G. Meijer, and D. M. Rayner. The adsorption of CO on group 10 (Ni, Pd, Pt) transition-metal clusters. *Phys. Chem. Chem. Phys.* **10** (2008) 6144.
- [290] I. Swart, F. M. F. de Groot, B. M. Weckhuysen, D. M. Rayner, G. Meijer, and A. Fielicke. The effect of charge on CO binding in rhodium carbonyls: From bridging to terminal CO. *J. Am. Chem. Soc.* **130** (2008) 2126.
- [291] J. T. Lyon, P. Gruene, A. Fielicke, G. Meijer, and D. M. Rayner. Probing C-O bond activation on gas-phase transition metal clusters: Infrared multiple photon dissociation spectroscopy of Fe, Ru, Re, and W cluster CO complexes. *J. Chem. Phys.* **131** (2009) 184706.
- [292] C. Kerpel, D. J. Harding, G. Meijer, and A. Fielicke. CO adsorption on neutral iridium clusters. *Eur. Phys. J. D* **63** (2011) 231.
- [293] A. Mantz, J.-P. Maillard, W. B. Roh, and K. N. Rao. Ground state molecular constants of  $^{12}\text{C}^{16}\text{O}$ . *J. Mol. Spectrosc.* **57** (1975) 155.
- [294] A. J. Lupinetti, S. Fau, G. Frenking, and S. H. Strauss. Theoretical analysis of the bonding between CO and positively charged atoms. *J. Phys. Chem. A* **101** (1997) 9551.
- [295] J. Roithova and D. Schröder. Selective activation of alkanes by gas-phase metal ions. *Chem. Rev.* **110** (2010) 1170.
- [296] D. Schröder and J. Roithova. Low-temperature activation of methane: It also works without a transition metal. *Angew. Chem., Int. Ed.* **45** (2006) 5705.
- [297] D. Schröder, J. Roithova, E. Alikhani, K. Kwapien, and J. Sauer. Preferential activation of primary C-H bonds in the reactions of small alkanes with the diatomic  $\text{MgO}^{++}$  cation. *Chem. Eur. J.* **16** (2010) 4110.
- [298] L. R. Brown, M. Loelte, and J. C. Hilico. Linestrengths of the  $\nu_2$  and  $\nu_4$  bands of  $^{12}\text{CH}_4$  and  $^{13}\text{CH}_4$ . *J. Mol. Spectrosc.* **133** (1989) 273.
- [299] H. M. Kaylor and A. H. Nielsen. Infrared spectrum and molecular constants of  $\text{CD}_4$ . *J. Chem. Phys.* **23** (1955) 2139.
- [300] X. P. Xing, B. Yoon, U. Landman, and J. H. Parks. Structural evolution of Au nanoclusters: From planar to cage to tubular motifs. *Phys. Rev. B* **74** (2006) 165423.
- [301] W. Huang and L. S. Wang. Probing the 2D to 3D structural transition in gold cluster anions using argon tagging. *Phys. Rev. Lett.* **102** (2009) 153401.

- [302] H. Handschuh, G. Ganteför, and W. Eberhardt. Vibrational spectroscopy of clusters using a magnetic bottle electron spectrometer. *Rev. Sci. Instrum.* **66** (1995) 3838.
- [303] T. P. Marcy and D. G. Leopold. A vibrationally resolved negative ion photoelectron spectrum of Nb<sub>8</sub>. *Int. J. Mass Spectrom.* **195** (2000) 653.
- [304] J. Oomens, B. G. Sartakov, G. Meijer, and G. von Helden. Gas-phase infrared multiple photon dissociation spectroscopy of mass-selected molecular ions. *Int. J. Mass Spectrom.* **254** (2006) 1.
- [305] J. D. Steill, J. Oomens, J. R. Eyler, and R. N. Compton. Gas-phase infrared multiple photon dissociation spectroscopy of isolated SF<sub>6</sub><sup>-</sup> and SF<sub>5</sub><sup>-</sup> anions. *J. Chem. Phys.* **129** (2008) 244302.
- [306] P. Kupser, J. D. Steill, J. Oomens, G. Meijer, and G. von Helden. IR spectroscopy of gas-phase C<sub>60</sub><sup>-</sup>. *Phys. Chem. Chem. Phys.* **10** (2008) 6862.
- [307] O. Hampe, M. Neumaier, A. D. Boese, J. Lemaire, G. Niedner-Schatteburg, and M. M. Kappes. Infrared multiphoton electron detachment spectroscopy of C<sub>76</sub><sup>2-</sup>. *J. Chem. Phys.* **131** (2009) 124306.
- [308] A. Fielicke, C. Ratsch, G. von Helden, and G. Meijer. The far-infrared spectra of neutral and cationic niobium clusters: Nb<sub>5</sub><sup>0/+</sup> to Nb<sub>9</sub><sup>0/+</sup>. *J. Chem. Phys.* **127** (2007) 234306.
- [309] H. Kietzmann, J. Morenzin, P. S. Bechthold, G. Ganteför, and W. Eberhardt. Photoelectron spectra of Nb<sub>n</sub><sup>-</sup> clusters: Correlation between electronic structure and hydrogen chemisorption. *J. Chem. Phys.* **109** (1998) 2275.
- [310] G. Wrigge, M. A. Hoffmann, B. von Issendorff, and H. Haberland. Ultraviolet photoelectron spectroscopy of Nb<sub>4</sub><sup>-</sup> to Nb<sub>200</sub><sup>-</sup>. *Eur. Phys. J. D* **24** (2003) 23.
- [311] H. Gronbeck, A. Rosen, and W. Andreoni. Structural, electronic, and vibrational properties of neutral and charged Nb<sub>n</sub> (n = 8,9,10) clusters. *Phys. Rev. A* **58** (1998) 4630.
- [312] V. Kumar and Y. Kawazoe. Atomic and electronic structures of niobium clusters. *Phys. Rev. B* **65** (2002) 125403.
- [313] T. R. Walsh. Relaxation dynamics and structural isomerism in Nb<sub>10</sub> and Nb<sub>10</sub><sup>+</sup>. *J. Chem. Phys.* **124** (2006) 204317.

- [314] G. M. H. Knippels, X. Yan, A. M. MacLeod, W. A. Gillespie, M. Yasumoto, D. Oepts, and A. F. G. van der Meer. Generation and complete electric-field characterization of intense ultrashort tunable far-infrared laser pulses. *Phys. Rev. Lett.* **83** (1999) 1578.
- [315] J. M. Bakker, V. J. F. Lapoutre, B. Redlich, J. Oomens, B. G. Sartakov, A. Fielicke, G. von Helden, G. Meijer, and A. F. G. van der Meer. Intensity-resolved IR multiple photon ionization and fragmentation of C<sub>60</sub>. *J. Chem. Phys.* **132** (2010) 074305.
- [316] D. A. Hales, L. Lian, and P. B. Armentrout. Collision-induced dissociation of Nb<sub>n</sub><sup>+</sup> (n=2–11) - Bond-energies and dissociation pathways. *Int. J. Mass Spectrom. Ion Processes* **102** (1990) 269.
- [317] M. B. Knickelbein and S. Yang. Photoionization studies of niobium clusters - Ionization-potentials for Nb<sub>2</sub>–Nb<sub>76</sub>. *J. Chem. Phys.* **93** (1990) 5760.
- [318] D. J. Harding, P. Gruene, M. Haertelt, G. Meijer, A. Fielicke, S. M. Hamilton, W. S. Hopkins, S. R. Mackenzie, S. P. Neville, and T. R. Walsh. Probing the structures of gas-phase rhodium cluster cations by far-infrared spectroscopy. *J. Chem. Phys.* **133** (2010) 214304.
- [319] D. J. Wales and J. P. K. Doye. Global optimization by basin-hopping and the lowest energy structures of Lennard-Jones clusters containing up to 110 atoms. *J. Phys. Chem. A* **101** (1997) 5111.
- [320] R. Ahlrichs, M. Bär, M. Häser, H. Horn, and C. Kölmel. Electronic-structure calculations on workstation computers - the program system Turbomole. *Chem. Phys. Lett.* **162** (1989) 165.
- [321] O. Treutler and R. Ahlrichs. Efficient molecular numerical-integration schemes. *J. Chem. Phys.* **102** (1995) 346.
- [322] F. Weigend. Accurate coulomb-fitting basis sets for H to Rn. *Phys. Chem. Chem. Phys.* **8** (2006) 1057.
- [323] D. Andrae, U. Häußermann, M. Dolg, H. Stoll, and H. Preuß. Energy-adjusted abinitio pseudopotentials for the 2nd and 3rd row transition-elements. *Theor. Chim. Acta* **77** (1990) 123.
- [324] K. Eichkorn, O. Treutler, H. Öhm, M. Häser, and R. Ahlrichs. Auxiliary basis-sets to approximate Coulomb potentials. *Chem. Phys. Lett.* **242** (1995) 652.

- [325] J. M. Tao, J. P. Perdew, V. N. Staroverov, and G. E. Scuseria. Climbing the density functional ladder: Nonempirical meta-generalized gradient approximation designed for molecules and solids. *Phys. Rev. Lett.* **91** (2003) 146401.
- [326] A. Fielicke, P. Gruene, M. Haertelt, D. J. Harding, and G. Meijer. Infrared spectroscopy and binding geometries of oxygen atoms bound to cationic tantalum clusters. *J. Phys. Chem. A* **114** (2010) 9755.
- [327] J. P. Perdew, K. Burke, and M. Ernzerhof. Generalized gradient approximation made simple. *Phys. Rev. Lett.* **77** (1996) 3865.
- [328] J. P. Perdew, M. Ernzerhof, and K. Burke. Rationale for mixing exact exchange with density functional approximations. *J. Chem. Phys.* **105** (1996) 9982.
- [329] H. B. Shore, J. H. Rose, and E. Zaremba. Failure of local exchange approximation in evaluation of  $H^-$  ground-state. *Phys. Rev. B* **15** (1977) 2858.
- [330] D. Lee, F. Furche, and K. Burke. Accuracy of electron affinities of atoms in approximate density functional theory. *J. Phys. Chem. Lett.* **1** (2010) 2124.
- [331] D. Lee and K. Burke. Finding electron affinities with approximate density functionals. *Mol. Phys.* **108** (2010) 2687.
- [332] B. Wang, H. J. Zhai, X. Huang, and L. S. Wang. On the electronic structure and chemical bonding in the tantalum trimer cluster. *J. Phys. Chem. A* **112** (2008) 10962.
- [333] S. M. E. Green, S. Alex, N. L. Fleischer, E. L. Millam, T. P. Marcy, and D. G. Leopold. Negative ion photoelectron spectroscopy of the group 5 metal trimer monoxides  $V_3O$ ,  $Nb_3O$ , and  $Ta_3O$ . *J. Chem. Phys.* **114** (2001) 2653.
- [334] H. J. Zhai, B. Wang, X. Huang, and L. S. Wang. Structural evolution, sequential oxidation, and chemical bonding in tritantalum oxide clusters:  $Ta_3O_n^-$  and  $Ta_3O_n$  ( $n=1-8$ ). *J. Phys. Chem. A* **113** (2009) 9804.
- [335] V. Dryza, M. A. Addicoat, J. R. Gascooke, M. A. Buntine, and G. F. Metha. Ionization potentials of tantalum-carbide clusters: An experimental and density functional theory study. *J. Phys. Chem. A* **109** (2005) 11180.
- [336] V. Dryza, J. F. Alvino, and G. F. Metha. Onset of carbon-carbon bonding in  $Ta_5C_y$  ( $y=0-6$ ) clusters: A threshold photoionization and density functional theory study. *J. Phys. Chem. A* **114** (2010) 4080.

- [337] V. Dryza, J. R. Gascooke, M. A. Buntine, and G. F. Metha. Onset of carbon-carbon bonding in the  $\text{Nb}_5\text{C}_y$  ( $y=0-6$ ) clusters: A threshold photo-ionisation and density functional theory study. *Phys. Chem. Chem. Phys.* **11** (2009) 1060.
- [338] H. J. Zhai, B. Wang, X. Huang, and L. S. Wang. Probing the electronic and structural properties of the niobium trimer cluster and its mono- and dioxides:  $\text{Nb}_3\text{O}_n^-$  and  $\text{Nb}_3\text{O}_n$  ( $n=0-2$ ). *J. Phys. Chem. A* **113** (2009) 3866.
- [339] V. Dryza, M. A. Addicoat, J. R. Gascooke, M. A. Buntine, and G. F. Metha. Threshold photoionization and density functional theory studies of the niobium carbide clusters  $\text{Nb}_3\text{C}_n$  ( $n=1-4$ ) and  $\text{Nb}_4\text{C}_n$  ( $n=1-6$ ). *J. Phys. Chem. A* **112** (2008) 5582.
- [340] J. M. Parnis, E. Escobar-Cabrera, M. G. K. Thompson, J. P. Jacula, R. D. Lafleur, A. Guevara-Garcia, A. Martinez, and D. M. Rayner. Cluster size selectivity in the product distribution of ethene dehydrogenation on niobium clusters. *J. Phys. Chem. A* **109** (2005) 7046.
- [341] N. Fukushima, K. Miyajima, and F. Mafune. Ionization energies of niobium carbide clusters  $\text{Nb}_n\text{C}_m$  ( $n=3-10$ ,  $m=0-7$ ). *J. Phys. Chem. A* **113** (2009) 2309.
- [342] P. Wurz and K. R. Lykke. Multiphoton excitation, dissociation, and ionization of  $\text{C}_{60}$ . *J. Phys. Chem.* **96** (1992) 10129.
- [343] V. N. Pham, T. N. Vu, and T. N. Minh. A new look at the structure and vibrational spectra of small niobium clusters and their ions. *J. Phys. Chem. C* **114** (2010) 13210.
- [344] H. Kietzmann, J. Morenzin, P. S. Bechthold, G. Ganteför, W. Eberhardt, D. S. Yang, P. A. Hackett, R. Fournier, T. Pang, and C. F. Chen. Photoelectron spectra and geometric structures of small niobium cluster anions. *Phys. Rev. Lett.* **77** (1996) 4528.
- [345] R. Fournier, T. Pang, and C. F. Chen. Structural characterization of niobium-cluster anions from density-functional calculations. *Phys. Rev. A* **57** (1998) 3683.
- [346] P. V. Nhat, V. T. Ngan, T. B. Tai, and M. T. Nguyen. Reply to "Comment on 'Electronic structures, vibrational and thermochemical properties of neutral and charged niobium clusters  $\text{Nb}_n$ ,  $n=7-12$ '". *J. Phys. Chem. A* **115** (2011) 14127.
- [347] Y. Huismans, A. Rouzee, A. Gijsbertsen, J. H. Jungmann, A. S. Smolkowska, P. S. W. M. Logman, F. Lepine, C. Cauchy, S. Zamith, T. Marchenko, J. M.

- Bakker, G. Berden, B. Redlich, A. F. G. van der Meer, H. G. Muller, W. Vermin, K. J. Schafer, M. Spanner, M. Y. Ivanov, O. Smirnova, D. Bauer, S. V. Popruzhenko, and M. J. J. Vrakking. Time-resolved holography with photoelectrons. *Science* **331** (2011) 61.
- [348] P. V. Nhat, V. T. Ngan, T. B. Tai, and M. T. Nguyen. Electronic structures, vibrational and thermochemical properties of neutral and charged niobium clusters  $\text{Nb}_n$ ,  $n=7-12$ . *J. Phys. Chem. A* **115** (2011) 3523.
- [349] A. Fielicke and G. Meijer. Comment on "Electronic structures, vibrational and thermochemical properties of neutral and charged niobium clusters  $\text{Nb}_n$ ,  $n=7-12$ ". *J. Phys. Chem. A* **115** (2011) 7869.
- [350] IR-MPD spectrum has been provided by Dr. A. Fielicke. The IR-REMPI spectrum is the result from a collaboration with V.J.F. Lapoutre and J.M. Bakker.



# List of publications

## *Gas-Phase Structures of Neutral Silicon Clusters*

M. Haertelt, J. T. Lyon, P. Claes, J. de Haeck, P. Lievens, and A. Fielicke  
J. Chem. Phys. **136** (2012) 064301.

## *Structure determination of neutral MgO clusters – hexagonal nanotubes and cages*

M. Haertelt, A. Fielicke, G. Meijer, K. Kwapien, M. Sierka, and J. Sauer  
Phys. Chem. Chem. Phys. **14** (2012) 2849.

## *Structure Determination of Anionic Metal Clusters via Infrared Resonance Enhanced Multiple Photon Electron Detachment Spectroscopy*

M. Haertelt, V. J. F. Lapoutre, J. M. Bakker, B. Redlich, D.J. Harding, A. Fielicke, and G. Meijer  
J. Phys. Chem. Lett. **2** (2011) 1720.

## *Infrared-Induced Reactivity of N<sub>2</sub>O on Small Gas-Phase Rhodium Clusters*

S. M. Hamilton, W. S. Hopkins, D. J. Harding, T. R. Walsh, M. Haertelt, C. Kerpel, P. Gruene, G. Meijer, A. Fielicke, and S. R. Mackenzie  
J. Phys. Chem. A **115** (2011) 2489.

## *Structural Diversity and Flexibility of MgO Gas-Phase Clusters*

K. Kwapien, M. Sierka, J. Döbler, J. Sauer, M. Haertelt, A. Fielicke, and G. Meijer  
Angew. Chem., Int. Ed. **50** (2011) 1716.

## *Probing the structures of gas-phase rhodium cluster cations by far-infrared spectroscopy*

D. J. Harding, P. Gruene, M. Haertelt, G. Meijer, A. Fielicke, S. M. Hamilton, W. S. Hopkins, S. R. Mackenzie, S. P. Neville, and T. R. Walsh  
J. Chem. Phys. **133** (2010) 214304.

*Infrared Spectroscopy and Binding Geometries of Oxygen Atoms Bound to Cationic Tantalum Clusters*

A. Fielicke, P. Gruene, M. Haertelt, D. J. Harding, and G. Meijer  
J. Phys. Chem. A **114** (2010) 9755.

*Infrared Induced Reactivity on the Surface of Isolated Size-Selected Clusters: Dissociation of N<sub>2</sub>O on Rhodium Clusters*

S. M. Hamilton, W. S. Hopkins, D. J. Harding, T. R. Walsh, P. Gruene, M. Haertelt, A. Fielicke, G. Meijer, and S. R. Mackenzie  
J. Am. Chem. Soc. **132** (2010) 1448.

*Communications: The structure of Rh<sub>8</sub><sup>+</sup> in the gas phase*

D. J. Harding, T. R. Walsh, S. M. Hamilton, W. S. Hopkins, S. R. Mackenzie, P. Gruene, M. Haertelt, G. Meijer, and A. Fielicke  
J. Chem. Phys. **132** (2010) 011101.

*Vibrational spectroscopy of neutral silicon clusters via far-IR-VUV two color ionization*

A. Fielicke, J. T. Lyon, M. Haertelt, G. Meijer, P. Claes, J. de Haeck, and P. Lievens  
J. Chem. Phys. **131** (2009) 171105.

*Directional states of symmetric-top molecules produced by combined static and radiative electric fields*

M. Härtelt, and B. Friedrich  
J. Chem. Phys. **128** (2008) 224313.

# Lebenslauf

Marko Härtelt, geboren am 13.02.1983 in Berlin, Deutschland

2002	Abitur an der Georg-Christoph-Lichtenberg Oberschule (Gymnasium), Berlin, Deutschland
2002 - 2008	Physikstudium an der Technischen Universität Berlin, Deutschland
2006 - 2008	Diplomarbeit am Fritz-Haber-Institut in der Abteilung für Molekülphysik bei Prof. B. Friedrich mit dem Titel: "Pseudo-First-Order Stark Effect in Symmetric-Top Molecules"
2008 - 2012	Anfertigung der Dissertation "Action Spectroscopy of Strongly Bound Clusters in the Gas Phase" unter Anleitung durch Prof. Dr. G. J. M. Meijer am Fritz-Haber-Institut der Max-Planck-Gesellschaft, Berlin, Deutschland



# Acknowledgements

Nach nun beinahe 6 Jahren wird es Zeit für mich vom Fritz-Haber-Institut Abschied zu nehmen. Während meiner Diplom- und Doktorzeit in der Abteilung für Molekülphysik habe ich eine Menge Menschen kennengelernt, welche die Zeit sehr angenehm gemacht haben und mich durch die Höhen und Tiefen, die wohl bei jedem wissenschaftlichen Projekt auftreten, begleitet haben. Die erfolgreiche Bearbeitung der verschiedensten Projekte an den unterschiedlichsten Setups, an denen ich in meiner Doktorzeit gearbeitet habe, wäre ohne die Vorarbeit und Unterstützung vieler Personen niemals möglich gewesen. Es ist sicher nicht möglich allen ausreichend zu danken, aber ich hoffe niemanden vergessen zu haben.

Mein Dank geht zunächst an meinen Direktor Prof. Gerard Meijer, der meinen Entschluss, nach der Diplomarbeit das Thema komplett zu wechseln, unterstützt hat. Für seine hilfreichen Beiträge zu den Experimenten und insbesondere zu den Manuskripten möchte ich ihm danken. Ohne seine Unterstützung wäre es wohl nicht so einfach gewesen eine neue Herausforderung für meine wissenschaftliche Zukunft zu finden.

Ein herzlicher Dank geht an meinen direkten Betreuer, meinen Gruppenleiter André Fielicke, der oft mit neuen Ideen für das Experiment ankam und mir die Freiheit gab, die Interessantesten auszuwählen. Er war sich nicht zu schade selbst das Signal zu suchen, oder am Experiment zu arbeiten, wobei es schwierig werden konnte ihn wieder vom Experiment zu trennen. Schon frühzeitig hat er mir die Gelegenheit gegeben, selbstständig die Strahlzeiten durchzuführen und dabei immer den Eindruck erweckt, das trotzdem das Optimum dabei herauskommt.

I would like to thank Dan Harding for the discussions we had and the countless calculations he contributed to this work. I hope he enjoyed our experiments as much as I did, although he called me a slave driver. I take my hat off to you for careful proofreading the whole thesis and correcting the endless grammar mistakes and in particular, correcting the same mistake even the hundredth time.

Alle Resultate dieser Doktorarbeit sind aus Kollaborationen entstanden, wobei die wohl bisher erfolgreichste die mit der Gruppe von Prof. Joachim Sauer war. Für die Vielzahl an Rechnungen von Karolina Kwapien und Marek Sierka an MgO Clustern möchte ich ihnen danken. Auch wenn es uns jetzt alle an andere Orte verschlägt, so sollten wir doch auch die übrigen Resultate noch angemessen veröffentlichen.

Vivike Lapoutre und Joost Bakker vom FOM Institut für Plasmaphysik danke ich für die Unterstützung bei allen FELICE Experimenten. Nur durch ihre beständige Arbeit am Setup war es möglich, die hier präsentierten Experimente erfolgreich abzuschließen. Joost, vielen Dank dafür, dass du immer alles dafür gegeben hast mich bei Laune zu halten, in den vielen Stunden, in denen nichts funktionierte, auch wenn eine der Nachtschichten für dich weniger erfreulich endete.

Special thanks to Peter Lievens and his group, in particular, Jorg de Haeck and Pieterjan Claes. Pieterjan, I will especially remember our second beamtime together, when there was only the two of us, and the measurement computers broke down two nightshifts in a row. That was the only time I made it to the "Tapperij't Kruikje" before they locked the door.

I am grateful to Jonathan Lyon, a former group member, and still very active collaborator. I really enjoyed the first few beamtimes with you, Jon, your famous July 4th barbecues and in particular your burgers I will really miss.

Without the continuous great efforts of Britta Redlich, Lex van der Meer and the whole FELIX staff to keep the FELs running, all the experiments would not have been possible. They always tried their best to deliver an optimal IR beam and to fulfill the user's demands. The latter probably being the most difficult part as some users tend to set their requirements higher than they can achieve with their own setups... It was amazing to see how fast they were able to fix problems with the FELs, which usually was much quicker than expected. Besides keeping the FELs running they always provided a lot of support to the experiments and even fixed a midnight water leak, such that most problems were already solved when we came in for the morning shift. Here, my thanks go to Rene van Buuren, who was also a great help for the FELICE experiments. I should not forget to mention the night operators, Cor Tito and Jules van Leusden, for taking care of dinner (and the FEL). Many thanks go to all the technicians at the FOM Institute, who helped to fix all the software and electronics problems, in particular, Gerben Kaas and Bob Krijger. Anouk and Sander, thanks again for refusing your FELIX shift and allowing me to perform my last experiment. I wish you all the best for your future in Nijmegen, or wherever you go, you all did really great work.

For two very nice, but somehow unsuccessful beamtimes – corrosion in a vacuum chamber I still find odd–, I would like to thank David Rayner, who also provided important input how to make the FELICE experiments running.

In den vergangenen Jahren habe ich viele Zimmerkollegen kommen und gehen sehen und alle waren für mich eine Bereicherung, da sie bei vielen kleinen Problemen helfen konnten und oft auch nur für die manchmal dringend nötige Ablenkung gesorgt haben. Moritz, Michael, Steven, Jon, Wolfgang, Janneke, und

Simon, vielen Dank dafür.

Mein besonderer Dank geht auch an die vielen anderen Doktoranden mit denen ich die letzten Jahre verbracht habe, Ludwig, Torsten, Frank, Dagmar, Christian S., Fabian, Dan, Frauke, Peter K., Cindy, Joop, Nadja, Stephan und Isabel. Insbesondere Stephan Putzke und Peter Zieger will ich für die letzten Jahre danken, die für viel Ablenkung in der Halle gesorgt haben.

Natürlich danke ich auch den vielen beteiligten Technikern in der Feinmechanik und im ELAB des Fritz-Haber-Instituts, die auch kurzfristig meine Aufträge bearbeiteten, damit sie bis zur nächsten Strahlzeit fertig waren.

Henrik und Wolfgang danke ich für ihre vielen Hinweise zu meinen Konstruktionszeichnungen. Petrik, dafür, dass er sie auch kurzfristig umgesetzt hat. Georg, Rolf, Manfred und Andreas haben immer schnell bei Problemen geholfen. Sandy danke ich für seine Unterstützung bei unseren Lasern und Uwe für seine Hilfe bei unseren KouDA Problemen.

Bas, Bretislav, Knut und Gert standen immer für Diskussionen zur Verfügung. Ohne Inga und Andrea wäre wohl die Atmosphäre in unsere Abteilung nicht so angenehm wie ich sie die letzten Jahre erlebt habe.

Meine übrigen Gruppenmitglieder habe ich natürlich nicht vergessen. Vielen Dank Philipp, für das Einarbeiten am Anfang meiner Doktorarbeit. Du hast zusammen mit Andreas, der verantwortlich für das VMI war und dem ich an dieser Stelle ebenfalls danke, ein tolles Setup aufgebaut. Yunjie, thanks for the first tests of my source. Christian and Alex, good luck with your theses. You both were assets for the group. John, I wish you all the best for your family. Burkhard, auch wenn wir nur kurz zusammen gearbeitet haben, vielen Dank, dass du versucht hast mir die Chemie näher zu bringen, auch wenn das wohl vergeblich war.

I am indebted to all who proofread this thesis, André, Dan, Alex, Jon, Joost, and Gerard, thank you a lot.

Prof. Thomas Möller danke ich dafür, dass er erneut die Aufgabe übernommen hat, meine Arbeit zu betreuen und als Gutachter zur Verfügung steht. Mein Dank geht auch an Frau Prof. Sabine Klapp, die den Vorsitz der Prüfungskommission übernommen hat.

Bleibt mir nur noch meiner Familie, meinen Eltern und meinem Bruder André sowie Pia, für ihre Unterstützung in den vergangenen Jahren zu danken. Ein Dank geht auch an alle meine Freunde für ihr beständiges Bemühen mir zu zeigen, dass es auch ein Leben neben der Wissenschaft gibt.

Marko Härtelt  
Berlin, Juli 2012